Development of Flexible Link Slabs using Ductile Fiber Reinforced Concrete

Lárusson, Lárus Helgi

Publication date:
2013

Document Version
Publisher's PDF, also known as Version of record

Development of Flexible Link Slabs using Ductile Fiber Reinforced Concrete

Lárus Helgi Lárusson

PhD Thesis

Department of Civil Engineering
Technical University of Denmark

2013

Supervisors:

Associate Professor Gregor Fischer, DTU Byg
Professor Henrik Stang, DTU Byg

Evaluation Committee:

Professor Giovanni Plizzari, University of Brescia, Italy
Assistant Professor Michael Lepech, Stanford University, USA
Associate Professor Christos Georgakis, DTU Byg

Development of Flexible Link Slabs using Ductile Fiber Reinforced Concrete

Printed in Lyngby, Denmark
Department of Civil Engineering
Technical University of Denmark
Byg R-284
ISBN 9788778773692
ISSN 1601-2917

Preface

This thesis is submitted in partial fulfillment of the requirements for the Danish Ph.D. degree. The thesis is based on experimental investigations and analysis carried out as part of the Ph.D. project: "*Development of flexible concrete joints for deck structures with deteriorated mechanical joints and corrosion damage*", undertaken at the Department of Civil Engineering at the Technical University of Denmark (DTU Byg), Kgs. Lyngby, Denmark between October 2008 and January 2013.

The principal supervisor of the Ph.D. project was Associate Professor Gregor Fischer from DTU Byg with co-supervisors Professor Henrik Stang also from DTU Byg,

Kgs. Lyngby, January 2013

Lárus Helgi Lárusson

Acknowledgments

First, I would like to express my deepest gratitude and sincere appreciation to my supervisors, Associate Professor Gregor Fischer and co-supervisor Professor Henrik Stang for their guidance, support, and patience during my time as a PhD student.

I would like to thank my colleagues, especially Ieva Paegle and Eduardo Nuno Borges Pereira for their close collaboration, endless support, and countless discussions during our studies. Furthermore, I would like to give special thanks to my colleague Christian Skodborg Hansen for his invaluable help and encouragement throughout our journey as PhD students. To them and all other fellow PhD students and colleges that have made my experience over the past years pleasant and memorable, both on a professional level and on a personal level, I would like to express my sincerest appreciation and thank them for their moral support and friendship.

I must also acknowledge and give thanks to the laboratory technicians at DTU Byg for their assistance and support during the seemingly endless hours spent in the laboratory fabricating test setups and specimens for my experiments.

Finally, I would like to dedicate this work to my family, my mother and father, my siblings, and especially to my son and his mother who have always given me their love, care and continuous encouragement for which I am eternally grateful.

Abstract

Civil engineering structures with large dimensions, such as multi-span bridges, overpasses and viaducts, are typically equipped with mechanical expansion joints. These joints allow the individual spans of the structure to undergo unrestrained deformations due to thermal expansions and load-induced deflections of adjacent spans. Mechanical expansion joints, commonly used between simply supported spans in bridge structures, tend to deteriorate and require significant maintenance activities. Deterioration is often caused by ingress of water and chlorides into the joints, which leads to corrosion of the joint and spalling of the surrounding concrete, and more importantly to corrosion of the bridge substructure including girders and bearings. Deterioration and the resulting rehabilitation and maintenance needs of such structures constitute a significant infrastructure deficiency. In this study, it is suggested to replace the mechanical expansion joint and implement a flexible, precast ductile concrete link slab element between simply supported bridge spans.

To design and analyze the suggested link slab element, each constituent of the element, i.e. the structural reinforcement and the cementitious composite material, as well as their interaction is investigated and characterized in detail. These characteristics are especially important as all aspects of the composite behavior of reinforcement and surrounding cementitious matrix are governed by the material properties of the constituents and their interfacial bond characteristics.

Research presented in this thesis focuses on four main aspects of the composite tensile behavior, including: i) the material characterization of the cementitious composites and reinforcement, ii) the interface between the reinforcement and surrounding matrix, iii) the load-deformation response and crack development of representative sections of the reinforced composites, and iv) detailing, designing and testing of large scale prefabricated link slab elements. In addition, an application of ductile Engineered Cementitious Composite (ECC) in prefabricated floor panels is presented in this thesis as an example of the versatility of the material and the applicability of the mechanisms investigated in the main part of this study.

The conventional combination of ordinary brittle concrete and elastic plastic steel reinforcement in tensile loading has in past research shown the typical localized cracking and debonding behavior at the steel rebar-concrete interface. In this thesis, focus is on combining relatively soft, elastic FRP reinforcement with ductile concrete, which is contrary to the conventional combination of matrix and reinforcement materials in structural engineering. The mechanical response and detailed deformation characteristics of FRP reinforced ECC are the focus of research described in this thesis.

In chapter 2 on material characterization, the material properties of the cementitious composites are characterized in terms of their elastic modulus and compression

strength, as well as the first tensile crack stress and strain. For ductile cementitious composites with multiple cracking such as ECC, the tensile stress–strain behavior is of particular interest as it illustrates the pseudo strain-hardening ability of ECC. By utilizing Digital Image Correlation (DIC), accurate crack widths and crack spacing measurements are obtained, which can characterize the tensile behavior of ECC.

In chapter 3 on interfacial bond, the bond slip behavior and crack development, between the reinforcement and surrounding cementitious matrix is investigated in a unique test setup with special emphasis on crack formation and development at the rebar-matrix interface during direct tensile loading. Utilizing a high definition DIC technique in a novel approach, detailed measurements of the crack formation and debonding process are obtained. It is found that ductile ECC, in contrast to conventional brittle concrete, reduces interfacial debonding significantly, resulting in a more uniform load transfer between the reinforcement and surrounding matrix.

In chapter 4 on the tension stiffening process, the load-deformation response and crack development of reinforced prisms, the tension stiffening and tension strengthening effects are addressed in particular. The tensile load-deformation response of reinforced concrete members is typically characterized by the tension stiffening effect, which relates to the degree of rebar-matrix interface degradation. The comparison of strain hardening ECC with conventional brittle concrete showed a tension strengthening effect in addition to the tension stiffening effect. This conceptually new tension strengthening effect is a direct result of the ability of ECC to maintain or increase its load carrying contribution in the post-cracking deformation regime. As a result of the multiple cracking ability, limited crack widths and additional load carrying ability of ECC, deformation compatibility between reinforcement and cementitious matrix is established as an important interfacial bond mechanism to maintain structural integrity at relatively large deformations and under cyclic loading.

The findings from the investigations on bond-slip, tension stiffening and tension strengthening are used in Chapter 5 as input for the design and analysis of the load-deformation response and the crack development of a prefabricated flexible link slab elements potentially connecting two adjacent bridge deck segments. The link slab element, composed of GFRP reinforced ECC, exhibited the same tension stiffening and tension strengthening behavior with limited crack widths as was observed in the reinforced prisms under monotonic and cyclic loading. The combination of ductile ECC and low stiffness GFRP resulted in the highly flexible link slab, capable of facilitating relatively large deformations, contrary to the heavily reinforced and stiff continuous link slabs implemented in the field. In addition, the structural details of the suggested link slab concept, including a de-bonded active middle section and passive load transfer zones at each end, concentrated the induced deformations in the active part of the link slab as intended. The uniform deformations with limited crack widths during both monotonic and cyclic loading indicate promising results for the concept, which will be implemented in a future full-scale field demonstration.

Resumé

Store bygningskonstruktioner, så som broer og viadukter med flere fag, er typisk udført med mekaniske dilatationsfuger. Disse samlinger tillader hvert fag at deformere uhindret på grund af termisk udvidelse og lastfremkaldte deformationer af de tilstødende fag. Mekaniske dilatationsfuger, typisk anvendt i broer med simpelt understøttede spænd, vil med tiden ødelægges og kræve omfattende renoveringsarbejde. Slid og nedbrydning er ofte forsaget af indtrængende vand og chlorider i fugerne, som vil føre til korrosion i fugen og spaltning af den omkringgivende beton, og endnu vigtigere, nedbrydning af den nær- og underliggende brokonstruktion og lejer. Nedbrydningen, og det efterfølgende reparations og vedligeholdelsesarbejde af fugerne, er disse konstruktioners svaghed. I denne afhandling foreslås det at udskifte mekaniske dilatationsfuger og i stedet implementere fleksible, duktile, præfabrikerede dilatationselementer imellem de simpelt understøttede brofag.

For at designe og beregne dilatationselementet, må armeringen og det cementbaserede kompositmateriale, såvel som deres samvirkning, undersøges og karakteriseres i detaljer. Disse karakteristikker er særlig vigtige, fordi alle aspekter af samvirkningen mellem armering og cement matrix er styret af deres materialeegenskaber og skillefladeegenskaber.

Forskningen der præsenteres i denne afhandling fokuserer på fire hovedemner indenfor sammenvirkningen mellem armering og cementkompositter udsat for trækbelastning: i) materialekarakterisering af cementkompositmaterialet og armeringen, ii) skillefladen mellem armering og cementkomposit, iii) last-deformationsforløbet og revneudviklingen af forskellige armerede cementkompositter, og iv) design og test af fuldskala præfabrikerede dilatationselementer. I tillæg hertil, er anvendelsen af cementbaserede kompositmaterialer i præfabrikerede dækelementer præsenteret som et eksempel på materialets gode egenskaber, alsidighed og praktisk brug af de førnævnte undersøgte emner.

Den konventionelle kombination af beton og stålarmering i en konstruktion udsat for træk, har vist sig at danne lokaliserede træk og skillefladerevner. I denne afhandling er fokus på at kombinere relativ slap FRP armering med duktile cementbaserede materialer, hvilket er en modsætning til de almindeligt brugte materialer, beton og stål. Det mekaniske respons og detaljerede karakteristikker af FRP armerede cementkompositter er fokus for forskningen i denne afhandling.

I kapitel 2 omhandlende materialekarakterisation, er materialegenskaberne af cementkompositterne karakteriseret ved deres elasticitetsmodul, trykstyrken, trækstyrken og tilhørende tøjning. For duktile cementkompositter med fint revnedannelsesmønster, er spændings og tøjningshistorien af særlig interesse, da den illustrerer tøjningshærdeegenskaber ved duktile cementkompositter.

I kapitel 3, om skillefladevedhæftning og revnedannelse mellem armering og det omkringliggende cementkompositmateriale, er disse fænomener undersøgt ved brug af et specielt testudstyr, hvor der især er lagt vægt på monitorering af revneinitiering og revnevækst i skillefladen mellem armering og matrixmaterialet. Ved brug af en digital billedkorrelationsteknik, blev der foretaget detaljerede målinger af revnedannelse og vækst. Det blev vist at det duktile cementkompositmateriale, i modsætning til konventionel beton, reducerer revnevæksten i skillefladerne betragteligt, hvilket resulterer i en bedre og mere jævnt fordelt lastoverførsel mellem armering og det omkringliggende cementmateriale.

I kapitel 4 om tøjningshærdeprocessen, er last-deformation responset og revneudviklingen i armerede betonprismer samt tøjningshærdeprocessen og tøjningsforstærkningsprocessen undersøgt. Last-deformationsresponset af armerede betonprismer er typisk karakteriseret ved tøjningshærdeprocessen, som relaterer til svækkelsen af skillefladen mellem armering og cementmatrix. Sammenligningen mellem tøjningshærdende og almindelig beton, viste en tøjningsforstærkning. Denne konceptuelt nye tøjningsforstærkende effekt er et direkte resultat fra de duktile cementbaserede kompositmaterialers egenskab, til at vedholde eller øge styrken efter revneinitiering. Som et resultat af evnen til at danne mange og tætte revner under belastning, begrænsede revnevidder og den ekstra styrke af de duktile cementbaserede kompositter, er deformationskompabilitet mellem armering og cementmatrixen hermed etableret som en vigtig skillefladem ekanisme, til at vedholde strukturel integritet ved store deformationer eller cyklisk belastning.

Resultaterne fra undersøgelserne af skillefladerevner, tøjningshærdning og tøjningsforstærkning er brugt i kapitel 5 som grundlag for design af beregning af last-deformationsresponset og revneudviklingen i et præfabrikeret fleksibelt dilatationselement, der kan forbinde to brofag. Dilatationselementet, der er konstrueret af glasfiberarmering og et duktilt cementkompositmateriale, viste den samme tøjningshærdning og tøjningsforstærkning, der var blevet påvist med mindre forsøgsemner, belastet statisk og cyklisk. Kombinationen af cementkompositmaterialet og glasfiberarmeringen resulterede i et fleksibelt dilatationselement, i stand til at optage store deformationer, i modsætning til visse andre allerede implementerede tunge, stive og kraftigt armerede dilatationselementer. Derudover er konstruktionsdetaljerne i dilatationselementkonceptet blevet undersøgt og udført, så de udnytter egenskaberne af det udviklede element bedst muligt. Dette medfører, at der opstår en jævn fordeling af revner med begrænset revnevidde i den fleksible den af elementet under både statisk og cyklisk belastning, hvilket er lovende resultater for konceptet, der skal implementeres i et fuld-skalaforsøg.

Publications

Appended paper:

Lárusson, L. H., Fischer, G. & Jönsson, J., 2013. Prefabricated floor panels composed of fiber reinforced concrete and a steel substructure. Engineering Structures, 46, pp. 104-115.

List of papers not appended:

Lárusson, L. H. & Fischer, G., 2012. Bond slip and crack development in FRC and regular concrete specimens longitudinally reinforced with FRP or steel under tensile loading. In proceedings: Bond in Concrete 2012: Bond, Anchorage, Detailing (BIC2012), Fourth International Symposium, Brescia, Italy, vol 2, pp. 847- 854.

Lárusson, L., Fischer, G. & Jönsson, J., 2011. Mechanical Interaction between Concrete and Structural Reinforcement in the Tension Stiffening Process. In procedings: High Performance Fiber Reinforced Cement Composites 6 (HPFRCC6), Springer, 2, pp. 247-254.

Lárusson, L. H. & Fischer, G., 2011. Flexible concrete link slabs used as expansion joints in bridge decks. Proceedings of the 9th International Symposium on High Performance Concrete - Design, Verification and Utilization, (eds) Wallevik, O. And Khrapko, M., New Zealand Concrete Society. ISBN 978-0-473-19287-7.

Lárusson, L. H. & Fischer, G., 2011. Flexible Fiber Reinforced Concrete Link Slabs used as Expansion Joints in Bridge Decks. In journal: Hawaiian Connections, vol 13, 3, pp. 6-7.

Lárusson, L. H., Fischer, G. & Jönsson, J., 2009. Mechanical interaction of Engineered Cementitious Composite (ECC) reinforced with Fiber Reinforced Polymer (FRP) rebar in tensile loading. In procedings: Advances in Cement-Based Materials, (eds) van Zijl and Boshoff, CRC Press/Balkema, Leiden, ISBN: 978-0-415-87637-7, pp. 83-90.

Fischer, G., Lárusson, L. H. & Jönsson, J., 2009. Prefabricated floor and roof panels with engineered cementitious composites (ECC). Proceedings of the 2009 Structures Congress - Don't Mess with Structural Engineers: Expanding Our Role, pp. 2199-2208.

Lárusson, L. H., Fischer, G. & Jönsson, J., 2008. Application of engineered cementitious composites in modular floor panels. In procedings: BEFIB 2008: 7th RILEM International Symposium on Fibre Reinforced Concrete, (eds) Gettu, R., RILEM Publications SARL, ISBN: 978-2-35158-064-6. pp. 483-493.

Abbreviations and Symbols

Abbreviations:

AASHTO	American Association of State Highway and Transportation Officials
ACI	American Concrete Institution
AFRP	Aramid Fiber Reinforced Polymer
AIJ	Architect Institute of Japan
ASTM	American Society for Testing and Materials
CEB-FIP	Euro-International Concrete Committee – International Federation for Prestressing
CFRP	Carbon Fiber Reinforced Polymer
CMOD	Crack Mouth Opening Displacement
COD	Crack Opening Displacement
DIC	Digital Image Correlation
ECC	Engineered Cementitious Composite
fib	The International Federation for Structural Concrete
FRC	Fiber Reinforced Concrete
FRCC	Fiber Reinforced Cementitious Composite
FRP	Fiber Reinforced Polymer
GFRP	Glass Fiber Reinforced Polymer
HCD	Hollow Core Deck
HS	High Strength (steel)
ICP	Integrally Cast Panel
ISMD	Integrated Structures-Materials Design
LS	Link Slab
LVDT	Linear Variable Differential Transformer
MP	Modular Panel
PVA	PolyVinyl Alcohol
R/C	Reinforced Concrete
RH	Relative Humidity
SCC	Self Consolidating Composite
SCTT	Single Crack Tension Test
SHCC	Strain Hardening Cementitous Composite
SLS	Service Limit State
ULS	Ultimate Limit State
w/c	Water-to-Cement ratio

Symbols:

$A_{c,cr}$	Cracked cross section area
$A_{c,eff}$	Effective cross sectional area
$A_{c,ucr}$	Un-cracked cross section area
A_c	Cross sectional area of concrete
A_s	Cross sectional area of reinforcement
C_s	Circumference of reinforcement
d	Rebar diameter
d_{GFRP}	GFRP rebar diameter
dz	infinitely small element
E	Elastic modulus
E_c	Elastic modulus of concrete
E_s	Elastic modulus of reinforcement
$\overline{E}_s$	Effective elastic modulus of reinforcement
f	Natural frequency
$F_{(loading)}$	Load values in hysteresis during loading
$F_{(unloading)}$	Load values in hysteresis during unloading
f_c	Stress in concrete
f_{ck}	Average compression strength
f_{cr}	First crack tensile strength
$\overline{f}_{cr}$	First crack average strength
f_{ctm}	Mean axial tensile strength
$\overline{f}_{max}$	Maximum average strength
f_s	Stress in reinforcement
f_{tu}	Ultimate tensile strength
f_y	Yield strength of steel
h	Height of bridge section
I_{eq}	Equivalent moment of inertia
J'_b	Complimentary energy
J_{tip}	Matrix toughness
L	Length
l_g	Measured composite length
L_{ls}	Active link slab length
L_{sp}	Length of span
l_{tr}	Transition length, i.e. debonding length
m	Mass
N	Load
n	Ratio between elastic modulus of steel and concrete ($n=E_s/E_c$)
N_b	Load carried by fiber bridging

N_c	Load carried by concrete
N_s	Load carried by reinforcement
P, P_s, P_c	Force, force in reinforcement, force in concrete
P_{cr}	Force at first crack
q	Uniformly distributed load
s	Slip between reinforcement and surrounding matrix (in debonding)
s_1	Critical slip between reinforcement and surrounding matrix
t	Time
T	Time of one period
u	Mid-span deflection
$u(t)$	Peak amplitude at time t
u_s, u_c	Displacement of reinforcement, displacement of concrete
u_x	Opening displacement in debonding (separation)
v_{Max}	Maximum deflection
w	Crack width
$W_{(loading)}$	Work required during loading
$W_{(one\ cycle)}$	Energy dissipation of one cycle
$W_{(unloading)}$	Work required during unloading
w_0, w_1	Critical crack opening parameters for cohesive laws
w_{int}	Transverse crack width at the rebar-matrix interface
w_{out}	Transverse crack width at the outer cover surface
x_0	Lower boundary for cyclic displacement
x_1	Upper boundary for cyclic displacement
α_T	Expansion coefficient
β	Tension stiffening factor (also known as bond factor)
β_{exp}	Measured tension stiffening while disregarding shrinkage effect
γ_1, γ_2	Coefficients for various constants
δ	Crack opening displacement
δ_a	Crack opening displacement referring to the remote ambient stress (also called steady state crack opening displacement)
ΔL_{Vol}	Length change due to volume changes
ΔL_Θ	Length change due to rotation
ΔT	Temperature variance
$\Delta\varepsilon_s$	Tension stiffening strain
$\Delta\varepsilon_{s,max}$	Maximum tension stiffening strain, just before first crack
$\Delta\varepsilon_T$	Strain change due to Thermal expansion
$\Delta\varepsilon_\Theta$	Strain change due to rotation
ε, ε_s, ε_c	Strain ($\Delta L/L$), strain in reinforcement, strain in concrete
ε_{equ}	Strain at equilibrium between stiffening and strengthening (conceptual)

ε_m	Average measured composite strain
ε_{max}	Strain at maximum tension stiffening
ε_{sh}	Shrinkage strain
ε_{sm}	Average strain in reinforcement
ε_{tu}	Ultimate tensile strain
ζ	Damping ratio
Θ	Rotation angle at support
Θ_{max}	Maximum rotation angle at support
ρ	Reinforcement ratio
σ^*_c	Cohesive tensile stress
σ_a	Remote ambient stress (also called steady state stress)
σ_c	Stress in concrete
$\overline{\sigma}_{c,1}$, $\overline{\sigma}_{c,2}$, $\overline{\sigma}_{c,3}$	Average concrete stress at consecutive loading phases
σ_{cr}	First crack stress of the matrix
σ_{ECC}	Cohesive tensile stress in ECC
σ_{peak}	Peak bridging stress
σ_s,	Stress in reinforcement
τ, τ_0, τ_{Max}	Bond stress, initial bond stress, maximum bond stress

Contents

Chapter 1

Introduction

1.1 Framework

Figure 1-1 Examples of damage due to deterioration of expansion joints, a): in pavement on top of expansion joint (WSDOT, 2011), b): in severely corroded expansion joint seen from below (TCPI, 2012) and c): in girders and pier caps with highly corroded steel bearings (Ho and Lukashnko, 2011).

Transportation structures, such as single or multi-span bridges, overpasses or viaducts extending over moderate- or relatively large lengths are typically designed with discontinuities at piers and abutments. These discontinuities, or joints, allow the individual spans of the structure to undergo unrestrained deformations due to thermal expansions and load-induced deflections of adjacent spans. Open joints, sliding plate-joints or open finger joints allow run-off water laden with aggressive chemicals to penetrate below the roadway surface and cause corrosion of the bridge deck and substructure including girders and bearings (see Figure 1-1). In an attempt to avoid these undesira-

ble conditions, joints are typically equipped with mechanical expansion joints, such as elastomeric compression seals, that seal and protect the substructure from the aggressive run-off water while allowing movement of adjacent spans. However, most of these solutions have a relatively short service life, as they tend to deteriorate and leak due to corrosion in and around the joints and subsequently require extensive maintenance activities.

In recent years, a trend has emerged to eliminate such expansion joints by employing a jointless bridge approach. In so-called integral or semi-integral bridge designs, the superstructure is integrally connected while the substructure is allowed to be discontinuous or continuous over supporting piers. The motivation of such bridge designs is a growing awareness that mechanical expansion joints for single and multi-span bridges cause more damage and distress than the secondary stresses that the joints were initially intended to prevent, i.e. stresses induced by longitudinal and flexural movements of the bridge spans over piers and abutments (Burke, 2009). In addition to the reduced maintenance cost, integral bridge constructions are generally less expensive in design and construction than bridges with mechanical joints due to the labor intensive detailing in the latter solution. In a survey of bridges in the USA and Canada it was reported that all the integral bridges inspected were performing well with only minor problem due to poor detailing, however several non-integral bridges were reported to have leaking expansion joints and major deterioration (Nicholson et al., 1997).

Although integral bridge design is well established in USA and Canada and getting increasingly popular around the world, they are not common practice in Europe. This is mainly due to inexperience among bridge designers, constructors and authorities with integral bridge design (Feldmann et al. 2010).

Another variation of the jointless bridge approach is the so-called link slab design (Caner and Zia, 1998), where secondary stresses are decreased by providing a debonded layer between the link slab and the discontinuous substructure, thus allowing the deformations to be distributed over a larger portion of the continuous bridge deck (see Figure 1-2). In the link slab design, the bridge deck is continuous while the bridge girders remain discontinuous and simply supported.

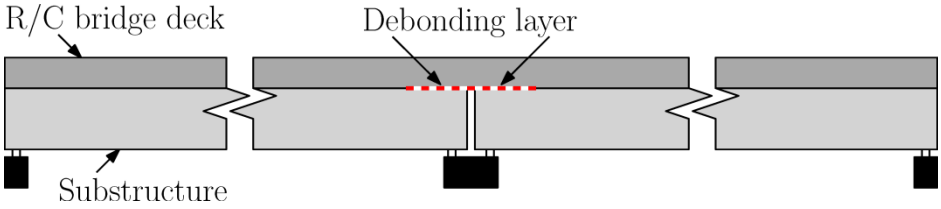

Figure 1-2 Schematic of the link slab concept with debonding layer, adopted from Caner and Zia (1998).

Investigations on such jointless deck structures using conventional steel reinforcement in concrete link slabs have indicated improved performance and economic feasibility (Caner and Zia, 1998). However, this concept requires a relatively large amount of steel reinforcement for crack control purposes and consequently provides a relatively large flexural stiffness and negative moment capacity at the joint between the spans. This contributes to a limited deformation capacity of the link slab and promotes of secondary stresses.

In an attempt to improve on the conventional reinforced concrete (R/C) link slab design, Lepech and Li (2009) suggested and implemented a link slab design in a full scale field demonstration utilizing a highly ductile Engineered Cementitous Composite (ECC). In doing so, it was possible to reduce some of the steel reinforcement for crack width control, required by the transportation authorities, due to the inherently tight crack widths in ECC. Consequently, the lower reinforcement ratio allowed the ECC link slab to behave similar to a hinge in comparison to the stiffer conventional concrete link slabs. Lepech and Li (2009) designed the ECC link slab in accordance with the American Association of State and Highway Transportation Officials (AASHTO).

In this thesis, a flexible, relatively thin precast link slab element, utilizing new and innovative structural materials with inherent performance benefits, such as highly ductile ECC and low stiffness non-corrosive Fiber Reinforced Polymer (FRP) reinforcement, is suggested. The novel design approach is proposed and investigated in order to further enhance the conventional link slab design. The combination of such structural materials, i.e. ECC reinforced with FRP, is expected to result in link slab constructions with high axial and rotational flexibility, limited crack widths and structural integrity, which ultimately lead to increased durability throughout the service life of the structures. It is therefore necessary to investigate both the potential benefits and limitations of utilizing ECC and FRP in a prefabricated link slab design by characterizing the composite behavior in terms of the load-deformation and cracking development during simulated loading conditions. Prefabricating the link slab element would furthermore eliminate the restrained shrinkage cracking which was reported in the previous ECC link slab field demonstration (Li and Lepech, 2005), shorten the construction time and reduce traffic disturbance.

The mechanical behavior of R/C or reinforced ECC structural elements is fundamentally governed by the material properties of the constituent materials (concrete and reinforcement), as well as by their mutual interaction which is facilitated by the interfacial bond characteristics and the relative slip between both materials. Understanding the composite interaction between reinforcement and surrounding cementitious matrix is essential for designers to accurately predict the various performance aspects, such as residual load and deformation capacity after cracking, crack widths and crack spacing, degree of interfacial debonding as well as potential ingress of aggressive substances. Consequently, by recognizing which sets of parameters affect or govern each

behavior, the composite design such as the link slab can be optimized to fulfill a performance driven design approach.

1.2 Brief literature review

Over the past decades, researchers have experienced that bond between reinforcement and surrounding concrete is an essential component in composite performance, affecting virtually all aspects of composite behavior, including crack width and crack spacing, short and long-term deflections, shear resistance, flexural- and axial load resistance, as well as energy absorption (Oehlers et al., 2012). However, although extensive work has been carried out on bond and the interfacial behavior of R/C over the last five decades, no general agreement on the relative significance of the various parameters affecting the intricate behavior of bond and cracking exists among researchers. Interfacial bond or bond stress is defined as the interaction and transfer of forces between reinforcement and surrounding matrix and is generally characterized by a bond – slip relationship which is typically obtained from pull-out tests (fib, 2010).

Cairns and Plizzari (2003), however, emphasized the necessity of reappraising the current standard methods of testing bond between reinforcement and surrounding concrete which were developed over 40 years ago. Cairns and Plizzari (2003) subsequently suggested a system of bond testing based on specific aspects of structural performance. Pedziwiatr (2008) furthermore describes the inadequacy of utilizing standard pull-out tests to predict or portray the actual behavior of tension zones in R/C members. In his overview, pull-out tests, particularly tests with short embedment lengths, lack a few key contributing components such as internal cracking which can cause large scatter in crack width and crack spacing.

A limited number of studies have directly measured the internal cracking and interfacial bond behavior, particularly during loading procedures. These kinds of studies do not only benefit future bond research, but also durability research where potential ingress pathways in cracked concrete or cementitious composites can be quantified.

Research focusing on the internal cracking in reinforced members, particularly around the rebar – matrix interface, is generally limited by the inherent difficulty of observing and measuring the cracking and debonding process occurring within the cementitious matrix. Although the presence of internal cracking was first documented over four decades ago (Broms, 1965; Goto, 1971), a limited number of investigations have attempted to characterize the internal crack behavior during loading. Jiang et.al. (1984), Pedziwiatr (2008), and Eckfeldt et al. (2009) all exposed the reinforcement in R/C prisms in novel test configurations while the crack formation and development, including the internal cracking at and rebar – matrix interface, were visually observed during tensile loading. In a different approach, Otsuka et al. (2003) utilized the ink-injection method (Broms, 1965; Goto, 1971) to monitor the crack process in reinforced Fiber Reinforced Cementitous Composite (FRCC) and reinforced strain hard-

ening FRCC prisms during tensile loading by utilizing an X-ray technique. Although these investigations have not produced detailed internal cracking measurements, they have contributed valuable information about the internal crack process and bond mechanism during and after loading.

Pease (2010) concluded in his work on the impact of cracking on durability of R/C that the interfacial damage is likely more important to reinforcement corrosion issues than surface crack widths. Quantifying the interfacial debonding mechanism is therefore essential in accurately assessing the durability of any steel reinforced structure susceptible to corrosion damage.

1.2.1 Reinforced Concrete (R/C)

Extensive experimental and theoretical research has been carried out on R/C members in direct tension to investigate the effect of different parameters, including concrete strength, composite interfacial bond, reinforcement ratio, cross section, rebar layout, and ratio between concrete cover to rebar diameter on the tension stiffening effect and cracking process (transverse cracks and splitting cracks) (Broms, 1965; Abrishami and Mitchell, 1996; Wollrab et al. 1996; Bischoff, 2001; Fields and Bischoff, 2004; Beeby and Scott, 2005; Lee and Kim, 2008).

Broms (1965) was among the first researchers to investigate crack width, crack spacing and internal cracking in R/C members under direct tension. In a comprehensive experimental program, Broms compared different cross section geometries and reinforcement ratios of both tension members as well as flexural members in order to characterize the cracking behavior.

Somayaji and Shah (1981) investigated an analytical formulation to predict the tension stiffening effect and cracking (crack widths and crack spacing) and compared the model to experimental results of reinforced mortar specimens. In their approach, a bond stress function was utilized instead of the commonly assumed local bond stress-slip relationship.

Abrishami and Mitchell (1996) examined splitting cracking extensively and suggested a modified formulation to predict the average concrete tensile stress after cracking (i.e. the tension stiffening effect) which accounts for the concrete cover – rebar diameter ratio. They concluded that larger rebar diameter increases the potential for splitting cracks, crack spacing increased with higher concrete strength, and higher concrete strength leads to increase an in tension stiffening.

Lee and Kim, (2008) also investigated splitting cracking in detail, but found that the tension stiffening effect and crack spacing decreased with increased concrete strength, contrary to what Abrishami and Mitchell (1996) reported.

Ouyang et al. (1997) presented a fracture energy model to predict the tension stiffening effect in R/C specimens. The model was based on formulations given by Ouyang

and Shah (1994) with slight modifications and showed good agreement with their experimental results.

Bischoff (2001) and Fields and Bischoff (2004) emphasized the importance of including shrinkage strain, which induced compression stresses in the reinforcement prior to loading, when analyzing tension stiffening. In their investigation, both the load shearing approach and strain stiffening approach were considered which yielded the same tension stiffening factor. Fields and Bischoff subsequently suggested an empirical tension stiffening factor which was shown to approximate the experimental results sufficiently.

Furthermore, Kaklauskas et al. (2009) presented an extensive numerical study on the influence of shrinkage and accompanying creep on tension stiffening of reinforced tension members and flexural beams. Subsequently a simple transformation formulation was proposed to eliminate the shrinkage affect from tension stiffening analysis.

In addition to a comprehensive experimental investigation, Beeby and Scott (2005) presented a semi-empirical formulation to predict the load-deformation and cracking behavior, which includes a bond-slip relationship and an internal cracking model.

The research examples described above illustrates some of the challenging aspects and limitations that should be considered when designing steel reinforced concrete structures that are loaded in tension, such as the link slab described by Caner and Zia (1998), and serve as background for the research described in this thesis.

1.2.2 Reinforced Fiber Reinforced Cementitious Composites (R/FRCC)

The growing number of research activities focusing on FRCC in reinforced members follows the increased attention that FRCC has gained in recent years due to its crack control and ductility characteristics. The increased attention is evident in the inclusion of FRCC in the new fib Model Code 2010 (fib, 2010) and numerous international conferences (e.g.: BEFIB, 2004; BEFIB, 2008; BEFIB, 2012). Comprehensive experimental and theoretical research has also been carried out on reinforced FRCC member in direct tension to investigate the influence of ductile deformation characteristics of FRCC as well as the effect and relations between various parameters.

Mitchell et al. (1996) were among the first researchers to comparatively examine the effect of steel fibers on tension stiffening and cracking in reinforced prisms in direct tension. They found that the addition of fibers significantly increased tension stiffening and ductility of the tension members and effectively reduced crack widths as well as prevented splitting cracks when compared to R/C members.

Noghabai (2000) investigated the load-deformation response and cracking of reinforced FRCC tension members using various fiber types, both metallic and polymeric. Test results were generally characterized by increased tension stiffening and extensive cracking. Additionally, Noghabai presents an analytical expression for the composite

response based on a fracture energy approach, the model was subsequently used in a parametric study.

Fischer and Li (2002) investigated the interactions of a highly ductile strain hardening ECC and steel reinforcement compared to that of identical R/C specimens in uniaxial tension. The combination of the highly ductile ECC matrix and steel reinforcement reviled load sharing and deformation compatibility, even after yielding of the reinforcement occurred. Consequently, debonding at the rebar – ECC matrix interface was decreased significantly compared to that of R/C.

Similar to the work by Fischer and Li (2002), Fantilli et al. (2005) investigated the strain compatibility of reinforced ductile strain hardening FRCC (R/FRCC) in direct tension. Fantilli incorporated theoretical expressions for the cohesive law for strain hardening FRCC in tension and the cohesive interface law into a numerical model and compared to experimental results.

Bischoff (2003) examined the tension stiffening effect of R/FRCC and R/C tension member during monotonic and cyclic loading. Subsequently an analytical formulation was developed to predict the smeared behavior as a material property of the cracked FRCC. Higher tension stiffening and lower crack spacing as well as smaller crack widths were reported for R/FRCC in comparison to R/C. Additionally, crack widths did not seem to increase during cyclic loading.

Rokugo et al. (2006) presented an experimental study were the load-deformation behavior of sprayed highly ductile FRCC with and without a steel mesh in direct tension were examined. The addition of the reinforcement mesh showed a superimposed load-deformation response of the constituents, even at low reinforcement ratio.

Hameed et al. (2010) experimentally investigated the effects of various FRCC and hybrid FRCC on tension stiffening in steel reinforced tension members. The result indicated that the hybrid combination of micro- and macro-fibers could effectively control the both the micro- and macro-cracking.

Tiberti et al. (2012) investigated the tension stiffening effect and cracking of steel reinforced FRCC prisms in direct tension in a comprehensive experimental study. The investigation focused on the load-deformation response, crack width and crack spacing while varying the cross sections, rebar diameter, reinforcement ratio, length of the specimens, fiber combination (micro- and macro-fibers), as well as testing R/C control tension specimens.

The research activities described in this section emphasize the enhanced structural performance obtained by adapting FRCCs in steel reinforced elements compared to that of R/C element subjected to tension. These enhanced performance characteristics consequently motivated the link slab design presented by Lepech and Li (2009).

1.2.3 Fiber Reinforced Polymer (FRP) reinforcement

The uses of FRP reinforcement, such as Glass Fiber Reinforced Polymer (GFRP), in reinforced concrete elements have also gained increased interest in recent years, mainly due to their non-corrosive nature and high load-to-weight ratio. Experimental investigations concerning tensile members reinforced with FRP have shown an increased tensile stiffening effect, however at the expense of increased crack widths in comparison to steel reinforced concrete due to FRPs lower stiffness (Bischoff and Paixao, 2004; Sooriyaarachchi and Pilakoutas, 2005).

Both Bischoff and Paixao (2004), and Sooriyaarachchi et al. (2005) reported experimental investigation of tension stiffening and cracking in of GFRP reinforced concrete tension members. Bischoff and Paixao compared GFRP reinforced tension members to R/C tension members and found tension stiffening and crack widths to be higher in the GFRP members, they furthermore showed that the increased tension stiffening effect was inversely proportional to the stiffness of the reinforcement. Bischoff and Paixao subsequently suggested an empirical expression for the tension stiffening factor. Both Bischoff and Paixao (2004), and Sooriyaarachchi et al. (2005) concluded that tension stiffening was independent of the reinforcement diameter.

Although a number of researches have examined FRP reinforced FRCC members in flexure (Li and Wang, 2002; Fischer and Li, 2003; Harajli, M., 2009; Lee et al., 2010; Wang and Belarbi, 2011; Qu et al. 2012), investigations on FRP reinforced FRCC in direct tension are limited, particularly FRPs reinforced strain hardening FRCCs. To the author's knowledge, the only studies available on FRP reinforced ECC (a highly ductile FRCC) members in direct tension is the authors previous work (Lárusson et al. 2009; Lárusson and Fischer, 2010).

The potential benefits of combining these innovative materials, i.e. FRP and FRCC in general and ECC in particular, in a composite link slab element have motivated the research activities presented in this thesis.

1.3 Scope of the work

The goal of this research project is to design, test and a analyze large scale, prefabricated, flexible link slab element, composed of highly ductile ECC reinforced with low stiffness FRP, capable of facilitating relatively large tensile deformations with a target tensile strain capacity of 1%. The flexible composite element needs to maintain structural integrity and durability during service-life cyclic actions while conforming to crack width limitations requirements. Furthermore, a relatively low stiffness (high flexibility) of the link slab element is desired in order for the two adjacent simply supported bridge spans, connected by the link slab, to undergo unrestrained deformations. To achieve this goal, a number of objectives are identified and investigated to verify the capability of the link slab and the constituents involved. To establish suf-

ficient and relevant background information to reach the goal, the following objectives are investigated in detail:

The requirements for the highly ductile ECC to be utilized in the link slab concept include high strain capacity, strain hardening behavior, multiple cracking, and limited crack widths to ensure durability during service-life. To verify that the ECC is able to exhibit these criteria, dog-bone shaped specimens are employed and tested in direct tension to obtain the stress – strain characteristics while crack initiation and development are monitored and measured with a high definition Digital Image Correlation (DIC) system. The criteria for the Fiber Reinforced Polymer (FRP) reinforcement to be applied in the flexible link slab design include a relatively soft axial load response, i.e. a low elastic modulus, a relatively large linear-elastic strain capacity, an adequate bond between reinforcement and surrounding matrix, and a high corrosion resistance. Subsequently the selected FRPs (based on characteristics given by the producer) are tested in direct tension to verify the desired requirements.

The interaction between the FRP reinforcement and surrounding ECC matrix is investigated and a relation between transverse cracking and the debonding at the rebar – matrix interface is quantitatively and qualitatively established. To accomplish this objective, a unique test setup is employed during direct tensile loading where reinforced members are constructed with a part of the reinforcement exposed. Thus, allowing the exposed rebar – matrix interface to by monitored with a DIC system during loading. This approach provides accurate crack measurements from the rebar – matrix interface to the concrete cover surface at all crack development stages. In addition to quantifying the rebar-matrix interaction, the objective of the interface analysis is also to provide an insight into the intricate debonding mechanism at the interface.

The composite load – deformation behavior as well as the crack formation and development of FRP reinforced ECC elements during monotonic tension and cyclic loading is subsequently established. The purpose of this inquiry is to obtain preliminary results in order to assess the potential and limitations of the composition for the link slab design. To achieve this objective, a reinforced prism test configuration is designed and constructed with the aim of concentrating the induced deformations in a representative section of the member. The load – deformation response is measured directly while the crack process on the representative section is monitored using a DIC technique.

Although long-term behavior, including cracking (both surface- and internal cracking), is inherently related to durability issues, direct durability assessment of the link slab is outside the scope of this thesis.

1.4 Overview of the thesis

The relationship between the different aspects of the work conducted throughout the Ph.D. study is presented schematically in Figure 1-3.

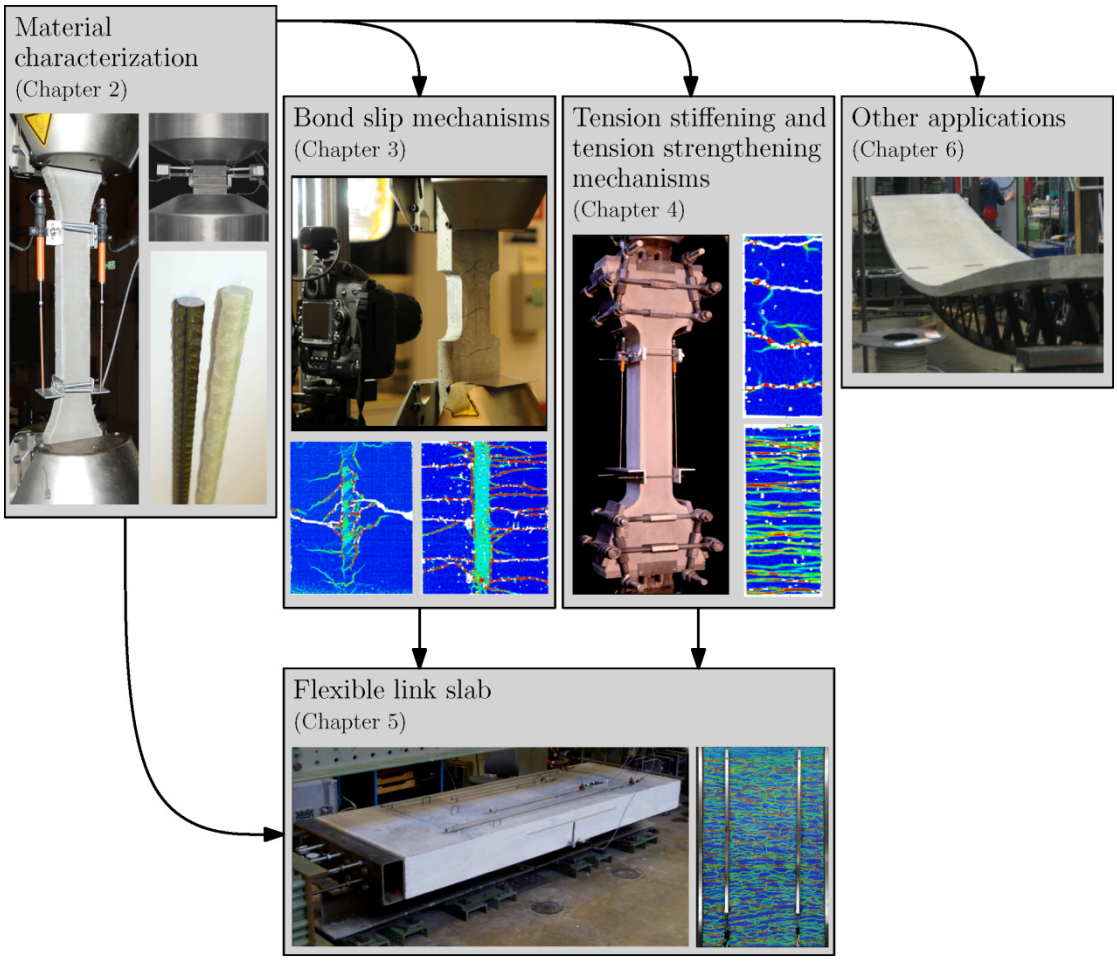

Figure 1-3 Schematic of experimental work presented in thesis.

Chapter 1: "*Introduction*", gives a general background and motivation to the present work, as well as the objectives and setup of the thesis.

Chapter 2: "*Material characterization*", provides an overview of the materials, i.e. the cementitious materials and reinforcement types, utilized in the experimental programs and analysis presented in this thesis. A brief background is given on fiber reinforced cementitious composites as well as the criteria to obtain strain hardening and multiple cracking. In addition, the various test setups and procedures used throughout this thesis to characterize the material behavior are presented. Examples of the most relevant material properties are given and discussed.

Chapter 3: "*Bond slip mechanisms*", investigates the interfacial interactions between reinforcement and surrounding cementitious matrix in detail in a unique test setup during direct tensile loading. The experimental investigation focuses on characterizing

the formation and propagation of transverse cracking and the resulting debonding, i.e. slip and opening (separation) at the rebar – matrix interface using a high definition Digital Image Correlation (DIC) technique in a novel approach. In addition, a closed form analytical solutions for slip between reinforcement and matrix, length of the debonded zone (transition length), as well as the load as a function of average transverse crack width, are derived and compared to test results.

Chapter 4: "*Tension stiffening and tension strengthening mechanisms"*, addresses the composite load – deformation behavior and crack formation and development of reinforced cementitious ties in direct tension. The tensile load – deformation response of the reinforced tension prisms are analyzed and characterized in terms of the tension stiffening process and the ability of the fiber reinforced cementitious composite to strengthen the member in tension, i.e. a tension strengthening effect. In the experimental program a representative section of reinforced prisms are investigated using DIC system to monitor the crack process, including the initiation and development of the crack widths and spacing, during monotonic tension and cyclic loading at relatively large tensile deformations.

Chapter 5: "*Flexible link slab*", presents the design and analysis of a large scale prefabricated flexible link slab elements tested in direct tension. The presented investigation focuses on the load – deformation response and crack development of flexible elements, composed of ductile ECC reinforced with low stiffness GFRP, during both monotonic tensile deformations and cyclic action. Additionally, structural details, such as anchorage between the link slab element and representative bridge decks at each end, a passive load transfer zone, and an active middle section is assessed to determine how effective the design redistributes the induced deformations.

Chapter 6: "*Other applications*", presents an extended summary of the appended paper: "*Prefabricated floor panels composed of fiber reinforced concrete and a steel substructure*" (Lárusson et al., 2013), in which a large scale novel application of ductile ECC in prefabricated, lightweight floor panels is examined. The investigation and analysis focuses on structural requirements during serviceability- and ultimate limit state loading, as well as addressing structural details. The mid span deflections, natural frequency and damping ratios are evaluated during serviceability loading, and the load capacity, deflections and failure mode are of particular interest during ultimate limit state loading. The investigation is presented in this thesis as an example of the versatility of the material and the applicability of the mechanisms investigated in the main part of this study.

Chapter 7: "*Conclusions*", summarizes the main findings and conclusions from the investigations and analysis presented throughout this thesis. Furthermore, an outlook for future work is presented and briefly discussed.

Bibliography

Abrishami, H. H. & Mitchell, D.,1996. Influence of splitting cracks on tension stiffening. ACI Structural Journal, , 93, pp. 703-710.

Beeby, A. & Scottt, R., 2005. Cracking and deformation of axially reinforced members subjected to pure tension. Magazine of Concrete Research, 57, pp. 611-621.

BEFIB 2004, Di Prisco, M., Felicetti, R. & Plizzari, G. (eds.), 2004. 6th International RILEM Symposium on Fibre-Reinforced Concretes (FRC) - BEFIB 2004, Bagneux, France, RILEM Publications S.A.R.L., ISBN: 2-912143-51-9, PRO39.

BEFIB 2008, Gettu, R. (eds.), 2008, 7th RILEM International Symposium on Fibre Reinforced Concrete: Design and Applications - BEFIB 2008, Bagneux, France, RILEM Publications S.A.R.L., ISBN: 978-2-35158-064-6, PRO60.

BEFIB 2012, Barros, J., Sena-Cruz, J., Ferreira, R., Vanlente, I., Acenha, M. & Dias, S. (eds), 2012. 8th RILEM International Symposium on Fibre reinforced concrete: Challenges and oppertunities. RILEM Publications S.A.R.L., ISBN: 978-2-35158-132-2, PRO88.

Bischoff, P. H. & Paixao, R. , 2004. Tension stiffening and cracking of concrete reinforced with glass fibre reinforced polymer (GFRP) bars. Canadian Journal of Civil Engineering, 31, pp. 579-588.

Bischoff, P. H., 2003. Tension stiffening and cracking of steel fiber-reinforced concrete Journal of Materials in Civil Engineering, 15, pp. 174-182.

Bischoff, P., 2001. Effects of shrinkage on tension stiffening and cracking in reinforced concrete. Canadian Journal of Civil Engineering, 28(3), pp. 363-374.

Broms, B. B., 1965. Crack width and crack spacing in reinforced concrete members. ACI Journal. Preceedings. Vol. 62. No. 10. pp 1237-1255.

Burke, M. J., 2009, Integral and Semi-Integral Bridges, John Wiley & Sons

Cairns, J. & Plizzari, G.,2003. Towards a harmonised European bond test Materials and Structures/Materiaux et Constructions, 36, pp. 498-506.

Caner, A. and Zia, P., 1998. Behavior and Design of Link Slabs for Jointless Bridge Decks, PCI Journal, May-June, pp. 68-80.

Feldmann, M., Naumes, J. & Pak, D., 2010. Economic and durable design of composite bridges with integral abutments, Directorate-General for Research and Innovation, European Commission, p. 140, ISBN: 978-92-79-14598-8

Eckfeldt, L., Schröder, S., Lemnitzer, L., Hamdan, A. and Curbach, M., 2009. Verbesserung der Vorhersage von sehr kleinen Rissbreiten (Improving the prediction of small crack widths). Final research report for the DIBt, TU Dresden, Germany

Fantilli, A., Vallini, P. & Mihashi, H. , 2005. Strain compatibility between HPFRCC and steel reinforcement. Materials and Structures / Materiaux et Constructions, RILEM Publications, 38, pp. 495-503.

fib, 2010. Bulletin 55: Model Code 2010 - First Complete Draft, Vol. 1, Chaps. 1–6, fib, Lausanne, Switzerland, 2010, p. 318, ISBN 978-2-88394-95-6.

Fields, K. & Bischoff, P. H., 2004. Tension stiffening and cracking of high-strength reinforced concrete tension members. ACI Structural Journal, 101, pp. 447-456.

Fischer, G. & Li, V.C., 2003. Deformation Behavior of Fiber-Reinforced Polymer Reinforced Engineered Cementitious Composite (ECC) Flexural Members under Reversed Cyclic Loading Conditions, ACI Structural Journal, Vol. 100, 1, pp. 25-35.

Fischer, G., Li, V., 2002. Influence of matrix ductility on tension-stiffening behavior of steel reinforced ECC. ACI Structural Journal, 99, pp.104-111.

Goto, Y., 1971. Cracks Formed in Concrete Around Deformed Tension Bars. ACI JOURNAL, Proceedings, Volume V. 68, No.4., pp. pp. 244-251.

Hameed, R., Turatsinze, A., Duprat, F. & Sellier, A., 2010. A study on the reinforced fibrous concrete elements subjected to uniaxial tensile loading KSCE Journal of Civil Engineering, Korean Society of Civil Engineers, , 14, pp. 547-556.

Harajli, M., 2009. Bond stress-slip model for steel bars in unconfined or steel, FRC, or FRP confined concrete under cyclic loading, Journal of Structural Engineering, 135, pp. 509-518.

Ho, E. & Lukashenko, J., 2011. Link Slab Deck Joints,TAC Conference & Exhibition -Trancportaion successes: Lets build on them. 2011 Annual Conference of the Transportation Association of Canada

Jiang, D. H., Shah, S. P. & Andonian, A. T., 1984. STUDY OF THE TRANSFER OF TENSILE FORCES BY BOND.. Journal of The American Concrete Institute, 81(3), pp. 251-259.

Kaklauskas, G., Gribniak, V., Bacinskas, D. & Vainiunas, P., 2009. Shrinkage influence on tension stiffening in concrete members Engineering Structures, 31, pp. 1305-1312.

Lárusson, L. H., Fischer, G. & Jönsson, J., 2009. Mechanical interaction of Engineered Cementitious Composite (ECC) reinforced with Fiber Reinforced Polymer (FRP) rebar in tensile loading. In procedings: Advances in Cement-Based Materials, (eds) van Zijl and Boshoff, ISBN: 978-0-415-87637-7, pp. 83-90, 2009, CRC Press/Balkema, Leiden.

Lárusson, L., Fischer, G. & Jönsson, J., 2010. Mechanical interaction of Engineered Cementitious Composite (ECC) reinforced with Fiber Reinforced Polymer (FRP) rebar in tensile loading. Advances in Cement-Based Materials - Proceedings of the International Conference on Advanced Concrete Materials, pp. 83-90.

Lee, G.-Y. & Kim, W.,2008. Cracking and tension stiffening behavior of high-strength concrete tension members subjected to axial load. Advances in Structural Engineering, 11, pp. 127-137.

Lee, W. K., Jansen, D. C., Berlin, K. B. & Cohen, I. E., 2010. Flexural cracks in Fiber-reinforced concrete beams with Fiber-reinforced polymer reinforcing bars, ACI Structural Journal, 107, pp. 321-329.

Lepech, M. D. and Li, V. C., 2009, Application of ECC for bridge deck link slabs, Materials and Structures, 42, pp. 1185-1195.

Li, V.C., and M. Lepech, 2005. Demonstration of Durable Link Slabs for Jointless Bridge Decks Based on Strain-Hardening Cementitious Composites – Michigan Department of Transportation research report RC- 1471Field, Michigan DOT, Lansing

Li, V. C. & Wang, S., 2002. Flexural Behavior of GFRP Reinforced Engieered Cementitious Composites Beams, ACI Materials Journal, Vol. 99, 1, pp. 11-21.

Mitchell, D., Abrishami, H. H. & Mindess, S., 1996. Effect of steel fibers and epoxy-coated reinforcement on tension stiffening and cracking of reinforced concrete ACI Materials Journal, 93, pp. 61-68.

Nicholson, B., Barr, J., Cooke, R., 1997. Integral bridges Report of a study tour to North America. Concrete Bridge Development Group, Century House, Telford Avenue, Crowthorne, Berkshire, United Kingdom, ISBN 0-7210-1524-7, pp. 93.

Noghabai, K., 2000. Behavior of tie elements of plain and fibrous concrete and varying cross sections ACI Structural Journal, 97, pp. 277-284.

Oehlers, D. J., Visintin, P. & Haskett, M., 2012. The ideal bond characteristics for reinforced concrete members. In proceedings: Bond in Concrete 2012: Bond, Anchorage, Detailing, Fourth International Symposium, Brescia, Italy, Vol. 1, pp. 679-686.

Otsuka, K., Mihashi, H., Kiyota, M., Mori, S. & Kawamata, A., 2003. Observation of Multiple Cracking in Hybrid FRCC at Micro and Meso Levels. Journal of Advanced Concrete Technology, 1(3), pp. 291-298.

Ouyang, C. & Shah, S., 1994. Fracture energy approch for predicting cracking of reinforced-concrete tensile members. ACI Structural Journal, 91, pp. 69-78.

Ouyang, C., Wollrab, E., Kulkarni, S. & Shah, S., 1997. Prediction of cracking response of reinforced concrete tensile members. Journal of structural engineering New York, N.Y., 123, pp. 70-78.

Pease B.J., 2010. Impact of cracking on durability of reinforced concrete – Experimental investigation on the influence of concrete cracking on ingress and reinforcement corrosion behavior, PhD thesis, Technical University of Denmark.

Pedziwiatr, J., 2008. Influence of internal cracks on bond in cracked concrete structures. ARCHIVES OF CIVIL AND MECHANICAL ENGINEERING, 8(3), pp. 91-105.

Qu, H., Li, H., Zhang, X. & Qu, H., 2012. Flexural tests of fiber-reinforced-concrete beams reinforced with FRP rebars Applied Mechanics and Materials, 166-169, pp. 1797-1800.

Rokugo, K., Lim, S.-C., Kanda, T., Kunieda, M. & Fujimoto, Y.,2006. Tensile Behavior of ECC Members With or Without Reinforcement. International RILEM Workshop on High Performance Fiber Reinforced Cementitious Composites in Structural Applications.

Somayaji, S. & Shah, S. P., 1981. Bond stress versus slip relationship and cracking response of tension members. Journal of The American Concrete Institute, 78(3), pp. 217-225.

Sooriyaarachchi H., Pilakoutas K., Byars E., 2005. Tension stiffening behaviour of GFRP-reinforced concrete, American Concrete Institute (ACI) SP-230, pp. 975-989.

TCPI, 2012. The Crittenden Press inc., obtained 02.08.12 http://www.facebook.com/TheCrittendenPress/photos, http://www.facebook.com/photo.php?fbid=361259520556572&set=a.361258807223310.108105.185406934808499&type=3&theater

Tiberti, G., Minelli, F. & Plizzari, G. A., 2012. Crack control in fibrous RC elements. In procedings: 8th RILEM International Symposium on Fibre reinforced concrete: Challenges and oppertunities, BEFIB 2012, Barros, J., et al. (eds).

Wang, H. & Belarbi, A., 2011. Ductility characteristics of fiber-reinforced-concrete beams reinforced with FRP rebars, Construction and Building Materials, 25, pp. 2391-2401.

Wollrab, E., Kulkarni, S., Ouyang, C. & Shah, S. Response of reinforced concrete panels under uniaxial tension. ACI Structural Journal, 1996, 93, pp. 648-657.

WSDOT, 2011. Washington state department of transportation, obtained 02.08.12 http://www.wsdot.wa.gov/Projects/US2/WestWenatcheePaving/photos.htm

Chapter 2

Material characterization

Structural behavior is largely influenced by the mechanical properties of the constituting materials. The four materials used throughout this thesis, i.e. conventional concrete, highly ductile Engineered Cementitous Composite (ECC), standard deformed steel rebars, and Glass Fiber Reinforced Polymer (GFRP) rebars are described in this chapter. The main characteristics of each constituent are discussed while methods and procedures to obtain them are explored. Conventional concrete and steel reinforcement represent the conventional materials used in most R/C structures, while ECC and GFRP represent new and innovative materials with favorable characteristics for structural applications such as the link slab concept presented in Chapter 1. The main objective of this chapter is to characterize the materials and to identify the potential benefits and limitations of utilizing the new materials in contrast to the conventional materials.

2.1 Background

The use of concrete spans a wide range of applications, such as roads, bridges, buildings, and infrastructures. The extensive use of concrete as a structural material is often attributed to its workability at fresh state, its strength at cured state, relatively low cost, and the advantage of being a readily available material from local suppliers. However, concrete is weak in tension and needs to be reinforced typically with steel in order to be viable for structural use. In the uncracked condition, concrete provides an effective protection to the reinforcement against corrosion. However, most R/C structures or elements are cracked to some degree, due to the brittle nature of concrete. As a result, R/C is susceptible to damage due to corrosion. In addition, due to adverse scenarios such as over-loading, exposure to harsh environments or incorrect detailing, R/C structures and elements can undergo a significant performance decrease. These unfavorable events can subsequently lead to increased cracking, concrete spalling, reinforcement corrosion, and eventually result in structural failure.

These vulnerabilities of conventional brittle concrete and corrosion-prone steel reinforcement have prompted the use of innovative and resilient building materials such

as Fiber Reinforced Cementitous Composites (FRCC) and corrosion resistant Fiber Reinforced Polymer (FRP) reinforcement.

The addition of randomly oriented discontinuous fibers in cementitious matrices has resulted in a wide range of performance enhancements, both at material and structural levels. The most important benefits attained by incorporating fibers in cement-based materials include the control and mitigation of the deleterious effect of shrinkage cracking, the increase of the post-cracking load carrying capacity and the enhancement of toughness. For structural purposes, the enhancement of toughness is generally recognized as the most significant effect achieved with fibers (Li and Fischer, 2002). Collectively, these composites are referred to as Fiber Reinforced Concretes (FRCs), or in more general terms Fiber Reinforced Cementitious Composites (FRCCs).

The tensile load – deformation behavior of FRCC is determined by the mechanical properties of the cementitious matrix, of the fibers, and by the fiber-matrix interaction properties. Numerous factors affect the complex fracture mechanisms in cementitious composites, such as the matrix stiffness and strength, the aggregate geometry, the fiber volume fraction, the fiber stiffness and strength, the existence of fiber surface treatments, the fiber geometry, as well as the fresh state rheological properties. A delicate balance between all constituents of FRCC is thus needed to achieve specific performance requirements.

In addition to a broad range of matrix compositions, a vast variety of fiber types and fiber geometries have been adopted by FRCC, such as steel, carbon, Kevlar, polypropylene, polyethylene, polyvinyl alcohol, as well as natural fibers (Bentur and Mindess, 2006). All these fibers can cater to a specific performance characteristic of the FRCC composite.

Li and Fischer (2002) described a so-called Integrated Structures-Materials Design (ISMD) approach where the material composition (fibers and matrix) is tailored to meet specific structural performance criteria, and thus quantitatively linking material microstructure, processing and material properties provided by micromechanics. Such an approach, when adapted correctly, inevitably leads to advanced structures designed with targeted performance and cost-efficient construction.

FRCCs can generally be divided into two subcategories based on the post-cracking behavior during tensile loading, that is strain softening- and pseudo strain-hardening composites. Strain softening FRCC show the ability to carry load after initial cracking due to fibers bridging the crack. However, the load carrying capacity decreases as tensile strain is increased and the crack localizes as fibers pull out and or rupture. Strain Hardening Cementitious Composites (SHCC) (RILEM TC 208-HFC, 2011), however, have the capability to increase its load carrying ability after initial cracking occurs under tensile loading. The pseudo strain-hardening behavior of SHCCs is the result of multiple cracks forming at increasing composite tensile stress. However, in order to obtain multiple cracking, the intricate interaction between the fibers and the surround-

ing matrix must satisfy a micromechanical design criteria at a single crack level (see section 2.1.1).

ECC (Engineered Cementitious Composite), used throughout this thesis, is one type of SHCC which has been specifically engineered to exhibit multiple cracking and strain hardening during tensile loading.

Figure 2-1 highlights the fundamental difference between normal (strain softening) FRCC and ductile SHCC in contrast to conventional brittle concrete which loses its tensile carrying capacity almost immediately after the first crack forms.

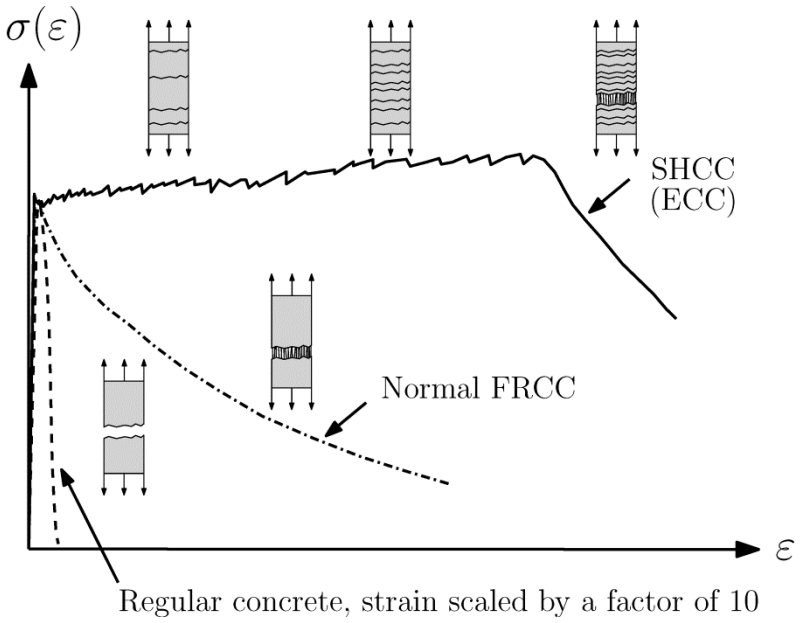

Figure 2-1 Schematic comparison of the stress-strain (σ - ε) response of ductile SHCC, typical strain softening FRCC and brittle concrete under tensile loading.

2.1.1 Strain hardening criteria

Based on the analysis and formulations for multiple cracking and steady state crack formation presented by Li and Leung (1992) and Li and Wu (1992), the following summarizes the main aspects and requirements for ECC to obtain multiple cracking and strain hardening.

The multiple crack behavior is fundamentally governed by two complementary requirements: i) the strength criterion and ii) the energy criterion (Marshall and Cox, 1988)

The strength criterion establishes that the peak bridging stress, σ_{peak}, exerted by the fibers in a cracked section must exceed the first cracking stress of the matrix, σ_{cr}, that is:

$$\sigma_{peak} > \sigma_{cr} \tag{2.1}$$

This requirement ensures that the applied stress prior to matrix cracking can be carried by the fibers bridging the crack plane after cracking has occurred.

The energy criterion is based on the assumption that the steady state cracking mode is achieved, i.e. the matrix crack propagation occurs at a constant ambient stress, σ_a, (also referred to as the steady state stress) for a constant crack opening displacement, δ_a, (or the steady state crack opening displacement). In this case, the stress distribution at the crack plane is uniform (flat crack configuration). This requirement can be expressed as an energy balance between the energy necessary to advance the matrix crack tip or matrix toughness (Jtip), the external work, and the energy dissipated by the bridging fibers, that is

$$J_{tip} = \sigma_a \delta_a - \int_0^{\delta_a} \sigma(\delta) d\delta \tag{2.2}$$

Where J_{tip} denotes the matrix toughness and δ denotes the crack opening displacement (COD) as illustrated in the σ – δ diagram in Figure 2-2.

Thus, by combining equation 2.1 and 2.2 the matrix toughness limit for multiple cracking can be expressed as:

$$J_{tip} < \sigma_{peak} \delta_{peak} - \int_0^{\delta_{peak}} \sigma(\delta) d\delta = J_{b'} \tag{2.3}$$

Where $J_{b'}$ denotes the complimentary energy.

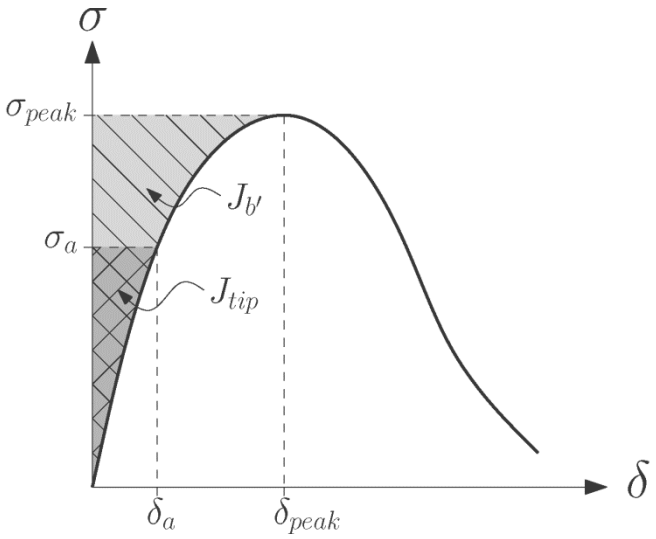

Figure 2-2 Bridging stress-crack opening curve, σ-δ, indicating the matrix toughness (J_{tip}), complimentary energy ($J_{b'}$) and relevant parameters.

2.2 Engineered Cementitious Composite (ECC)

Engineered Cementitious Composite (ECC) is one type of SHCC which was developed in the early 1990's, specifically engineered to exhibit pseudo strain hardening behavior during tensile loading (Li, 1993). The design of ECC is based on the micromechanical tailoring of the composite properties, considering the complex interaction mechanisms between the fibers and the surrounding matrix, as described in the previous section. The optimal interaction between the composite constituents results in multiple cracking rather than in the localization of a single crack prior to failure, ultimately yielding a considerably ductile behavior during loading (Li, 1998). ECC typically exhibits a relatively high tensile strain capacity of 2-4% at limited crack widths of 150-250 μm (Rokugo et al., 2009, Lárusson et al. 2011). Other researchers have reported crack widths in ECC of 50-80 μm (Li, 1993; Weiman and Li, 2003, Lepech and Li, 2006).

2.2.1 Composition of ECC

ECC typically constitutes a Self Consolidating Concrete (SCC). It is composed of fine-grained materials, including fine sand, a relatively high amount of fly ash, chemical admixtures, water and a moderate amount of PolyVinyl Alcohol (PVA) fibers. Table 2-1 shows the typical mixture proportions for the PVA-ECC used throughout this study.

Table 2-1 Typical mixture proportions for one cubic meter of PVA-ECC

Cement	Fly Ash	Sand (<0.18mm)	Quartz powder	Water	Super plasticizer	Viscosity agent	PVA fibers (2% by vol.)
[kg/m^3]	[kg/m^3]	[kg/m^3]	[kg/m^3]	[l/m^3]	[kg/m^3]	[gr/m^3]	[kg/m^3]
430	860	150	150	320	4.3	480	26

The absence of coarse aggregates in the cementitious matrix is related to the design concept of ECC. The required fracture properties of the matrix are best attained when aggregates of smaller size are utilized. Furthermore, the use of smaller aggregates was shown to contribute for better fiber dispersion and lead to the appropriate fiber-matrix interfacial bonding properties (Li and Lepech, 2005).

The PVA fibers used in this study have a length of 8 mm, a diameter of 40 μm and were developed for optimal performance in ECC while meeting specific micromechanical design requirements to enable strain hardening in the composite (Li et al., 2001).

2.2.2 Applications of ECC

In recent years ECCs have been utilized in numerous field applications, most of which require limited crack widths, reduced cross sections, or a high tensile strain capacity.

Examples of applications include link slabs in bridges, retrofitting of dam claddings and irrigation channels, the surface repair of retaining walls, a bridge deck replacement, or even dampers for high-rise reinforced concrete buildings.

Figure 2-3a shows an example of a steel reinforced ECC link slab integrally connecting two adjacent bridge deck spans, while the substructure girders are un-coupled. The link slab application utilizes the deformability and small crack widths of ECC in a continuous expansion joint construction, which significantly reduced bridge-deck maintenance demands during service life of the structure (Lepech and Li, 2009).

Figure 2-3b depicts the Mitaka Dam, which was retrofitted in 2003 with a 30 mm layer of ECC to minimize water penetration. The ECC was sprayed on top of the deteriorated existing concrete surface on the up-stream side of the dam, covering approximately 500 m^2 (Kojima et al., 2005; Kunieda and Rokugo, 2006).

In Figure 2-4 an example of steel reinforced ECC coupling beams incorporated in high-rise buildings as seismic dampers is shown. The precast ECC beams where designed to facilitate large deformations under earthquake actions by utilizing the considerably high energy dissipation of the ECC member without requiring extensive repair work afterwards (Maruta et al. 2005; Kunieda and Rokugo, 2006).

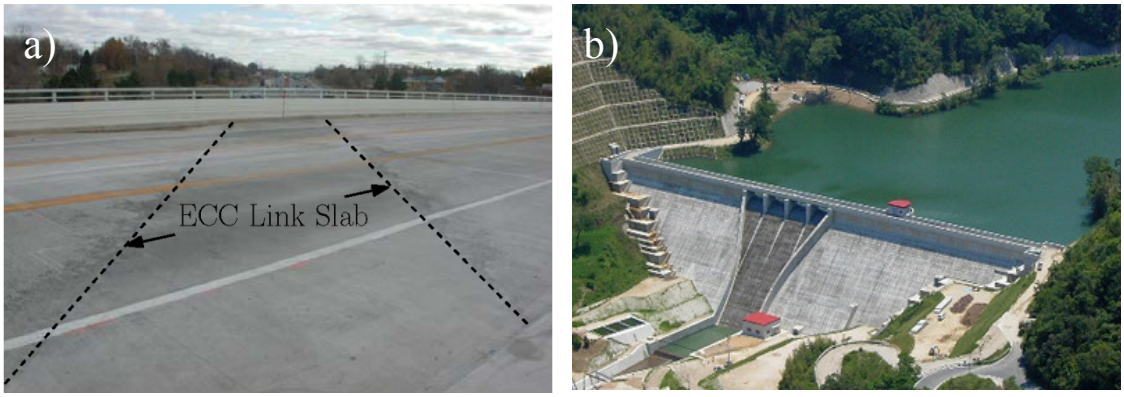

Figure 2-3 Examples of structural applications of SHCC/ECC: a) A continuous steel reinforced ECC link slab in Michigan 2005 (Li and Lepech, 2009). b) The Mitaka Dam on Nishi-Nomi island in Japan, where the up-stream side of the dam was retrofitted with a thin overlay of ECC in 2003 (JDF, 2012).

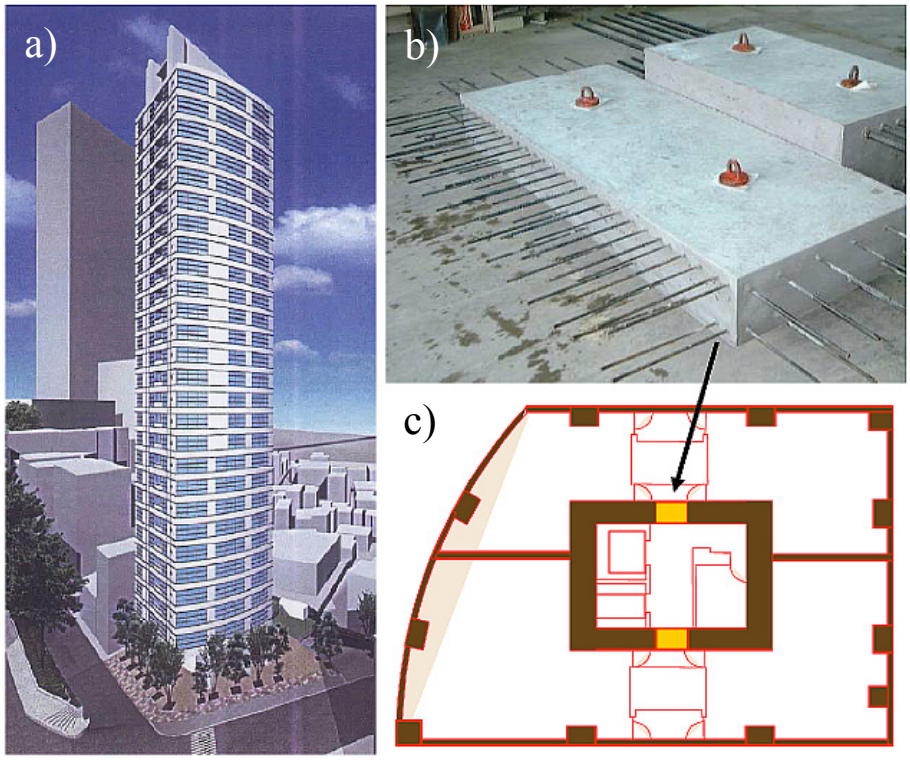

Figure 2-4 Example of ECC used in steel reinforced dampers in high-rise reinforced concrete buildings in Tokyo and Yokohama in 2004 and 2005 (Maruta et al. 2005; Kunieda and Rokugo, 2006).

2.3 Test methods and procedures

The mechanical characterization of conventional FRCCs is mostly focused on quantifying the contribution of the fibers to the improvement of the tensile behavior. The contribution of the fibers is particularly visible in the post-cracking stage of the tensile response. However, because conventional FRCCs typically show a strain softening behavior in tension, the direct tension tests are difficult to perform due to unloading instabilities at cracking. The back analysis based on the results of flexural tests is therefore preferred, as it also allows the indirect derivation of the most relevant fracture parameters.

Different flexural test configurations have been proposed for FRCC, such as the three point bending beam tests (EN 14651-5; ASTM C1609) and the four point bending beam tests (UNI 11039). Beam tests results however generally exhibit a relatively large scatter, particularly FRCCs with low fiber content ($V_f < 1.0\%$), mainly due to the relatively small fracture areas and low number of fibers bridging the crack planes (Minelli and Plizzari, 2011). Because of this large scatter, the characteristic values (5% fractal) are much lower than the mean values and consequently do not adequately represent the structural properties of the material. However, alternative test configurations, such as round panel tests (ASTM C1550-10), allow stress redistribution to oc-

cur during testing which result in much large fracture areas with a high number of fibers bridging the crack planes. This stress redistribution consequently results in a lower scatter of the test results, which implies a more realistic and reliable characterization of structural properties.

The round panel test proposed by ASTM (ASTM C1550-10) however is a relatively large and bulky specimen, 800 mm in diameter, 75 mm thick and weighs roughly 90 kg. Due to its size and weight, the panel is difficult to handle and place in test configuration. In addition, the ASTM round panels are typically too large for most standard servo-controlled loading machines (Minelli and Plizzari, 2011). In order to alleviate some of the disadvantages and restrictions associated with the ASTM panels, new smaller round panel tests, 600 mm in diameter, 60 mm thick and weight approximately 40 kg, have been suggested by Minelli and Plizzari (2011) in order to develop more practical test procedures. These small round panel tests have consistently showed the same low scatter of the test results as the ASTM round panel test results.

These beam tests and round panel tests, as well as splitting load tests such as the wedge-splitting test (Linsbauer and Tschegg, 1986) and compact tension test (Hillemeier and Hilsdorf, 1977), all derive the fracture parameters of the cementitious composites indirectly. Ideally, these parameters could be obtained from direct tension tests. However, due to the difficulty associated with performing direct tension tests, particularly in FRCCs that exhibit strain-softening behavior as previously mentioned, most researchers in the past have preferred the indirect approach, which is well known and established.

SHCCs materials in general and ECC in particular, are designed to optimize the tensile behavior, which is most pronounced in the post-cracking tensile response in tension. Due to the pseudo-strain hardening behavior and resulting stress redistribution, in contrast with the typical strain softening behavior observed in conventional FRCCs, the mechanical properties of SHCC materials are ideally obtained in direct tension.

This is typically achieved by characterizing the tensile stress – strain behavior of dogbone shaped (dumbell shaped) specimens or coupon specimens during direct tension (Kanda and Li, 2006; Naaman et al., 2007; Rokugo et al., 2009). The most relevant parameters obtained from these tests are the first peak stress (first crack), the strain at first peak stress, the ultimate stress (strength), the strain at ultimate stress, the crack development (crack widths and crack spacing) and the overall shape of the stress – strain response. Alternatively, the Single Crack Tension Tests (SCTT) can be utilized to characterize the material behavior in tension, as discussed in the subsequent section 2.3.2.

The research activities within this thesis focus primarily on the characterization of tensile behavior of ECC members. It is therefore highly relevant to investigate ECC in direct tension, i.e. using dogbone specimens (see section 2.3.1) and notched coupon specimens (see section 2.3.2). Other relevant material properties such as the compres-

sion strength and modulus of elasticity of ECC were characterized adopting the same procedure as described for conventional concrete in section 1.2.1. Additionally, shrinkage properties of the ECC composite used were characterized using the drying shrinkage tests described in section 2.3.3.

2.3.1 Dogbone tests

The tensile stress – strain response of ECC was measured using dog-bone shaped specimens, with a representative cross section of 25 mm x 50 mm and a representative length of 210 mm, loaded in direct tension as shown in Figure 2-5. Two linear variable differential transducers (LVDTs) monitored the longitudinal displacements over a 190 mm representative portion of the specimens (Figure 2-5b).

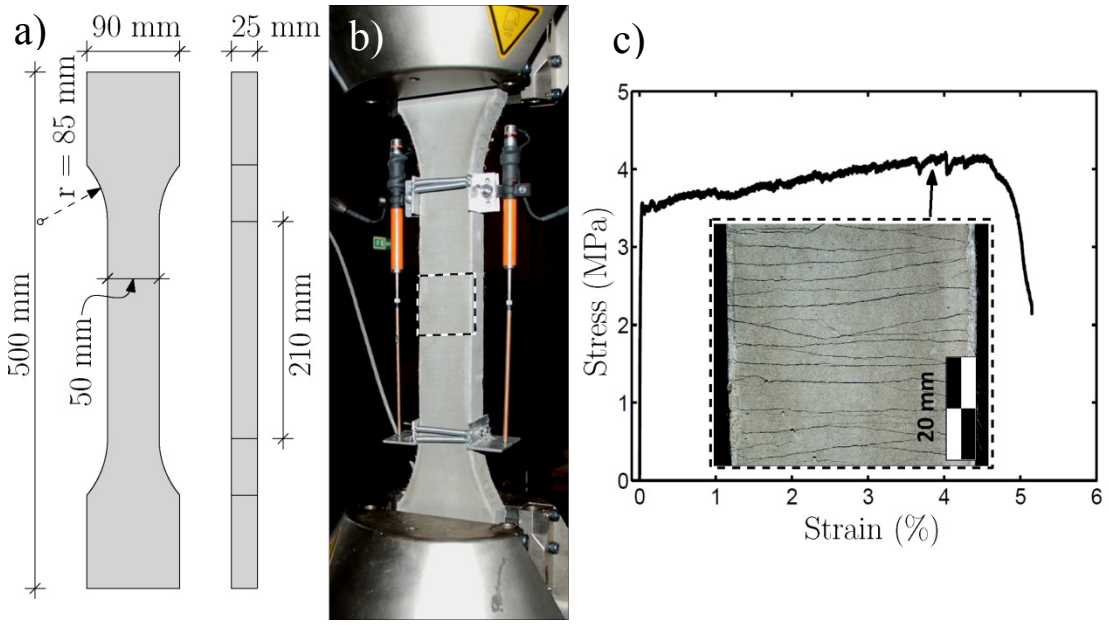

Figure 2-5 a): Geometry of an ECC dog-bone shaped specimen, b): direct tension test setup including supports and LVDT's, and c): example of tensile stress-stain response of an ECC specimens and the resulting crack pattern at approximately 4% strain.

Direct tensile loading was applied to the specimens in a displacement controlled configuration at a displacement rate of 1 mm per minute (actuator piston displacement).

The Digital Image Correlation (DIC) technique was used to monitor the global and local surface deformations, including crack widths, crack spacing and the overall crack development at the surface the dog-bone shaped specimens during tensile testing. Detailed measurements were obtained with DIC by placing virtual strain gauges (typically 1-2 mm long) at all transverse cracks along a center guideline of the measured area (see Figure 2-6). Detailed information on the DIC technique employed throughout this study can be found in Pereira (2012).

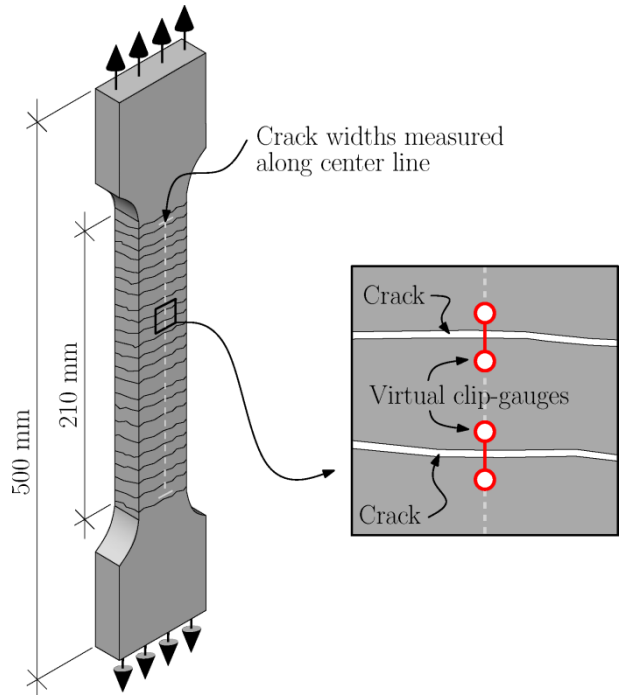

Figure 2-6 Schematic of a dog-bone shaped specimen used to characterize ECC's tensile behavior. Utilizing a Digital Image Correlation (DIC) system, the close-up view shows positioning of virtual clip gages used to monitor the crack opening displacements.

By utilizing the DIC technique, the crack width and crack spacing evolution could be tracked in detail. An example of the crack width and crack spacing evolution is shown in Figure 2-7 as a function of tensile strain.

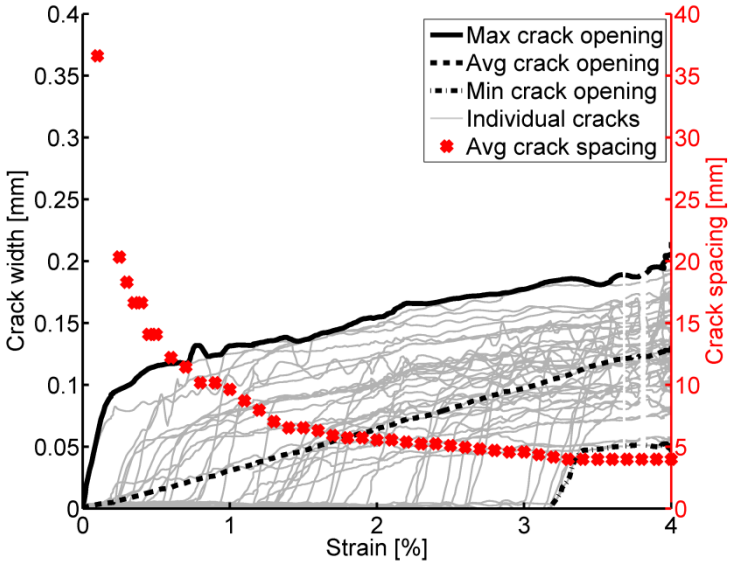

Figure 2-7 Example of crack opening and crack spacing of as a function of tensile strain obtained with DIC on a ECC dogbone specimen.

In the example shown in Figure 2-7, the maximum crack width of 0.2 mm was reached at 4% tensile strain, while crack saturation is reached at 3.2% tensile strain. The crack width vs. strain relationship is generally characterized by a bi-linear path, with an initial sharp crack opening phase followed by a moderate and steady increase of crack width (see Figure 2-7). During the first phase of crack opening, the fibers bridging the crack are not fully engaged, whereas in the second phase, the fibers are fully engaged and primarily exhibit a combination of elastic deformation of the fibers and fiber rupture.

2.3.2 Single crack tension test (SCTT)

An alternative way to assess the tensile properties of ECC is to measure the stress – crack mouth opening displacement (σ – CMOD) of a single crack during direct tensile loading. This tensile response may be subsequently used to define a cohesive law for ECC in tension.

SHCC materials such as ECC are designed to develop multiple cracks in tension until crack saturation is reached at critical crack spacing. Due to the inherent difficulty associated with isolating and observing a single crack in such materials, special Single Crack Tension Test (SCTT) specimens were prepared and tested. These small coupon specimens were notched on all sides, resulting in a representative cross-section (8 mm x 30 mm) as shown in Figure 2-8a. The nominal tensile stress values were obtained by dividing the tensile load by the representative cross-section area. Special care was taken to minimize to width of the notch (0.5 mm) in order to minimize the risk of obtaining multiple crack planes.

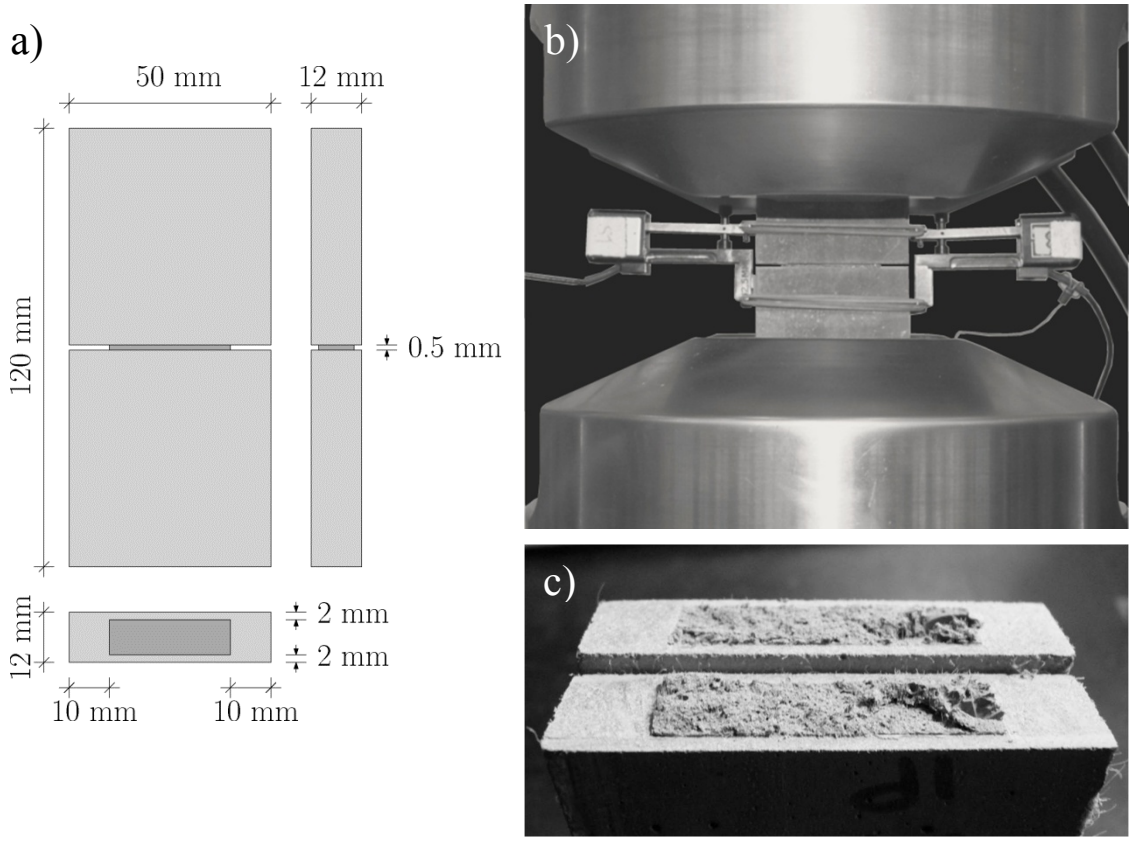

Figure 2-8 a): SCTT specimen geometry used in the assessment of the tensile stress-crack opening behavior, b): tensile test setup for SCTT specimen including supports and clip gages, and c): a single crack plane obtained after testing.

Load was applied in a deformation controlled configuration with a constant axial displacement rate of 0.3 mm/min using clip gauges on each side measuring the average CMOD (δ) (see Figure 2-8b). Pereira et al. (2012) developed the specific geometry and load rate used in this study to directly assess tensile stress – crack opening behavior of SHCCs such as ECC.

Examples of the σ – CMOD responses obtained from four ECC SCTT specimens are shown in Figure 2-9. These results seem to define the envelope of a characteristic tensile stress-crack width behavior of ECC. In order to relate the single crack responses obtained with the SCTT specimens to the cracking behavior observed in a specimen with multiple cracking, e.g. Figure 2-5, the crack width evolution for three cracks obtained with DIC on an ECC dogbone specimen are also shown in Figure 2-9. The tensile stress capacity of any specimen with multiple cracking is limited by the weakest crack. Accordingly, the lower limit of the peak σ – CMOD response envelope obtained from the SCTT specimens represents the upper stress limit observed in the dogbone specimen. That is, the lower limit of the peak stress of the SCTT specimen results governs the stress capacity of the dogbone specimen (see Figure 2-9).

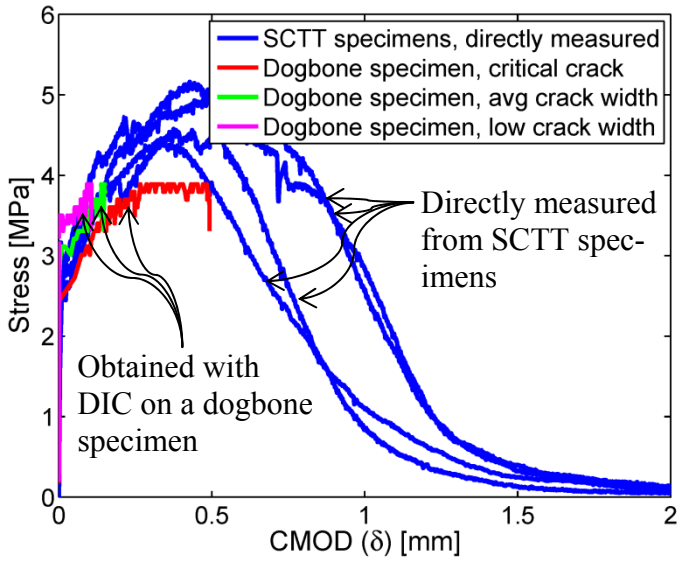

Figure 2-9 Examples of stress – crack mouth opening displacement (σ – CMOD) responses obtained from four SCTT specimens and comparison to the measurements obtained with DIC on a dogbone specimen. The critical crack in the dogbone specimen is the crack that ultimately localizes.

2.3.3 Drying shrinkage testing

Because of the high volume of fine grain materials, such as fly ash and cement, and the absence of coarse aggregates in the composition of ECC, shrinkage is more pronounced when compared to conventional concrete. Consequently, since shrinkage directly influences the composite behavior and the ECC-reinforcement interaction (e.g. when assessing the tension stiffening effect), the characterization of shrinkage in ECC is of particular interest. The drying shrinkage test setup and geometry was based on ASTM C 1148 – 92a (2002). The drying shrinkage of the ECC was measured using 270 mm long, free shrinkage prisms with a cross-section of 25x25 mm^2. The air temperature during testing was 20°C ± 3°C at approximately 60-80% relative humidity (RH). In the example shown in Figure 2-10 the drying shrinkage measured over a 30 day period level out at 0.12-0.14% strain. These results are in reasonable agreement with measurements of Wang and Li (2005), which showed drying shrinkage deformations of ECC to be 0.12% at approximately 60% RH.

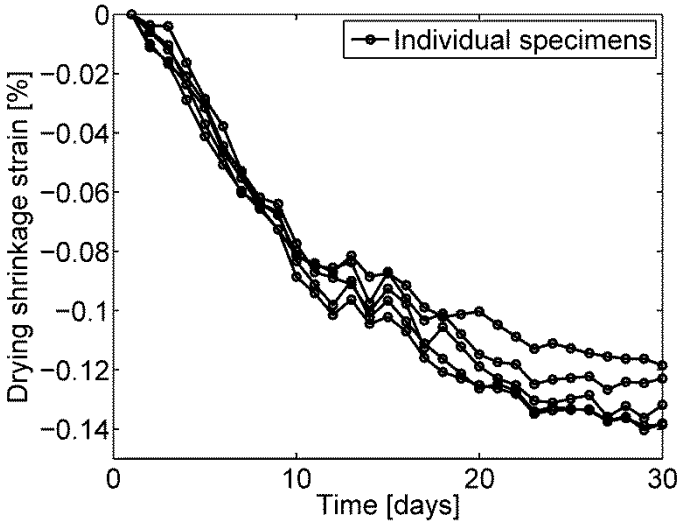

Figure 2-10 Example the drying shrinkage measurements of five ECC specimens.

2.4 Conventional concrete

The concrete composition used in this study represents the "conventional solution", typically adopted in structural applications such as link slabs (Caner and Zia, 1998), as investigated in this study. The concrete mixture is a typical composition containing cement, sand, gravel and water. The w/c ratio was 0.42 and the largest aggregate size limited to 8mm to increase its workability and leading to a Self Consolidating Concrete (SCC) composition. In addition, the mixture was designed to obtain the same compression strength as ECC used throughout this study.

Table 2-2 shows the mix proportions for the conventional concrete used throughout this study.

Table 2-2 Mixture proportions for one cubic meter of normal concrete

Cement [kg/m^3]	Sand (0-4 mm) [kg/m^3]	Sea stone (4-8 mm) [kg/m^3]	Water [l/m^3]
370	160	1130	760

2.4.1 Test methods and procedures for concrete mechanical characterization

To obtain the compression strength and elastic modulus of the concrete used in this study, standard cylinder specimens according to EN 12390-3 (2009) were prepared with a height of 200 mm and a diameter of 100 mm. The specimens were cured in water the first 7 days and subsequently allowed to air dry at constant temperature of 20°C ± 3°C at approximately 60-80% relative humidity (RH) until testing was carried out. The compression strength was determined after 28 days.

Due to the difficulties of testing concrete in direct tension, the cracking strength of conventional concrete was assessed indirectly by performing the splitting tensile test (Brazilian test) according to EN 12390-6 (2009).

2.5 Reinforcement

Previous versions of the link slab design have exclusively employed deformed steel reinforcement. As part of the innovative solution presented in this thesis, a different type of reinforcement rebar was adopted in the link slab design. The intention was primarily to decrease the stiffness of the elements as well as to increase the retrievable deformations during service life.

Considering the specific purpose of obtaining a flexible link slab design, introduced in Chapter 1, three main features for the reinforcement were searched: i) a relatively soft axial load – deformation response (low elastic modulus); ii) a relatively large linear-elastic strain capacity (decrease permanent deformations); iii) a high corrosion resistance. Among the many different commercially available reinforcement types (steel, plastics or mineral), Fiber Reinforced Polymer (FRP) rebars are being applied increasingly in the construction industry, mostly due to their non-corrosive nature and high load bearing capacity. FRPs exhibit a linear-elastic load – deformation response and generally have lower elastic modulus than steel. Figure 2-11 illustrates the general stress – strain ranges of different reinforcement types, i.e. Carbon Fiber Reinforced Polymer (CFRP), High Strength (HS) steel strand, Aramid Fiber Reinforced Polymer (AFRP), Glass Fiber Reinforced Polymer (GFRP) and standard steel.

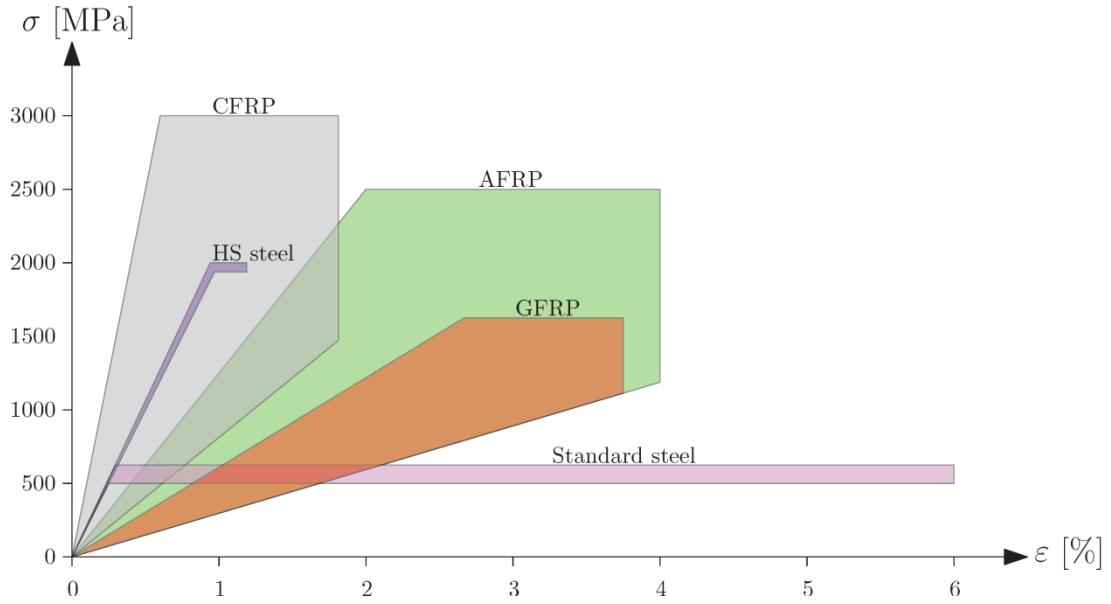

Figure 2-11 Approximate stress-strain response ranges of various reinforcement types based on Model code 2010 (fib, 2010).

Both GFRP and AFRP exhibit the desired features for the link slab design. However, because AFRP rebars are significantly more expensive and less available product, GFRP was chosen for the link slab design.

The GFRP rebars used in this study are a commercially available under the name Aslan100®, produced by Hughes Brothers Inc. (Aslan, 2012), and with an elastic modulus of 46 GPa and an average diameter of 6.3 mm (see Figure 2-12a). Glass fiber strands are impregnated in thermosetting resin (vinyl-ester), wound together with a helical wrap and coated with rough silica sand. The resin primarily glues the glass fibers together to achieve an effective utilization. However, the resin also protects the fibers from chemical attack such as chloride, high pH levels and alkaline damage. The deformed external part of the rebar (due to the helical wrap) and the sand enhances the bond between the rebar and surrounding concrete.

In comparison to the relatively soft load-deformation response of the GFRP reinforcement, standard deformed steel rebars were examined as well.

The steel reinforcement rebars have an average diameter of 6 mm, average rib spacing of 4.92 mm, and an average rib height of 0.3 mm (see Figure 2-12b).

Figure 2-12 Rebars tested in this study, a) GFRP and b) standard steel.

2.5.1 Tensile properties of the reinforcement rebars

The tensile testing of the reinforcement rebars (steel and GFRP) was carried out under displacement controlled tensile loading, at a displacement rate of 1 mm per minute. Three test specimens of each type were used, with a 300 mm representative length, to characterize the tensile properties of the reinforcement rebars. The GRRP rods ends were embedded into steel cylinders 150 mm long, 35 mm of outer diameter, 10 mm of inner diameter and with internal threading. The cylinders were filled with epoxy paste mixed with silica sand to increase the bond. The GFRP segments were subsequently tested by clamping the cylinders on each end of the rods in the hydraulic actuator with the hydraulic grips. In addition to the measurements obtained from the servo-hydraulic, 50 mm clip gauges were utilized to measure the displacements directly up to 60% of the ultimate load capacity of the GFRP rods. Examples of the tensile stress - strain results obtained for the steel and the GFRP rebars are shown in Figure 2-13.

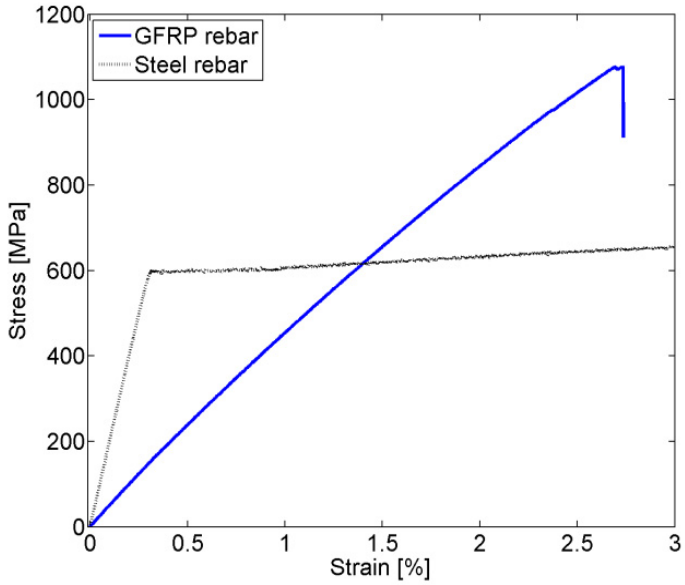

Figure 2-13 Typical tensile stress-strain responses for bare GFRP- and steel rebars from direct tension testing.

2.6 Conclusions

In this chapter the materials utilized in the research activities presented in this thesis were introduced and characterized, including the cementitious composites and reinforcements.

The innovative materials presented in this chapter, i.e. the considerably ductile ECC and the low stiffness GFRP rebars, have reviled enhanced characteristics regarding the application in consideration, in contrast to the conventional structural materials that are typically applied, that is, the conventional concrete and the standard deformed steel rebars. These characteristics include a considerably high strain capacity (2-4% tensile strain) and limited crack widths (150-200 μm) of ECC, a relatively low stiffness (46 GPa) and a tensile linear strain capacity (2.5%) of the GFRP, which are highly attractive for the proposed flexible link slab design which aims to a minimum tensile strain capacity of 1%.

The methods and procedures, both standardized and specialized, described in this chapter are utilized to characterize the fundamental material properties throughout this thesis in succeeding chapters. Detailed results from the material tests carried out in each experimental program, which are subsequently reported in each chapter.

Bibliography

Aslan, 2012. Hughes brothers inc., producers of Aslan 100 GFRP rebars, http://aslanfrp.com/

ASTM C1609/C1609M-07, 2010. Standard Test Method forFlexural Performance of Fiber-Reinforced Concrete (Using Beam With Third-Point Loading), Annual Book of ASTM Standards, ASTM International,West Conshohocken, PA.

ASTM Standard C 1148 – 92a, 2002. Standard test method for measuring the drying shrinkage of masonry mortar". ASTM International, West Conshohocken, PA, 2003, DOI: 10.1520/C1148-92AR08, www.astm.org.

Bentur, A. & Mindess, S., 2006. Fibre reinforced cementitious composites. Modern concrete technology series. Taylor & Francis.

BS EN 12390-3:2009 (BS EN), 2009. Testing hardened concrete. Part 3: Compressive strength of test specimens. British-Adopted European Standard. British Standards Institution, London, UK, BSI.

BS EN 12390-6:2009 (BS EN), 2009. Testing hardened concrete. Part 6: Tensile splitting strength of test specimens. British-Adopted European Standard. British Standards Institution, London, UK, BSI.

Caner, A. and Zia, P., 1998. Behavior and Design of Link Slabs for Jointless Bridge Decks, PCI Journal, May-June, pp. 68-80.

EN 14651-5, 2005. Precast Concrete Products—Test Method for Metallic Fibre Concrete—Measuring the Flexural Tensile Strength, Europ. Standard, Brussels, Belgium, p. 20.

fib, 2010. Bulletin 55: Model Code 2010 - First Complete Draft, Vol. 1, Chaps. 1–6, fib, Lausanne, Switzerland, 2010, p. 318, ISBN 978-2-88394-95-6.

Hillemeier, B. & Hilsdorf, H., 1977. Fracture mechanics studies on concrete compounds, Cement and Concrete Research, 7 (5), pp. 523-535.

Japan Dam Foundation (JDF), 2012. Picture of the Mitaka Dam after renovation. Obtained: 15.09.12. http://damnet.or.jp/cgi-bin/binranA/enAll.cgi?db4=3254

Kanda, T. & Li, V. C., 2006. Practical design criteria for saturated pseudo strain hardening behavior in ECC. Journal of Advanced Concrete Technology, 4(1), pp. 59-72.

Kojima, S., Sakata, N., Kanda, T. & Hiraishi, T., 2004. Application of Direct Sprayed ECC for Retrofitting Dam Structure Surface -Application for Mitaka-Dam.Concrete Journal, 42 (5), pp. 135-139. (in Japanese)

Kunieda, M. & Rokugo, K., 2006. Recent progress on HPFRCC in Japan required performance and applications. Journal of Advanced Concrete Technology, 4, pp. 19-33

Larusson, L., Fischer, G. & Jonsson, J., 2011. Mechanical interaction between concrete and structural reinforcement in the tension stiffening process, in: G.J. Parra-Montesinos, H.W. Reinhardt, A.E. Naaman (Eds.), High performance fiber reinforced cementitious composites 6, RILEM state of the art reports, vol. 2, Springer, Ann Arbor, USA, pp. 247–254.

Lepech, M. D. & Li, V. C., 2006. Long Term Durability Performance of Engineered Cementitious Composites. Restoration of Buildings and Monuments, 12(2), pp. 119-132.

Lepech, M. D. & Li, V. C., 2009, Application of ECC for bridge deck link slabs, Materials and Structures, 42, pp. 1185-1195.

Li, V. C. & Fischer, G., 2002. Reinforced ECC - An Evolution from Materials to Structures. Proceedings of the First FIB Congress, Proceedings of the First FIB Congress, Osaka, Japan, Oct. 2002, pp.105-122.

Li, V. C. & Leung, C. K. Y., 1992. Steady state and multiple cracking of short random fiber composites. ASCE J. of Engineering Mechanics, 118 (11), pp. 2246-2264.

Li, V. C., Wang, S. & Wu, C., 2001. Tensile strain-hardening behavior or polyvinyl alcohol engineered cementitious composite (PVA-ECC) ACI Materials Journal, American Concrete Institute, 98, pp. 483-492.

Li, V. C., 1993. From micromechanics to structural engineering -the design of cementitious composites for civil engineering applications Structural Engineering/Earthquake Engineering, 10, pp. 1-34.

Li, V. C., 1998. Engineered Cementitious Composites - Tailored Composites Through Micromechanical Modeling. Fiber Reinforced Concrete: Present and the Future edited by N. Banthia, in Fiber Reinforced Concrete: Present and the Future edited by N. Banthia, A. Bentur, A. and A. Mufti, Canadian Society for Civil Engineering, Montreal, pp. 64-97.

Li, V. C., & H. C. Wu, 1992. Conditions for Pseudo Strain-Hardening in Fiber Reinforced Brittle Matrix Composites, J. Applied Mechanics Review, V. 45, No. 8, August, pp. 390-398.

Li, V. C. & Lepech, M., 2006. General Design Assumptions for Engineered Cementitious Composites. Proceedings of International RILEM workshop on HPFRCC in structural applications, Proceedings of Int'l RILEM workshop on HPFRCC in structural applications, Published by RILEM SARL, pp. 269-277.

Linsbauer, H. & Tschegg, E., 1986. Fracture energey determination of concrete with cube shaped specimens (in german), Zement und Beton, 31, pp. 38-40.

Marshall, D. & Cox, B., 1988. A J-integral method for calculating steady-state matrix cracking stresses in composites Mechanics of Materials, 7, pp. 127-133.

Maruta, M., Kanda, T., Nagai, S. & Yamamoto, Y., 2005. New High-Rise RC Structure Using Pre-Cast ECC Coupling Beam. Concrete Journal, 43 (11), pp. 18-26. (in Japanese)

Minelli, F. & Plizzari, G., 2011. A New Round Panel Test for the Characterization of Fiber Reinforced Concrete: A Broad Experimental Study. Journal of Testing and Evaluation, 39, pp. 889-897.

Model Code 2010, Ed. Joost Walraven, Volume 1 of Model Code 2010: First Complete Draft, Fédération Internationale du Béton, Volume 55 of fib bulletin

Naaman, A. E., Fischer, G. & Krustulovic-Opara, N., 2007. Measurments of tensile properties of fiber reinforced concrete: draft submitted to ACI committee 544. In Reinhart, H. W. And Naaman, A. E. Editors, RILEM International Workshop on High Performance Fiber - Reinforced Cement Composites, number Pro. 53 in RILEM Proceeding, RILEM S.A.R.L., pp. 3-12.

Pereira, E. B., Fischer, G. & Barros, J. A., 2012. Direct assessment of tensile stress-crack opening behavior of Strain Hardening Cementitious Composites (SHCC). Cement and Concrete Research, 42(6), pp. 834-846.

Pereira, E. N. B., 2012. Processes of Cracking in Strain Hardening Cementitious Composites, PhD thesis, University of Minho.

RILEM, 2011. Strain Hardening Cement Composites (SHCC): Structural Design and Performance: State-of-the-Art Report of the RILEM Technical Committee (TC) 208-HFC, SC3, Ed. Li, V. C.

Rokugo, K., Kanda, T., Yokota, H. & Sakata, N., 2009, Applications and recommendations of high performance fiber reinforced cement composites with multiple fine cracking (HPFRCC) in Japan Materials and Structures, 42, pp. 1197-1208.

Rokugo, K., Kanda, T., Yokota, H. & Sakata, N., 2009. Applications and recommendations of high performance fiber reinforced cement composites with multiple fine cracking (HPFRCC) in Japan Materials and Structures, Springer Netherlands, 42, pp. 1197-1208.

UNI 11039, 2003. Steel Fiber Reinforced Concrete—Part I: Definitions, Classification Specification and Conformity— Part II: Test Method for Measuring First Crack Strength and Ductility Indexes, Italian Board for Standardization, Rome, Italy.

Weimann, M. B. & Li, V. C., 2003. Drying shrinkage and crack width of an Engineered Cementitious Composites (ECC). Brittle Matrix Composites – International Symposium: No 7 7 2003, Issue 7, pp. 37-46.

Chapter 3

Bond slip mechanisms

In this chapter, the interfacial bond and relative slip response between the two different cementitious matrices (ductile ECC and conventional concrete) and the two types of reinforcing materials (low-stiffness GFRP and standard deformed steel) is described. The four combinations are investigated in a unique test setup with special emphasis on crack formation and development at the rebar-matrix interface during direct tensile loading. The experimental results are furthermore compared to analytical expressions in terms of slip, debonding length as well as their load-transverse crack opening response.

3.1 Introduction

Structural performance in general and durability in particular of any reinforced concrete structure is closely correlated with the magnitude and severity of cracking exhibited in the structure. The loss of structural performance due to cracking can be attributed to a decrease in composite interaction between reinforcement and surrounding concrete matrix, while reinforcement corrosion is related to among other things ingress of aggressive substances through the crack planes. Consequently, interfacial bond, characterizing the interaction and load transfer between reinforcement and matrix, will affect structural response and durability at serviceability limit state. In practice, design criteria for reinforced concrete structures are often governed by a limited crack width defined by codes of practice such as Eurocode and ACI building codes (EC2, 1991; ACI 318, 2002).

Although extensive studies have been carried out on surface crack widths and crack spacing of reinforced cementitious members in tension (e.g. Watstein and Parsons, 1943; Broms, 1965; Frosch, 1999), limited research is found that correlates surface crack widths and crack widths at rebar-matrix interface. Such correlation is needed in order to assess durability in terms of potential ingress paths for corroding substances that decrease the service-life of the structure. In addition, accurate knowledge of the geometry and propagation of cracking within structural elements allows researchers to utilize material characteristics more efficiently which will effectively result in more realistic predictions of the structural performance.

A limited number of studies have directly measured the internal cracking and interfacial bond behavior, due to the complications of observing the fracture process confined within a cementitious matrix. Nevertheless, studies carried out on reinforced prisms subject to direct tension with novel approaches such as: ink-injections used by Broms (1965) and Goto (1971) and more recently X-ray technique used by Otsuka et al. (2003) have provided essential information about internal cracking behavior.

Furthermore, research by Jiang et.al. (1984) and Pedziwiatr (2008), presented innovative experimental setups, were the interface between reinforcement and cementitious matrix was exposed while tensile loading was applied. In doing so, Jiang and Pedziwiatr were able to monitor the actual formation and development of primary transverse cracking as well as internal cracking and observe the interfacial debonding behavior. The limitation of such tests however is the lack of full confinement around the reinforcement.

In this study, the reinforcement – matrix interface of reinforced cementitious prisms were investigated during direct tensile loading in a novel test-setup. Reinforced prisms were fabricated with a portion of the longitudinal reinforcement exposed, i.e. the concrete cover was removed from a small segment. During direct tensile testing, high definition digital image correlation (DIC), similar to previous investigations (Pereira et al. 2011, 2012; Pease et al. 2012), was utilized to monitor the exposed reinforcement – matrix interface, allowing for detailed measurements of the initiation and propagation of cracking and debonding.

Additionally, closed form analytical solutions for slip between reinforcement and matrix, length of the transition zone, as well as the load as a function of average transverse crack width, were derived and compared to test results. The analytical solutions are based on a shear lag model and force equilibrium for a reinforced cementitious member with a single transverse crack.

3.2 Theory

Bond, or interfacial bond, describes the mechanism that defines the interactions and transfer of force between reinforcement and concrete and effectively influences width and spacing of transverse cracks (fib, 2010). The bond-slip interaction is furthermore considered a governing mechanism in tension stiffening as it determines the degree of composite interaction between two adjacent layers, i.e. the rate of degradation of force transfer (Oehlers et al., 2012). Expressions for the debonding process have been derived and refined by researchers in the past (Nilson 1972; Somayaji and Shah 1981; Balázs 1993; Fantilli, 2009; Hansen and Stang, 2012). Based on these formulations, in particular formulations by Hansen and Stang, a concise description of the governing equations is given here as a background to the analysis presented in this chapter. From an overall force equilibrium in a reinforced concrete member, the following must be satisfied in any chosen section:

$$P = P_s + P_c = \sigma_s A_s + \sigma_c A_c \tag{3.1}$$

where P is the total applied load, P_s, σ_s and A_s denote the force, the stress and the cross sectional area of the reinforcement respectively, while P_c, σ_c and A_c denote the force, the stress and the cross sectional area of the concrete matrix respectively.

In this analysis, a reinforced cementitious tensile member with a single transverse crack is examined, see Figure 3-1a. The analytical description of the tensile member is based on the shear lag model by Volkersen (1938) and extensions in Hansen and Stang (2012). To summarize the most important limitations of this approach, the assumptions of the model are given as: The adherents are considered linear elastic, bond line is infinitely thin, i.e. discrete cracking is assumed (Hillerborg et al., 1976), bond line is only deformed and loaded in shear, bending and bending related stress is neglected, small strains are assumed, and axial load is distributed evenly in the adherent cross section.

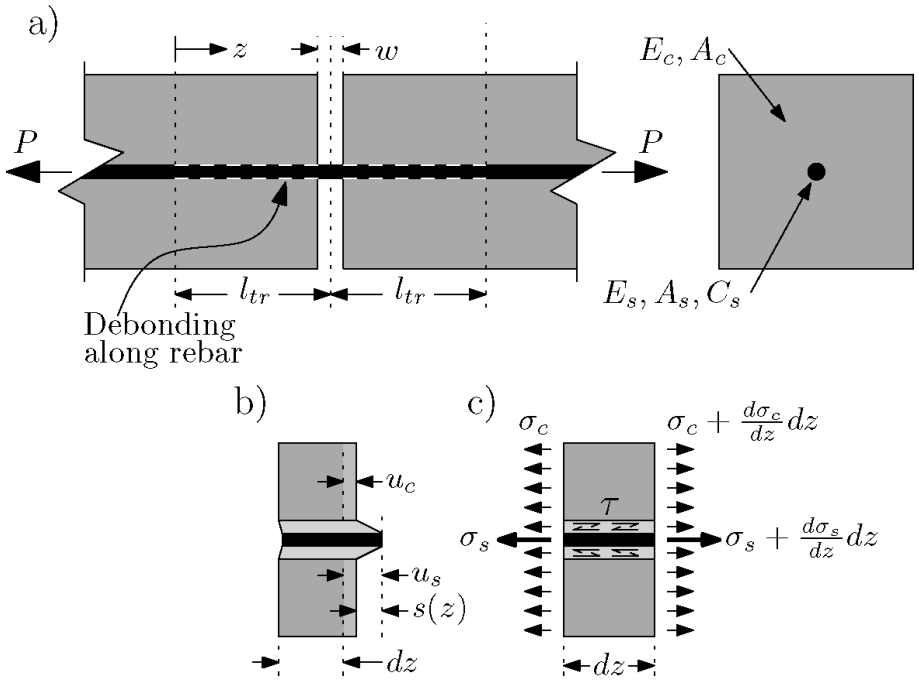

Figure 3-1 a): Schematic illustration of a single transverse crack in a reinforced concrete member, b): displacements in a infinitely small reinforced element (dz) and c): corresponding forces acting on the infinitely small element.

When the tensile member is loaded, a transverse crack of crack width, w, is assumed to initiate, see Figure 3-1a. As soon as the transverse crack appears, debonding is initiated along the rebar. Since the opening of the crack is considered uniform, the slip, s, at the transverse crack is defined as $s=w/2$. The length of the debonded zone is defined as the transition length, l_{tr}. Outside the debonded zone, full composite interaction is assumed, thus $\varepsilon_c = \varepsilon_s$. When the crack with, w, is increased, the response of the member, such as load, slip between adherents, transition length, shear stress distribu-

tion etc. can be derived as a function of *w*. The derivation of the governing equations for the tensile member can be carried out as follows:

Slip, *s(z),* is defined as the difference between the displacement of the reinforcement u_s and the displacement of the concrete, u_c (see Figure 3-1b):

$$s(z) = u_s(z) - u_c(z) \tag{3.2}$$

Assuming an elastic behavior and differentiating with respect to *z*, equation 3.2 yields:

$$\frac{ds}{dz} = \frac{du_s}{dz} - \frac{du_c}{dz} = \varepsilon_s - \varepsilon_c = \frac{\sigma_s}{E_s} - \frac{\sigma_c}{E_c} \tag{3.3}$$

where E_s and E_c are the modulus of elasticity of the reinforcement and concrete respectively.

By differentiating again with respect to *z*, the following expression is obtained:

$$\frac{d^2s}{dz^2} = \frac{d\varepsilon_s}{dz} - \frac{d\varepsilon_c}{dz} = \frac{1}{E_s}\frac{d\sigma_s}{dz} - \frac{1}{E_c}\frac{d\sigma_c}{dz} \tag{3.4}$$

In an infinitely small rebar element *dz* of the reinforced member (see Figure 3-1c), force equilibrium can be written as:

$$\frac{d\sigma_s}{dz} = \frac{C_s\,\tau}{A_s} \tag{3.5}$$

where C_s is the circumference of the reinforcement and τ is the bond stress between reinforcement and matrix.

Likewise, for an infinitely small concrete segment *dz* of the reinforced member (see Figure 3-1c), force equilibrium is written:

$$\frac{d\sigma_c}{dz} = -\frac{C_s\,\tau}{A_s} \tag{3.6}$$

By substituting the force equilibrium given in equations 3.5 and 3.6 into equation 3.4, one can obtain:

$$\frac{d^2s}{dz^2} = \frac{1}{E_s}\frac{C_s\,\tau}{A_s} + \frac{1}{E_c}\frac{C_s\,\tau}{A_s} = \left(\frac{1}{E_sA_s} + \frac{1}{E_cA_s}\right)C_s\tau \tag{3.7}$$

Equation 3.7 can be simplified by isolating the constants and defining γ_1:

$$\begin{aligned} \frac{d^2s}{dz^2} - \gamma_1^2\tau &= 0 \\ \gamma_1^2 &= \left(\frac{1}{E_sA_s} + \frac{1}{E_cA_s}\right)C_s \end{aligned} \tag{3.8}$$

This second order differential equation represents the basic relationship between second derivative of local slip *s(z)* and local bond stress τ.

In order to solve equation 3.8, an expression for the bond stress-slip interface is needed. One of the more common approaches is by assuming the local bond stress to be a function of the local slip and furthermore presuming a linear hardening interface law. Hansen and Stang (2012) suggested a hardening cohesive law with an initial bond stress component τ_0:

$$\tau(s) = \tau_0 + \left(\frac{\tau_{max} - \tau_0}{s_1}\right) s \quad for\ 0 < s < s_1$$
$$\tau(s) = 0 \quad for\ s > s_1 \tag{3.9}$$

where τ_{max} is the maximum bond stress and s_1 is the critical slip.

Equation 3.8 can now be re-written by introducing the interface law from equation 3.9 as follows:

$$\frac{d^2 s}{dz^2} - \gamma_1^2 \left(\frac{\tau_{max} - \tau_0}{s_1}\right) s - \gamma_1^2 \tau_0 = 0 \tag{3.10}$$

A solution to this inhomogeneous second order differential equation is essentially composed of two parts, i.e. the homogeneous solution and the particular solution. As given by Hansen and Stang (2012), the general solution for this expression is given as:

$$s(z) = A \sinh(\gamma_2 z) + B \cosh(\gamma_2 z) - \frac{\tau_0 s_1}{\tau_{max} - \tau_0}$$
$$\gamma_2^2 = \left(\frac{1}{E_s A_s} + \frac{1}{E_c A_s}\right)\left(\frac{\tau_{max} - \tau_0}{s_1}\right) C_s \tag{3.11}$$

where the constants A and B are determined from the boundary conditions as previously described, i.e. $s(l_{tr}) = w/2$ and at $s(0) = 0$.

Using the general solution for slip $s(z)$ from equation 3.11, it is now possible to obtain a formulation for the transition length l_{tr} at the boundary condition $ds/dz=0$ at $z=0$ as follows:

$$l_{tr} = \frac{\cosh^{-1}\left(1 + \frac{w(\tau_{max} - \tau_0)}{2 s_1 \tau_0}\right)}{\gamma_2} \tag{3.12}$$

Inserting the transition length l_{tr} into the formulation for slip $s(z)$, the expression for slip simplifies to:

$$s(z) = \frac{2 s_1 \tau_0 \sinh\left(\frac{\gamma_2 z}{2}\right)^2}{\tau_{max} - \tau_0} \tag{3.13}$$

It should be noted that the expression for slip in equation 3.13 is independent of the crack width w, due to that the origin of z is defined at the end of the transition length, l_{tr}, which is a function of w.

To derive an expression for the load as a function of crack width *P(w)*, equation 3.1 is re-written and combined with equation 3.3 which yields:

$$\frac{ds}{dz} = \frac{\sigma_s}{E_s} - \frac{\sigma_c}{E_c} = \frac{P_s}{E_s A_s} - \frac{P_c}{E_c A_c} = \frac{P - P_c}{E_s A_s} - \frac{P_c}{E_c A_c} \tag{3.14}$$

Which can be re-written as follows:

$$P = \frac{ds}{dz} E_s A_s + P_c \left(1 + \frac{E_s A_s}{E_c A_c}\right) \tag{3.15}$$

Differentiating equation 3.13, inserting z = l_{tr} and substituting the result into equation 3.15, the load – crack opening expression, *P(w)*, is obtained as:

$$P(w) = \left(\sqrt{\frac{w{C_s}^2(4s_1\tau_0 + w(\tau_{max} - \tau_0))}{4s_1\gamma_1^2}} + \sigma_c^*(w)A_c\right)\left(1 + \frac{E_s A_s}{E_c A_c}\right) \tag{3.16}$$

where $\sigma^*_c(w)$ is the tensile cohesive concrete stress in the concrete crack plane, i.e. the cohesive law for concrete in tension.

The bond-slip relationship for the rebar-matrix interface was defined in this section, while the cohesive laws for concrete in tension are given in section 3.3.1.

3.3 Materials

3.3.1 Cementitious materials

Figure 3-2d highlights the fundamental difference between normal (strain softening) FRCC, ductile SHCC in contrast to regular brittle concrete which loses its tensile carrying capacity almost immediately after the first crack forms. Furthermore, the post-cracking cohesive laws for a single crack in conventional concrete (Figure 3-2a), strain softening FRCC (Figure 3-2b) and strain hardening SHCC (ECC) (Figure 3-2c) as they are typically modeled are also shown.

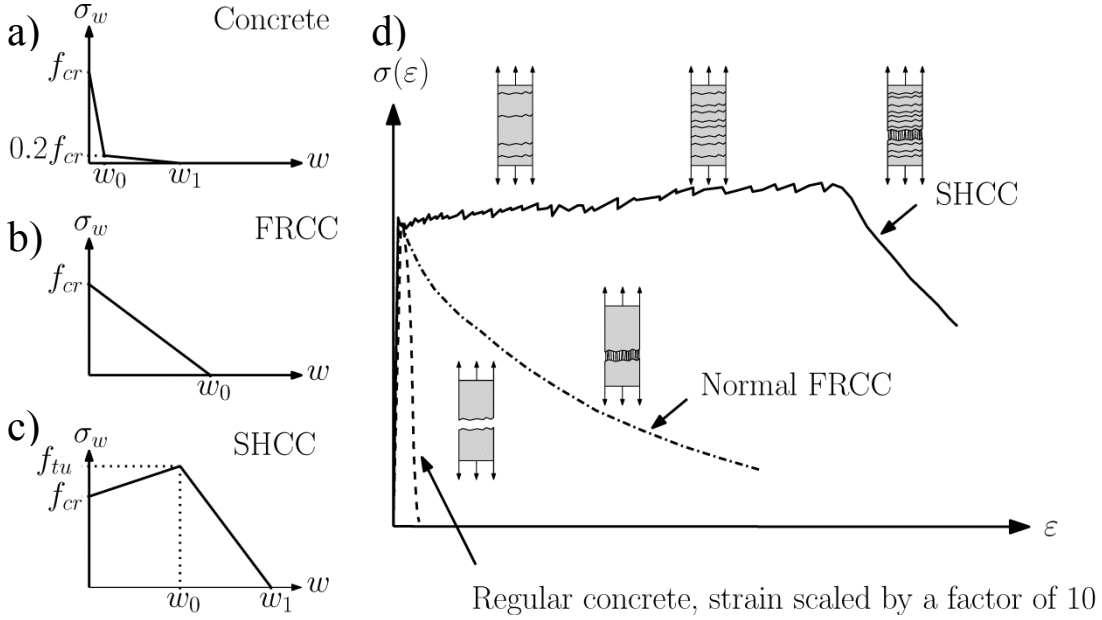

Figure 3-2 Constitutive laws for uniaxial tensile behavior of a single crack in a) conventional concrete (based on Model code 2010), b) strain softening FRCC and c) strain hardening SHCC. d): Schematic comparison of ductile SHCC (ECC), typical strain softening FRC and brittle concrete under tensile loading.

3.3.2 Material testing results

The material characteristics in this study were obtained as described in Chapter 2.

Both concrete and ECC were found to have the same compressive strength while ECC exhibited a modulus of elasticity two thirds of that of regular concrete (see Table 3-1). ECC however showed increased load capacity (pseudo strain hardening) over 2% tensile strain with maximum crack widths of approximately 0.15 mm. Figure 3-3a shows crack opening – strain development of individual cracks in a dog-bone shaped ECC specimen in direct tension using DIC. Figure 3-3b shows stress – CMOD results of five SCTT ECC specimens.

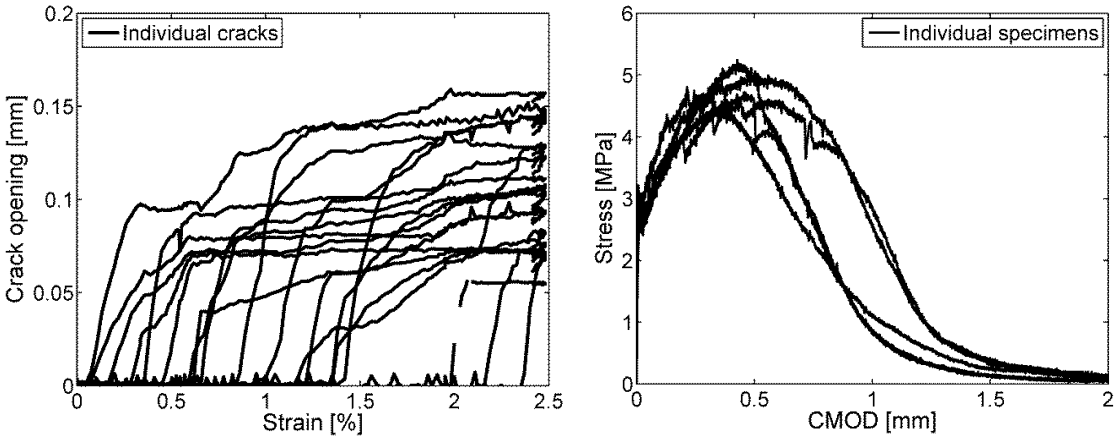

a) *b)*

Figure 3-3: Crack width-strain results for a dog-bone shaped tensile specimen in monotonic tension and b): Stress-CMOD results for four SCTT specimens in tensile loading.

Based on the compression strength of concrete, the stress-crack opening relationship for concrete was obtained based on recommended values from the CEB-FIP model code (fib, 2010).

Due to the difference in elastic modulus, the two reinforcement types (steel and GFRP) exhibit distinct different stress – strain behaviors, the GFRP with a relatively low stiffness has an elastic-brittle load response whereas the steel with a relatively high stiffness has an elastic-plastic load response. Table 3-1 summarizes relevant parameters deduced from material testing.

Table 3-1 Material parameters; f_{ck}: average compression strength, f_{cr}: tensile strength of first crack, f_y: tensile yield strength, f_{tu}: ultimate tensile strength, ε_{tu}: ultimate tensile strain, E: elastic modulus, w_0 and w_1 for ECC are crack width at maximum and crack width when stress drops to zero respectively. w_0 and w_1 for concrete refer to the bi-linear stress-crack opening relationship (see Figure 3-2a and c).

	f_{ck} [MPa]	f_{cr} [MPa]		E [GPa]	w_0 [mm]	w_1 [mm]
Concrete	67	4.1 †	-	33	0.0387 †	$5 \cdot w_0$ †
ECC	66	3.3-3.6 *	3.0-3.2 **	20	0.4	1.2

	f_y [MPa]	f_{tu} [MPa]	ε_{tu} [%]	E [GPa]
Steel rebar's	600	680	6.9	202
GFRP rebar's	-	1050	2.5	46

† Tensile strength obtained with splitting tensile tests (Brazilian tests).
†† Based on CEB-FIP model code 2010 recommendations (fib, 2010).
* First crack strength of dog-bone specimens, ultimate tensile stress capacity, f_{tu}, of: 4.1-4.6 MPa.
** First crack strength of SCTT specimens, ultimate tensile stress capacity, f_{tu}, of: 4.4-5.2 MPa.

3.4 Experimental program

3.4.1 Composite test setup

Regular concrete and ECC were examined experimentally in combination with regular steel reinforcement and GFRP reinforcement in four different reinforcement–matrix type compositions: i.e., steel reinforced concrete (R/C), steel reinforced ECC (R/ECC), GFRP reinforced concrete (GFRP/C) and GFRP reinforced ECC (GFRP/ECC).

To observe the actual interface of reinforcement and surrounding matrix during direct tensile loading, a 400 mm long, 100 mm wide and 35 mm thick reinforced prisms were prepared with a reduced width at the mid section, i.e. dogbone shaped specimens. At the mid section a 50 mm stretch of the concrete cover was removed, on each side of the reinforcement, revealing the longitudinal reinforcement slightly.

Two rebars, 6 mm in diameter, extended throughout the entire length of the specimens, 54 mm apart, were placed in the center of the prisms, resulting in a clear concrete cover thickness of approximately15 mm relative to the thickness of the prisms (see Figure 3-4). In the steel reinforced prisms (R/C and R/ECC), the rebars were welded to a steel anchor plate at both ends. In the GFRP reinforced prisms (GFRP/C and GFRP/ECC), 80 mm long cylinder threaded on the outside and inside, were glued around each end of the GFRP rebars using epoxy and subsequently secured to steel anchor plates at both ends of the prisms (see Figure 3-4).

The 60x35 mm^2 representative cross section resulted in a reinforcement ratio ρ = 2.8% for the steel reinforced members and ρ = 3.1% for the GFRP reinforced members due to a slightly larger diameter of the GFRP rebars (d_{GFRP} = 6.3 mm).

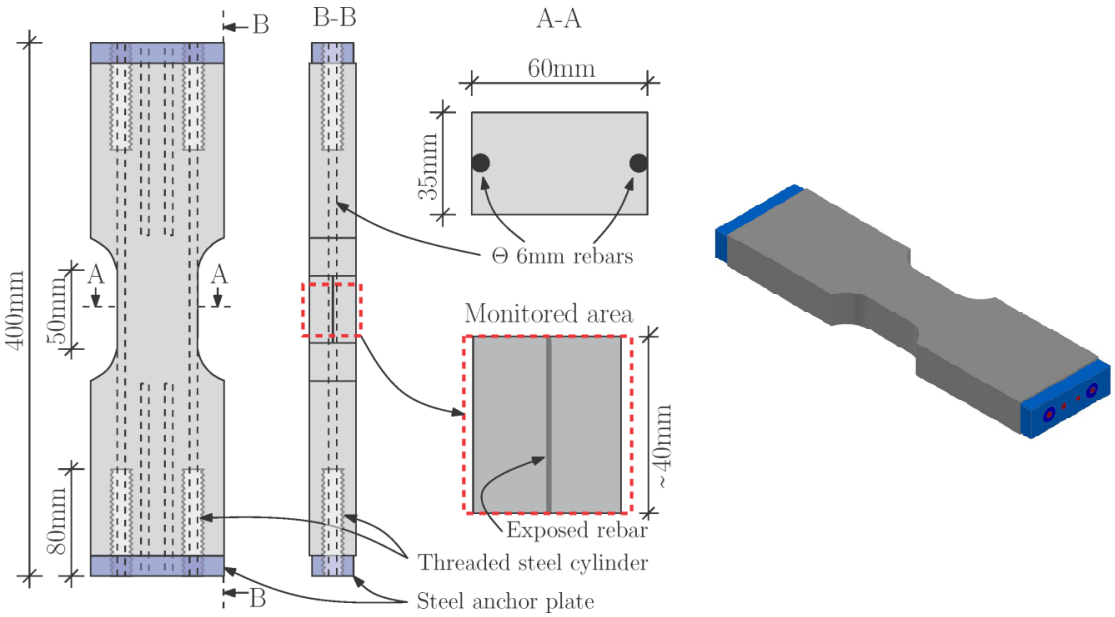

Figure 3-4 Geometry and layout of reinforced prism used to evaluate the rebar-matrix interface in tensile loading.

The composite prisms where situated in the actuators grips and clamped directly into a ridged testing frame (Figure 3-5a). A displacement controlled tensile loading was applied with an actuator displacement rate of 0.5 mm per minute.

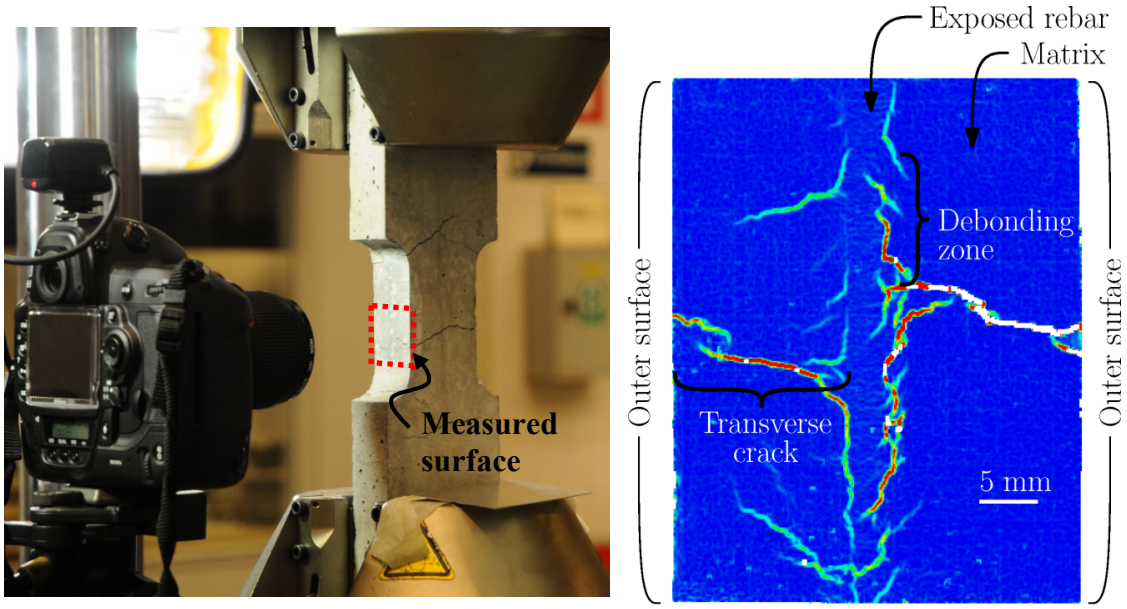

a) *b)*

Figure 3-5 a) Example of a reinforced prism in the test setup and b): example of image correlation analysis (DIC), blue color indicates zero deformation while color changes depict principle strain intensities (indicating a crack or slip) on the measured surface (see B-B in Figure 3-4).

Before testing was initiated a stochastic spray pattern was applied to the specimen's representative surface with the partially exposed rebar (see B-B in Figure 3-4) in order to monitor the area of interest using DIC. The digital image analysis allowed for all cracks on the observed area to be tracked as they initialized and developed during loading. In the post-processing of the DIC, a series of so-called virtual clip gauges were positioned on the displacement field, on either side of the transverse cracks and debonding zones (see Figure 3-6).

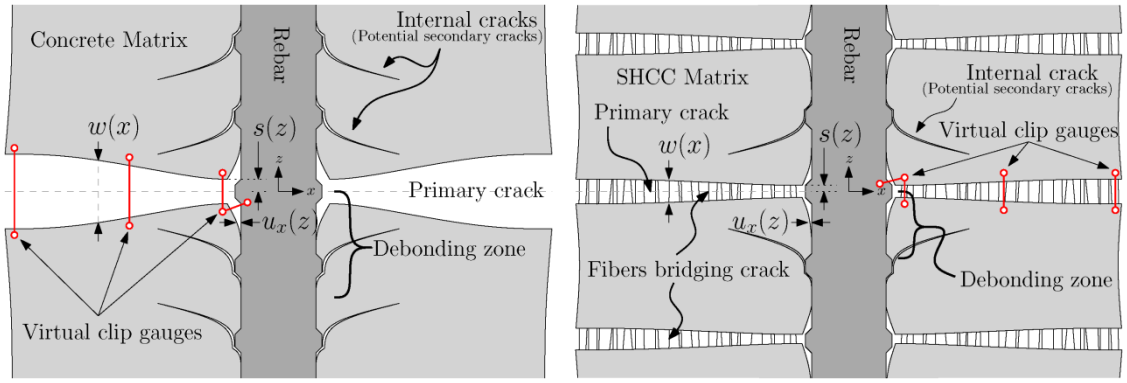

a) R/C *b) R/SHCC*

Figure 3-6 Schematic illustrations of deformations around reinforcement in a): R/C and b): R/SHCC (R/ECC).

The first transverse crack to initiate on either side of the reinforcement was chosen for detailed analysis from the rebar-matrix interface to the outer surface of the matrix. Furthermore, the debonding along the rebar-matrix interface (because of the transverse crack) was analyzed in detail as well. Figure 3-5 shows a) an example of a GFRP/C prism being tested and b) the strain field obtained using DIC on an R/C specimen. The figure exemplifies the transverse cracking and resulting branching and debonding along the length of the longitudinal rebar. The first transverse crack was chosen for analysis to minimize the effects of surrounding cracks and crack branching.

The schematic illustration given in Figure 3-6 exemplifies the interfacial difference between R/C and R/ECC members in tensile loading.

3.4.2 Composite test results

In this section the crack widths and crack width profiles, *w(x)*, from the experimental program are analyzed in detail during initiation and propagations of transverse cracks. Furthermore, the debonding mechanism, i.e. slip, *s(z)*, and opening, *u(z)*, displacements are analyzed and related to reinforcement strain and transverse crack width development.

Figure 3-7 shows visual interpretation of the displacement measurements, i.e. strain field, where blue color indicates zero strain while color changes depict strain intensities which represent cracks.

Examples are shown for all composition types at three different rebar strain levels obtained by DIC during tensile loading process. Strains are obtained by measuring a point-to-point displacement of a virtual clip gage over the length of the exposed rebar using DIC, i.e. $\varepsilon_{rebar}=\Delta L/L$. Figure 3-7 furthermore gives an insight into the conjunction of crack networks found in reinforced members.

White areas depict un-computed facets due to either excessive deformations or inadequate surface pattern, i.e. not recognized in DIC analysis.

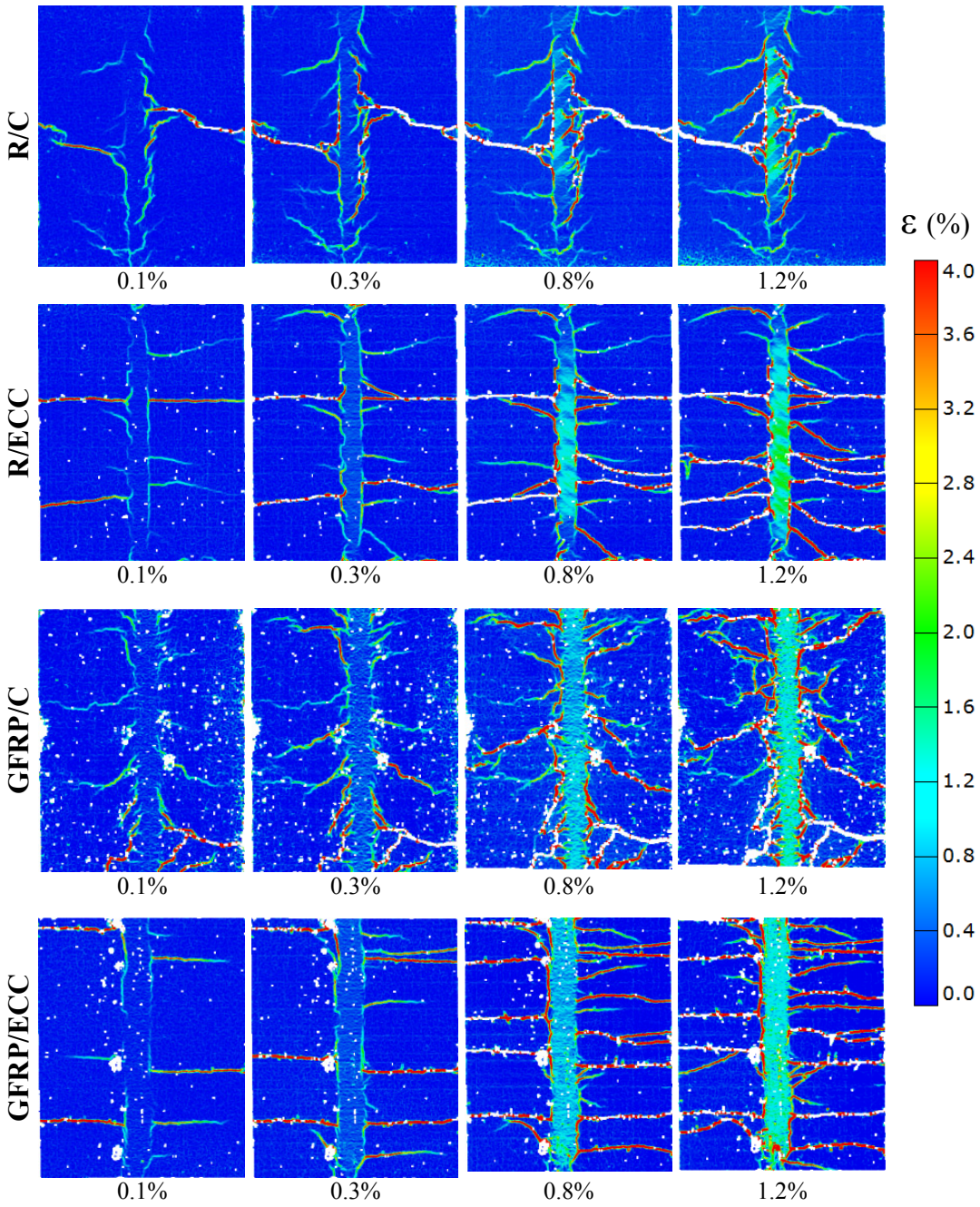

Figure 3-7 Crack development in all composition types during tensile loading obtained by the DIC process. Comparison is made at different rebar strain levels.

Based on the DIC analysis (as illustrated in Figure 3-7) the following results are obtained: First the transverse crack is examined and subsequently the resulting debonding of the rebar – matrix interface is investigated. The strain in the exposed reinforcement is obtained and referenced to in the following results.

Transverse crack width development

Figure 3-8a through to Figure 3-11a show crack width profiles along the x-axis (perpendicular to the rebar) for a representative transverse crack of all composition types. Measurements are obtained from the rebar – matrix interface to the outer surface of

the matrix (Figure 3-6) at different rebar strain levels. Furthermore, the corresponding stress transfer across the crack profile is presented in Figure 3-8b - Figure 3-11b, based on the constitutive law for concrete and ECC, as shown in Figure 3-2, and the measured crack opening profile. The constitutive stress – crack opening law used for concrete was based on recommendations by CEB-FIP model code (fib, 2010) (see Table 3-1), while the constitutive law for ECC was based on the results obtained from SCTT results (see Figure 3-3b and Table 3-1).

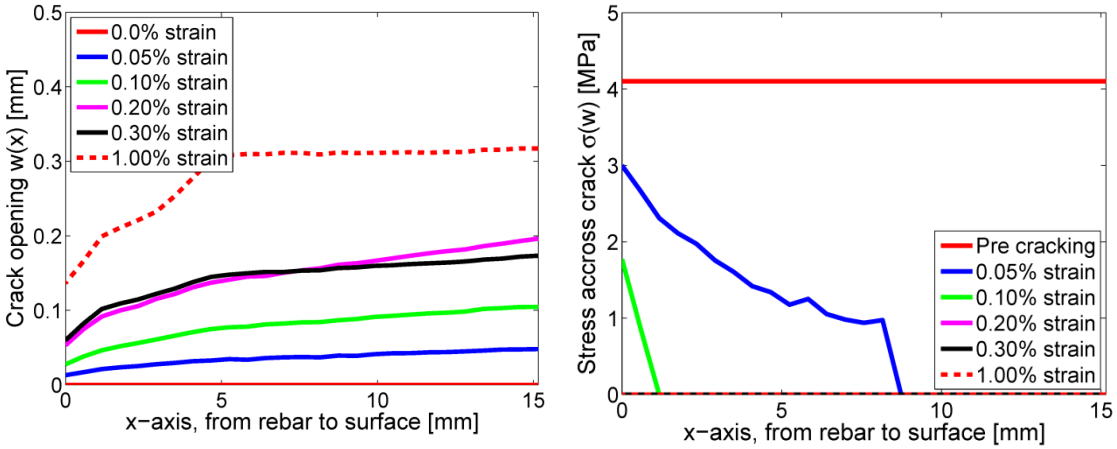

a) R/C *a) R/C*

Figure 3-8 a): Crack opening profile for a transverse crack in R/C at different rebar strain levels and b): the corresponding stress transfer across the crack based on the cohesive law for concrete in tension, $\sigma_{c*}(w)$, shown in Figure 3-2 and fracture mechanical parameters given in Table 3-1.

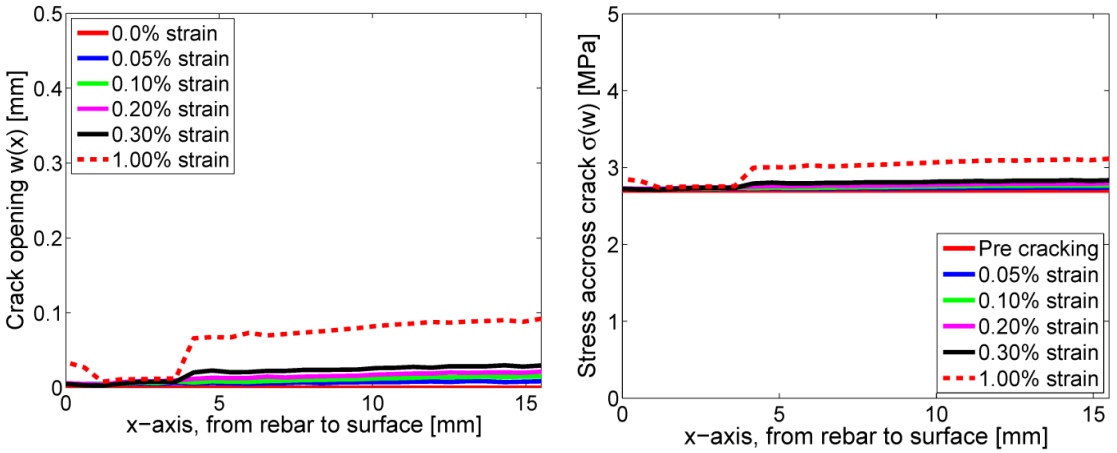

a) R/ECC *b) R/ECC*

Figure 3-9 a): Crack opening profile for a transverse crack in R/ECC at different rebar strain levels and b): the corresponding stress transfer across the crack based on the cohesive law for ECC in tension, $\sigma_{ECC}(w)$, shown in Figure 3-2 and fracture mechanical parameters given in Table 3-1.

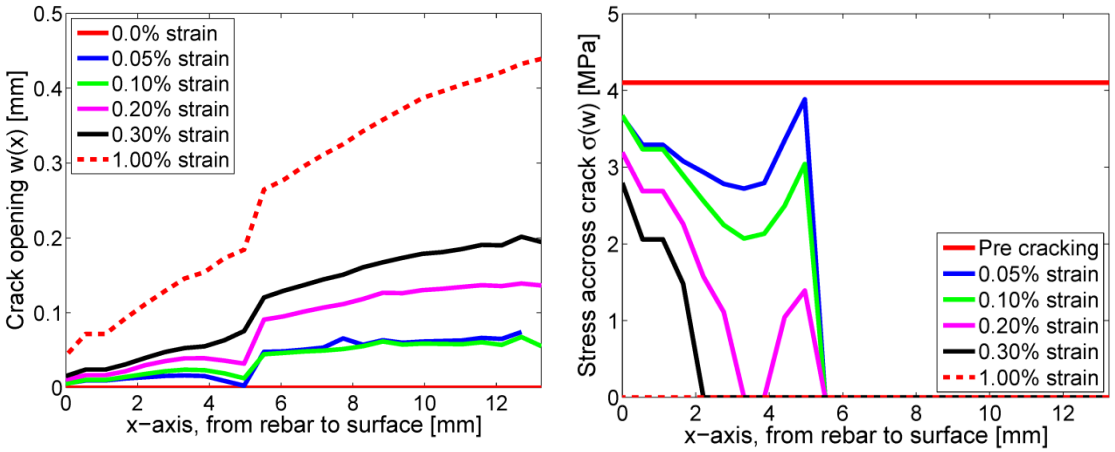

a) GFRP/C *b) GFRP/C*

Figure 3-10 a): Crack opening profile for a transverse crack in GFRP/C at different rebar strain levels and b): the corresponding stress transfer across the crack based on the cohesive law for concrete in tension, σ_c(w), shown in Figure 3-2 and fracture mechanical parameters given in Table 3-1.*

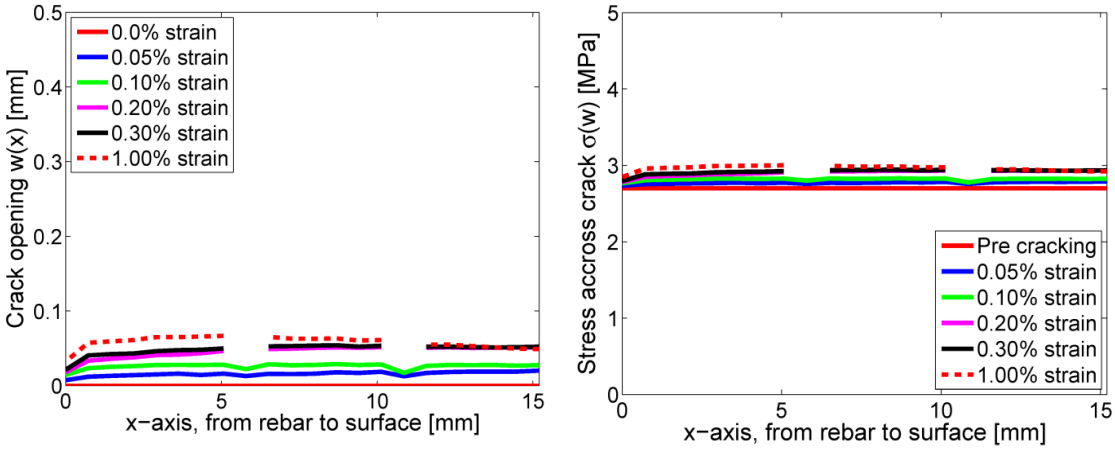

a) GFRP/ECC *b) GFRP/ECC*

Figure 3-11 a): Crack opening profile for a transverse crack in GFRP/ECC at different strain levels and b): the corresponding stress transfer across the crack based on the cohesive law for ECC in tension, $\sigma_{ECC}(w)$, shown in Figure 3-2 and fracture mechanical parameters given in Table 3-1.

3.4.3 Debonding displacement development

Figure 3-12 and Figure 3-13 show the global slip, *s(z)*, and opening, $u_x(z)$, displacement measurements for all composition types along the rebar (*z*-axis) at different rebar strain levels. In the global analysis the origin of the z-axis ($z = 0$) is positioned at the start of the measuring length as shown in Figure 3-12 and Figure 3-13.

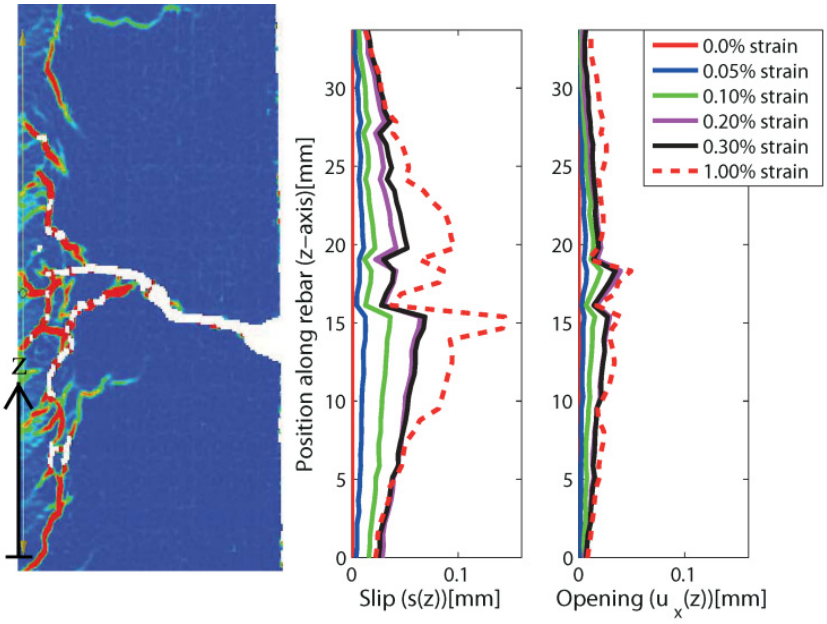

a) R/C

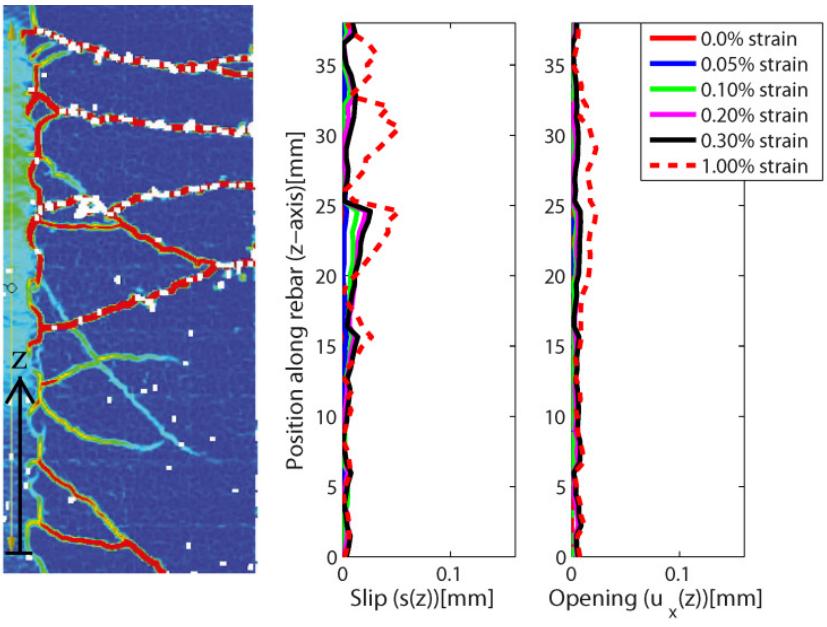

b) R/ECC

Figure 3-12 Debonding displacement profiles, slip s(z), and opening, $u_x(z)$, along the rebar (z-axis) in a): a R/C specimen and b): a R/ECC specimen at different strain levels. Vertical dotted line in a) shows the position along the reinforcement where slip measurements changed direction.

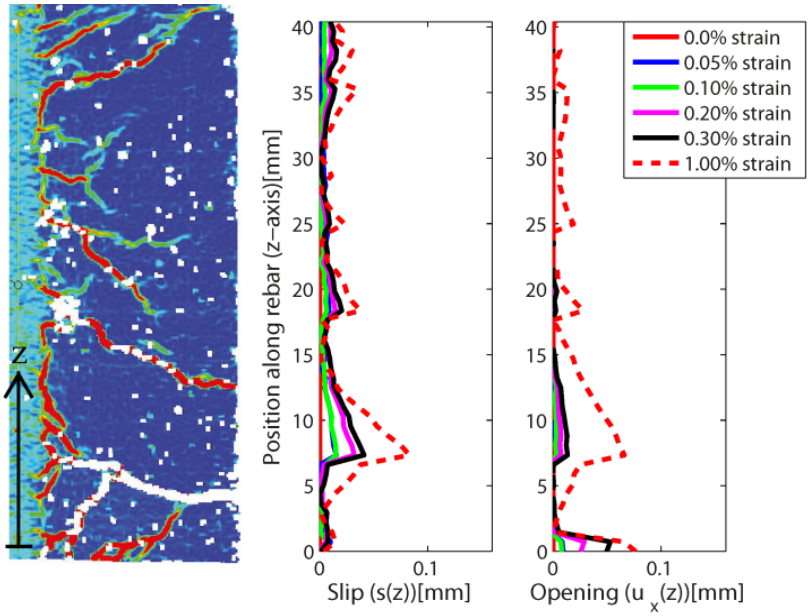

a) GFRP/C

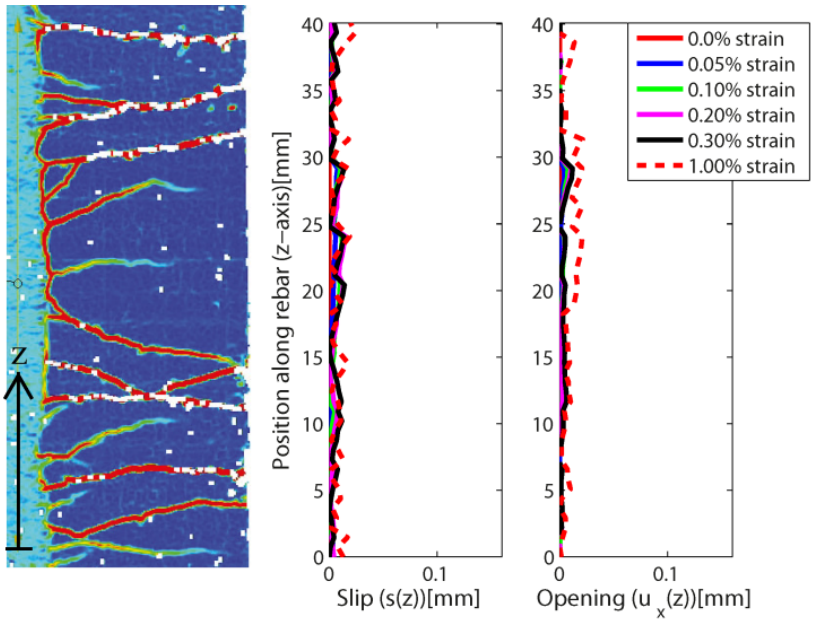

b) GFRP/ECC

Figure 3-13 Debonding displacement profiles, slip s(z), and opening, $u_x(z)$, along the rebar (z-axis) in a): GFRP/C specimen and b): GFRP/ECC specimen at different strain levels.

Furthermore, Figure 3-14 through to Figure 3-17 show examples of local slip *s(z)* and local opening $u_x(z)$ displacement measurements, i.e. a closer view of the slip and opening measurements presented in Figure 3-12 and Figure 3-13, for all composition types along the rebar at different rebar strain levels.

In the local analysis the origin of the measurements is defined at the intersection of the transverse crack with the reinforcement. Measurements are shown for a 4 mm length along the rebar in order to minimize any distortion from neighboring cracks and or overlapping debonding zones. It is noted that the local debonding measurements, shown in Figure 3-14, were obtained from a transverse crack on the left hand side of the rebar (see Figure 3-7) which developed at a slightly later strain stage than the global debonding taken on the right hand side of the rebar (Figure 3-12a).

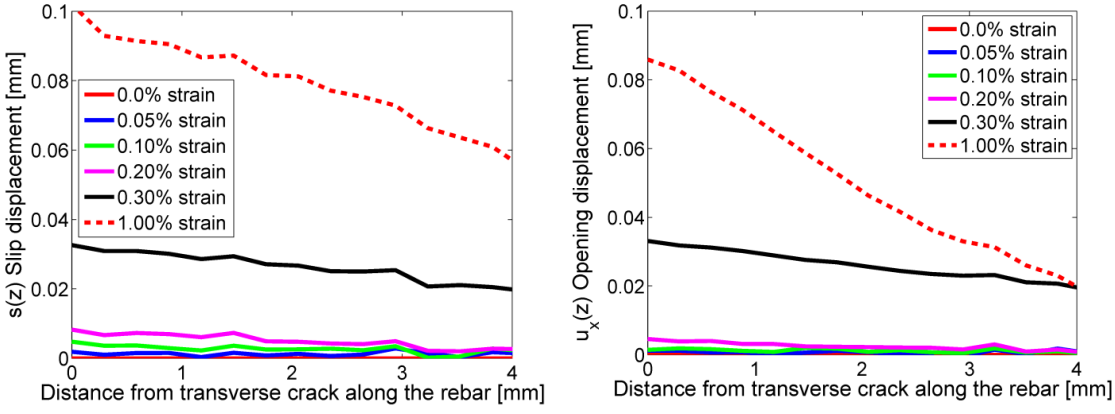

a) R/C *b) R/C*

Figure 3-14 Debonding displacement profiles resulting from a transverse crack in R/C, a): sliding displacement, slip s(z), and b): opening displacement, $u_x(z)$, at different rebar strain levels.

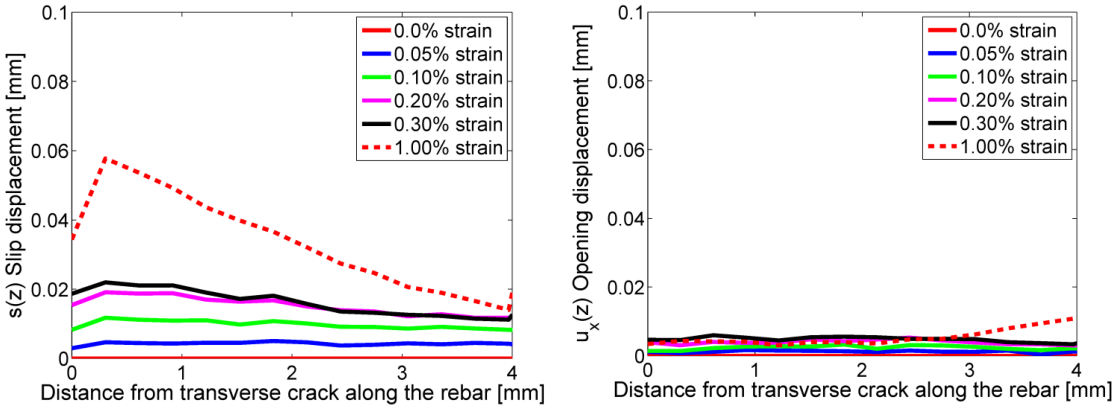

a) R/ECC *b) R/ECC*

Figure 3-15 Debonding displacement profiles resulting from the transverse crack in R/ECC showed in Figure 3-8b, a): sliding displacement, slip s(z), and b): opening displacement, $u_x(z)$, at different rebar strain levels.

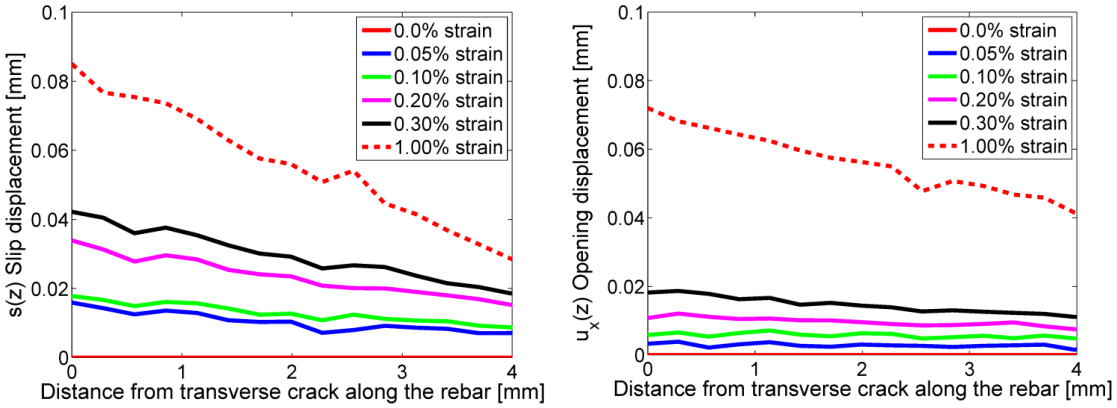

a) GFRP/C *b) GFRP/C*

Figure 3-16 Debonding displacement profiles resulting from the transverse crack in GFRP/C showed in Figure 3-10a, a): sliding displacement, slip s(z), and b): opening displacement, $u_x(z)$, at different rebar strain levels.

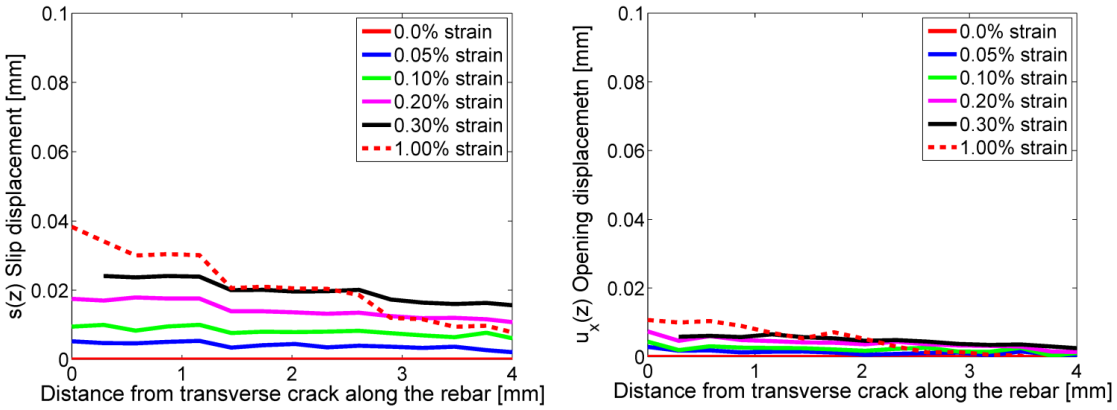

a) GFRP/ECC *b) GFRP/ECC*

Figure 3-17 Debonding displacement profiles resulting from the transverse crack in GFRP/ECC showed in Figure 3-10b, a): sliding displacement, slip s(z), and b): opening displacement, $u_x(z)$, at different rebar strain levels.

3.5 Discussion

3.5.1 Transverse crack width development

The transverse crack profiles shown in Figure 3-8a through to Figure 3-11a illustrate the fundamental difference between regular brittle concrete and strain hardening ECC where crack width opening is drastically reduced due to fibers bridging. It is noted that sudden drops in crack widths close to the rebar – matrix interface indicate crack branching, which was found to be significantly greater in reinforced concrete members.

At small crack widths, concrete is able to transfer stress according to the cohesive law for concrete (see Figure 3-2a), but rapidly loses any stress transfer capacity once the crack becomes larger, e.g. w>0.175 mm. Applying the cohesive law, $\sigma(w)$, to the crack profile, $w(x)$, the theoretical stress transfer in cracked concrete is shown in Figure 3-8b and Figure 3-10b. According to the cohesive law for ECC (see Figure 3-2a), fiber bridging in ECC facilitates a uniformly increasing stress transfer across the crack as is shown in Figure 3-9b and Figure 3-11b.

In Figure 3-8a through to Figure 3-11a, only the results from GFRP/C indicates that crack width would increase with increased cover thickness (x > 15 mm). However, it is noted that such behavior, where cover thickness is correlated with crack width, was observed at higher strain levels for the R/C example shown in Figure 3-8a, as well as in all primary cracks of all R/C specimens. Contrary to concrete reinforced specimens, ECC reinforced member consistently indicated that increased cover thickness (x > 15mm) would not drastically change crack widths at the outer surface.

Table 3-2 summarizes the transverse crack width opening for the different compositions at the interface w_{int} and at the outer surface w_{out} as well as the ratio between the two parameters.

Table 3-2 Crack width openings at reinforcement-matrix interface ($x=0$) and at outer surface ($x=15$) for various rebar tensile strain levels corresponding to Figure 3-8 and Figure 3-10.

		Rebar strain levels				
		0.05%	**0.10%**	**0.20%**	**0.30%**	**1.00%**
RC	w_{int} (x=0) [mm]	0.013	0.028	0.053	0.060	0.137
	w_{out} (x=15) [mm]	0.048	0.105	0.196	0.173	0.317
	$\boldsymbol{w_{int} / w_{out}}$	**0.27**	**0.26**	**0.27**	**0.35**	**0.43**
R/ECC	w_{int} (x=0) [mm]	0.005	0.005	0.006	0.005	0.034
	w_{out} (x=15) [mm]	0.009	0.015	0.021	0.030	0.092
	$\boldsymbol{w_{int} / w_{out}}$	**0.61**	**0.35**	**0.27**	**0.17**	**0.37**
GFRP/C	w_{int} (x=0) [mm]	0.005	0.005	0.011	0.015	0.043
	w_{out} (x=13) [mm]	0.055	0.056	0.136	0.195	0.439
	$\boldsymbol{w_{int} / w_{out}}$	**0.09**	**0.09**	**0.08**	**0.08**	**0.10**
GFRP/ECC	w_{int} (x=0) [mm]	0.007	0.014	0.018	0.021	0.032
	w_{out} (x=15) [mm]	0.020	0.028	0.051	0.052	0.049
	$\boldsymbol{w_{int} / w_{out}}$	**0.37**	**0.52**	**0.35**	**0.41**	**0.66**

It was observed that most of the transverse cracks intercept the rebar (primary cracks) or initiate at the rebar (internal cracks) at an angle, and that the debonding zone tends to propagate to one side of the transverse crack depending on the angle of the crack

relevant to the longitudinal direction of the reinforcement (see Figure 3-7). This behavior was particularly distinct at low strain levels. However, at higher strain levels this process becomes less clear as branching increases and the conjunction of cracks close to the rebar becomes more complex, particularly in reinforced concrete specimens. Furthermore, contrary to reinforced ECC specimens, internal cracks in reinforced concrete members rarely reach the outer surface, but rather propagate towards the primary cracks.

3.5.2 Debonding displacement development

The global debonding displacement results, shown in Figure 3-12 and Figure 3-13, give a good indication of the interface degradation transpired during loading. The distinct difference in interfacial behavior between reinforced concrete- and reinforced ECC members is emphasized in the slip, s, and opening displacement, u_x, measurements. The crack bridging, load carrying capacity and inherent multiple cracking attributes of ECC, results in considerably less debonding displacement (both sliding and opening) in reinforced ECC members when compared to that of reinforced concrete members.

The local bond slip- and opening- development shown in Figure 3-14 through to Figure 3-17 was found to propagate intermittently, similar to that of the crack development in ECC shown in Figure 3-3 where crack opening displacement of individual cracks are dependent on the development of surrounding cracks. That is, while crack opening in an arbitrary crack advanced, the crack opening of a neighboring crack subsided or halted before advancing again. This can be seen in global and local results when the measured debonding displacement is compared at different rebar strain levels.

By directly comparing local slip- $s(w)$ and opening- $u_x(z)$ displacements measurements, presented in Figure 3-14 through to Figure 3-17 within the elastic regime of the reinforcement (up to 0.3% tensile strain), the displacement path for each debonding zone is shown in Figure 3-18 and Figure 3-19. Although these results correspond to local measurement, they give a general indication about the ratio between slip and opening displacement next to a primary crack in the four composition types.

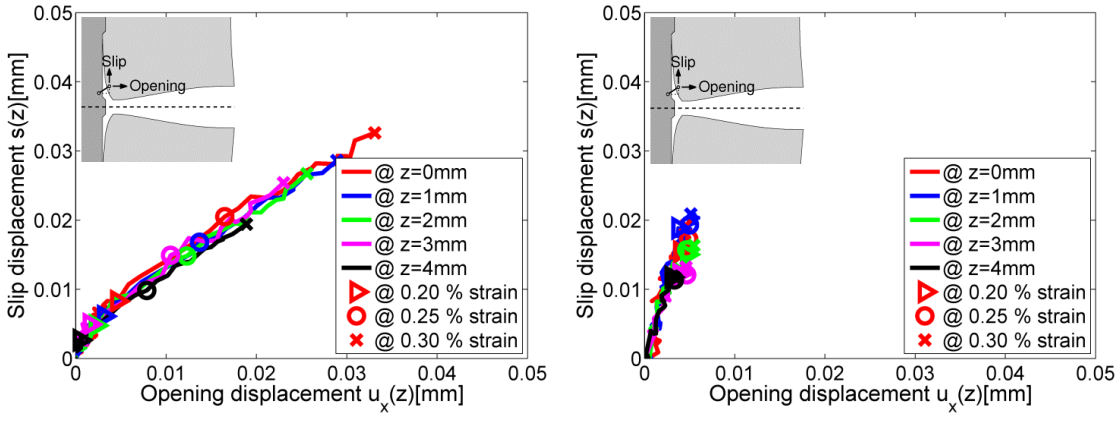

a) R/C *b) R/ECC*

Figure 3-18 Local sliding displacement, slip s(z), Vs. opening displacement, $u_x(z)$, of the debonding zone for tensile stain of the reinforcement up to 0.3 % at different distances along reinforcement for a): R/C and b): R/ECC. Markers depict strain levels: 0.20 %, 0.25 % and 0.30 %.

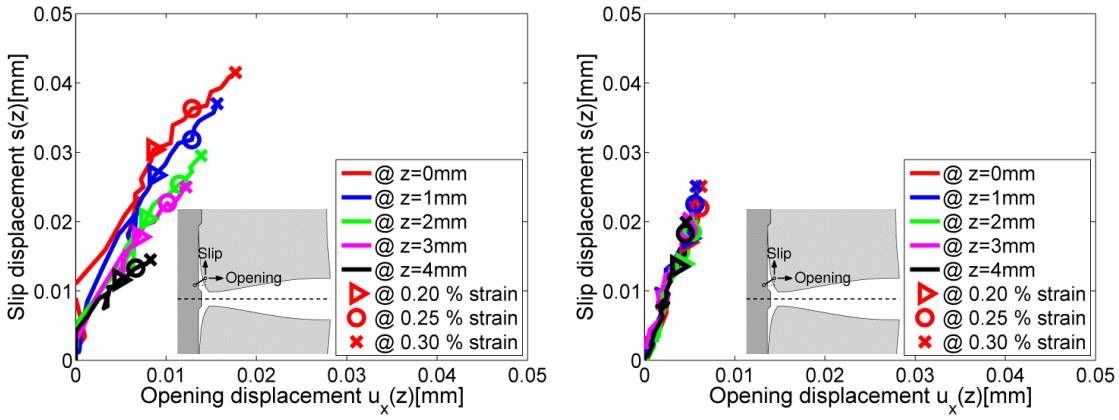

a) GFRP/C *b) GFRP/ECC*

Figure 3-19 Local sliding displacement, slip s(z), Vs. opening displacement, $u_x(z)$, of the debonding zone for tensile stain of the reinforcement up to 0.3 % at different distances along reinforcement for a): GFRP/C and b): GFRP/ECC. Markers depict strain levels: 0.20 %, 0.25 % and 0.30 %.

From Figure 3-18 and Figure 3-19 the ratio between slip *s(z)* and opening $u_x(z)$ is: ~1.0 for R/C, ~3.4 for R/ECC, ~2.3 for GFRP/C and ~4.0 for GFRP/ECC. At a certain critical rebar strain level, a local decrease in opening $u_x(z)$ displacement was observed initiating at tensile strain levels of: ~0.2-0.6% for R/C, ~0.3-0.4% for R/ECC, ~0.4-0.5% for GFRP/C and ~0.2-0.3% for GFRP/ECC. This behavior was often accompanied by intermediate discontinuity or even decrease of slip *s(z)*. These observations suggest the activation of mechanical interlocking mechanisms, which presents itself in conical cracks around the rebar circumference (Goto, 1971; Lutz and Gergely, 1967, Fantilli et al., 2007; Chao et al., 2009). At the activation of mechanical interlocking,

the conical cracks act as wedges against the rebar and the rebar ribs and effectively transfer forces directly across the rebar – matrix interface.

3.5.3 Slip measurements and Theory

To calculate the transition length l_{tr} and the slip *s(z)* using equations 3.12 and 3.13, the cohesive interface law (equation 3.9) needs to be defined. In Figure 3-20, three variations of the linear hardening bond stress-slip (τ-s) relations from equation 3.9 are presented. For the transition length and slip calculations, the relationship shown in Figure 3-20b is chosen with an initial non-zero bond value, τ_0, defined here as being $\tau_{max}/2$. Based on measurements (Table 3-1) and recommendations in the CEB-FIP model code (fib, 2010), the following parameter values are used: τ_{max} = 10.2 MPa, τ_0 = 5.1 MPa and s_1 = 0.2 mm.

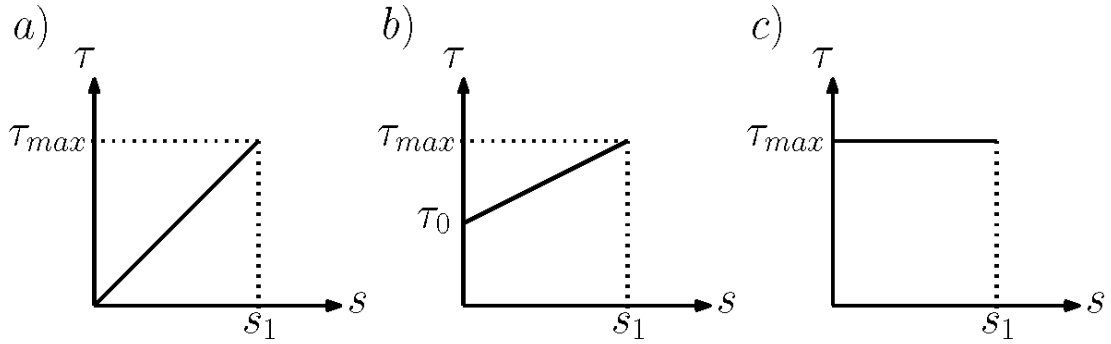

Figure 3-20 Variations of the constitutive interface model used.

The slip can now be calculated from equation 3.13 while the transition length is obtained from equation 3.12.

Figure 3-21 shows a comparison between the theoretical slip results and the measured results of the global slip along the reinforcement for R/C and GFRP/C (see Figure 3-12 and Figure 3-13). The comparison is shown for different transverse crack widths, referring to different transition lengths and rebar strain level (see Figure 3-21). For convenience, the origin of the horizontal axis (z-axis) for the analytical results is redefined at the intersection of transverse crack and rebar. As mentioned in previous subsection, the transverse cracks have a tendency to intersect the reinforcement at an angle rather than being perpendicular to the rebar. As a result, debonding displacements propagate notably more to one side of the intersecting transverse crack as debonding initiates. This tendency is evident where slip measurements at the transverse crack are higher than *w/2* (the theoretical prediction). Subsequently as loading is increased, debonding has the tendency to shift active direction, and or propagate intermediately. Therefore, to make a sensible comparison between the analytical solution (equation 3.13) and the test result, the input transverse crack width value needs to be chosen carefully to ensure that the measured crack branch width corresponds to the measured debonding.

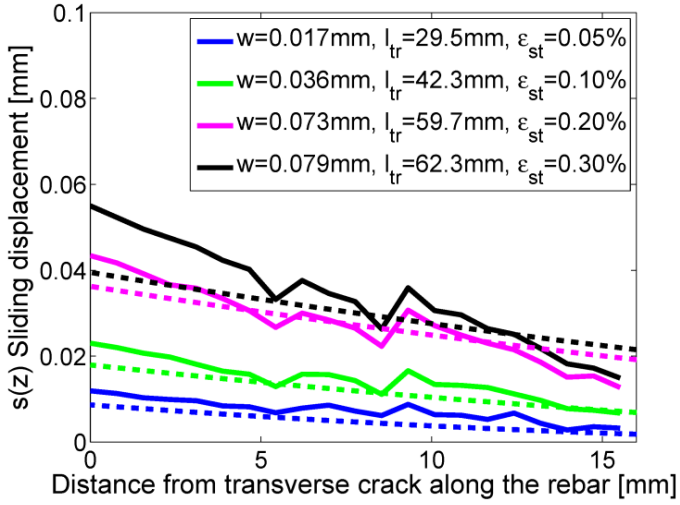

a) R/C

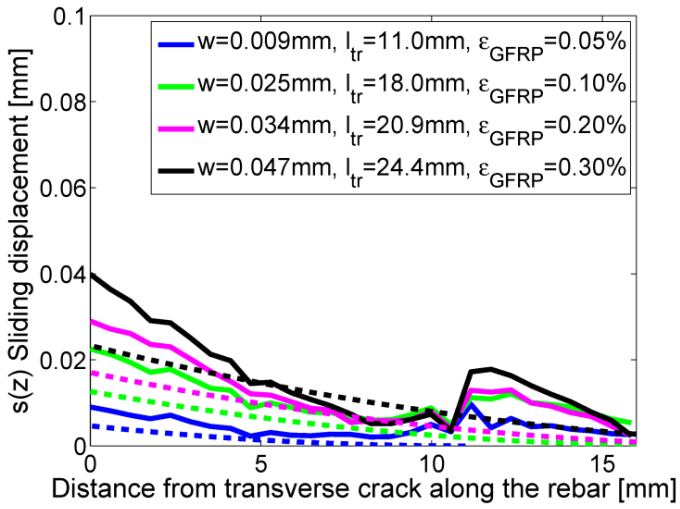

b) GFRP/C

Figure 3-21 Comparison between theoretical slip values obtained from equation 3.13 (dashed lines) and the actual measured global slip s(z) values (continuous lines) for a): R/C and b): GFRP/C. The origin of the vertical axis (z-axis) is positioned at the intersection of the transverse crack with the reinforcement.

In Figure 3-21, the measured slip decreases rapidly when compared to the analytical predictions. As mentioned earlier the theoretical predictions initially underestimate the slip for both R/C and GFRP/C configurations. However, with increased distance from the crack plane and increased loading, the theoretical predictions overestimate the slip. Based on the trajectory of the slip measurements for R/C, the slip will reach zero at approximately 20-22 mm distance from the transverse crack, while GFRP/C does so at approximately 8-12 mm distance (see Figure 3-21), which is generally lower than the predicted values. Furthermore, the activation of mechanical interlocking, or wedge behavior, is observed in slip- and in opening- displacement measurements

for GFRP/C. In Figure 3-21b, at approximately 8-10 mm, slip development is halted at ~0.1% rebar strain (ε_{GFRP}) and subsequently decreases at ~ 0.3% rebar strain.

3.5.4 Load vs. crack opening measurements and Theory

In Figure 3-22 a comparison is shown between the analytical expression (equation 3.16) and the load – crack opening results from R/C and GFRP/C tests. In addition, the reinforcement strain for the experimental results is indicated at four different strain levels, i.e. 0.05%, 0.10%, 0.20% and 0.30%.

Three variations of the interface law are incorporated into equation 3.16 and are presented as P1, P2 and P3. In P1, τ_0 starts at 0 (Figure 3-20a), in P2, τ_0 is equal to $\tau_{max}/2$ (Figure 3-20b) and in P3, τ_0 is equal to τ_{max} (Figure 3-20c).

As in the transition length and slip calculations, the analytical expression for the load-crack opening relies on input values obtained from material testing and recommended values given by the CEB-FIP model code (fib, 2010). Furthermore, to compensate for the lower first cracking load values observed during testing, P1, P2 and P3 for concrete are presented for f_{ctm} = 4.1 MPa and f_{ctm} = 2.1 MPa. Other material input parameters include: τ_{max} = 10.2 MPa, τ_0 = 5.1 MPa, s_1 = 0.2 mm, $w_{0,concrete}$ = 0.0387 mm, $w_{1,concrete} = 5 \cdot w_{0,concrete}$, $f_{cr,ECC}$ = 3.0 MPa, $f_{ctu,ECC}$ = 4.5 MPa, $w_{0,ECC}$ = 0.4 mm and $w_{1,ECC}$ =1.2 mm.

The load – crack opening response of an R/C specimen (Figure 3-22a) shows a steady crack width growth up to ~70μm (~0.15% strain) at which point crack growth decelerates but continues up to ~110μm at 0.3% strain. The test result seems to fit in between the analytical predictions P2 and P3 (with f_{ctm} = 2.1 MPa) up to ~0.15% strain, but both overestimate at early crack opening. In the test result for a GFRP/C specimen (Figure 3-22b) a so called “snap back” behavior was observed at ~0.1% strain (~50μm crack width) due to the initiation of another crack outside of the DIC area, thereafter the crack growth continued at a steady pace up to ~110μm at 0.3% strain. The analytical solutions P3 (with f_{ctm} = 2.1 MPa) seems to best fit the experimental results for GFRP/C.

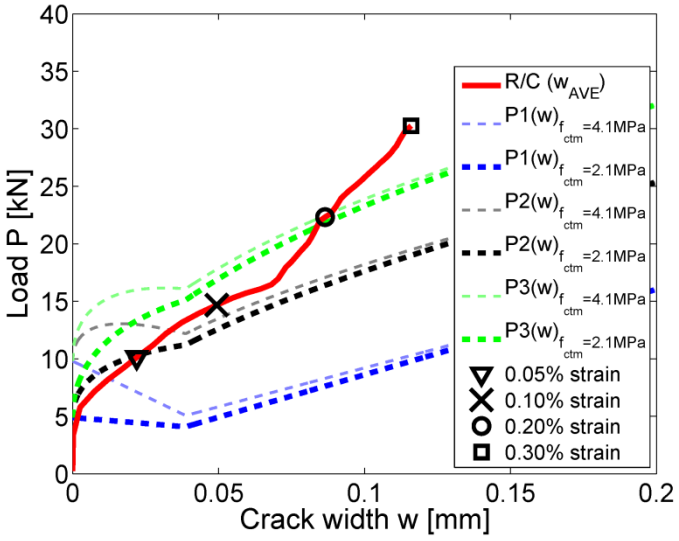

a) R/C

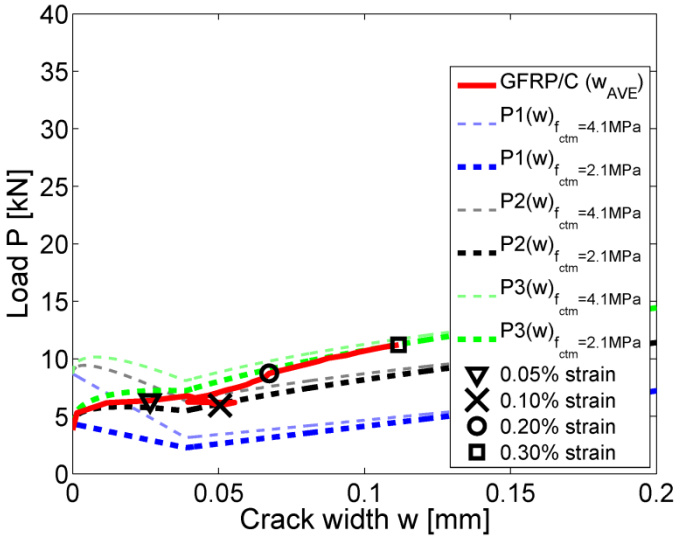

b) GFRP/C

Figure 3-22 Load-crack opening results for a): R/C and b): GFRP/C in comparison to the three variations of the analytical solutions for the load-crack opening relationships given by equation 3.16 (P1, P2 and P3). Test results are shown up to a rebar strain of 0.3% with a: triangle, cross, circle and square markers indicating: 0.05%, 0.1%, 0.2% and 0.3% rebar strain respectively.

The first crack load in the experimental results was found to be lower than material tests indicated. This could for example, be explained by a slight eccentricity in the test setup which would cause cracking to occur asymmetrically and at a lower load than expected.

Additionally, it should be noted that in the analytical assessment of a reinforced element, matrix and reinforcements are assumed stress free prior to loading. This however is not the case when matrix shrinkage is taken into consideration. Shrinkage in-

duced deformations will introduce a tensile stress component into the matrix and a compression stress component into the reinforcement (Bischoff 2001, Lárusson et al. 2009). Moreover, fine grain cementitious composites such as ECC will be subject to even larger shrinkage deformations than conventional concrete due mainly to lack of coarse aggregates in ECC (Wang and Li 2006, Lárusson et al. 2013). As a result, the first crack strength of reinforced tensile members will exhibit cracking sooner than material tests might indicate.

Figure 3-23 shows load – crack opening results for R/ECC and GFRP/ECC specimens for loading up to 0.3% rebar strain. Furthermore, the theoretically derived expression for load as a function of crack width (equation 3.16) is presented for comparison with the constitutive law for ECC (Figure 3-2a) (based on parameters obtained with SCTT specimens). It is however acknowledged that the analytical solution refers to a reinforced concrete element with only a single crack plane.

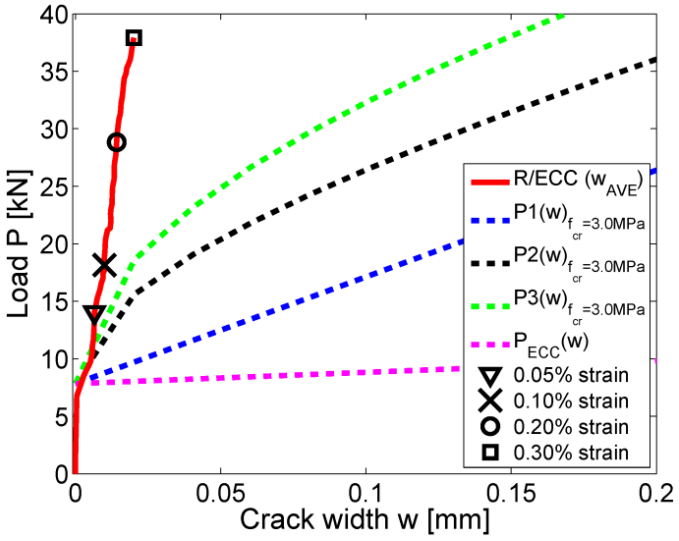

a) R/ECC

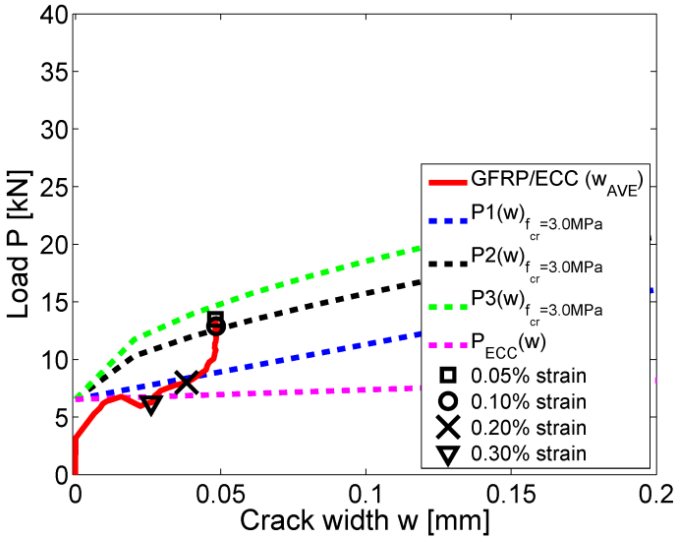

b) GFRP/ECC

Figure 3-23 Load-crack opening results for a): R/ECC and b): GFRP/ECC in comparison to the three variations of the analytical solutions for the load-crack opening relationships given by equation 3.16 (P1, P2 and P3). Test results are shown up to a rebar strain of 0.3 % with a: triangle, cross, circle and square markers indicating: 0.05%, 0.1%, 0.2% and 0.3% rebar strain respectively.

The first crack load value in R/ECC test agrees well with the SCTT results, whereas a slightly lower first crack load value was observed in GFRP/ECC test. After crack initiation in the R/ECC specimen the load – crack opening response initially seems to converge with the P2-P3 predictions but at an average crack width of ~7µm, crack development is almost completely suspended up to 0.3% strain (~20µm). Immediately after first crack formation occurred in the GFRP/ECC test specimen, the crack width

increases up to an average crack width of ~40μm at which point the crack width response changes only slightly up to 0.3% strain (see Figure 3-23).

The higher initial crack width observed in the GFRP/ECC tests is a result of the softer response of the GFRP rebar when compared to stiffer steel reinforcement in R/ECC.

As a result of the intermediate suspension or deceleration of crack development in an arbitrary crack (as observed in all test compositions), the theoretically derived expression for P(w) cannot fully converge with the experimental results, as the analytical expression assumes development of a single crack. Furthermore, due to crack bridging and load carrying capacity of ECC, the intermediate development of cracks in ECC reinforced members will produce a load – crack opening response that will diverge from the analytical solution after the second crack.

3.6 Conclusions

This chapter presents experimental observations of the interfacial bond behavior of reinforced cementitious prisms in direct tension and comparison to a theoretical model. The unique test setup presented in this study utilizes an image-based deformation analysis to measure the formation, propagation and opening of transverse tensile cracks and resulting debonding damage along the reinforcement in a quantitative and qualitative manner. Four different combinations of reinforcement and cementitious composites were tested in direct tensile loading, i.e., steel reinforced concrete (R/C), steel reinforced ECC (R/ECC), GFRP reinforced concrete (GFRP/C) and GFRP reinforced ECC (GFRP/ECC). To summarize the main findings of this experimental work, the following aspects can be emphasized:

The proposed novel test configuration with a partially exposed reinforcement in combination with the high definition DIC technique allows for the initiation and development of cracking to be monitored and quantified in detail at a micro-scale.

The overall (global) cracking in reinforced concrete specimens (R/C and GFRP/C) were shown to be localized in comparison to the more even distribution of cracks observed in reinforced ECC specimens (R/ECC and GFRP/ECC). Furthermore, considerably less crack branching was observed at the rebar – matrix interface in reinforced ECC members than reinforced concrete members, although some crack branching and or merging occurred close to the outer surface (cover) of the ECC matrix.

The transverse cracking process of reinforced ECC members consistently showed multiple cracking with considerably smaller crack widths than those in reinforced concrete members. As a result, the stress transfer across a transverse crack interface in reinforced concrete members diminishes rapidly as crack width increased, whereas stress transfer across transverse cracks in reinforced ECC members increase with increased crack widths.

As evident in the measured slip and opening displacements, the overall degradation of the rebar – matrix interface is distinctly more severe in reinforced concrete than reinforced ECC members at any load stage.

A general ratio between local slip and opening displacements for all four reinforcement – matrix combinations were presented based on local measurements. The obtained local ratios furthermore seem to approximate the global behavior reasonably.

The bulk part of internal cracks in reinforced ECC members become secondary cracks as loading is increased, whereas internal cracks in reinforced concrete all seem to propagate towards the closest primary crack.

Onset of mechanical interlocking was observed in all four reinforcement – matrix combinations, initiating at approximately 0.2-0.4% rebar strain. It is noted that a distinction is made between the initiation of internal cracks, and the onset of mechanical interlocking as opening displacement is halted or decreased.

The closed form solution for load – crack width presented in this study predicts the results for reinforced concrete members with a reasonable accuracy. It was shown that by adapting a linear hardening cohesive law with an initial bond – stress component (τ_0) into the analytical solution, good correlation was achieved with the test results for R/C up to ~0.15% strain and for GFRP/C up to 0.30%.

Due to the fiber bridging and the inherent limited crack width of ECC, the test results for R/ECC and GFRP/ECC rapidly diverged from the analytical predictions after fist crack initiation. This behavior emphasizes the limitations of the model to predict members displaying multiple cracking.

Initial crack openings in GFRP/ECC were found to be larger than those of R/ECC as a result of the less stiff GFRP reinforcement, in comparison to steel reinforcement.

Based on the experimental results presented in this study, it may be concluded that the combination of ECC and structural reinforcement will effectively decrease crack widths and debonding damage when compared to reinforced concrete. The limited crack widths and moderate debonding damage will furthermore result in tougher and more durable structural elements in terms of structural integrity and durability.

Bibliography

ACI committee 318 (ACI 318), 2002. Building Code Requirements for Structural Concrete (ACI 318-02) and Commentary (318R-02). American Concrete Institute.

Balazs, G. L., 1993. Cracking analysis based on slip and bond stresses. ACI Materials Journal, 90(4), pp. 340-348.

Bischoff, P., 2001. Effects of shrinkage on tension stiffening and cracking in reinforced concrete. Canadian Journal of Civil Engineering, 28(3), pp. 363-374.

Broms, B. B., 1965. Crack width and crack spacing in reinforced concrete members. ACI Journal. Preceedings. Vol. 62. No. 10. pp 1237-1255.

BS EN 12390-3:2009 (BS EN), 2009.Testing hardened concrete. Part 3: Compressive strength of test specimens. British Standards Institution, London, UK, BSI

BS EN 12390-3:2009. Testing hardened concrete. Part 3: Compressive strength of test specimens. British-Adopted European Standard

Chao, S. H., Naaman, A. E. & Parra-Montesinos, G. J., 2009, Bond Behavior of Reinforcing Bars in Tensile Strain-Hardening Fiber-Reinforced Cement Composites ACI Structural Journal, 106, pp. 897-906.

Eurocode 2 (EC2), 1991, European Prestandard, ENV 1992-1-1 / 1991 (December 1991). Eurocode 2. Design of Concrete Structures - Part 1. General Rules and Rules for Buildings European Committee for Standardization, Comité Européen de Normalisation CEN.

Fantilli, A. P., Mihashi, H. & Vallini, P., 2009. Multiple cracking and strain hardening in fiber-reinforced concrete under uniaxial tension. Cement and Concrete Research, 39(12), pp. 1217-1229.

Fantilli, A. P., Vallini, P. & Mihashi, H., 2007. Crack profile in RC, R/FRCC and R/HPFRCC members in tension. Materials and Structures/Materiaux et Constructions, 40(10), pp. 1099-1114.

fib, 2010. Bulletin 55: Model Code 2010 - First Complete Draft, Vol. 1, Chaps. 1–6, fib, Lausanne, Switzerland, 2010, p. 318, ISBN 978-2-88394-95-6.

Frosch, R. J., 1999. Another Look at Cracking and Crack Control in Reinforced Concrete. ACI Structural Journal, V. 96, No. 3, pp. 437-442.

Goto, Y., 1971. Cracks Formed in Concrete Around Deformed Tension Bars. ACI JOURNAL, Proceedings, Volume V. 68, No.4., pp. pp. 244-251.

Hansen, C. S., & Stang, H., 2012. Modeling and characterization of strengthened concrete tension members Engineering Fracture Mechanics, 82, pp. 85-99.

Hillerborg, A., Modéer, M. & Petersson, P.E., 1976. Analysis of crack formation and crack growth in concrete by means of fracture mechanics and finite elements. Cement and Concrete Research, 6(6), pp. 773-781.

Jiang, D. H., Shah, S. P. & Andonian, A. T., 1984. STUDY OF THE TRANSFER OF TENSILE FORCES BY BOND.. Journal of The American Concrete Institute, 81(3), pp. 251-259.

Lárusson, L. H., Fischer, G. & Jönsson, J., 2009. Mechanical interaction of Engineered Cementitious Composite (ECC) reinforced with Fiber Reinforced Polymer (FRP) rebar in tensile loading.. s.l., CRC Press/Balkema, Leiden.

Lárusson, L. H., Fischer, G. & Jönsson, J., 2013. Prefabricated floor panels composed of fiber reinforced concrete and a steel substructure. Engineering Structures, 46(0), pp. 104-115.

Larusson, L., Fischer, G. & Jonsson, J., 2011. Mechanical interaction between concrete and structural reinforcement in the tension stiffening process, in: G.J. Parra-Montesinos, H.W. Reinhardt, A.E. Naaman (Eds.), High performance fiber reinforced cementitious composites 6, RILEM state of the art reports, vol. 2, Springer, Ann Arbor, USA, pp. 247–254

Lepech, M. D. & Li, V. C., 2006. Long Term Durability Performance of Engineered Cementitious Composites. RESTORATION OF BUILDINGS AND MONUMENTS, 12(2), pp. 119-132.

Li, V. C., 1993. From micromechanics to structural engineering -the design of cementitious composites for civil engineering applications. Structural Engineering/Earthquake Engineering, 10(2), pp. 1-34.

Lutz, L. & Gergely, P., 1967. Mechanics of bond and slip of deformed bars in concrete American Concrete Institute - Journal, 64, pp. 711-721.

Nilson A. H., 1972. Internal measurements of bond slip. ACI Journal, 69(7), pp. 439-441.

Oehlers D.J., Visintin P. & Haskett M., 2012. The ideal bond characteristics for reinforced concrete members. In: J.W. Cairns, G. Metelli and G. A. Plizzari (eds), Bond in Concrete 2012 – General Aspects of Bond, Volume 1. Bond in Concrete 2012: Bond, Anchorage, Detailing. Fourth International Symposium, Brescia, Italy, 17th - 20th June 2012

Otsuka, K., Mihashi, H., Kiyota, M., Mori, S. & Kawamata, A., 2003. Observation of Multiple Cracking in Hybrid FRCC at Micro and Meso Levels. Journal of Advanced Concrete Technology, 1(3), pp. 291-298.

Pease B.J., 2010. Impact of cracking on durability of reinforced concrete – Experimental investigation on the influence of concrete cracking on ingress and reinforcement corrosion behavior, PhD thesis, Technical University of Denmark.

Pease B.J., Michel A., Thybo A.E.A. & Stang H., 2012. Estimation of elastic modulus of reinforcement corrosion products using inverse analysis of photogrammetric measurements for input in corrosion-induced cracking model, In: Proceedings of IABAMAS 2012 (6th International Conference on Bridge Maintenance, Safety and Management), July 8-12, Villa Erba, Italy.

Pedziwiatr, J., 2008. Influence of internal cracks on bond in cracked concrete structures. ARCHIVES OF CIVIL AND MECHANICAL ENGINEERING, 8(3), pp. 91-105.

Pereira, E. B., Fischer, G. & Barros, J. A., 2012. Direct assessment of tensile stress-crack opening behavior of Strain Hardening Cementitious Composites (SHCC). Cement and Concrete Research, 42(6), pp. 834-846.

Pereira, E., Fischer, G. & Barros, J., 2011. Image-based detection and analysis of crack propagation in cementitious composites. Proceedings of International RILEM Conference on Advances in Construction Materials Through Science and Engineering.

RILEM, 2011. Strain Hardening Cement Composites (SHCC): Structural Design and Performance: State-of-the-Art Report of the RILEM Technical Committee (TC) 208-HFC, SC3, Ed. Li, V. C.

Rokugo, K., Kanda, T., Yokota, H. & Sakata, N., 2009, Applications and recommendations of high performance fiber reinforced cement composites with multiple fine cracking (HPFRCC) in Japan Materials and Structures, 42, pp. 1197-1208.

Somayaji, S. & Shah, S. P., 1981. Bond stress versus slip relationship and cracking response of tension members. Journal of The American Concrete Institute, 78(3), pp. 217-225.

Volkersen, O., 1938. Die Nietkraftverteilung in Zugbeanspruchten Nietverbindungen mit konstanten Laschenquerschnitten. Luftfahrtforschung, 15, pp. 4-47.

Wang, S. & Li, V., 2005. Polyvinyl Alcohol Fiber Reinforced Engineered Cementitious Composites: Material Design and Performances. RILEM PROCEEDINGS PRO, Volume 49, pp. 65-74.

Watstein. D. & Parsons, D. E., 1943. Width and spacing of tensile cracks in axially reinforced concrete cylinders. Journal of research. National Bureau of standards. Vol. 31. No. RP1545. pp 1-24

Weimann, M. B. & Li, V. C., 2003. Drying shrinkage and crack width of an Engineered Cementitious Composites (ECC). Brittle Matrix Composites – International Symposium, No 7, Issue 7, pp. 37-46.

Xi, Y. & Bazant, Z. 1999. Modeling chloride penetration in saturated concrete, Journal of Materials in Civil Engineering, 11, 1, pp. 58-65.

Chapter 4

Tension stiffening and tension strengthening mechanisms

The work presented in this chapter focuses on the interaction between structural reinforcement and cementitious composite under tensile loading. The tension stiffening effect of concrete surrounding reinforcing bars is investigated and quantified in terms of composite load-deformation response, crack formation in the cementitious material, and overall performance increase in monotonic and cyclic loading configurations. The tension stiffening and tension strengthening mechanisms are investigated in this study using representative tensile prisms of conventional deformed steel reinforcement and relatively soft and elastic GFRP reinforcement embedded in normal concrete and ductile ECC.

4.1 Introduction

The mechanical interaction between structural reinforcement such as standard steel embedded in a cementitious matrix such as concrete has been defined as the tension stiffening effect. It represents the degree of restraint on the deformation of a reinforcing bar embedded in partially uncracked concrete under uniaxial tension. The effect is assumed to be most pronounced when the composite prism is fully uncracked. Upon formation of cracking in the concrete, the tension stiffening effect is gradually reduced due to the presence of transverse cracks, which allow the rebar to deform with less restraint compared to uncracked concrete. While the uncracked and partially cracked concrete is able to restrain the respective segments of the rebar between the cracks from deforming as much as the segments located at a crack, it is not able to provide the composite with an increased strength compared to the rebar alone. The increase in load due to the presence of the uncracked or partially cracked concrete in the elastic deformation regime of the rebar is caused by the resulting increase in composite stiffness, requiring a higher load to deform the rebar to an overall tensile extension comparable to that of the rebar alone.

Aside from the load-deformation response, the characteristics of the crack formation in the concrete in terms of crack width and crack spacing are important observations leading to conclusions on the expected durability of reinforced concrete structures.

The objectives of this study are to assess and analyze the tensile load-deformation behavior of conventional steel reinforcement and Glass Fiber Reinforced Polymer (GFRP) reinforcement embedded in conventional concrete and ductile Engineered Cementitious Composites (ECC) with strain hardening and multiple cracking behavior in tension. The information obtained from this experimental investigation are then compared to established models of the tension stiffening effect and are also used as input in the design of structural composite elements with specified deformation capacity and cracking characteristics. Primary focus is on the combination of relatively soft and elastic GFRP reinforcement and concrete with a ductile deformation behavior in tension for the purpose of developing a flexible concrete composite to absorb imposed deformation with relatively low resistance and limited crack widths.

4.1.1 Tension stiffening

The tension stiffening behavior of steel reinforced concrete and SHCC materials composites has been investigated in previous studies (Fischer and Li 2002, Fantilli et al. 2005, Mihashi et al. 2007). In reinforced concrete and SHCC composites, the load-deformation behavior can be schematically represented as shown in Figure 4-1.

In the schematic illustration given in Figure 4-1 the composite tensile response can be divided into four deformation stages, stage 1: elastic response of the composite, stage 2: formation of transverse cracks, stage 3: crack saturation in R/C and stabilized load response in R/ECC, and stage 4: yielding of the steel reinforcement. Due to the strain hardening and multiple cracking characteristics of SHCC materials in general and ECC in particular, the load-deformation response of the R/ECC composite is substantially different with increased resistance beyond crack formation in the elastic and inelastic deformation stages of the steel reinforcement. In addition to the load and ductility enhancements shown in Figure 4-1, the limited crack widths in reinforced ECC compared to conventional reinforced concrete can be expected to impact the serviceability limit state and lead to improved durability.

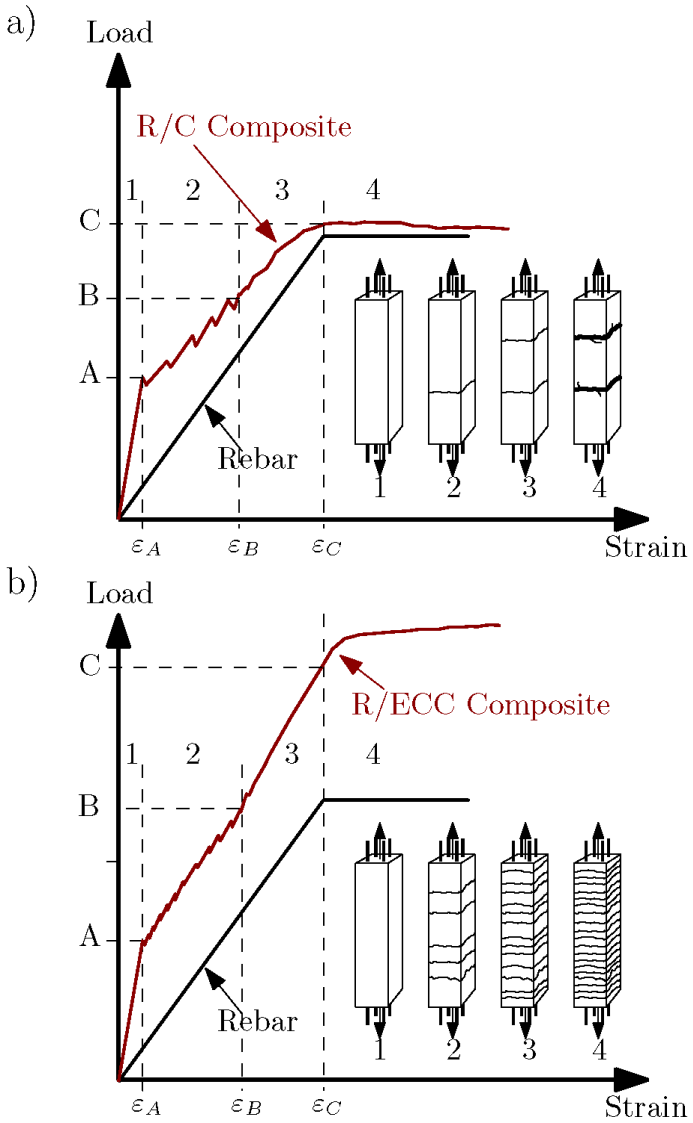

Figure 4-1 Schematic illustration of tension stiffening and crack formation: a) shows R/C and b) shows R/ECC. "A" and ε_A are load and corresponding strain of first crack respectively, "B" and ε_B are load and strain at crack saturation / stabilized response respectively, "C" and ε_C are load and strain at yielding of reinforcement respectively.

The tension stiffening effect has been established as the contribution of the concrete to the tensile load-deformation response of reinforced concrete, that is, the additional stiffness that the concrete provides in comparison to the stiffness of the bare rebar due to the restraining of deformations of the reinforcement. When transverse cracking initiates and develops in the tensile prism, the tension stiffening decreases as more cracks form and crack widths increase as the interface between reinforcement and concrete gradually debonds.

The parameters governing the tension stiffening effect are the reinforcement ratio, reinforcement diameter and distribution of the reinforcement, the tensile strength of

concrete, bond strength, concrete cover thickness, the loading history and the curing conditions (Ouyang et al. 2007).

Various analytical and empirical models have been introduced in the published literature, including models proposed by the American Concrete Institute (ACI, committee 224.2R) and the International Federation for Structural Concrete (CEB-FIP Model codes) that predict the composite tensile load-strain response of reinforced concrete member using analytical and empirical relationships. In the ACI approach, an effective concrete cross sectional area $A_{c,eff}$ is introducing to reduce the axial stiffness of the composite member in order to accounted for the tension stiffening effect. In the CEB-FIP model code approach, however, the stress-strain response of the embedded reinforcement is modified to account for the contribution of the concrete, that is, the tension stiffening effect.

Model approaches, based on fracture mechanics utilizing the fracture energy equilibrium of reinforced concrete, cracks and their common interfaces (Bazant and Oh, 1983; Ouyang and Shah, 1994), have been proposed and found to match quite well with the various experimental data.

Wollrab et al. (1996), summarized the results and findings from an experimental program carried out on steel reinforced concrete panels in direct tension, with different reinforcement ratios, rebar spacing and concrete strengths. Their findings suggested that first crack strength increased with decreased rebar spacing while being independent of the reinforcement ratio. Furthermore, the average concrete contribution, that is tension stiffening, was shown to increase with decreasing reinforcement ratio.

The work of Bischoff (2001) and Fields and Bischoff (2004) emphasized the importance of including concrete shrinkage strains when analyzing the composite behavior of reinforced concrete members in tension. The shrinkage strain causes compressive stress in the reinforcement prior to actual tensile loading and consequently decreases the axially applied load needed to crack the specimen. By assuming or measuring the drying shrinkage of unrestrained concrete and implementing the results in a model, a reasonable prediction of the tension stiffening was obtained in the form of a revised tension stiffening factor $\beta=f_c/f_{cr}$ (also known as the bond factor), were f_c is the average tensile stress in the concrete and f_{cr} is the concrete cracking strength.

Sooriyaarachchi and Pilakoutas (2005) experimentally examined the influence of the reinforcement ratio, concrete strength and rebar diameter on tension stiffening of GFRP reinforced concrete in direct tension. Their test setup with embedded strain gauges in the GFRP rebar allowed them to deduce the actual strain profile along the length of the rebar during testing. Results indicate that tension stiffening increases as reinforcement ratio was decreased while the rebar sizes did not seem to have any influence. Increased tension stiffening behavior was also observed with higher concrete strength. Contrary to Sooriyaarachchi and Pilakoutas conclusions, Bischoff and Paixao (2004) reported that tension stiffening was independent of both reinforcement

ratio and concrete strength when concrete shrinkage is taken into consideration. They reported experimental results and an analysis of tension stiffening and cracking of steel reinforced- and GFRP reinforced concrete ties with varying reinforcement ratios in direct tension. Their findings included that concrete reinforced with GFRP exhibited greater tension stiffening than steel reinforced members. Bischoff and Paixao furthermore introduced and examined an empirical model for predicting the average stress carried by the cracked concrete in GFRP and steel reinforced tensile specimens in comparison to models based on CEB-FIP (1978) and ACI (1986). Both the CEB-FIP and the ACI model approaches presented by Bischoff and Paixao rely on the effective area of the cracked section to account for tension stiffening, however, they were both found to be valid only for a limited range of reinforcement ratios.

Fischer and Li (2002) investigated the tension stiffening effect of steel reinforcement embedded in ductile ECC in contrast to normal brittle concrete (R/C) in direct tension. In their investigation, the mechanism of strain compatibility between the reinforcement and the cementitious material in the elastic and inelastic deformation regime has been introduced for reinforced ductile concrete materials. This deformation compatibility resulted in a decrease in crack widths and spacing and thus minimized damage due to interface deterioration between reinforcement and the confining concrete matrix.

Inspired by Fischer and Li (2002) the strain compatibility of reinforced ductile concrete material was further examined by Fantilli et al. (2005) where the focus was on comparing various mechanical models for tension stiffening based on bond-slip analysis. Their research concluded that the mechanical response of a reinforced ductile concrete is independent of to the bond-slip relationship due to the strain compatibility between reinforcement and cementitious matrix.

In this study, the authors investigate the combination of ductile concrete with relatively soft and elastic GFRP reinforcement, which in principle is contrary to the conventional combination of steel reinforcement with stiff elastic and plastic response and concrete with brittle behavior in tension. The objective of this study is to understand the interaction mechanism of the composite constituents and based in this to develop a structural deformation element with relatively soft load-deformation response and limited crack widths at relatively large imposed tensile strains on the order of 1%.

4.2 Review of tension stiffening modeling

The interaction between the reinforcement and surrounding concrete during tensile deformations can be characterized either by the load transfer between the two materials (load sharing approach) or by employing a tension stiffening strain concept which neglects the concrete contribution in tension while increasing the stiffness of the bare reinforcement (Bischoff, 2001).

4.2.1 Load sharing approach

In the load sharing approach, the reinforcement and the concrete are considered to carry tensile forces based on their un-cracked effective stiffness in the un-cracked state and their relative area proportions in the cross-section. At this stage, strain in the concrete is equal to strain in reinforcement ($\varepsilon_c = \varepsilon_s$). Once the concrete reaches its tensile cracking strength (f_{cr}), the axially applied composite load N in an R/C member in direct tension is primarily carried by the reinforcement ($N=N_s=f_s*A_s$) at a specific crack location, where f_s is the stress and A_s is the cross sectional area of the reinforcement. A relatively small amount is carried by the concrete (N_c) at the cracked section, mainly due to aggregate interlocking, which decreases as crack width increases.

For a reinforced fiber reinforced cementitious composite (R/FRCC) member in tension, upon crack formation the fibers bridging the crack are activated and will carry a part of the load (N_b). Depending on the nature of the FRCC (strain softening or strain hardening), the crack will either gradually grow with decreasing stresses being transferred across the crack (as $f_c<f_{cr}$) in the case of tension softening materials, or reach a certain stress level f_c, higher than that at first crack formation ($f_c>f_{cr}$) in the case of strain hardening materials (ductile concrete), at which point the composite will form another crack.

Load transfer between the reinforcement and surrounding matrix increases as slip gradually decreases along the length of the specimen (in both directions away from the crack plane) until full composite interaction is reached and $\varepsilon_c = \varepsilon_s$ again.

The load equilibrium at any cross section of a tension member can then be written as:

$$N = N_s + (N_c + N_b) \tag{4.1}$$

where N is the total applied load. The concrete contribution is thus derived by subtracting the contribution of the reinforcing bar from the applied load (taking the bridging load N_b as part of the concrete). The average load carried by the concrete can therefore be defined as:

$$N_c = A_c f_c = A_c \beta f_{cr} \tag{4.2}$$

where fc is the average concrete stress and β is the tension stiffening factor ($\beta=f_c/f_{cr}$).

More details on the load sharing approach is found in Collins and Mitchell (1991).

4.2.2 Tension stiffening strain approach

In this approach a tension stiffening strain $\Delta\varepsilon_s$ is used to increase the stiffness of bare reinforcement, the average strain in the reinforcement is thus given as:

$$\varepsilon_{sm} = \varepsilon_s - \Delta\varepsilon_s \tag{4.3}$$

where ε_s is the strain in the reinforcement at a fully cracked plane and the tension stiffening strain $\Delta\varepsilon_s$ is equal to:

$$\Delta\varepsilon_s = \beta\Delta\varepsilon_{s,max} = \frac{\beta\, f_{cr}\, A_c}{E_s\, A_s} \qquad (4.4)$$

where $\Delta\varepsilon_{s,max}$ is the strain difference between the composite and the reinforcement (ε_s) just before first crack occurs. It should be noted that the tension stiffening factor β here is the same factor as described in the load sharing approach.

For the strain development in the composite, the basic underlying assumption is that the average reinforcement strain, ε_{sm}, is equal to the average measured composite strain ε_m over a representative measured length l_g. This assumption holds as long as several cracks are observed over the measured length l_g.

4.3 Modeling tension stiffening

In the 1978 CEB-FIP model code the tension stiffening factor ($\beta=f_c/f_{cr}$), which is based on the tension stiffening strain concept, can be derived as a function of the composite members strain (ε_m):

$$\beta(\varepsilon_m) = -\frac{n\rho}{2}\left(\frac{\varepsilon_m}{\varepsilon_{cr}}\right) + \sqrt{(1+n\cdot\rho)^2 + \frac{(n\rho)^2}{4}\left(\frac{{\varepsilon_m}^2}{{\varepsilon_{cr}}^2}\right)} \qquad (4.5)$$

Where n is the ratio between the elastic modulus of the reinforcement (E_s) and the concrete (E_c) ($n=E_s/E_c$), ρ is the reinforcement ratio and ε_{cr} is the strain at initial cracking. It should be noted that in the revised 1990 CEB-FIP model code the tension stiffening factor β is given by a constant value of 0.4 for monotonic loading.

Numerous variations of empirical models to predict the tension stiffening factor β have been proposed in the past resulting in a wide range of predictions as shown in Figure 4-2.

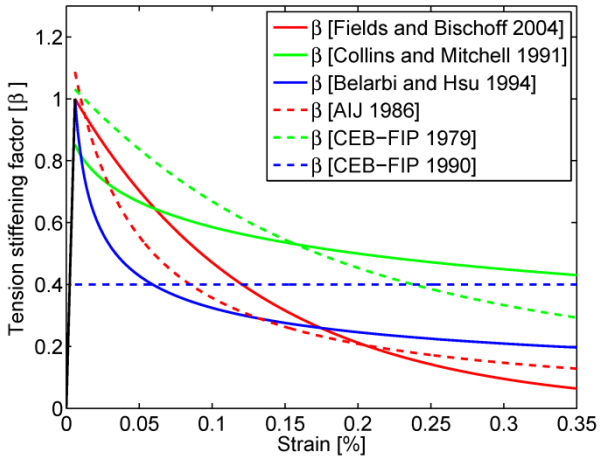

Fields and Bischoff (2004):

$$\beta(\varepsilon_m) = e^{-800\cdot(\varepsilon_m-\varepsilon_{cr})} \tag{4.6}$$

Collins and Mitchell (1991):

$$\beta\ (\varepsilon_m) = \left(1+\sqrt{500\cdot\varepsilon_m}\right)^{-1} \tag{4.7}$$

Belarbi and Hsu (1994):

$$\beta\ (\varepsilon_m) = \left(\frac{\varepsilon_{cr}}{\varepsilon_m}\right)^{-0.4} \tag{4.8}$$

AIJ recommendations (1986):

$$\beta\ (\varepsilon_m) = (2000\cdot\varepsilon_m + 0.8)^{-1} \tag{4.9}$$

1990 CEB-FIP model codes:

$$\beta = 0.4 \tag{4.10}$$

Figure 4-2 Example of different beta factors for R/C composites from related research.

All of the above mentioned model predictions (except for CEB-FIP, 1990) assume a descending branch after initial cracking occurs.

The pre-compression of the steel reinforcement induced by shrinkage of the cementitious matrix has to be accounted for to accurately describe the mechanical interaction of a composite member. Due to shrinkage, the stiffness of the composite at the start of the loading process consists only of the contribution of the concrete as the reinforcement is in compression and effectively only adds to the initial tensile loading in the concrete.

The revised tension stiffening factor suggested by Bischoff (2001) is based on the 1978 CEB-FIP model code which is taking shrinkage of the concrete into account:

$$\beta = \beta_{exp}\left(1+\frac{n\rho}{1+n\rho}\frac{\varepsilon_{sh}}{f_{cr}/E_c}\right) - \frac{n\rho}{1+n\rho}\frac{\varepsilon_{sh}}{f_{cr}/E_c} \tag{4.11}$$

Here β_{exp} is the measured tension stiffening while neglecting the effect of concrete shrinkage and ε_{sh} is the initial shrinkage strain of the member at loading.

Based on formulation presented by Bischoff and Paixao (2004), the tension stiffening effect can be expressed with regards to the effective reinforcement stiffness ($\bar{E}_s$) by defining an effective concrete area $A_{c,eff}$ and reformulating in terms of the members strain ε_m as a function of applied load P:

$$\varepsilon_m = \frac{P}{E_c A_{c,eff}} = \frac{P}{E_c\left(A_{c,cr} + \left(A_{c,ucr}+A_{c,cr}\right)\left(\frac{P_{cr}}{P}\right)^3\right)} \tag{4.12}$$

Where $A_{c,cr}$ and $A_{c,ucr}$ is the cracked and uncracked cross sections and P_{cr} is the load at first crack. This formulation for the effective concrete area is analogous to the moment of inertia used to predict beam deflections used in ACI (1986).

4.4 Research significance and motivation

Lepech and Li (2009) described a full scale field demonstration where ECC was introduced into a steel reinforced continuous expansion joint, also known as a link slab. The design approach of the link slab was to resist a moment due to end rotation of the adjacent spans. As a result of the moment demand and the limitations on the working stress of the reinforcement (40% of yield stress f_y), the link slab had a relatively high steel reinforcement ratio and consequently did not behave as a joint. Expanding on this field study, the authors are aiming at developing a link slab with a relatively low stiffness to maintain the intended hinge at the support between two adjacent bridge spans. The investigations of the interaction between GFRP reinforcement and ductile concrete presented herein are a preliminary stage in the development of this flexible GFRP reinforced ECC joint.

4.5 Experimental program, material properties

4.5.1 Material properties of reinforcement and cementitious matrices

The compressive strengths of both concrete and ECC were found to be the similar at about 60 MPa. The elastic modulus of the ECC matrix, however, was found to be 16 GPa and less than half of that of the concrete at 38 GPa. The concrete tensile strength was slightly higher than that of ECC and showed the typical brittle failure mode whereas the ECC was able to maintain its loading capacity up to a strain of 4% (see Figure 4-3a). An example of the crack opening development and average crack spacing measurements obtained using DIC are depicted in Figure 4-3b. The crack widths were found to be below 0.16 mm and average crack spacing was found to be 4.0 mm at 2.5% tensile strain.

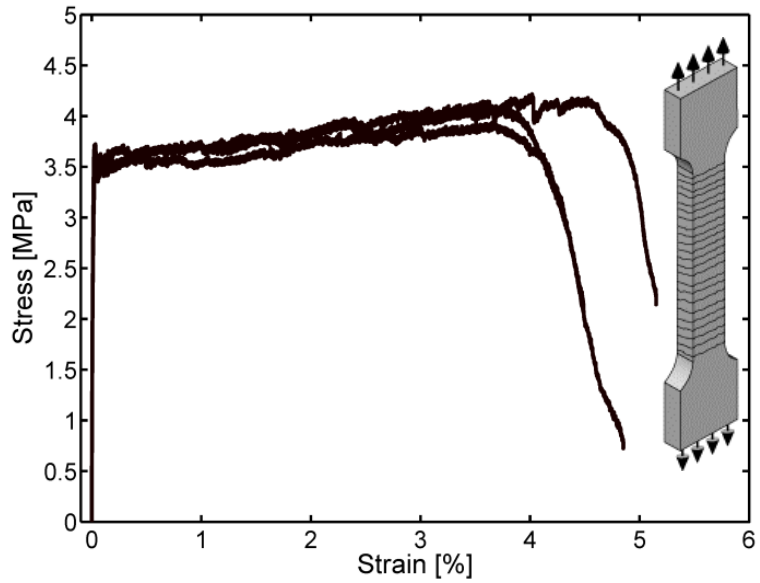

a)

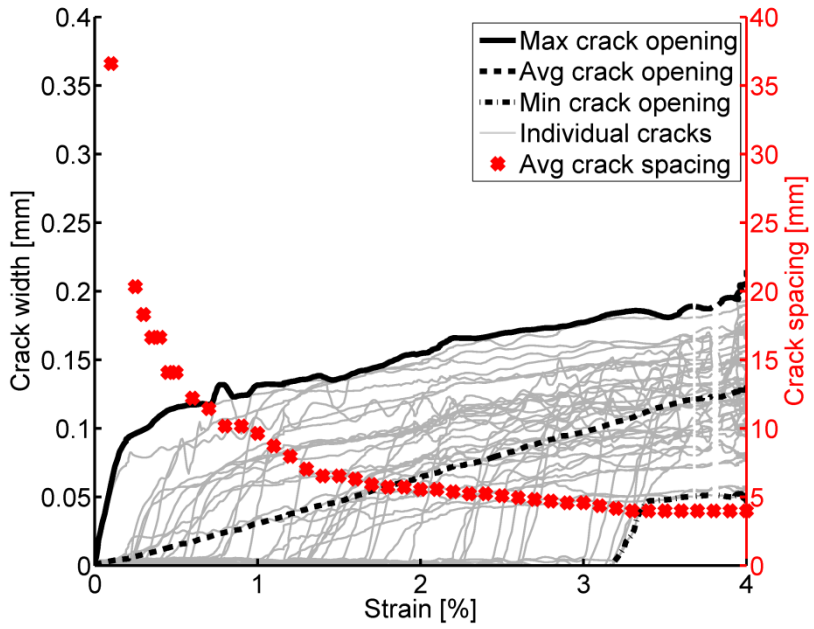

b)

Figure 4-3 a) Stress-strain responses of three dogbone-shaped ECC tensile specimens in direct tension. b) Development of crack opening and crack spacing as a function of tensile strain obtained with DIC.

The two reinforcement types (steel and GFRP) have distinct different stress-strain behaviors. The GFRP with a relatively low stiffness has an elastic-brittle load response whereas the steel with a relatively high stiffness has an elastic-plastic load response as shown in Figure 4-4.

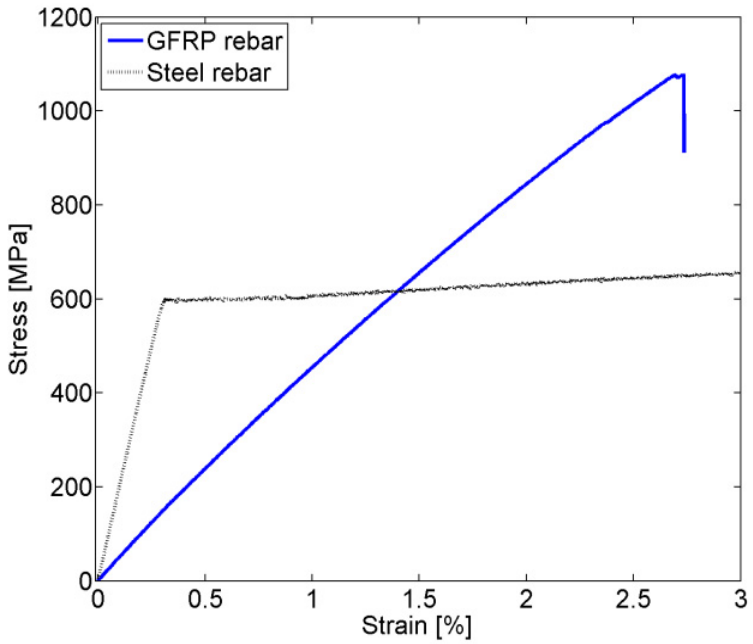

Figure 4-4 Typical stress-strain responses for bare GFRP- and steel rebars from tension testing.

Table 4-1 shows the parameters deduced from material testing, which are used later in modeling of the composite response.

Table 4-1 Material parameters: f_{cu} and ε_{cu} refer to the ultimate compression strength and strain, f_t is the tensile strength, ε_{cr} is the strain at first crack, ε_y is the tensile strains at yielding, f_y is the tensile yield strength, f_{tu} is the ultimate tensile strength and ε_{tu} is the ultimate tensile strain. All values are average values.

	f_{cu} [MPa]	ε_{cu} [%]	f_t [MPa]	ε_{cr} [%]	f_{tu} [MPa]	ε_{tu} [%]	E [GPa]
Concrete	61	0.12	4.1 *	-	-	-	38
ECC	60	0.22	3.5 **	0.02 **	4.0	4.0	16
	f_y [MPa]	ε_y [%]	f_{tu} [MPa]	ε_{tu} [%]	E [GPa]		
Steel rebar's	600	0.3	680	6.9	202		
GFRP rebar's	-	-	1050	2.5	46		

* Value obtained from splitting tensile testing (Brazilian test), according to EN 12390-6.
** First crack values.

4.6 Experimental program, Composite test

4.6.1 Composite test setup

In this experimental program, the composite behavior of four compositions of reinforcement and cementitious materials were analyzed in a direct tension configuration. The cementitious matrices that were examined included conventional concrete and

ECC with material properties stated above. These matrices were combined with either steel reinforcement or GFRP reinforcement to result in four different types of composite specimens: a) steel reinforced concrete (R/C), b) steel reinforced ECC (R/ECC), c) GFRP reinforced concrete (GFRP/C) and d) GFRP reinforced ECC (GFRP/ECC).

The experimental assessment of the tension stiffening effect has typically been conducted using prism shaped specimens in which the axial load was applied at the reinforcing bar and then transferred to the cementitious matrix via interfacial bond stresses (Somayaji and Shah, 1981; Abrishami and Mitchell, 1996; Fischer and Li, 2002). This testing configuration, however, experienced premature failure, usually in the exposed part of the reinforcement, which was not surrounded by matrix and where the maximum tensile stresses occur in the rebar. To prevent such premature failures, the specimen shape and mechanism of applying the axial load was modified in this study. The specimens were 1000 mm long dog-bone shaped elements, with a 400 mm representative length of a constant cross section of 100 mm x 100 mm. The ends of the specimens were widened to 300 mm width to facilitate an external clamping system through which the axial load was applied (Figure 4-5). Four rebars were positioned in the cross-section in two rows with 50 mm spacing and 25 mm cover, extending throughout the entire longitudinal direction and protruding 100 mm from the ends of the specimens.

In specimens a) and b) with steel reinforcement, rebars with a diameter of 6 mm were used, resulting in a reinforcement ratio ρ of 1.14%. In specimens c) and d), the GFRP reinforcement had a diameter of 6.3 mm corresponding to a reinforcement ratio ρ of 1.26%.

After casting the specimens remained in the casting moulds for 2 days and were subsequently wrapped in wet burlap and cured at room temperature until testing at 28 days.

The clamping system (Figure 4-5) secured the composite specimens firmly at both ends to ensure a fixed connection between the specimen and the load frame. Eight post-tensioning fixtures were used to confine the ends of the specimen and were each tensioned to approximately 30 kN with turnbuckle like segments (see Figure 4-5). At application of the axial load, the particular arrangement of the post-tensioning fixtures resulted in a further increase in clamping forces and therefore in an increase in the confinement of the ends of the specimens. The protruding reinforcement ends were anchored prior to testing to prevent pullout by welding of the steel reinforcement to the clamping plates (in the R/C and R/ECC specimens) and by using epoxy glue and steel sleeves (in GFRP/C and GFRP/ECC specimens).

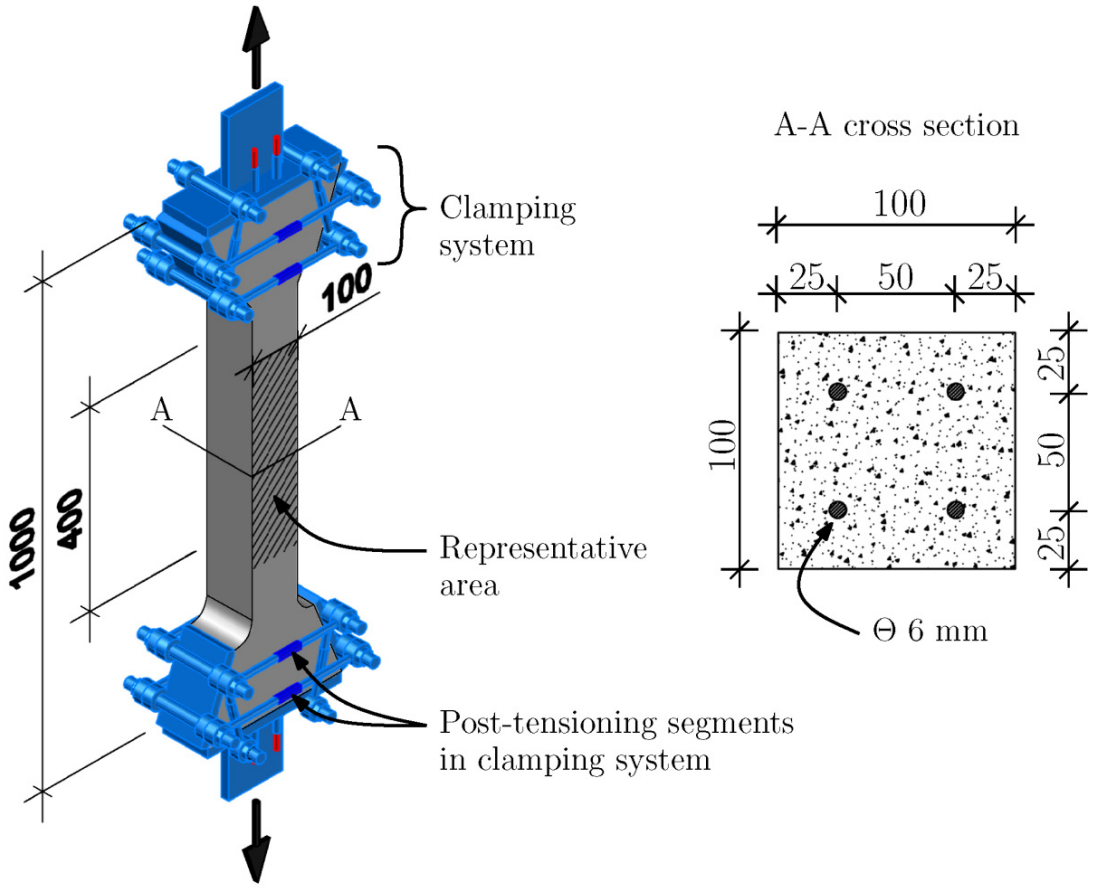

Figure 4-5 Illustrations of the direct tension test setup and a cross section of the corresponding reinforced members. The clamping system with the post-tensioning segments is positioned at the ends of the specimen.

Deformations of the representative area of the composite members were measured using two LVDTs as well as by analyzing digital images taken of the specimen surface (DIC) during the test with the main focus on crack formation and development during load application (as was illustrated in section 2.3, Figure 2-6).

Three specimens of each composite type were axially loaded in tension first monotonically followed by cyclic loading. In the monotonic loading stage, the specimens were loaded up to a predefined strain level (1.2-1.4% tensile strain) in direct tension at an actuator displacement rate of 0.5 mm/minute. Before the cyclic loading sequence was initiated, the specimens were kept at the predefined strain level while the specimen surfaces were examined for cracking. Cyclic loading involved 1,000 load cycles subjecting the specimen to tensile loading between 0.5% and 1% tensile strain over the representative area.

In addition to the twelve specimens testing using the procedure described above, three GFRP/ECC specimens were subjected to 10,000 displacement controlled deformation

cycles using the LVDTs mounted on the specimen side to apply cyclic deformations between 0.3% and 1% tensile strain in the representative section.

The target tensile strain of 1% was chosen as it represents the desired minimum strain capacity of the previously mentioned GFRP reinforced ECC link slab design. Furthermore, the cyclic loading represents the fatigue loading expected to occur in such a link slab during its service life.

4.7 Experimental results

4.7.1 Monotonic tensile loading; Load-strain response of composite members

The tensile load-deformation responses of the reinforced composites were analyzed by measuring the load and longitudinal deformations over a representative length with a constant cross section. The specimens were subjected to direct tension in a displacement controlled configuration.

Figure 4-6 compares the structural response of the steel reinforced R/C and R/ECC specimens during monotonic tensile loading. The response of the bare steel reinforcement is also shown in the graph for reference. Similarly, the load-deformation behavior of the GFRP/C and GFRP/ECC specimens and the bare GFRP reinforcement are shown in Figure 4-7.

Considering the conceptual response phases illustrated in Figure 4-1, and comparing them to the experimental results shown in Figure 4-6 and Figure 4-7, the following observations can be made:

In the steel reinforced ECC (R/ECC) composites (Figure 4-6), first cracking can be observed at a tensile strain of 0.01-0.03% corresponding to an axial load ranging between 10-30 kN followed by a reduced composite stiffness in the R/ECC members. After the initial crack formation, the load-strain response is essentially linear (stabilized load response) from 0.1% up to 0.39% strain when yielding of the reinforcement can be observed at a tensile load in the composite of 94-98 kN. The monotonic tensile loading of the R/ECC members was discontinued at 1.2-1.5% strain, corresponding to tensile loads of 99-104 kN. After yielding occurred in the R/ECC composites the difference between the composite load response and that of the load response of the bare reinforcement, that is the average load carried by the ECC, is measured to be 30-35 kN. This difference was maintained until loading was discontinued and is illustrated in Figure 4-6. This tensile load carrying ability of the R/ECC composites is due to the pseudo strain hardening behavior of ECC.

In the R/C members first cracking is observed at 0.01-0.03% tensile strain and a load range of 14-18 kN. Subsequently the R/C composite response exhibited a gradual decrease in composite stiffness until the steel reinforcement yields at approximately 67

kN and the composite response essentially becomes the same as the response of the bare reinforcement (see Figure 4-6). Crack saturation is observed at 0.14-0.23% strain corresponding to an axial load between 45 and 66 kN.

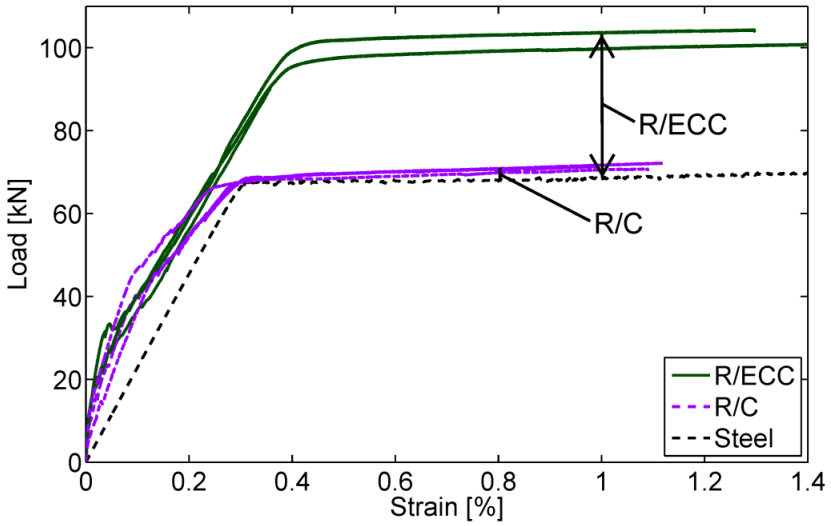

Figure 4-6 Structural response of steel reinforced concrete (R/C) and steel reinforced ECC (R/ECC) specimens during monotonic tensile loading. The average load carried by concrete in R/C and ECC in R/ECC members is indicated on graph.

After yielding of the reinforcement within the R/C composite occurs, tensile stresses can still exist in the concrete between cracks, however the deformed steel rebars are unable to transfer forces greater than the yield force of the steel across the transverse cracks and hence the tension stiffening effect is reduced to zero (Bischoff, 2001).

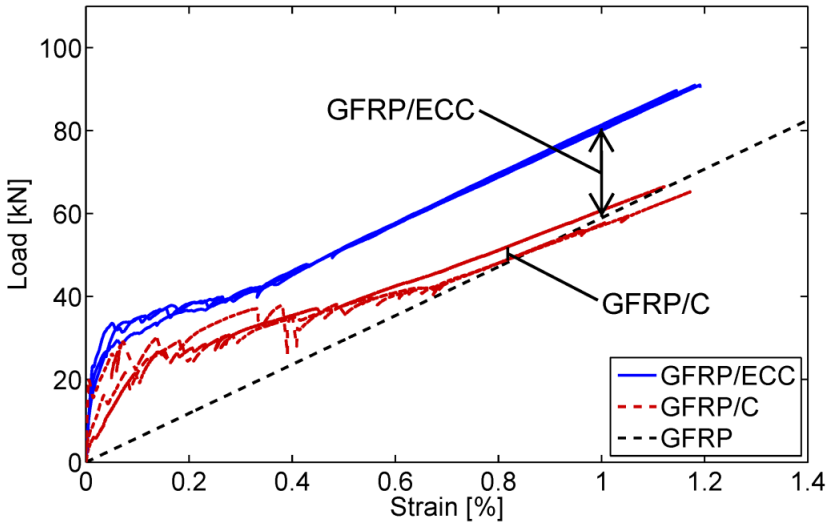

Figure 4-7 Structural response of GFRP reinforced concrete (GFRP/C) and GFRP reinforced ECC (GFRP/ECC) specimens during monotonic tensile loading. The average load carried by concrete in GFRP/C and ECC in GFRP/ECC members is indicated on graph.

In Figure 4-7 the GFRP/ECC specimens cracking initiated at 0.01-0.02% strain at an axial load ranging between 16-21 kN followed by a reduced composite stiffness. From approximately 0.4% tensile strain and until loading was discontinued at 1.1-1.2% tensile strain the composite stiffness of the GFRP/ECC members increase again (see Figure 4-7), showing a constant parallel response to that of the bare GFRP rebars. The difference between the composite load response of the GFRP/ECC specimens and that of the load response of the bare GFRP reinforcement is measured to be 22 kN.

The GFRP/C specimens show a similar behavior to the GFRP/ECC specimens up to about 0.4% strain but at lower load levels (see Figure 4-7). After 0.1% tensile strain the tension stiffening effect in the GFRP/C specimens gradually approaches zero as the composite stiffness approaches that of the bare GFRP reinforcement. Loading of the GFRP/C specimens was discontinued 1.0-1.2% strain, corresponding to a load range of 14-18 kN.

It should be noted that in Figure 4-6 and Figure 4-7 no offset of the bare reinforcement due to shrinkage of the concrete or ECC has been accounted for. This shrinkage induced offset of the reinforcement response will be accounted for and discussed in a following section on tension stiffening.

Imposed composite strains and the corresponding load values for the different response phases (as illustrated in Figure 4-1) for all composite types can be found in Table 4-2.

Table 4-2 Experimentally obtained load and strain values from monotonic tensile loading of composite specimens.

	First crack		Crack saturation		Rebar yielding		Test stopped	
	Strain [%]	Load [kN]	Strain [%]	Load [kN]	Strain [%]	Load [kN]	Strain [%]	Load [kN]
R/ECC	0.01-0.03	10-30	-	-	0.39	94-98	1.2-1.5	99-104
R/C	0.01-0.03	14-18	0.14-0.2	45-66	0.24-0.29	67	1.0-1.1	72
GFRP/ECC	0.01-0.02	16-21	-	-	-	-	1.1-1.2	90
GFRP/C	0.01-0.03	6-20	0.4-0.7	35-42	-	-	1.0-1.2	58-67

Values were assessed from Figure 4-6 and Figure 4-7 according to Figure 4-1.

4.7.2 Monotonic tensile loading; Crack formation and development of composite members

The surface deformations, in particular crack formation and crack widths in the representative section of the specimens were obtained utilizing a DIC system. Figure 4-8 illustrates the differences in surface crack formation and development for all composite types from 0.2-1.0% tensile strain with increments of 0.2% strain. The observed surface areas shown in Figure 4-8 are 100 mm wide and approximately 260 mm long.

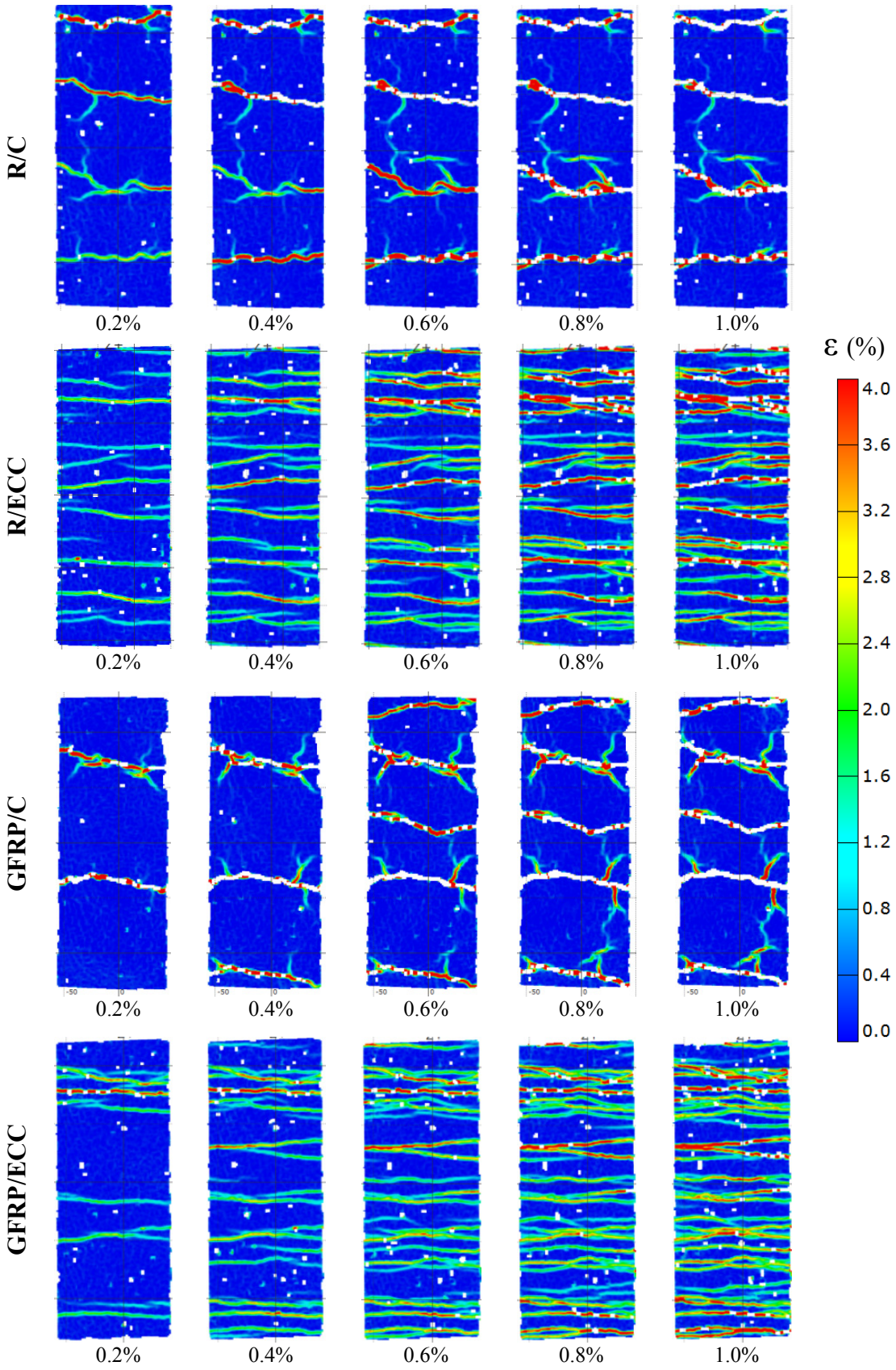

Figure 4-8 Surface crack development on all composites types during tensile loading at strain levels 0.2-1.0%.

The multiple crack formation observed on the ECC specimens (R/ECC and GFRP/ECC) differs substantially from the discrete crack formation in the conventional reinforced concrete members (R/C and GFRP/C) as shown in Figure 4-8. Furthermore, the formation of new cracks is more gradual over the tensile strain increments in the GFRP reinforced members as opposed to that in the steel reinforced specimens where most crack initiate at lower strain levels (see Figure 4-8).

The development of crack width of individual cracks can be traced accurately throughout the deformation process by employing an image-based monitoring system (DIC). Figure 4-9 shows the evolution of crack openings of all cracks on the measured representative surface as a function of strain, extracted from the analysis for a single member of each composition types.

From Figure 4-8 and Figure 4-9 crack saturation in the ECC members (R/ECC and GFRP/ECC) are not reached within the strain range which the composite members were tested. This is in good agreement with the measured crack width development in the ECC material testing where new cracks form up until the ultimate tensile strain capacity is reached at 3-5% (see Figure 4-3b).

In Figure 4-9, the crack maximum crack widths at 1.0% tensile strain were ~0.65 mm in R/C, ~0.87 mm in GFRP/C, ~0.29-0.21 mm in R/ECC, and ~0.15 mm in GFRP/ECC.

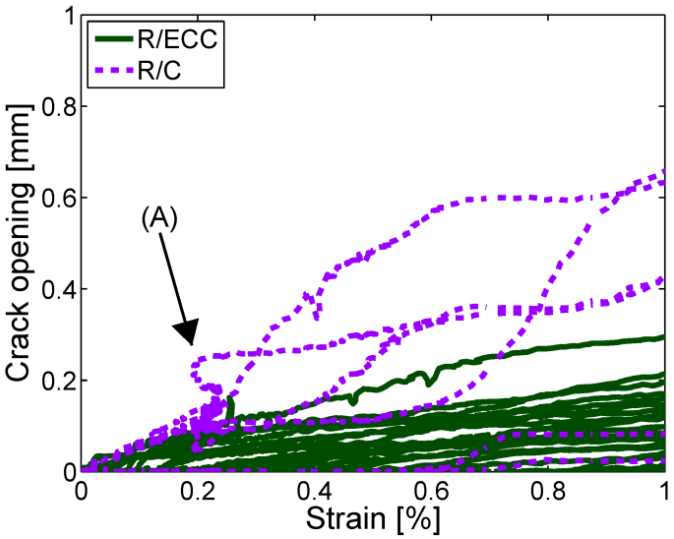

a) R/C and R/ECC

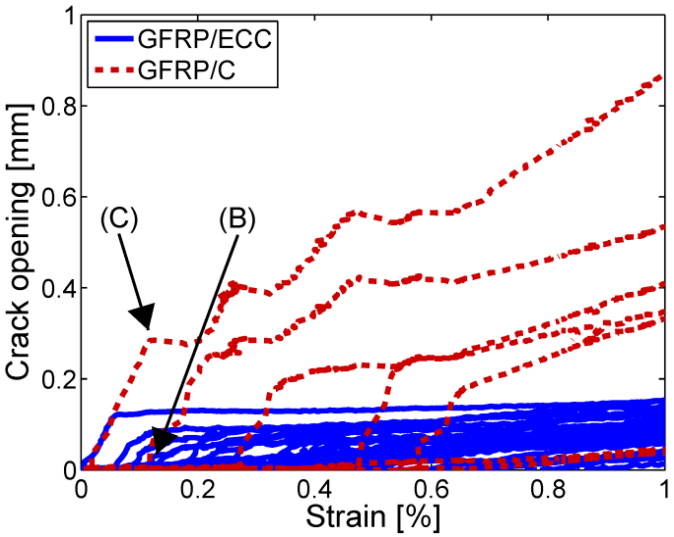

b) GFRP/C and GFRP/ECC

Figure 4-9 Development of crack opening vs. strain in a): R/C in comparison to R/ECC, (A) indicates where strain is halted due to opening of a crack at another location. b): GFRP/C in comparison to GFRP/ECC. (B) shows the formation of a new crack while (C) indicates where further crack opening is suspended due to (B).

The crack spacing for the composite members were obtained from the DIC analysis. The average crack spacing in R/C members was 70 mm while GFRP/C members exhibited a slightly lower average spacing of 60 mm. Due to multiple cracking in ECC, the crack spacing in reinforced ECC members were significantly lower, measuring average crack spacing of 14.5 mm and 13 mm in R/ECC and GFRP/ECC members respectively.

4.7.3 Cyclic loading

Cyclic loading sequences of 1,000 cycles were carried out after initial monotonic tension tests in a displacement-controlled testing configuration. Load-strain responses during 1,000 cycles for R/C and R/ECC members are shown in Figure 4-10a, and for GFRP/C and GFRP/ECC members in Figure 4-10b.

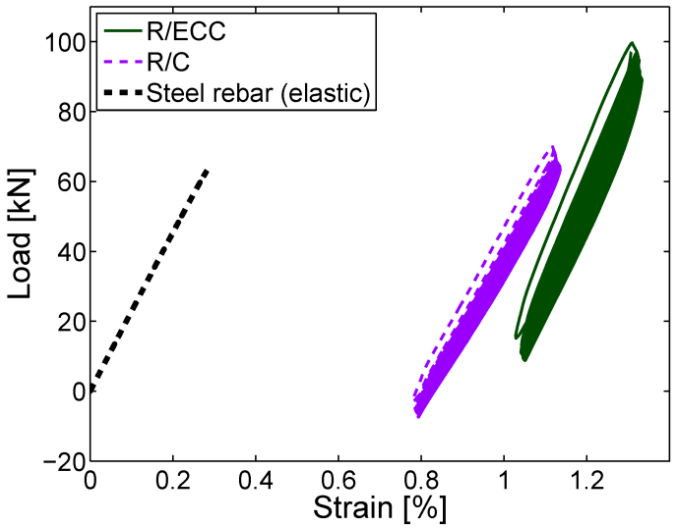

a) R/C and R/ECC

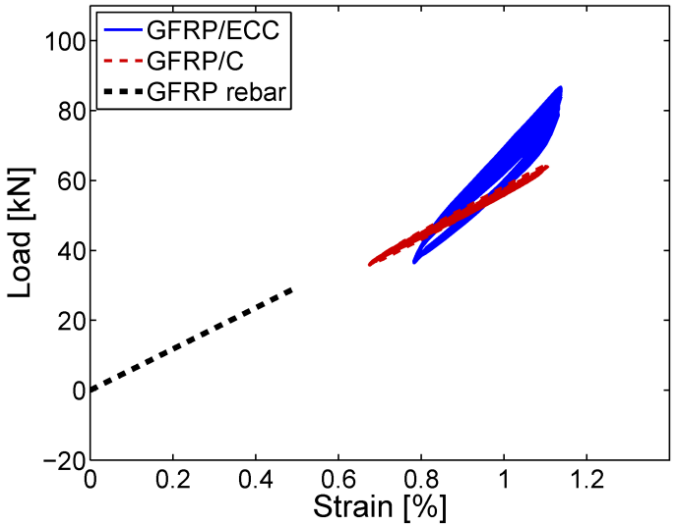

a) GFRP/C and GFRP/ECC

Figure 4-10 Cyclic loading hysteresis for: a) representative R/C and R/ECC and b) representative GFRP/C and GFRP/ECC tension members during 1000 cycles. The bare elastic response of the steel rebar and the bare response of the GFRP rebar up to 0.5% strain are shown for comparison.

In Figure 4-10 the stiffness of R/ECC is slightly stiffer than that of R/C while GFRP/ECC shows a significantly stiffer response than GFRP/C. To quantitatively

compare the responses of the four different composite types during cyclic loading, the measured axial composite stiffness E·A [N/mm^2·mm^2] is quantified in Table 4-3. Based on the cyclic load-strain responses shown in Figure 4-10 the stiffness of R/C, R/ECC, GFRP/C and GFRP/ECC are determined and summarized in Table 4-3.

The softer response of the R/C specimen relative to the elastic response of the bare steel rebar in Table 4-3 is due to the fact that the bare steel rebar shows axial stiffness during purely elastic response, whereas the steel in the R/C composite is stretched up to inelastic.

Table 4-3 Axial stiffness EA of the tested specimen types obtain from experimental data

	R/C	R/ECC	GFRP/C	GFRP/ECC	Steel rebar*	GFRP rebar
E·A [N/mm^2·mm^2]	$20.6 \cdot 10^6$	$27.9 \cdot 10^6$	$6.4 \cdot 10^6$	$13.4 \cdot 10^6$	$23.0 \cdot 10^6$	$5.6 \cdot 10^6$

* Linear elastic part of the load-displacement response.

In addition, the composite behavior of a representative GFRP/ECC specimen subjected to 10,000 cycles was analyzed in more detail using an LVDT to control the cyclic loading sequence (see Figure 4-11). The use of predefined displacement levels enables an energy based assessment of the degradation of the composite interaction between the reinforcement and its surrounding matrix, which is represented by the hysteresis loop on the load-deformation response (see Figure 4-11).

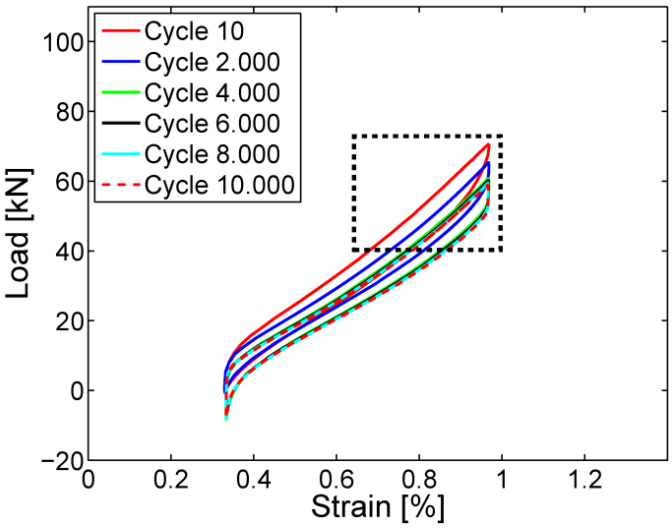

a) GFRP/ECC

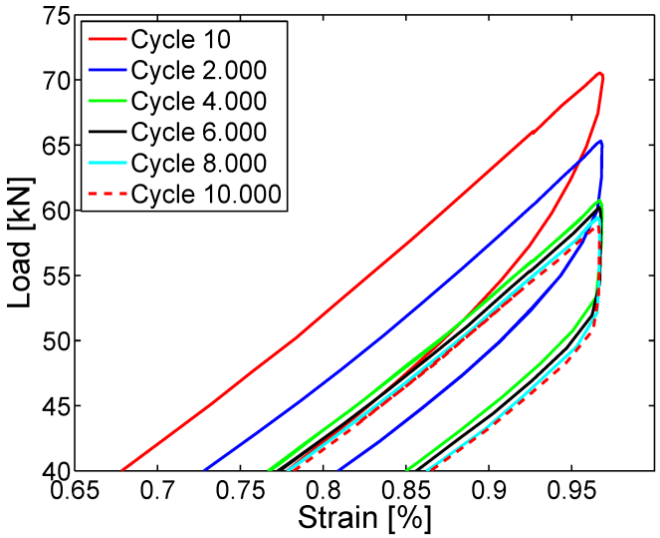

b) GFRP/ECC

Figure 4-11 Cyclic loading hysteresis for a representative GFRP/ECC tension member loaded to 10.000 cycles. a) Overall cyclic response, b) close-up view of the upper end of the response shown in a).

Figure 4-11 shows the upper crest of the load hysteresis decrease from approximately 70 kN down to approximately 60 kN during the first 4,000 cycles and maintains approximately the same load level until 10,000 cycles are completed.

The energy dissipated in the system during one cycle is defined as the difference between the overall mechanical work during loading and unloading over the measured displacement interval, i.e. the area inside the hysteresis of a single cycle in a load-displacement graph. Energy dissipation can be quantified by integrating the force (load) with respect to the displacement given as:

$$W_{(one\ cycle)} = W_{(loading)} - W_{(unloading)} = \int_{x0}^{x1} \left(F_{(loading)}\right) \cdot dx - \int_{x1}^{x0} \left(F_{(unloading)}\right) \cdot dx \quad (4.13)$$

where $W_{(one\ cycle)}$ is the energy dissipation of one cycle (in N·m or J), x_0 and x_1 are the lower and upper boundaries of the cyclic loading displacement interval (in m), and $F_{(loading)}$ and $F_{(unloading)}$ are the load values (in N) of the loading and unloading part of the hysteresis respectively.

Based on analysis of the hysteresis loops displayed in Figure 4-11, Table 4-4 shows the calculated dissipated energy of individual cycles according to equation 4.13 given above.

Table 4-4 Energy dissipation assessment during cyclic testing

	10th cycle	2,000th cycle	4,000th cycle	6,000th cycle	8,000th cycle	10,000th cycle
	[N·m (J)]	[N·m (J)]	[N·m (J)]	[N·m (J)]	[N·m (J)]	[N·m (J)]
$W_{(loading)}$	98.0	88.1	79.7	78.4	77.5	77.0
$W_{(unloading)}$	76.9	72.3	63.6	62.5	61.5	61.3
$W_{(one\ cycle)}$	21.2	15.8	16.2	15.9	16.0	15.7

4.7.4 Tension stiffening

The contribution of the concrete in the response of the reinforced member during tensile loading of each composition type was determined by using the load approach (Collins and Mitchell, 1991) while taking shrinkage of the concrete into account. Figure 4-12 through to Figure 4-15 show: a) the composite load-strain response along with the offset bare rebar response a due to shrinkage, b) the corresponding contribution of the concrete (obtained by subtracting the reinforcement response from the composite response) and c) the surface crack formation and development (corresponding to A-F from a) and b)) by utilizing DIC of representative members of all four material compositions during monotonic tensile loading. The color changes in the DIC output figures (A-F) depict strain intensities which indicate cracks on the measured surface.

It should be noted that the shrinkage effect in conventional concrete is assumed to be 230 μ strain as recommended by Bischoff (2001). Similarly, the shrinkage effect in ECC was assumed to be 400 μ strain based evaluation of unrestrained drying shrinkage measurements of ECC (see section: 2.3.3 and Lárusson et al. (2013)) and shrinkage measurements presented by Li and Lepech (2004) and Wang and Li (2006) in comparison to conventional concrete shrinkage.

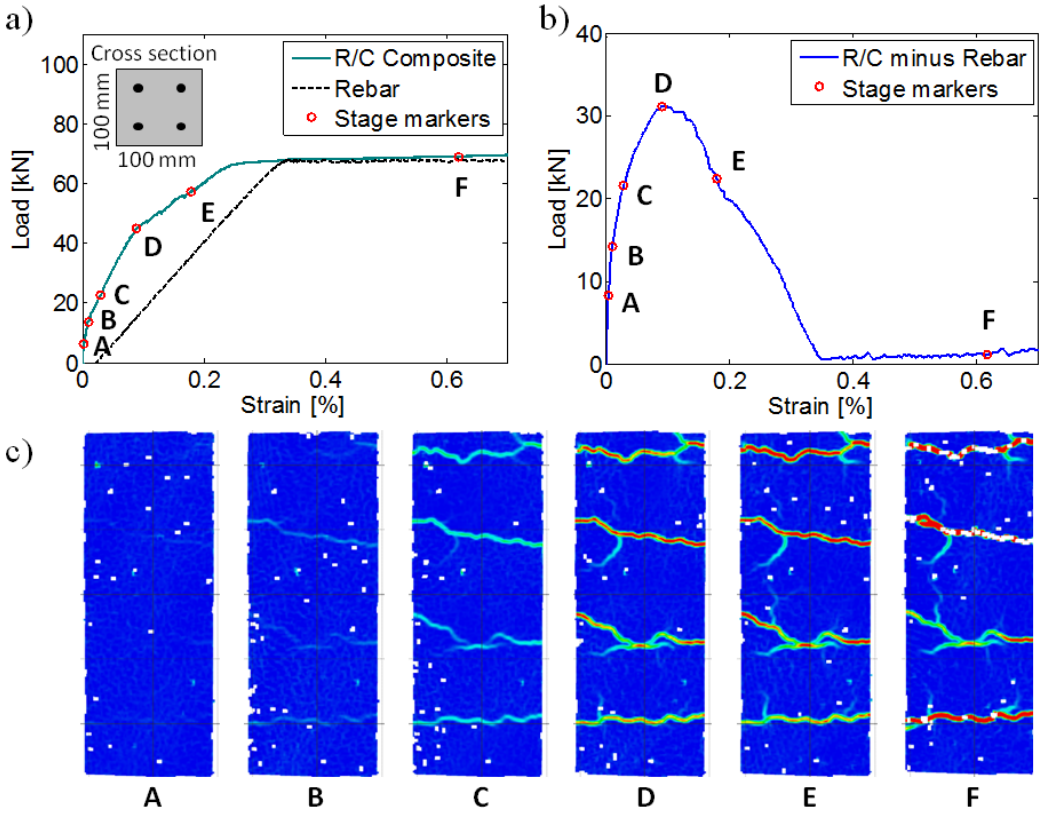

Figure 4-12 A representative R/C tension member, a) shows a composite response along with the response of the bare rebars. b) Shows the contribution of the concrete to the tensile loading. Stage markers referring to the image analysis of the representative area is shown in c) A-F. Shrinkage effect is assumed to be 230μ strain (Bischoff, 2001).

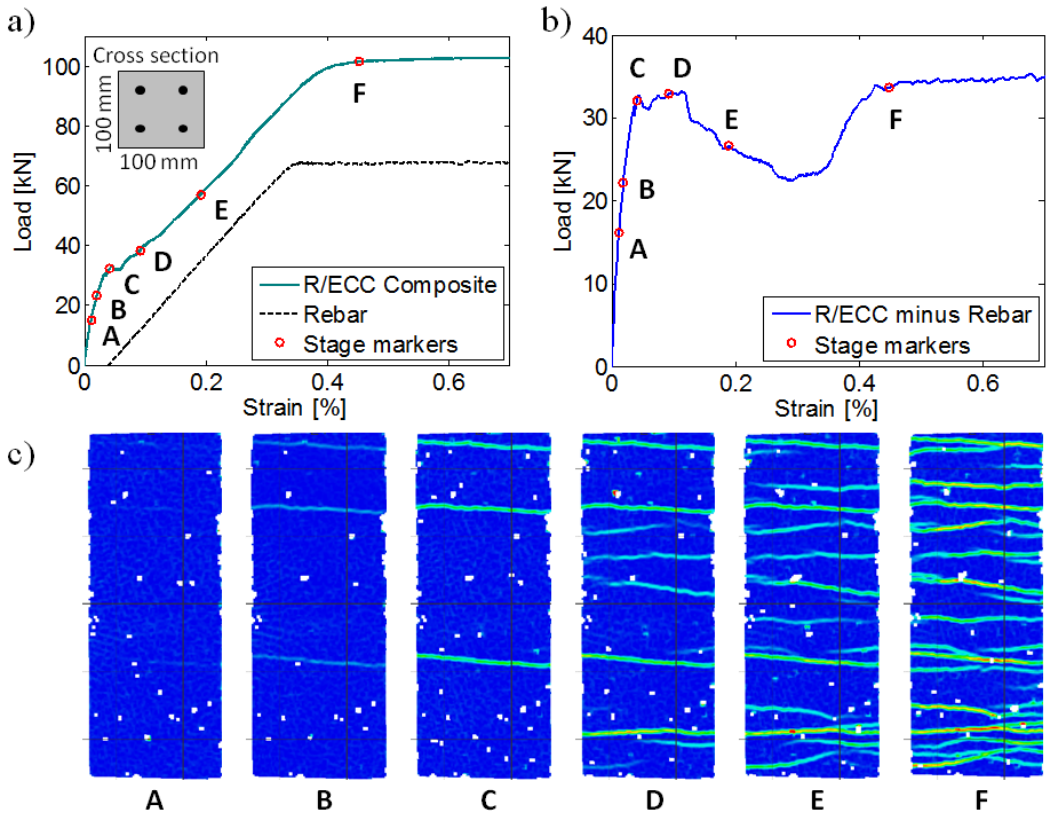

Figure 4-13 A representative R/ECC tension member, a) shows a composite response along with the response of the bare rebars. b) Shows the contribution of ECC to the tensile loading. Stage markers referring to the image analysis of the representative area is shown in c) A-F. Shrinkage effect is assumed to be 400μ strain.

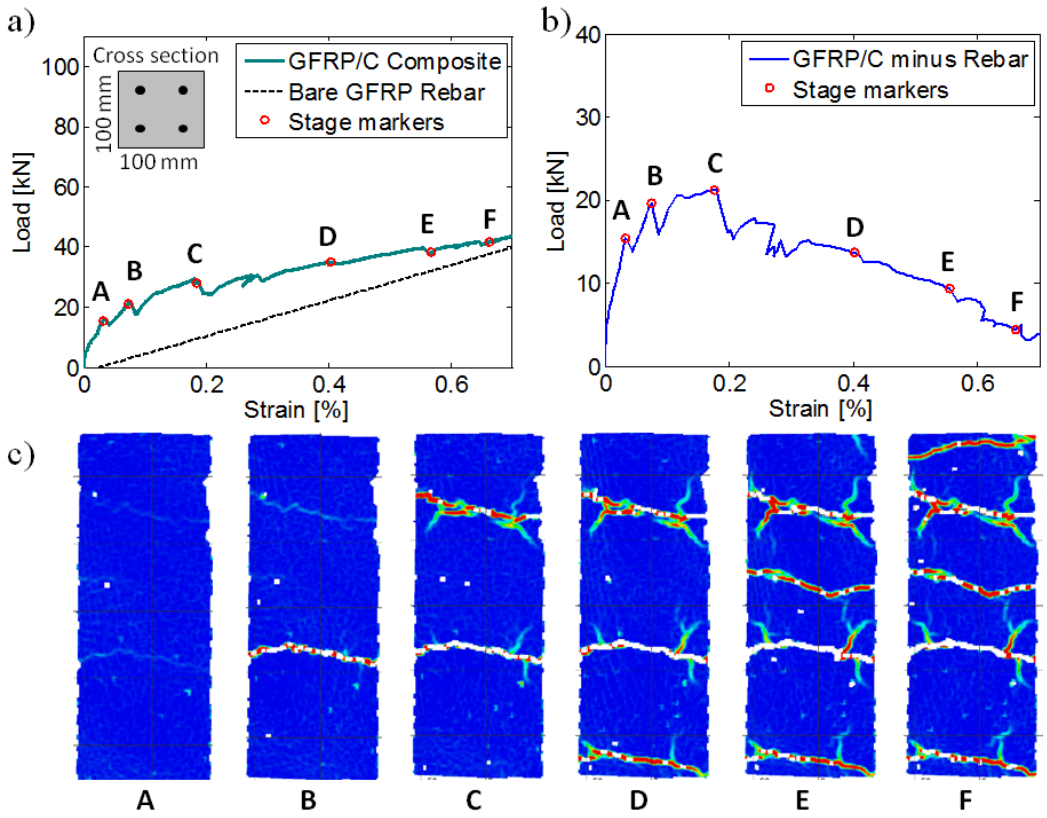

Figure 4-14 A representative GFRP/C tension member, a) shows the composite response along with the response of the bare rebars. b) Shows the contribution of the concrete to the tensile loading. Stage markers referring to the image analysis of the representative area is shown in c) A-F. Shrinkage effect is assumed to be 230μ strain (Bischoff, 2001).

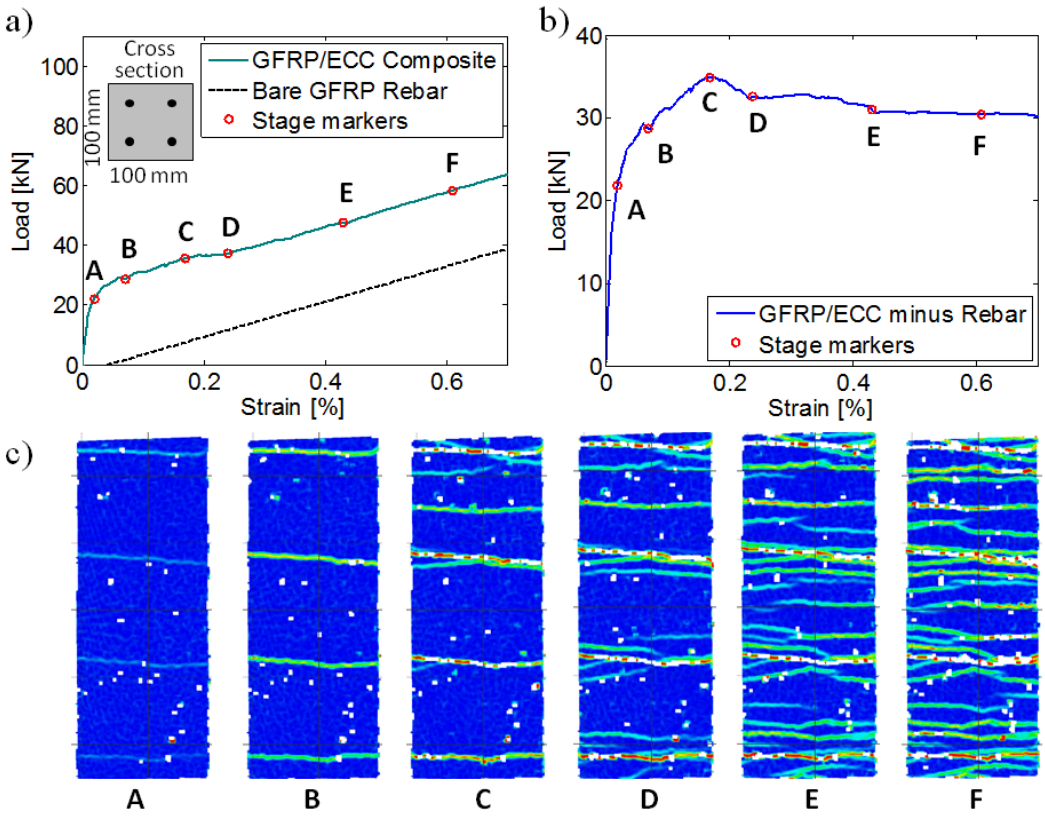

Figure 4-15 A representative GFRP/ECC tension member, a) shows a composite response along with the response of the bare rebars. b) Shows the contribution of ECC to the tensile loading. Stage markers referring to the image analysis of the representative area is shown in c) A-F. Shrinkage effect is assumed to be 400μ strain.

4.8 Discussion

4.8.1 Monotonic tensile loading

The variance in the load-deformation response of a reinforced tensile member is strongly affected by the number of cracks formed within a predetermined interval, that is: lower numbers of cracks result in a slight inconsistency between identical specimens whereas a higher number of cracks yield a greater consistency. Therefore, due to the relatively low count of cracks observed on the representative area of both R/C and GFRP/C members (see Figure 4-8), the load-strain response differ slightly within each composition type, particularly during crack formation (see Figure 4-6 and Figure 4-7). When strain levels are increased and more cracks form, the scatter decreases as all three specimens of each composition type (R/C and GFRP/C) approach the same load-strain response.

Accordingly, the larger number of cracks observed on R/ECC and GFRP/ECC members (see Figure 4-8) resulted in a comparatively consistent load–strain response with-

in each composition type (see Figure 4-6 and Figure 4-7). The changes in number of cracks and magnitude of cracking for each composition are shown in Figure 4-8 to illustrate the difference in crack development and corresponding strain evolution. The higher number of cracks observed on the reinforced ECC members effectively results in limited crack widths, below 300 μm for R/ECC and below 0.160 μm for GFRP/ECC (see Figure 4-9), which indicates limited debonding at the ECC-rebar interface. Furthermore, as a result of the load shearing mechanism and deformation compatibility between the reinforcement and ECC, the interfacial bond stresses are expected to be less than that of reinforced concrete members, and accordingly debonding will be limited at the rebar-ECC interface.

This assumption is furthermore consistent with the research activities on the bond-slip mechanism presented in Chapter which showed limited debonding at the rebar-matrix interface associated with low transverse crack widths of reinforced ECC specimens.

The relatively large difference in crack spacing observed in reinforced ECC member (13-14 mm at 1% strain) and that of material testing of ECC (7-8 mm at 1% strain) is primarily due to a size effect of the specimens and the presence of the reinforcement bars which affect the stress distribution in the matrix.

In Figure 4-6 and Figure 4-7 the onset of the smooth load-deformation responses of the reinforced concrete members (R/C and GFRP/C) indicate that crack saturation has occurred, this is furthermore confirmed in the crack development analysis shown in Figure 4-9. However, in the case of the reinforced ECC members (R/ECC and GFRP/ECC) (from Figure 4-6 and Figure 4-7) the smooth load-deformation response does not represent crack saturation. In the crack width analysis of the reinforced ECC members in Figure 4-9 new cracks form during the entire loading process and the smooth load-deformation response is attributed to the multiple cracking and load carrying ability of ECC in the reinforced ECC members.

As more cracks form, and the axial stiffness decreases, the initial crack-opening-displacement becomes more gradual as opposed to the initial crack-opening displacement jumps during early crack formation. This is even more evident in GFRP reinforced members (GFRP/C and GFRP/ECC) as opposed to steel reinforced members (R/C and R/ECC) due to the relatively soft response of GFRP.

GFRP reinforced tension members develop cracks in a more evenly distributed fashion and crack saturation in the GFRP/C occurs at a larger strain compared to that in the R/C composites where most cracks form at relatively low strain levels. This is apparent in Figure 4-8 and Figure 4-9 where cracks develop at an even spacing in GFRP/C up to 0.6% tensile strain as opposed to R/C where most cracks form below 0.05% tensile strain. However, both the R/ECC and the GFRP/ECC show a gradual crack development over the measured interval.

The comparison of the load-deformation response of the R/ECC composites to that of the reinforcement alone (Figure 4-6) suggests a delayed and more gradual yielding

phase of the composite, which is the transition from the elastic to the inelastic part of the load-strain response. The delayed yielding process is partially due to the shrinkage of the cementitious composite surrounding the reinforcement and partially due to the evenly distributed displacements as a result of the multiple cracking provided by the ECC to the surrounding reinforcement.

In Figure 4-6 and Figure 4-7 the shrinkage induced offset of the bare reinforcement is not illustrated due to the higher shrinkage strain value of ECC (assumed 0.04%) to that of normal concrete (0.023% (Bischoff, 2001)) as a result of the high cementitious content and lack of large aggregates in ECC. However, the assumed shrinkage strain for ECC is most likely underestimated considering that the unrestrained drying shrinkage of ECC found to be 0.12-0.14% (see Figure 2-10) as well as unrestrained shrinkage strain measurements by Wang and Li (2005) which reported shrinkage in ECC to be about 0.10-0.15%, approximately 80% higher than for normal concrete.

The relatively large difference in strain levels at which yielding occurs in the steel reinforced composites (from 0.24-0.29% for R/C up to 0.39% for R/ECC) furthermore indicates the influence of shrinkage and evenly distributed displacements on the composite response during tensile loading. This issue will be addressed in more detail in the following section on tension strengthening and stiffening (section: 4.8.3).

4.8.2 Cyclic loading

From the load-deformation behavior during 1,000 cycles shown in Figure 4-10, for all composition types, an increased stiffness is observed in the reinforced ECC specimens (R/ECC and GFRP/ECC) in comparison to that of the reinforced concrete specimens (R/C and GFRP/C). This is quantified and summarized in the stiffness assessment given in Table 4-3. The increased stiffness can be explained by the ability of the ECC to provide structural integrity by maintaining interfacial bond in the composite, which becomes most evident during repeated inelastic deformations. The ductile behavior of ECC composites result in less degradation of the rebar-matrix interface due to the ability of ECC to form multiple cracks with limited crack width at relatively high tensile strain levels, thus effectively distributing strain over a large area and lowering localized strain levels.

Although ECC exhibits a considerably ductile behavior in direct tension (similar to that of soft alloys), the cyclic behavior of ECC differs substantially from that of ductile metals in that it is unable to recover its energy dissipation mechanism under inelastic deformations. Consequently, the energy dissipation of ECC is expected to be relatively small (Li and Fischer, 2002). Nevertheless, as a result of the load carrying contribution of ECC at relatively large tensile strains the energy dissipation associated with each cycle is larger for the reinforced ECC specimens than that of the reinforced concrete specimens.

The cyclic test of 10,000 cycles, shown in Figure 4-11 for a representative GFRP/ECC composite member, shows that the cyclic load-displacement response approaches a steady-state. This suggests that the degradation of the interfacial bond between the GFRP and the surrounding ECC matrix has diminish and further damage at the interface is limited. This can furthermore be seen in the corresponding energy dissipation evolution summarized in Table 4-4.

4.8.3 Tension strengthening and stiffening processes

The tension stiffening effect represents the ability of the concrete to stiffen the tensile response of the reinforcement by restraining deformations of the reinforcement in segments between transverse crack, while the full longitudinal tensile load is assumed to be carried by the reinforcement in the cracked plane of reinforced concrete members (R/C and GFRP/C). However, only part of the longitudinal tensile load at the crack location is carried by the reinforcement in the reinforced ECC members (R/ECC and GFRP/ECC), the rest of the load is carried by the cementitious composite. This additional load carrying capability in the reinforced ECC members can be defined as tension strengthening. Although it is difficult to distinguish between the tension stiffening effect and the tension strengthening effect during the load-deformation response, the conceptual difference becomes apparent when tension stiffening diminishes in reinforced concrete (Figure 4-12 and Figure 4-14) where as reinforced ECC maintains or increases its additional load levels (see Figure 4-13 and Figure 4-15). In the case of R/ECC, once yielding of the reinforcement occurs, tension strengthening is maintained while tension stiffening is assumed to be zero (see conceptual model in Figure 4-16).

Based on R/C and R/ECC test results a conceptual model for tension strengthening and tension stiffening is presented in Figure 4-16 where the two effects separated. Initially, tension stiffening is predominantly contributing in the ECC's response in the composite member. After maximum load is reached, at ε_{max}, the tension stiffening effect starts to decrease and becomes zero once the reinforcement yields at ε_y. The tension strengthening effect is primarily due to fiber bridging and the subsequent load carrying ability of ECC once cracking has occurred (at N_{cr} and ε_{cr}). Because of the load sharing between the reinforcement and ECC at any crack location, the presence of the reinforcement restricts the cracks from being fully engaged after crack formation. When strain is increased the cracks become more engaged and the tension strengthening effect exhibits a gradual ascending increase in load contribution (see tension strengthening in Figure 4-16). Equilibrium is reached where the stiffening effect and the strengthening effect cross (ε_{equ}) at which point the tension strengthening effect becomes the predominant mechanism and the additional load carrying capability is either maintained or increased. The maximum strengthening effect can either exceed the maximum stiffening effect, as in the R/ECC example in Figure 4-13, or be

maintained below the maximum stiffening effect, as in the GFRP/ECC example in Figure 4-15.

The tension strengthening effect in GFRP/ECC members can also be observed, however, due to the prolonged tension stiffening phase (see GFRP/C in Figure 4-14) and because the maximum strengthening effect does not exceed the maximum stiffening effect, the transition from stiffening to strengthening levels out (see Figure 4-14). That is, after equilibrium is reached the load does not increase.

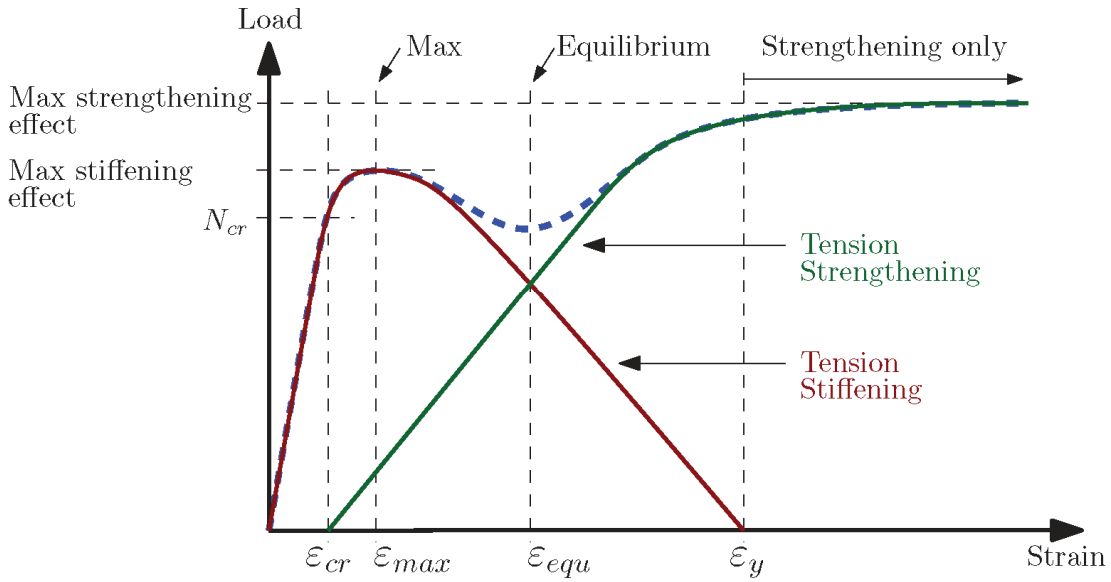

Figure 4-16 Conceptual model for the tension strengthening and stiffening process.

For comparison with the conceptual model (Figure 4-16), the concrete contribution and the ECC contribution from the composite responses of R/C and R/ECC respectively (from Figure 4-12 and Figure 4-13) are plotted in Figure 4-17.

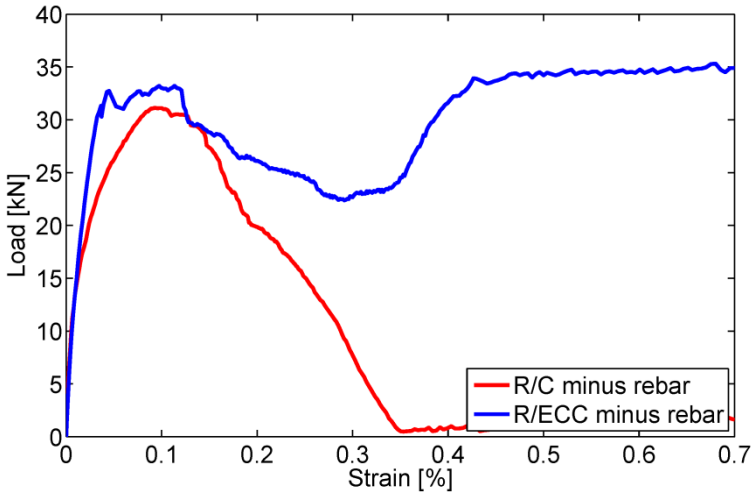

Figure 4-17 The concrete and the ECC contribution in the composite response of R/C and R/ECC respectively.

The transition from the stiffening effect to the strengthening effect is mainly responsible for the intermediate load decrease between 0.1-0.4% strains in Figure 4-17. However, the offset of the reinforcement due to the shrinkage of the ECC as well as the difference between the tensile behavior of the bare reinforcement and that of the steel reinforcement embedded in ECC as a result of the strain compatibility and load sharing ability affect the intermediate load decrease.

Accordingly, the response of the bare GFRP reinforcement would also be an inaccurate approximation of the response of the actual reinforcement in GFRP/ECC composite members when obtaining ECC's contribution.

In addition to the stiffness of the matrix and the reinforcement, an underlying mechanism of tension stiffening is the bond-slip process associated with each transverse crack. The bond-slip process describes and quantifies the degradation of the interface between the reinforcement and surrounding matrix. However, in tension strengthening the bond-slip process is less important because of the compatible deformation behavior and increased load sharing between reinforcement and ECC which decreases localized debonding (see chapter 3).

In Figure 4-12 and Figure 4-13 the difference in the composite strain levels at which yielding of the reinforcement is observed in R/C (approximately 0.24%) and in R/ECC (approximately 0.39%) is most likely due to a number of factors, including: shrinkage of concrete and ECC which introduces a compression strain into the reinforcement prior to loading being applied, strain localization in R/C as opposed to the distributed deformations and load sharing capability in R/ECC, and the resulting strain compatibility of reinforced ECC in contrast to strain localization in reinforced regular concrete.

Due to the confinement provided by ECC in R/ECC members, the response of the bare reinforcement is not identical to that of the reinforcement in the composite. This is evident as the yielding phase is transitioning from elastic to in-elastic in the bare rebar which is distinctly "sharper" in contrast to the more "smooth" transition seen in the reinforced composites (seen Figure 4-12 and Figure 4-13).

The strain measurements of the composite members do not correspond exactly to the actual strains of the reinforcement within the composite members. This is due to that the active length of the embedded reinforcements exceeds the measured length of the composite (400 mm is this experimental program) due to bond-slip surrounding the reinforcement, causing the composite response to appear softer than what is expected.

From the tension stiffening responses for reinforced concrete members depicted in Figure 4-12 and Figure 4-14 (using the load approach), it can be seen that initial cracking occurs well before the maximum load contribution of concrete or is reached. That is, the first cracking average stress, $\bar{f}_{cr}$, is lower than the maximum average stress, $\bar{f}_{max}$, observed in concrete. This contradicts some previous research findings on R/C and GFRP/C tensile specimens (Noghabai, 2000; Fields and Bishoff, 2004; Bischoff and Paixao, 2004) which show that immediately after the first cracking stress is reached, corresponding to the first crack load, the average stress in the concrete will decrease. That is, $\bar{f}_{cr}$ is equal to $\bar{f}_{max}$. However, in cases where the tension specimens have multiple reinforcement bars as well as a relatively low reinforcement ratio, as is reported in the current experimental program, similar behavior has been reported (Wollrab et al., 1996) where $\bar{f}_{cr}$ is lower than $\bar{f}_{max}$.

This behavior, where maximum stress exceeds the first cracking stress, can be explained by looking at how average tensile stresses in concrete develop in a reinforced concrete member. When a reinforced member is subjected to tensile loading, the stresses in the uncracked concrete are assumed to be uniform. Once the concrete cracks the localized stresses decrees in the vicinity of the cracks, see Figure 4-18 a), and the average tensile stress in the concrete and the average concrete stress becomes $\bar{\sigma}_{c,1}$. The localized increase and decrease in concrete stress is governed by two cohesive laws; i) the cohesive law for concrete in tension which characterizes the stress-crack opening relationship and ii) the cohesive shear law which characterizes the bond-slip relationship. Based on the crack width, the crack profile from the surface to the reinforcement as well as internal crack planes, the concrete is able to carry some stresses across the cracked planes. And based on the bond between the reinforcement and the surrounding concrete, stresses get transferred into the concrete from the reinforcement in the vicinity of the crack. If the crack widths are low and the debonding is limited the member is able to an develop average stress $\bar{\sigma}_{c,2}$, when loading is increased, that is larger than the cracking stress, σ_{cr}, and larger than $\bar{\sigma}_{c,1}$ (see Figure 4-18b). Once the stress capacity of the concrete is reached, $\bar{\sigma}_{c,2}$, the average concrete stress decreases due to excessive debonding which limits the amount of stress which

is transferred into the concrete and the average stress becomes $\bar{\sigma}_{c,3}$, lower than $\bar{\sigma}_{c,1}$ (Figure 4-18c).

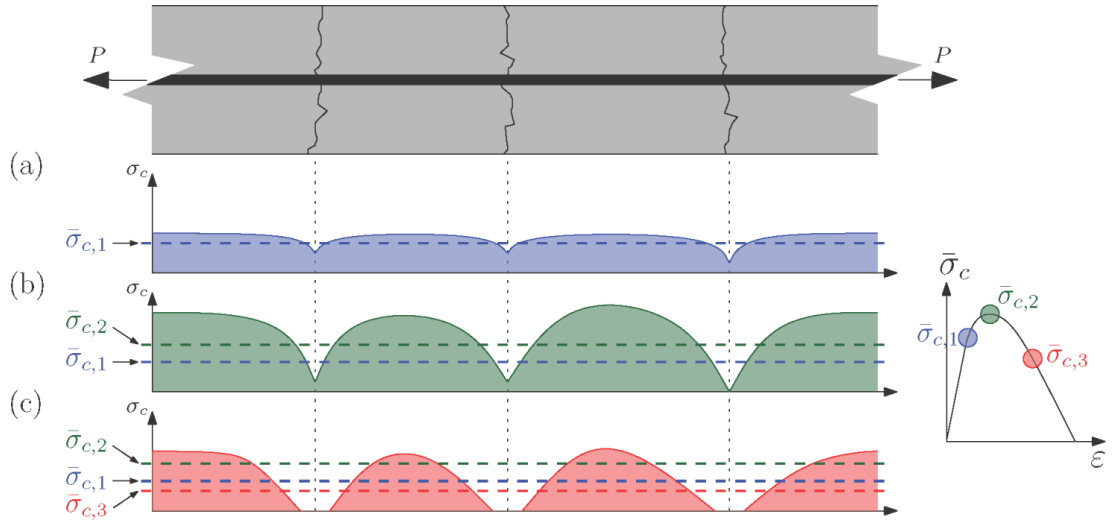

Figure 4-18 Schematic representation of the stress distribution and average stress in concrete in a reinforced concrete element: a) initially after crack formation ($\bar{\sigma}_{c,1}$), b) at maximum average stress ($\bar{\sigma}_{c,2}$) and c) at decreasing average stress ($\bar{\sigma}_{c,3}$).

In the example of the R/C specimen shown in Figure 4-12, for example, the maximum (average) load is reached at 0.09% tensile strain which corresponds to the maximum crack opening of 0.06 mm from Figure 4-9a. At this point four transverse cracks have developed, all of which initiated simultaneously below 0.01% tensile strain (see Figure 4-9a).

In Figure 4-19 the tension stiffening effects of R/C and GFRP/C members from Figure 4-12b and Figure 4-14b are compared to some of the previously established models of the tension stiffening effect given in Figure 4-2. In AIJ (1986), CEB-FIP (1978) and Bishoff & Paixao (2004) model predictions the first crack stress, f_{cr}, is defined as being equal to the maximum average stress, $\bar{f}_{max}$, observed in the concrete in the test results, that is $\beta=\bar{f}_c/\bar{f}_{max}$. In addition, the ACI formulation, presented in equation 4.12, also compared to the test results choosing the first crack loads (P_{cr}) values of 22 kN and 10 kN for R/C and GFRP/C respectively.

The parabolic-like shape of the tension stiffening effect in R/C and GFRP/C members are distinctly different to the model predictions given by AIJ, CEB-FIP and Bishoff & Paixao. The main differences can be seen in the pre load-peak phase where R/C and GFRP/C test results exhibit a gradual decrease in stiffness up to maximum loading followed by a seemingly straight descending branch (see comparison in Figure 4-19) where as the models assume a descending branch immediately after first crack load is reached.

The ACI model seems to provide a more suitable prediction where the initial load increase is accounted for. Although the ACI perdition fails to converge with the test results, the general form of the model mimics test results behavior reasonably.

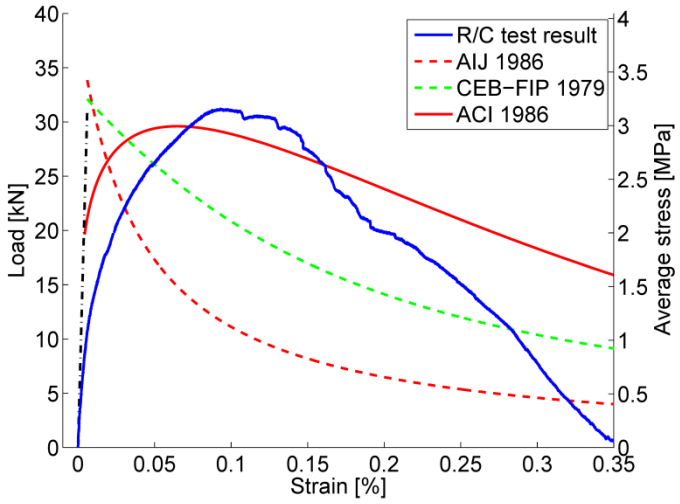

a) R/C

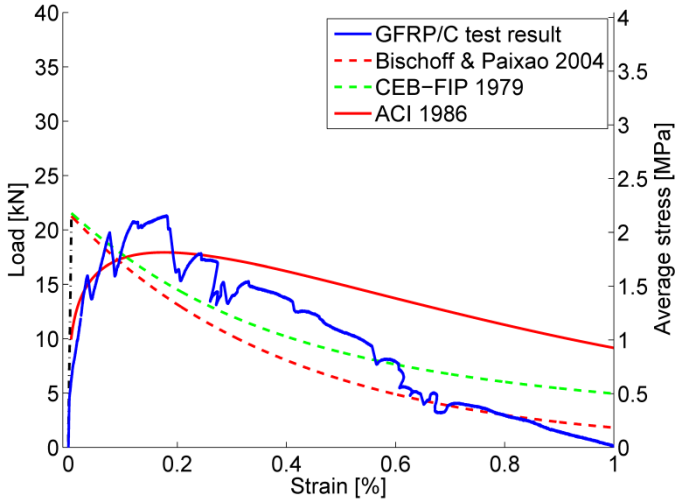

b) GFRP/C

Figure 4-19 The tension stiffening effect of: a) R/C and b) GFRP/C in comparison to different tension stiffening model perditions.

4.9 Conclusions

This study concerns evaluation and analysis of concrete and ECC tensile members reinforced with normal steel or GFRP during the tension stiffening process. In addition to the tension stiffening effect observed in reinforced concrete and reinforced ECC tensile member, a tension strengthening effect is observed and identified in rein-

forced ECC specimens. Based on these findings, a conceptual model for the tensile contribution of ECC is presented where the tension stiffening and tension strengthening are conceptually defined and schematically represented as overlapping events.

The additional strengthening effect results in significant improvement of the composite response in terms continued load shearing between the matrix and reinforcement, and consequently decreases degradation of the interface. This leads to strain compatibility which maintains structural integrity of the composite throughout monotonic- and cyclic testing.

GFRP reinforced members were furthermore shown to increase tension stiffening when compared to steel reinforced members as a result of the softer response of GFRP in comparison to that of steel.

The cracking process of reinforced ECC consistently showed multiple cracking with considerably smaller crack widths and crack spacing than those in reinforced concrete. The influence of the linear elastic strain deformations of GFRP in the reinforced composites also resulted in a larger number of cracks forming at even strain intervals when compared to steel reinforced members, which corresponds to closer crack spacing.

The increase in tension stiffening after initial cracking occurs when average stress in the concrete surpasses the first crack stress. This behavior depends on a number of factors including: bond between concrete and the reinforcement, which allows stresses to build up in the concrete blocks between transverse cracks, and the reinforcement layout.

The tension stiffening analysis of reinforced ECC members reviled a strong indication that the bare reinforcement response is an inaccurate representation of the actual reinforcement response embedded in the composite members due to the confinement provided by ECC.

Finally, the tensile strain behavior of ductile ECC and low E-modulus GFRP are shown to be compatible resulting in a good composite interaction and strain compatibility during short term and long term loading. The relatively low composite stiffness conserved structural integrity and tight crack widths found in GFRP/ECC members are highly desirable attributes for link slab design.

Bibliography

ACI Committee 224, 1986. Cracking of Concrete Members in Tension (ACI 224.2R-86), ACI JOURNAL, Proceedings V. 83, No. 1, Jan.-Feb., pp. 3-13.

ACI committee 224, 2004. Cracking of concrete members in direct tension, reported by ACI committee 224, ACI 224.2R-92, reapproved 2004

AIJ, 1986. Recommendations for Design and Construction of Partially Prestressed Concrete (Class II) Structures, Architectural Institute of Japan, (in Japanese)

Bazant, Z. & Oh, B. , 1983. Spacing of cracks in reinforced-concrete. Journal of structural engineering-ASCE, 109, pp. 2066-2085.

Belarbi, A., and Hsu, T.T.C., 1994. Constitutive laws of concrete in tension and reinforcing bars stiffened by concrete. ACI Structural Journal, 91, pp. 465–474.

Bischoff, P. H. & Paixao, R., 2004. Tension stiffening and cracking of concrete reinforced with glass fibre reinforced polymer (GFRP) bars. Canadian Journal of Civil Engineering, 31, pp. 579-588.

Bischoff, P., 2001. Effects of shrinkage on tension stiffening and cracking in reinforced concrete, Canadian Journal of Civil Engineering, 28, pp. 363-374.

CEB-FIP, 1978. CEB-FIP model code for concrete structures (MC78). 3rd ed. Comité Euro-International du Béton (CEB), Paris.

CEB-FIP, 1990. CEB-FIP Model Code 1990 (MC90), Design Code, Comité Euro-International du Béton (CEB), Thomas Telford Services Ltd., London, 1993, pp. 437.

Collins, M.P., and Mitchell, D. Prestressed concrete structures. Prentice-Hall Inc., Englewood Cliffs, N.J. 1991.

Fantilli, A., Vallini, P. & Mihashi, H. , 2005. Strain compatibility between HPFRCC and steel reinforcement. Materials and Structures / Materiaux et Constructions, RILEM Publications, 38, pp. 495-503.

Fields, K. & Bischoff, P. H. Tension stiffening and cracking of high-strength reinforced concrete tension members. ACI Structural Journal, 2004, 101, pp. 447-456.

Fischer, G., Li, V., 2002. Influence of matrix ductility on tension-stiffening behavior of steel reinforced ECC. ACI Structural Journal, 99, pp. 104-111.

Lárusson, L., Fischer, G. & Jönsson, J., 2011. Mechanical Interaction between Concrete and Structural Reinforcement in the Tension Stiffening Process. In procedings: High Performance Fiber Reinforced Cement Composites 6 (HPFRCC6), Springer, 2, pp. 247-254.

Lárusson, L. H., Fischer, G. & Jönsson, J., 2009. Mechanical interaction of Engineered Cementitious Composite (ECC) reinforced with Fiber Reinforced Polymer (FRP) rebar in tensile loading. In procedings: Advances in Cement-Based Materials, (eds) van Zijl and Boshoff, ISBN: 978-0-415-87637-7, pp. 83-90, 2009, CRC Press/Balkema, Leiden.

Lepech, M., and Li, V. C., ”Design and Field Demonstration of ECC Link Slabs for Jointless Bridge Decks”, in proceedings of CONMAT-5, 2005, pp. 22-24.

Li, V.C., and Fischer G., 2002. Reinforced ECC - An Evolution from Materials to Structures, Proceedings of the First FIB Congress, Osaka, Japan, Oct., pp. 105-122.

Noghabai, K., 2000. Behavior of tie elements of plain and fibrous concrete and varying cross sections ACI Structural Journal, 97, pp. 277-284.

Ouyang, C & Shah, S., 1994. Fracture energy approach for predicting cracking of reinforced-concrete tensile members. ACI Structural Journal, 91, pp. 69-78.

Ouyang, C., Wollrab, E., Kulkarni, S. & Shah, S., 1997. Prediction of cracking response of reinforced concrete tensile members. Journal of structural engineering New York, N.Y., 123, pp. 70-78.

Şahmaran, M., Lachemi M., Hossain K.M.A. & Li, V.C.,2009. Internal curing of engineered cementitious composites for prevention of early age autogenous shrinkage cracking, Cement and Concrete Research Volume 39, Issue 10, October, pp. 893-901.

Sooriyaarachchi H., Pilakoutas K., Byars E., 2005. Tension stiffening behaviour of GFRP-reinforced concrete, American Concrete Institute (ACI) SP-230, pp. 975-989.

Wang, S. and V. C. Li., 2005. Polyvinyl Alcohol Fibre Reinforced Engineered Cementitious Composites: Material Design and Performances, Proceedings of Int'l workshop on HPFRCC in structural applications, Honolulu, Hawaii, pp. 104-111.

Wang, S., Li, V.C., 2007. Engineered Cementitious Composites with High-Volume Fly Ash, ACI Materials Journal, Volume 104, Issue 3, pp. 233-241

Wollrab, E., Kulkarni, S., Ouyang, C. & Shah, S., 1996. Response of reinforced concrete panels under uniaxial tension. ACI Structural Journal, 93, pp. 648-657.

Chapter 5

Flexible link slab

In this chapter, an alternative to conventional link slab design is proposed and investigated in a large scale experimental program. The new link slab design features a relatively thin, prefabricated link slab element composed of highly ductile ECC and reinforced with low stiffness GFRP reinforcement. The experimental investigation focuses on the load – deformation response and crack development of flexible elements during both monotonic tensile deformations and cyclic action. The combination of ductile ECC and low stiffness GFRP is expected to result in the highly flexible link slab, capable of facilitating relatively large deformations, contrary to the heavily reinforced and stiff conventional link slabs implemented in the field.

5.1 Introduction

Expansion joints in bridge structures are designed to facilitate both rotations and lateral movements between simply supported adjacent bridge spans due to thermal expansions, shrinkage, creep and girder deflections due to service loads. Expansion joints are furthermore designed to protect the substructure from exposure to corroding substances by providing a watertight seal between the adjacent bridge decks over piers and at abutments.

Traditionally, mechanical expansion joints have been used in bridge structures, but deterioration of its components often results in diminished performance of the joints due to either:

- Accumulation of debris within the joint which can affect its intended functionality and induce undesirable strains in the structure.
- Corrosion of deck reinforcement and spalling of concrete
- Leakage of water through the expansion joint and subsequent corrosion and spalling of bridge decks, bridge girders and girder bearings (see examples in Figure 1-1 and Figure 5-1).

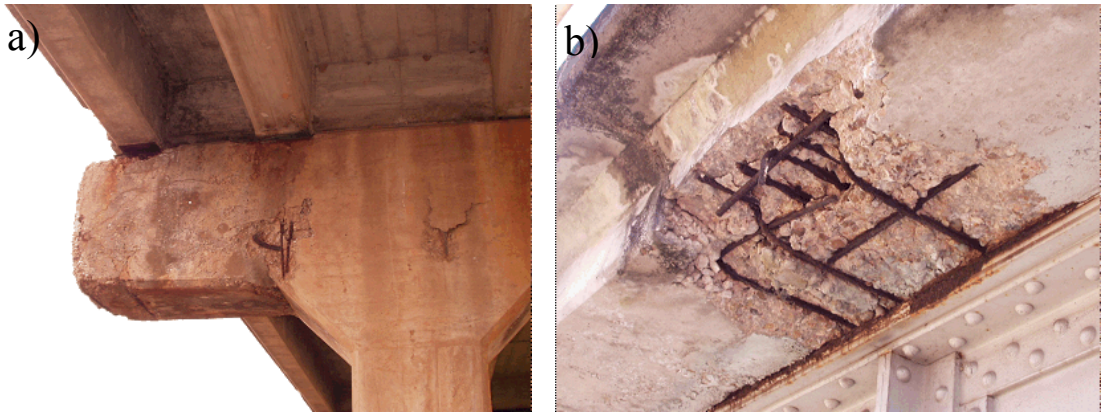

Figure 5-1 Examples of damage due to deterioration and leaching of expansion joints. a): A corroded bridge cantilever pylon below expansion joint and b): a highly corroded R/C deck due to a poorly maintained joint (Webb, 2005).

Numerous examples of deteriorated bridge girders and support structures due to faulty and leaking expansion joints have been reported in Alampalli (1998) and Aktan et al. (2002), and as a consequence, mechanical expansion joints have been found to have a negative economical impact at all stages during the service life of structures (Wolde-Tinsae and Klinger, 1987).

Due to these inherent durability problems and the high cost of installing, maintaining and replacing mechanical expansion joints, continuous and jointless bridge decks have been suggested as an alternative design concept (Burke, 2009).

One type of jointless bridge design includes a so-called Link Slab, which is a reinforced concrete element between two spans of the bridge connected to the substructure with dowels and partially with a debonding layer. The concept of a link slab is to design the bridge girders as discontinuous and simply supported while the reinforced concrete (R/C) bridge deck is kept continuous. This concept and the simplified design procedures presented by Caner and Zia (Caner and Zia 1998) have been adapted in bridge- and highway structures since they were first introduced. Although the concrete link slab may lead to reduced maintenance and long-term rehabilitation costs, some detailed aspects such as crack width control and limited deformation capacity of reinforced concrete still need to be resolved.

5.1.1 Review of previously used ECC link slab design

Based on Caner and Zia's design recommendations (Caner and Zia 1998), further research activities (Kim and Li 2003; Kim et al. 2004; Lepech and Li 2005) suggested the use of a ductile concrete material known as ECC reinforced with standard steel reinforcement. Subsequently a full-scale field demonstration was carried out in collaboration with the Michigan Department of Transportation (Lepech and Li 2009) (see Figure 5-2).

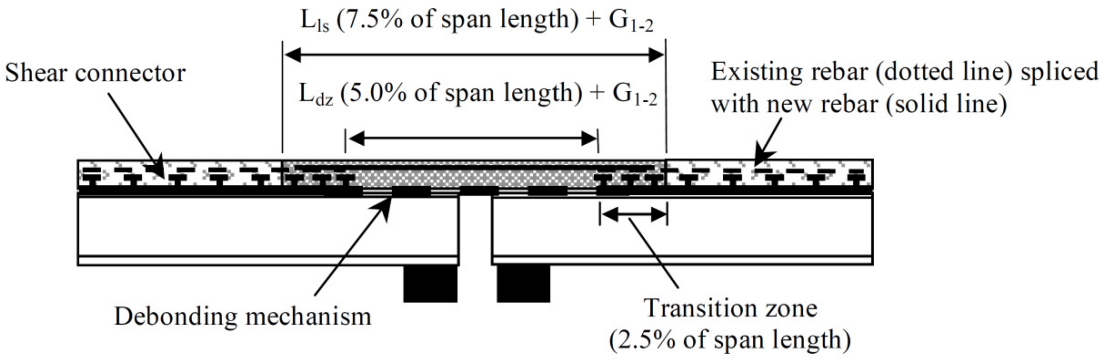

Figure 5-2 Schematic of the ECC link slab implemented in Michigan (Lepech and Li, 2005)

The design approach used by Lepech and Li was to design the link slab to resist an expected moment due to end rotations of the adjacent spans. As a result of the moment demand and restrictions on the working stress of the reinforcement, which was limited to 40% of the yield strength, the link slab was heavily reinforced and consequently did not behave as a joint. Due to the relatively high steel reinforcement ratio generally used, the resulting large bending stiffness of the link slab and consequently the negative moment generated in the joint are undesirable effects and deserve additional consideration.

However, in addition to the high ductility and tight crack widths in ECC, other durability performance aspects of ECC for structural applications has been previously investigated and reported, including: freeze-thaw, harsh environmental exposure and abrasive wear (Li et al., 2004; Lepech and Li, 2006), and found to perform well.

5.1.2 Suggested design concept

By utilizing the ductile behavior of ECC reinforced with corrosion resistant Glass Fiber Reinforced Polymers (GFRP) rebars in a prefabricated composite link slab design, the aim of this study is to implement a slender link slab design concept with a relatively low stiffness.

The inherent multiple cracking attribute of ECC limits crack widths and crack spacing, and provides evenly distributed deformations over the active part of the link slab. Furthermore, the relatively low stiffness of GFRP reinforcement (approximately 1/4 of steel) ensures a low stiffness composite element and a corrosion resistant design. Contrary to the design approach of Caner and Zia, and Lepech and Li where the link slabs have a relatively high stiffness, a low stiffness link slab is highly desirable herein in order to accommodate deformations between the adjacent spans without significant moment- or axial resistance. This is achieved by adapting a low reinforcement ratio and GFRP reinforcement.

Due to the strain compatibility between GFRP reinforcement and ECC, the composite response results in low degradation of rebar-matrix interface which improves durability in terms of static and cyclic loading. In the suggested design concept all deformations are intended to be restricted to the middle active part of the link slab while the passive ends provide firm anchorage to the adjacent spans.

Although the prefabricated link slab investigated in this study is designed to enable both unrestrained rotation as well as axial length changes, the experimental program carried out herein focuses solely on axial deformations. A schematic of the GFRP reinforced ECC link slab concept is presented in Figure 5-3 where the thin link slab element connects the two adjacent bridge spans.

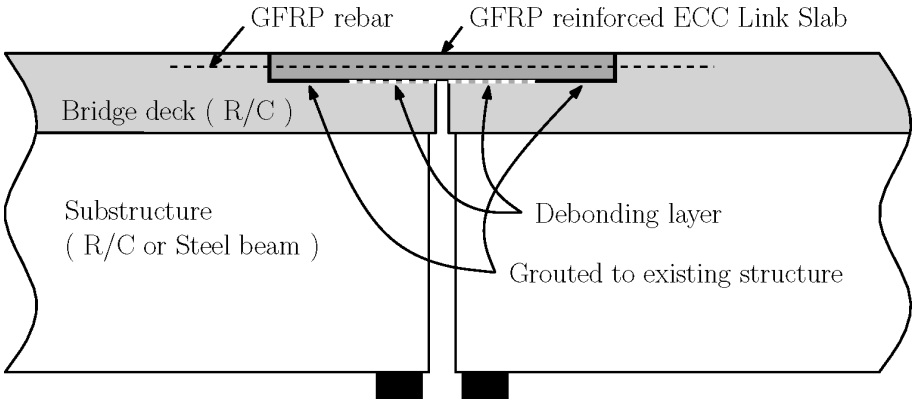

Figure 5-3 Proposed GFRP reinforced ECC link slab concept.

In previously presented work, the composite interaction of ECC and GFRP under tensile loading was analyzed in detail with respect to tension stiffening and crack formation (Lárusson 2009, Lárusson 2011), and bond and interface deterioration (Lárusson 2012) where a comparison was made with the behavior of different compositions of reinforced concrete members (see Figure 5-4). The results of these investigations showed a fully composite interaction of the GFRP reinforced ECC under tensile loading with compatible deformation behavior at relatively large inelastic deformations. Consequently, deterioration of the composite interface between GFRP and ECC were found to be insignificant compared to that in conventional reinforced concrete.

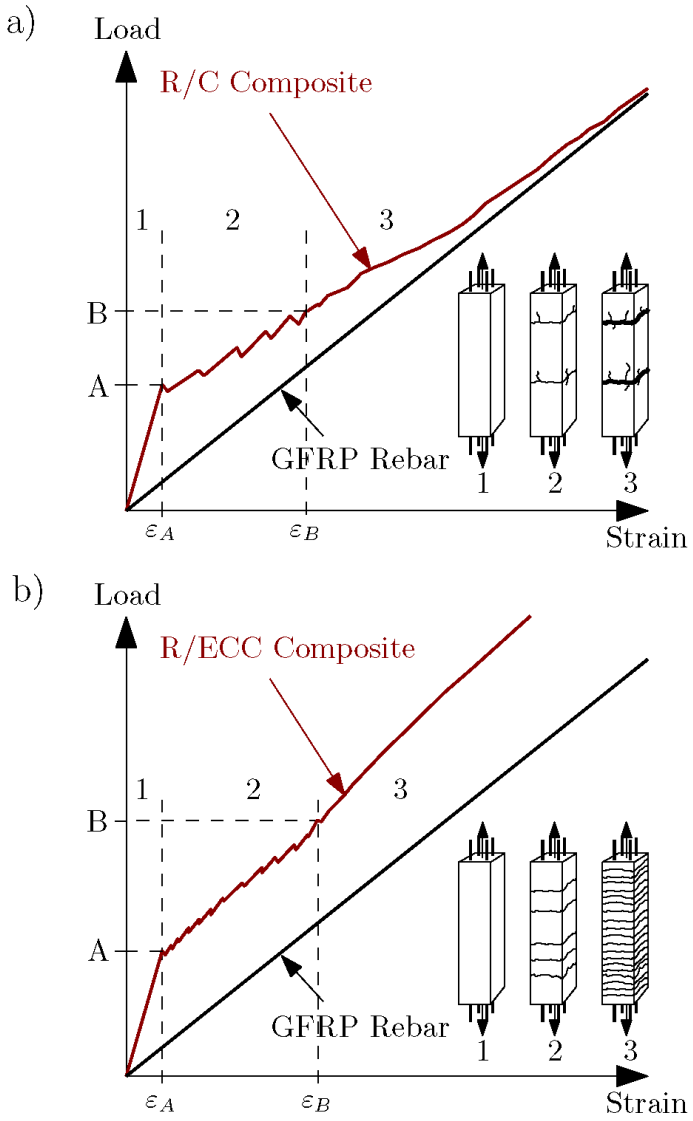

Figure 5-4 Schematic illustration of the tension stiffening process and crack formation in: a) GFRP reinforced concrete (GFRP/C) and b) GFRP reinforced ECC (GFRP/ECC). "P_A" and ε_A are load and corresponding strain of first crack respectively, and "P_B" and ε_B are load and strain after crack saturation occurs respectively.

Utilizing a prefabrication process for a relatively thin GFRP reinforced ECC link slab element allows the precise manufacturing of the element in which sufficient dimensional precision can be accomplished. In addition, a reduced installation time can potentially be achieved in actual field implementation by employing prefabricated elements in either retrofitting applications or in new bridge structures. In a similar prefabricated ECC link slab concept reported by Yamaguchi et al. (2008), an existing expansion joint was removed and a prefabricated ECC link slab panel was installed in only 8 hours in a full-scale field implementation.

One of the structural details of the proposed link slab concept is the transition zone, which is intended to ensure a continuous driving surface between spans and therefore

will transfer forces generated in the deformation process of the link slab to the adjacent deck structure. In the ECC link slab field implementation carried out in Michigan, shear studs provided the essential anchorage needed to secure the transition zone (see Figure 5-2), which is described in detail elsewhere (Qian et al., 2009).

Due to practical issues, shear studs were not considered a viable option to connect the prefabricated link slab suggested in this study directly to the bridge deck or girders within the length of the prefabricated element. In the suggested design herein, a transition zone was accomplished by providing additional reinforcement segments in the passive parts of the link slab ends. The protruding reinforcement segments at each end of the prefabricated link slabs were then cast into the concrete deck structure (see Figure 5-3). A detailed description of the link slab design and the layout of the transition zone are given in the section5.3.2 describing the experimental program.

5.2 Materials

5.2.1 Characterization of ECC

The first crack in the dogbone specimens in this study occurred at a stress level of approximately 3.5 MPa and ultimately reached 4.1-4.6 MPa at tensile pseudo-strain capacity of 1.5-2.3 % (see Figure 5-5a. Crack opening development and average crack spacing measurements obtained using DIC are depicted in Figure 5-5b. The maximum crack widths were found to be approximately 0.12 mm at 1.0% tensile strain and below 0.16 mm at 1.7 % tensile strain.

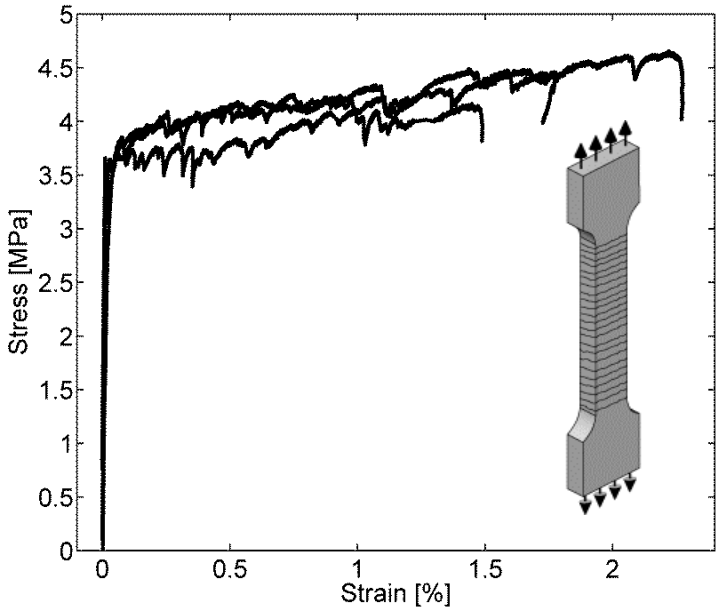

a)

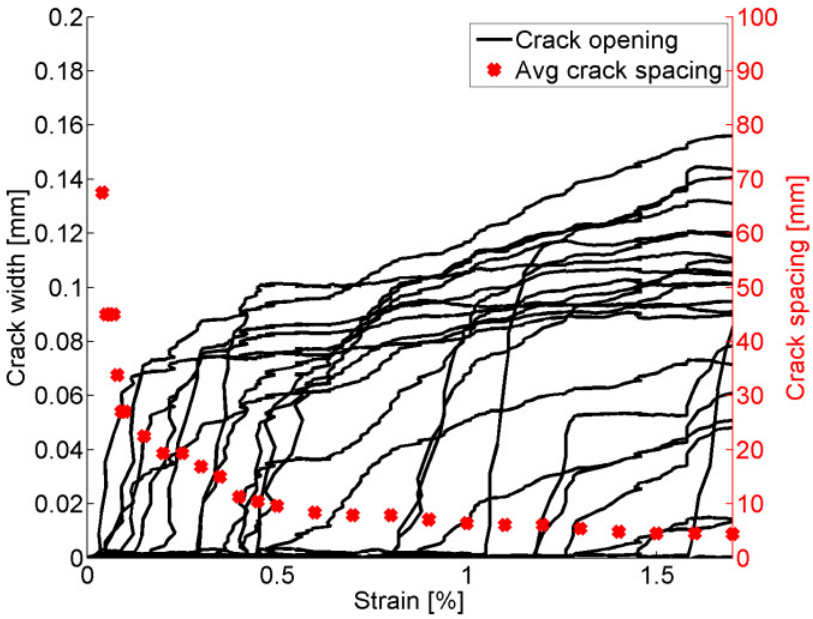

b)

Figure 5-5 a) Stress – strain response of three dogbone-shaped tensile specimens in direct tension. b) Development of crack opening and crack spacing as a function of tensile strain obtained with DIC.

5.2.2 Reinforcement

Two types of GFRP reinforcement bars were used in the experimental program, the first type (GFRP1) had a average diameter of 6.3 mm and is a commercially available product called: Aslan 100 (Hughes Brothers Inc.), consisting of tightly aligned glass fibers wrapped in a helix formation, impregnated with a polymeric resin and coated with sand to increase the bond between rebar and surrounding concrete. The second rebar type (GFRP2) was a smooth surface rebar with a circular circumference with an average diameter of 6.9 mm. Prior to testing, GFRP2 was painted with epoxy and subsequently sand-coated. Both rebar types, GFRP1 and GFRP2, were tested in direct tension and found to have an average elastic modulus of 48 and 46 GPa respectively, and an ultimate strain capacity of 2.4-2.8% (see Figure 5-6).

It should be noted that the elastic modulus was obtained at 1.0% tensile strain, however after 1.0% strain GFRP2 exhibited a softer response, i.e. lower stiffness as is shown in Figure 5-6.

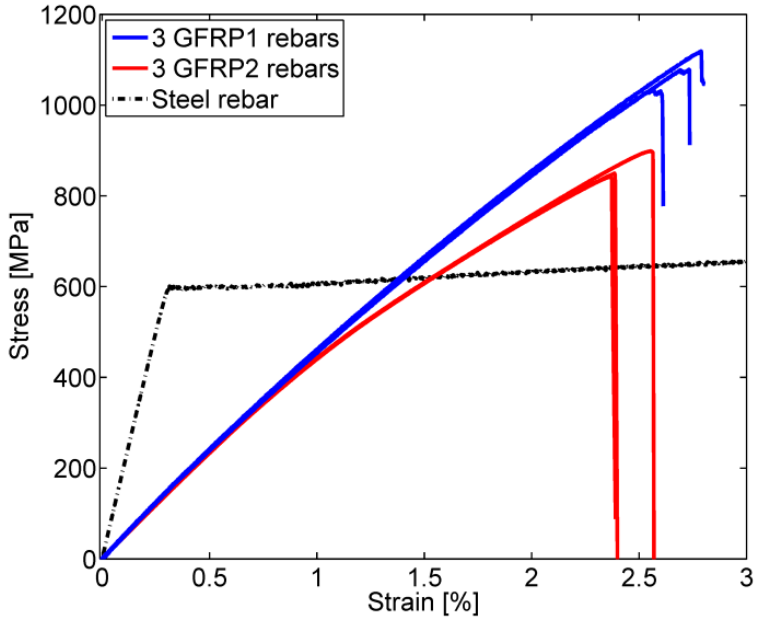

Figure 5-6 Stress-strain results for three GFRP1 rebars and three GFRP2 rebars, for comparison the response of a standard steel rebar is shown as well.

5.3 Experimental program

5.3.1 Test Setup

The test setup represented the ends of two adjacent bridge spans with steel girders and the reinforced concrete (R/C) deck integrally connected with the prefabricated GFRP reinforced ECC link slab (see Figure 5-3). Each section of the bridge spans was 1.5 m

long with a 250 mm high and 1 m wide R/C deck structure resting on a 300 mm high and 300 mm wide HE-300B steel beam, resulting in a total structural height of 550 mm. The whole bridge joint setup rested on rollers while one end was secured to a fixed point and a horizontal load was applied to the opposite end by an actuator capable of applying tensile load up to 1000 kN (see Figure 5-7).

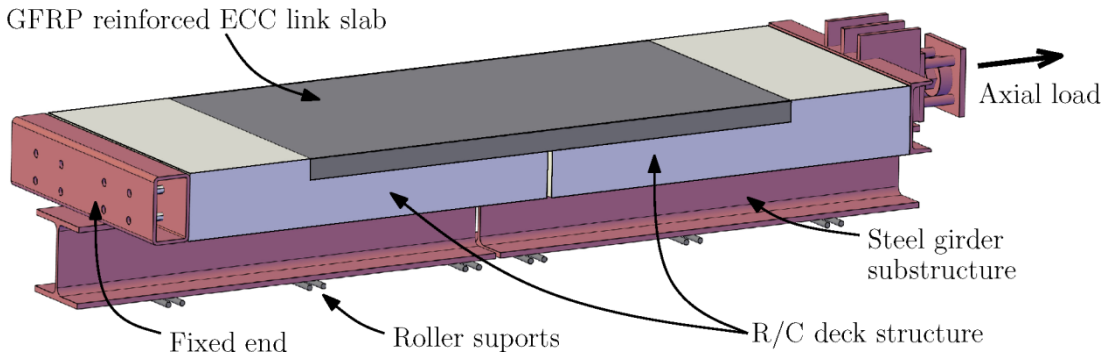

Figure 5-7 Test setup with link slab bridging the two adjacent representative bridge decks.

5.3.2 Geometry and dimensions of the prefabricated link slab

A total of four GFRP reinforced ECC link slabs (LS1-LS4) were fabricated and tested in the representative bridge joint configuration (Figure 5-7). The link slabs were prepared with identical external geometry with a total length of 2 m, 1 m wide and a thickness of 75 mm (Figure 5-8).

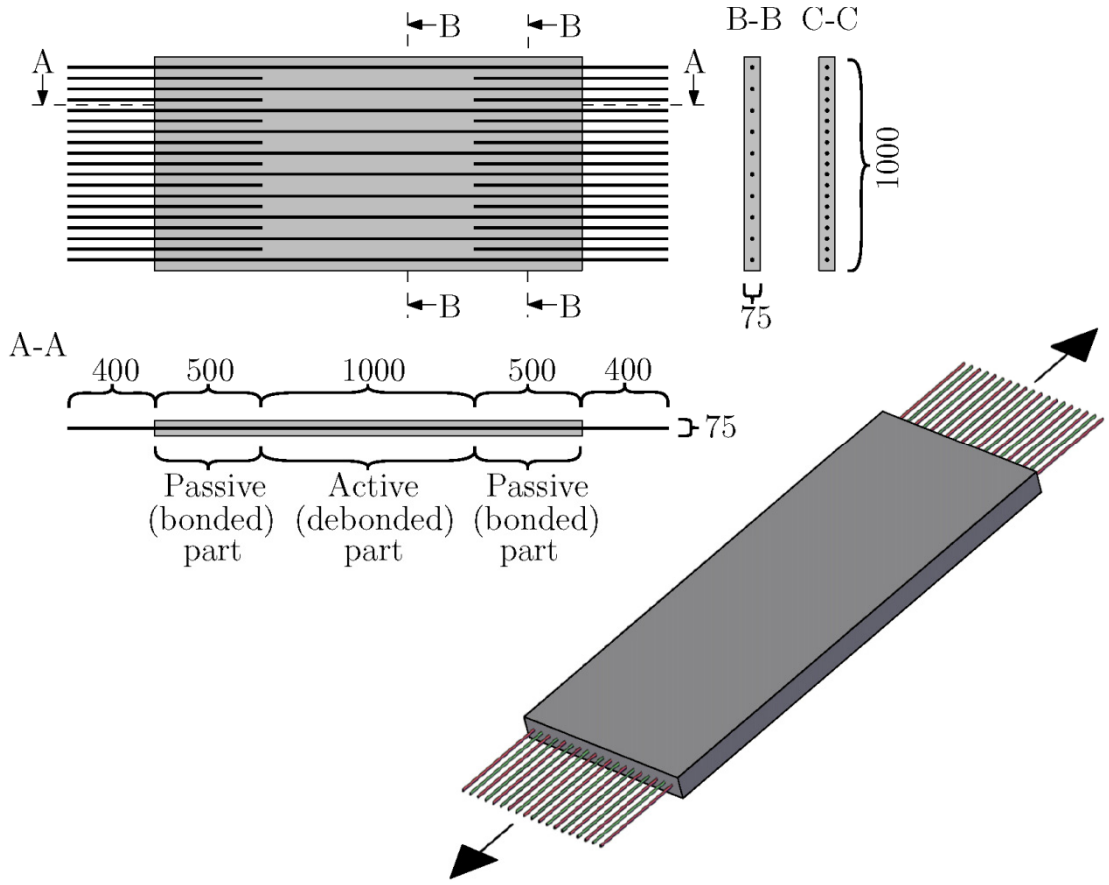

Figure 5-8 Geometry and example of primary and secondary reinforcement layout for LS1. Section A-A shows a GFRP rebar throughout the length of the element. Section B-B shows the cross-section of the de-bonded zone reinforced with GFRP. Section C-C shows the cross-section of the transition zone with primary and secondary reinforcement. Dimensions are given in mm.

In link slabs LS1, LS2 and LS4, a varying amount of primary GFRP reinforcement bars with 2.8 m length were positioned longitudinally throughout the length of the link slabs at ~38 mm depth (half the slab thickness), extending 0.4 m out of the ECC slab at each end to facilitate the load transfer from the link slabs to the surrounding R/C deck structure. Furthermore, additional secondary reinforcement segments with 0.9 m length were embedded approximately 0.5 m into each end of the slab (between the primary rebars) to further increase the load transfer from the passive part of the link slab to the R/C deck (section (C) in Figure 5-8). The reinforcement layout for LS3 was identical to that of LS1, LS2 and LS4 with the exception that the primary and secondary GFRP reinforcement extended only 0.15 m out of ECC slab (see Figure 5-9).

The additional reinforcement segments provided increased axial stiffness and strength to the ends of the link slab and thereby directing the expected deformations to occur over the softer 1 m long active middle part of the link slab (section (B) in Figure 5-8). To further increase the effectiveness of the transition zone in the bonded area (see

Figure 5-3), a transverse rib pattern was provided in the bonded area of the prefabricated elements. To enable unrestrained deformations of the active part of the link slab the interface to the R/C deck below the active part was intentionally debonded using a layer of roofing paper and plastic sheeting. An overview of the rebar layout for all link slabs is given in Figure 5-9.

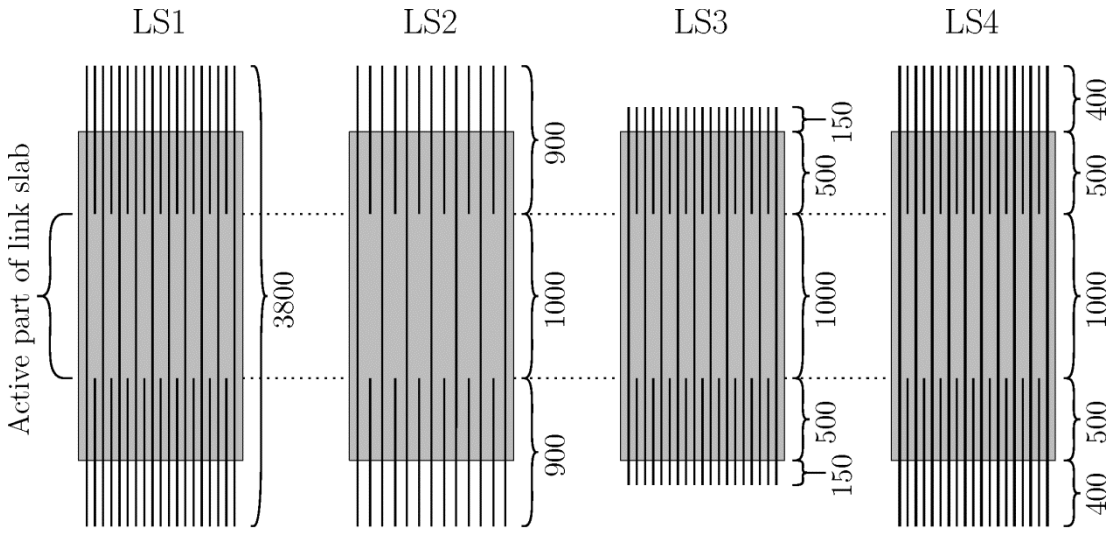

Figure 5-9 Plane view of rebar layout in all link slabs. Dimensions are given in mm.

In the active part the reinforcement ratio of specimen was 0.42% for LS1 (prefabricated), 0.30% for LS2 (prefabricated), 0.42% for LS3 (cast in place), and 0.50% for LS4 (prefabricated), see Table 5-1. The small rebar size in the suggested design was chosen in order to maximize the rebar circumference while maintaining the relatively low reinforcement ratio and to evaluate the effect on crack width and crack spacing.

Table 5-1 Overview of reinforcement arrangement, diameter and resulting reinforcement ratio in link slabs; casting method for all link slabs.

Link slab	Nr of primary bars	Bar diameter* [mm]	Reinforcement ratio ρ [%]	Casting method	GFRP type	Link slab type
LS1	10	6.3	0.42	Prefabricated	GFRP1	New construction
LS2	7	6.3	0.30	Prefabricated	GFRP1	Less reinforcement
LS3	10	6.3	0.42	Cast in place	GFRP1	Cast in place
LS4	10	6.9	0.50	Prefabricated	GFRP2	Different reinforcement

* Nominal values.

The prefabricated specimens (LS1, LS2 and LS4) were cast into specially built formwork with the reinforcement in place. Immediately after casting, the specimens were covered with Plexiglas panels as well as plastic sheets to prevent evaporation of water. After 2 days of curing, the link slabs were demolded and wrapped in damp cloths and covered with plastic sheeting until they were installed into the test setup. The cast in place link slab (LS3) was covered with plastic sheeting after casting and after two days the formwork on the sides of the specimen was removed. Subsequently the slab was covered with damp cloths and plastic sheeting until testing commenced.

5.3.3 Link slab installation procedure

A primary objective in the experimental program was to implement a thin prefabricated link slab element in between adjacent bridge deck structures to simulate either a new structure, or a reconstruction of an existing structure. Link slab elements LS1, LS2 and LS4 were all prefabricated before being placed in between representative adjacent bridge spans. For comparison, link slab element LS3 was cast in place with an identical cross section as LS1.

The installation procedure for the prefabricated link slab elements was implemented as follows:

“Prefabricated elements”

The prefabricated link slab elements LS1, LS2 and LS4 where all fitted with a debonding layer on the bottom side of the active part of the slabs. Subsequently the elements were positioned between two adjacent reinforcement lattices of the bridge deck sections (on top of the steel girder substructures) (see Figure 5-10a). Once the elements were aligned, self consolidating concrete (SCC) was poured to complete the R/C bridge deck with the link slab integrally connecting the two bridge decks (Figure 5-7).

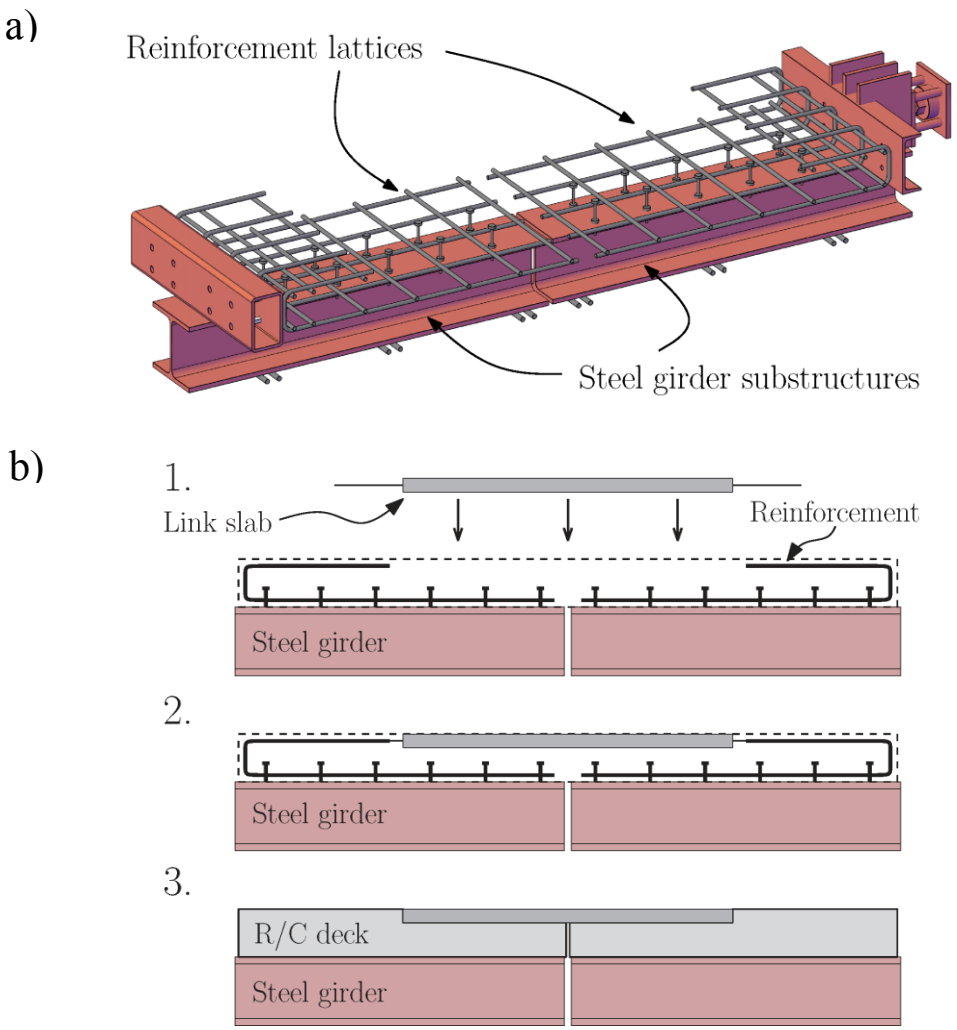

Figure 5-10 a): Reinforcement lattice of a representative bridge deck section on top of the steel beam substructure. b): Installation sequence for prefabricated link slab; 1: link slab lowered into deck reinforcement lattice, 2: link slab position adjusted, 3: SCC poured around link slab to complete R/C deck.

"Cast in place scenario"

After LS1 and LS2 had been tested, preparations were made to cast LS3 in place in a retrofitting scenario. The 2 m link slab panel (LS2) was removed from the representative R/C bridge deck setup and a 1 m long debonding layer was fitted onto the R/C structure using plastic sheeting (centered between both sides) (see Figure 5-11). 150 mm deep holes were then drilled into the R/C decks in order to secure the primary and secondary reinforcement which were grouted into place (see Figure 5-11). Subsequently, LS3 was cast in place on top of the R/C deck structures.

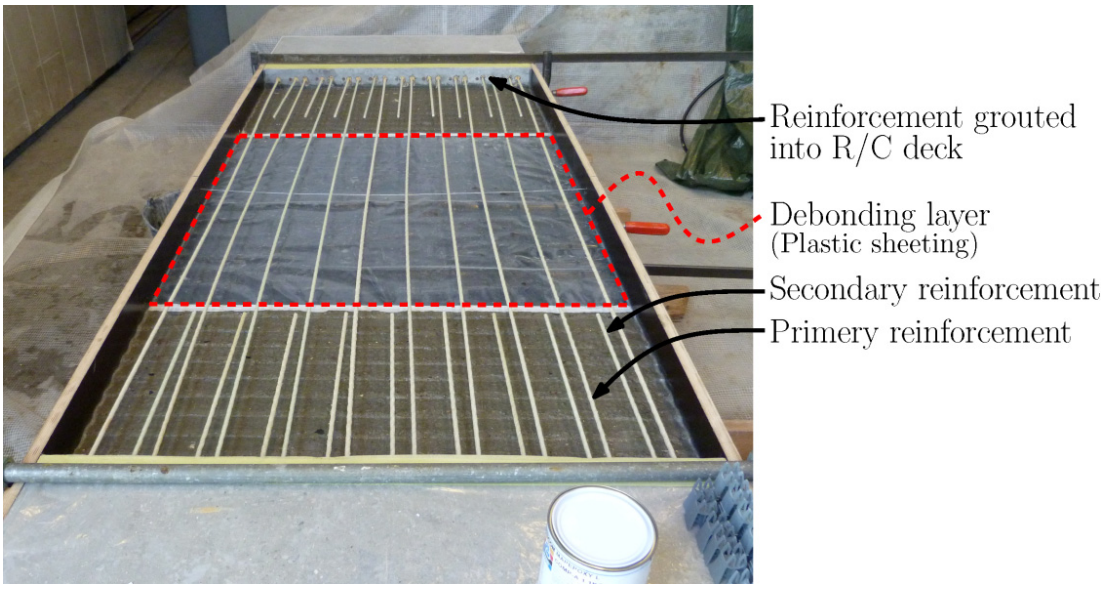

Figure 5-11 Primary and secondary GFRP reinforcement grouted into the R/C deck structure as well as debonding layer centered between the two adjacent deck structures prior to casting LS3 in place.

5.3.4 Loading configuration and sequence

The specimens were loaded in direct tension with the actuator at one end of the structure and a fixed rigid support at the other end (see Figure 5-7). A hydraulic actuator loaded the structure in a displacement-controlled configuration while eight LVDTs monitored deformations of the specimen. Two LVDTs measured longitudinal deformations in the active section of the link slab, two LVDTs measured the deformations over the entire specimen (Figure 5-12) and four LVDT's monitored the opening of the gap between the adjacent bridge sections. Furthermore, a high definition Digital Image Correlation (DIC) system was employed to monitor surface deformations on the top surface of the link slab during testing. The use of the DIC enabled the tracking of the formation and development of individual cracks on the exposed surface of the specimen by employing virtual strain gauges (typically 5-10 mm long) monitoring the transverse cracks (see Figure 5-12). Crack widths and development of all cracks along three representative lines were monitored on top of the active part of link slabs during loading (see Figure 5-12).

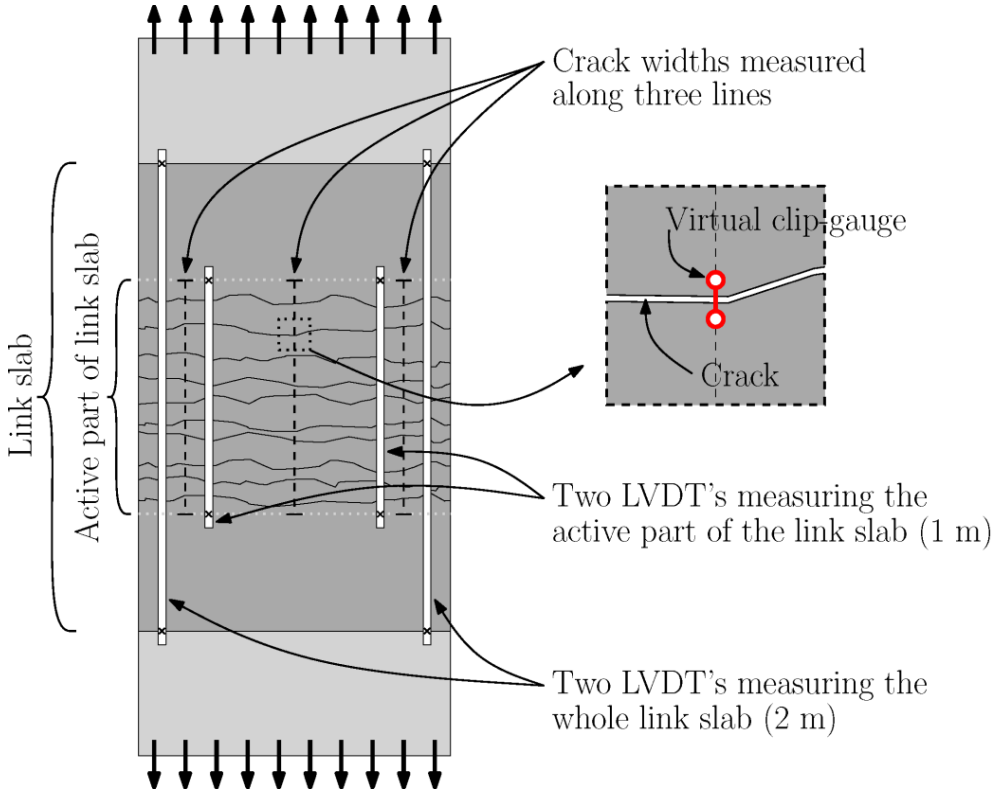

Figure 5-12 Schematic view of measurements taken on top of link slab during testing.

Static loading was applied in a number of load sequences up to a target tensile strain of 1.0%, equivalent to 10 mm elongation of the active part of the link slab. For each of the strain increments, ten repetitions were carried out where the specimens were loaded up to a predetermined tensile strain level and subsequently fully unloaded. The incremented load sequence was carried out in order to examine the link slab elements after each strain increase in terms of crack development on the active section as well as performance of the transition zone.

After static loading had been carried out, the link slab specimens were subjected to cyclic loading between approximately 0.7% and 1.0% tensile strain in order to evaluate and characterize the fatigue response of the composite elements, in particular the crack widths and load-deformation response. The cyclic loading is intended to represent the deformations expected to occur in a link slab element due to thermal expansions and deflections of the bridge spans.

5.4 Test results and observations

5.4.1 Composite load-deformation response: static loading

Figure 5-13 and Figure 5-14 show the structural response of the 1 m long active part of the link slabs during tensile loading sequences up to a target tensile strain of 1.0 %.

For each of the loading sequences, a number of loading and unloading repetitions were carried out. Additionally, the tensile response of bare GFRP reinforcement is compared to the composite response in order to evaluate the tension stiffening effect.

In the first loading sequence of LS1, shown in Figure 5-13a, the elastic response of the link slab reaches approximately 230 kN, before the ECC slab exhibits plastic deformations when cracks start developing. All subsequent load sequences converge in a path defining an upper limit load-strain envelope, which is slightly stiffer than that of the GFRP reinforcement alone. At 1.0% tensile strain, equivalent to 10 mm elongation of the active section, the composite response of the link slab has reached 380 kN. At this point the difference between the bare GFRP reinforcement and the composite link slab has increased to about 240 kN as opposed to the initial 230 kN contribution of the ECC matrix which shows an increased tension stiffening effect. The permanent longitudinal deformation in the link slab after complete unloading was measured to be ~0.4 % in the active section, or ~4.0 mm of the 10 mm elongation previously imposed.

Specimen LS2 (Figure 5-13b) reaches approximately 180 kN tensile load before cracking initializes. Due to technical difficulties with the test setup during this test, the last static loading sequence (the last hysteresis loop in Figure 5-13b) is missing in the load-deformation response of LS2. The upper limit of the load-deformation envelope of LS2 (up to approximately 0.85% tensile strain) shows a stiffness of the composite link slab section parallel to that of the bare GFRP reinforcement. This indicates that no reduction has occurred in the tensile contribution of ECC in the composite response at increased tensile strain levels. Permanent elongation of LS2 after unloading from 1.0% tensile strain was measured to be approximately 5.0 mm, equivalent to 0.5% tensile strain.

The load-deformation response of LS3 (Figure 5-14a) shows cracks initiating at 175 kN and reaches 375 kN at 1.0% tensile strain. The tensile contribution of ECC in LS3 appears to be constant throughout the applied loading sequences when the composite response of the link slab is compared to that of the bare GFRP reinforcement, i.e. the tension stiffening effect. The continuous contribution of ECC shows a sustained composite behavior which suggests insignificant degradation of the reinforcement – matrix interface. A permanent tensile elongation of 4.0 mm (0.4% strain) was measured after unloading from the 10 mm imposed elongation (1.0% tensile strain) during the load sequences.

In Figure 5-14b, the load-strain response of LS4 is shown. The link slab starts to form cracks at approximately 200 kN, however the tensile load-carrying contribution of ECC decreases as tensile strain is increased. Unloading from 1.0% tensile strain leaves a permanent deformation of 5mm (0.5% strain). The initial tensile load carried by ECC decreases from ~200 kN down to ~150 kN at the end of the load sequence (at 1.0% strain) when the contribution of the bare GFRP reinforcement is subtracted from the composite response of LS4. This decreased composite behavior indicates either

the degradation of the rebar-matrix interface and or the breakdown of the tensile load carrying ability of ECC.

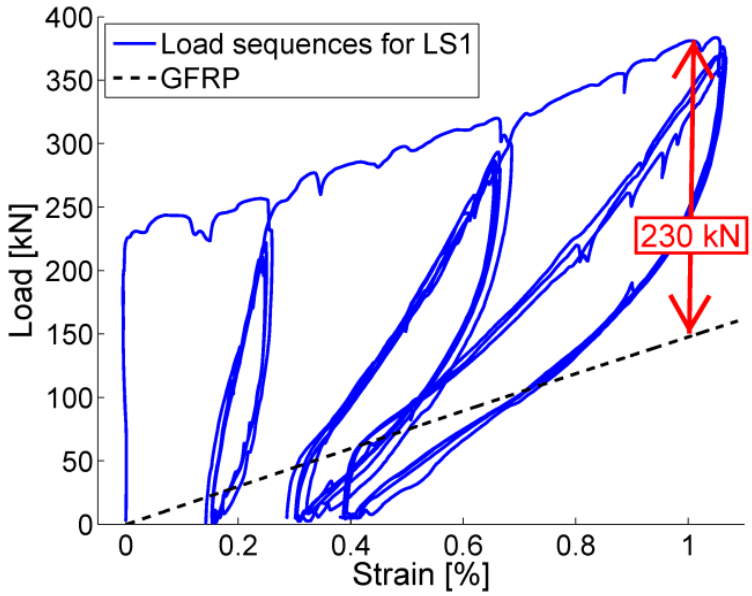

a) LS1

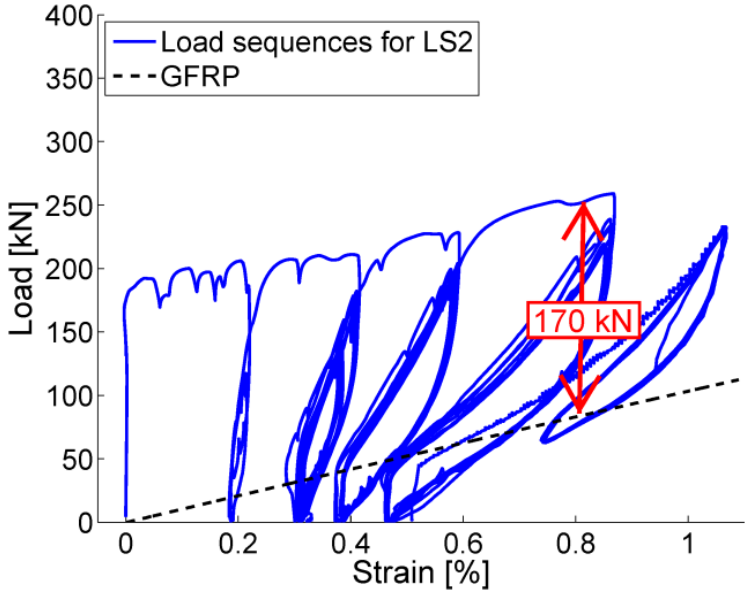

b) LS2

Figure 5-13 Structural response of the active middle part of the link slab a): LS1 and b) LS2. For comparison the response the bare GFRP reinforcement is also shown.

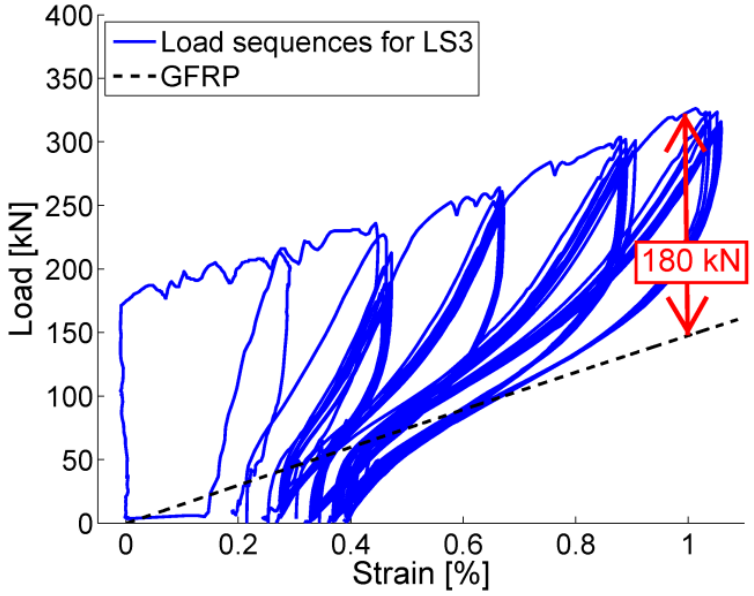

a) LS3

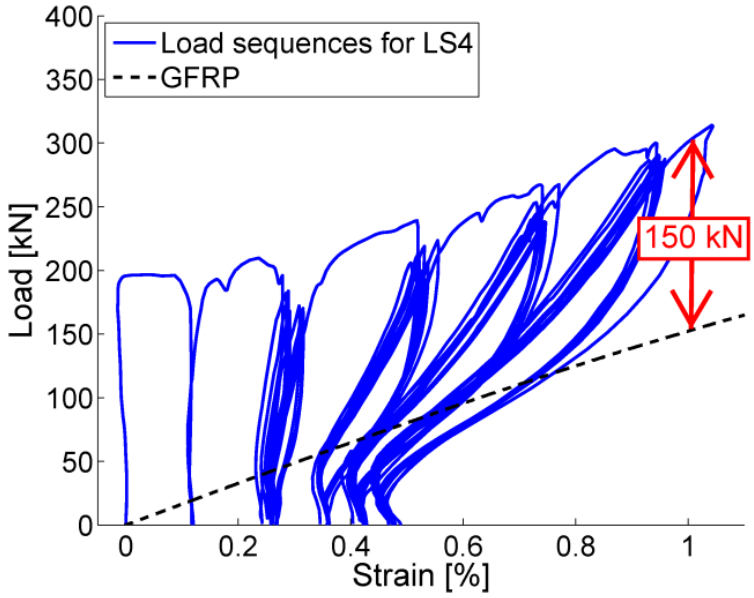

b) LS4

Figure 5-14 Structural response of the active middle part of the link slab a): LS3 and b) LS4. For comparison the response the bare GFRP reinforcement is also shown.

5.4.2 Composite load-deformation response: cyclic loading

Following the static loading sequences up to the target tensile strain level of 1.0%, cyclic loading of the link slabs was applied. The motivation for subjecting the link slabs to cyclic loading was to replicate the fatigue circumstances which the link slab

joints are designed to facilitate as a result of thermal expansions (volume changes) as well as deflection of the bridge spans.

LS1 was subjected to cyclic loading applied in a displacement-controlled procedure between 0.6% and 1.0% tensile strain (see Figure 5-15). After approximately 300 cycles a technical malfunction occurred in the LVDT gauge which controlled the loading, causing the actuator to instantly overload the test setup which subsequently resulted in an abrupt failure of the link slab. However, during the first 300 cycles the load-strain hysteresis shown in Figure 5-15 exhibited no change in response which indicates an insignificant degradation of the composite behavior during the cyclic loading. This implies that the composition of GFRP reinforcement and ECC is well suited for the tensile fatigue in terms of maintaining structural integrity of the link slab.

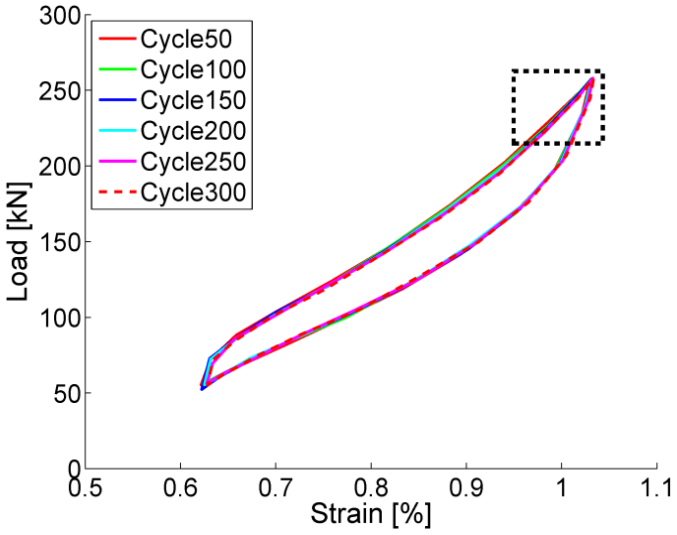

a) LS1

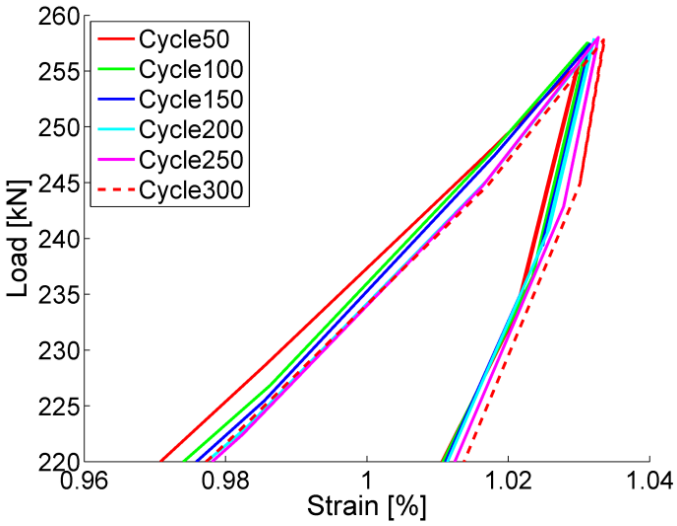

b) LS1

Figure 5-15 Load-strain hysteresis from cyclic testing of LS1. a): overall cyclic response and b): enlarged crest of the hysteresis.

For LS2, a 1000 cycle loading sequence was applied between 0.75% and 1.1% tensile strain (see Figure 5-16). The enlarged load-deformation response (in Figure 5-16b) shows a decreased load response, from 230 kN at the 100th cycle to 200 kN at the 1000th cycle, however, the response appears to be approaching a steady hysteresis path in the last 300-400 cycles. The observed load decrease suggests that the composite interaction in LS2 diminishes steadily throughout the cyclic loading sequence. Although the load responses of the link slabs are not directly of interest, the decrease in load response indicates a diminishing composite interaction which is un-desirable in order to maintain structural integrity. A steady load-deformation response would

however indicate that an certain equilibrium has been reached where the structural performance is sustainable.

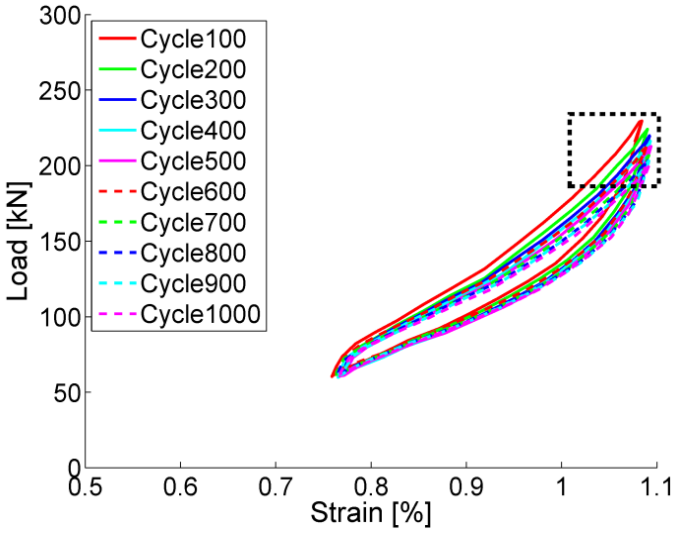

a) LS2

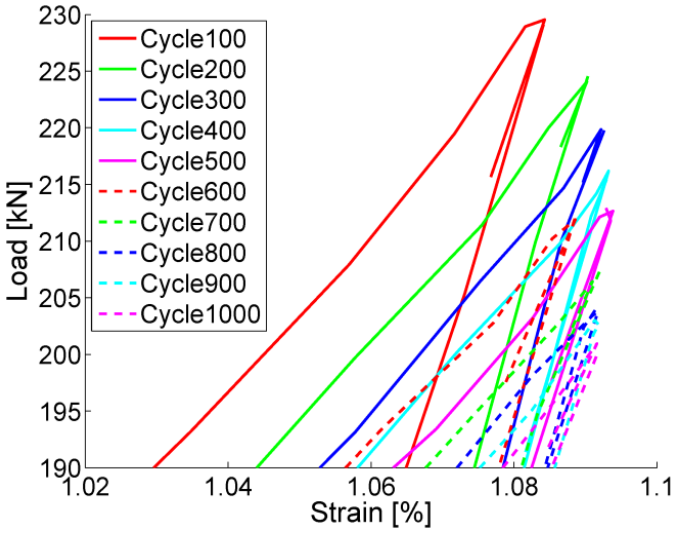

a) LS2

Figure 5-16 Load-strain hysteresis from cyclic testing of LS2. a): overall cyclic response and b): enlarged crest of the hysteresis.

Cyclic loading of LS3 and LS4 where discontinued shortly after they were initialized due to failure of the load transfer zone and rupture of the rebars respectively. More details are given in one of the subsequent sections.

5.4.3 Crack formation and development

By utilizing Digital Image Correlation (DIC) analysis, the global displacement field on the exposed surface of the link slabs was obtained. By employing virtual strain gauges in the post processing of the images (see Figure 5-12), the crack formation and crack width development of individual cracks can be monitored and analyzed in detail at each load increment. Figure 5-17a shows a link slab in the test setup and Figure 5-17b shows an example of the output from the DIC analysis of images from the exposed surface of the active section of the link slab.

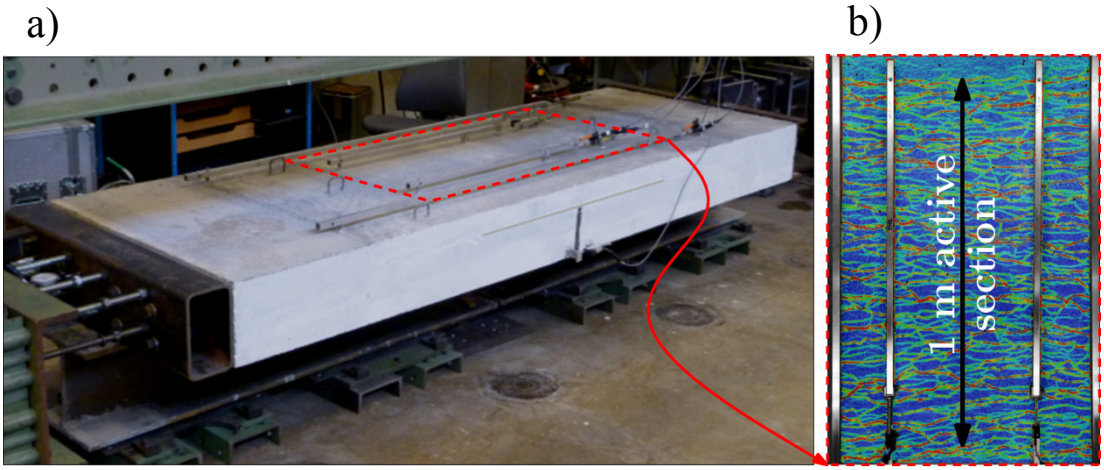

Figure 5-17 a): An overview of a link slab in the test setup and b): example of a DIC analysis output, presented here as a strain field overlay on the actual image. The areas observed with DIC were approximately 1.1-1.2 m long and 0.6-0.7 m wide.

Figure 5-18 shows a visual interpretation of the displacement field measurements on top of the active part of link slabs during the loading process. For a comparative overview of the crack development, examples are shown for all link slabs at four different tensile strains levels: 0.1%, 0.3%, 0.6% and 1.0% obtained by DIC analysis where color changes indicate increasing crack widths.

White areas depict un-computed regions due to either excessive deformations or insufficient surface contrast, which cannot be recognized in the DIC analysis, while local strain levels refer to the color contour scale from 0-4% strain shown in Figure 5-18.

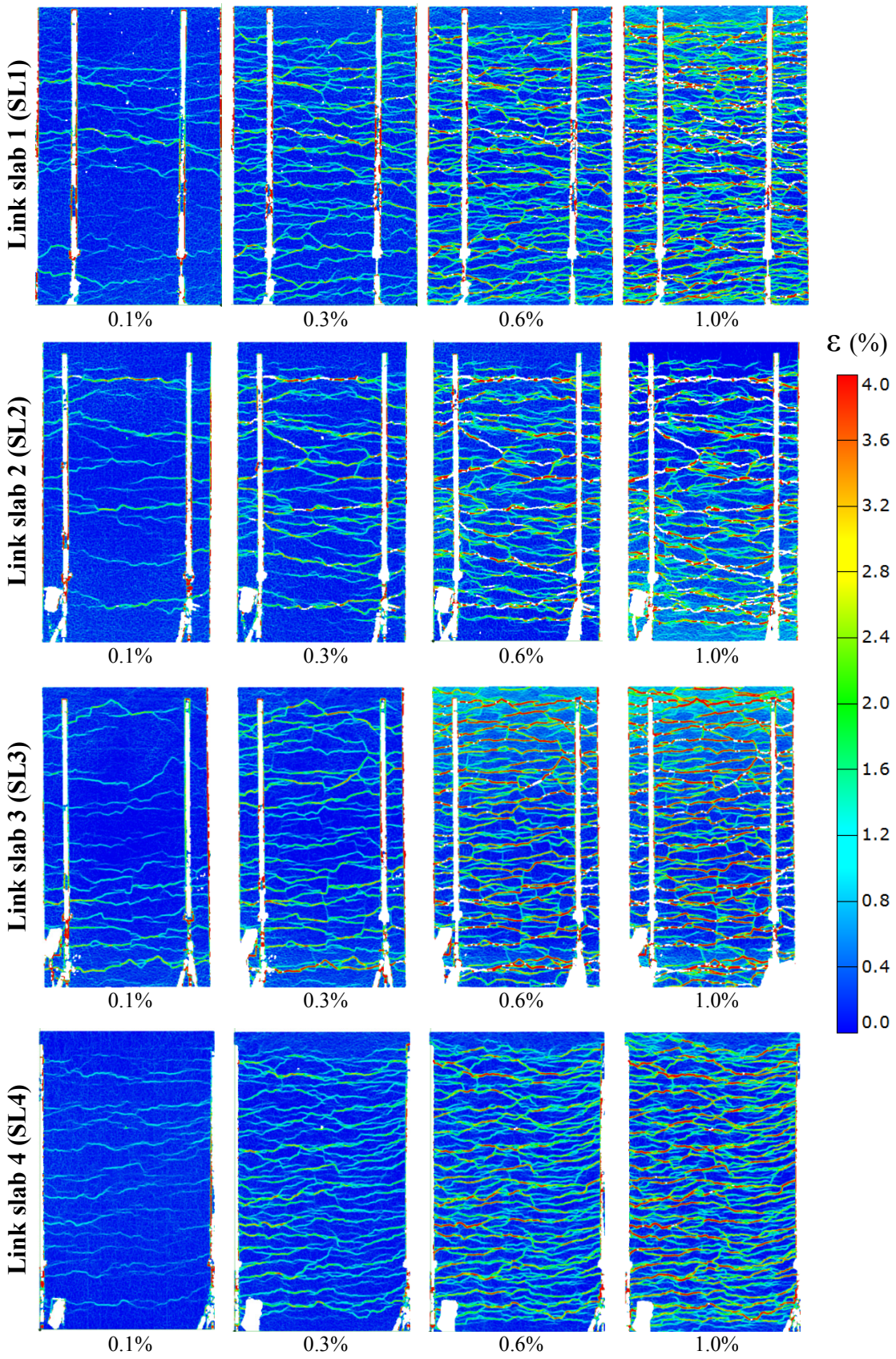

Figure 5-18 Examples of digital image correlation analysis (DIC), blue color indicates zero strains while color changes depict strain intensities (indicating a crack) on the measured surface.

Using the DIC analysis, the crack width development of all cracks on three representative lines (see Figure 5-12) on the surface of the active part of the link slabs are shown in Figure 5-19 and Figure 5-20 as a function of imposed tensile deformations (strain). Furthermore, envelopes of the crack width measurements (maximum and minimum) along with the average crack widths during loading

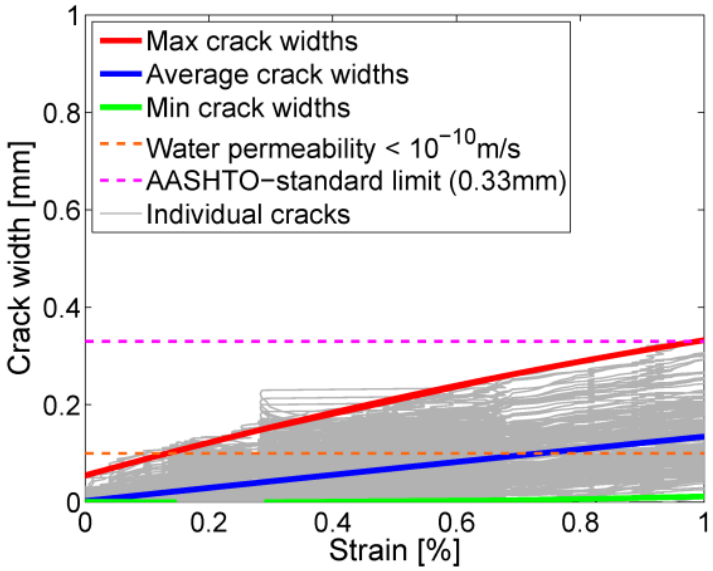

a) LS1

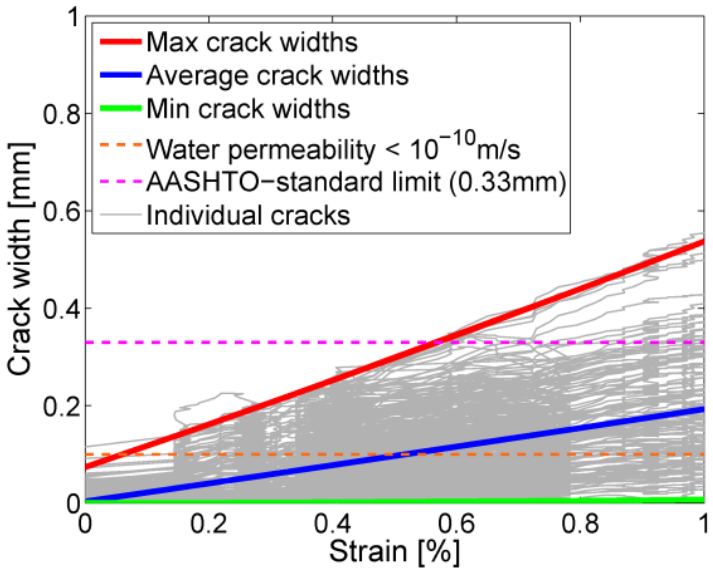

b) LS2

Figure 5-19 Development of crack opening as a function of strain during tensile loading of a): LS1 and b): LS2. The AASHTO crack width limit of 0.33 mm for highway bridges (AASHTO, 2002) is shown for comparison as well as the threshold for water permeability of 10^{-10} m/s (Wang et al., 1997).

In Figure 5-19 and Figure 5-20 a crack width limit of 0.1 mm refers to water permeability similar to that of un-cracked concrete (Tsukamoto, 1990; Wang et al., 1997; Lawler et al., 2002) and a crack width limit of 0.33 mm refers to structural guidelines of AASHTO for highway bridge structures (AASHTO, 2002).

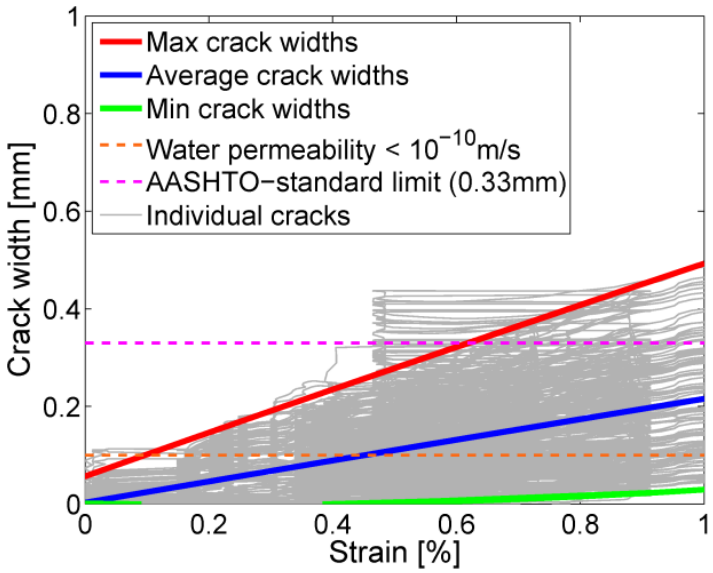

a) LS3

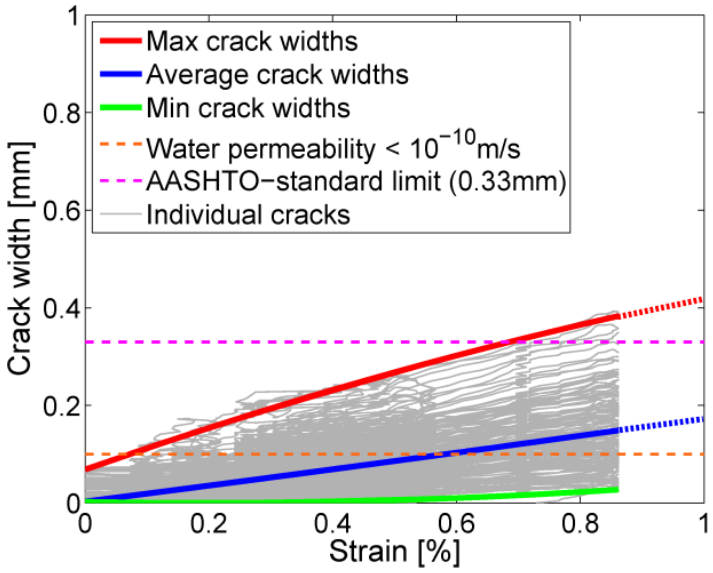

b) LS4

Figure 5-20 Development of crack opening as a function of strain during tensile loading of a): LS3 and b): LS4. The AASHTO crack width limit of 0.33 mm for highway bridges (AASHTO, 2002) is shown for comparison as well as the threshold for water permeability of 10^{-10} m/s (Wang et al., 1997).

Due to the number of load sequences carried out during static loading where the specimens were loaded and unloaded repeatedly, the maximum crack width at early tensile

straining is slightly exaggerated because the cracks are not able to fully close when specimen is unloaded.

For LS1 a total of 207 cracks were measured along the three representative lines (Figure 5-12), 136 cracks in LS2, 117 cracks on LS3 and 158 cracks were measured on LS4. The number of cracks observed over a certain length is directly proportional to the crack spacing as well as crack widths measured. This can be seen by comparing the number of cracks to the measured crack widths shown in Figure 5-19 and Figure 5-20 where the highest number of cracks (LS1) corresponds to the smallest crack widths and the lowest number of cracks (LS2) corresponds to the largest crack widths.

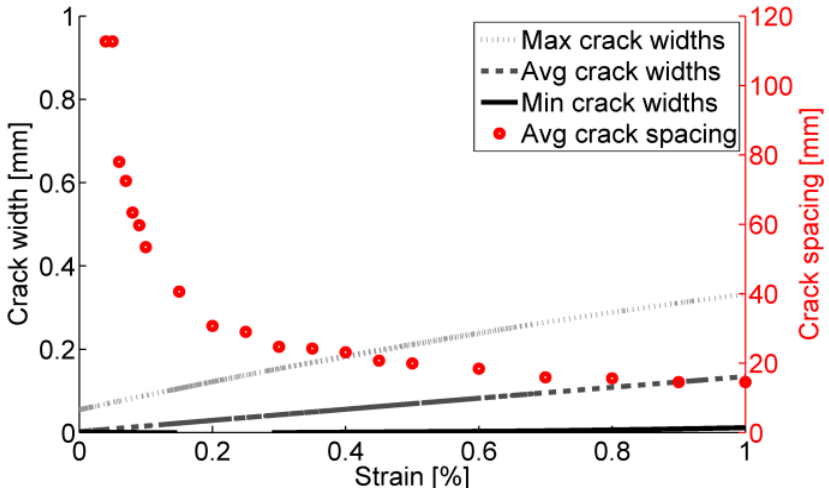

a) LS1

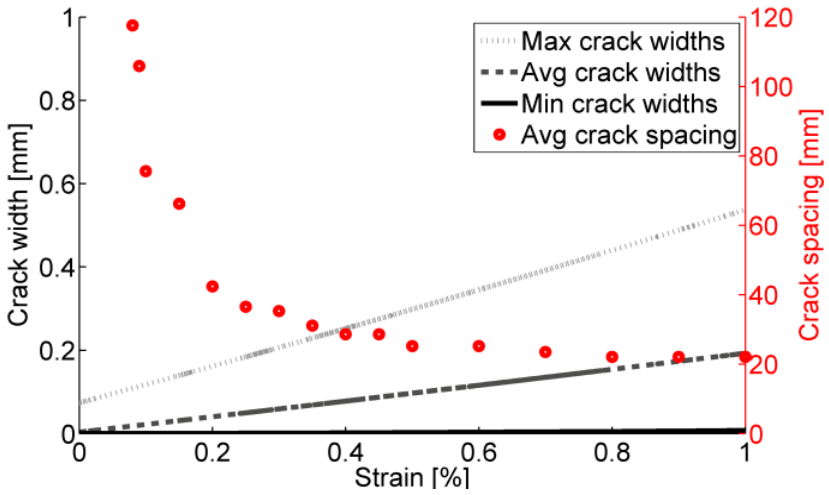

b) LS2

Figure 5-21 Average crack spacing in comparison to maximum, average and minimum crack widths compared with development of crack spacing as a function of tensile strain for a): LS1 and b): LS2.

From the DIC analysis the average crack spacing can be obtained as a function of tensile strain. In Figure 5-21 and Figure 5-22 the average crack spacing is compared to the maximum, average and minimum crack width as a function of tensile strain. At 1.0% strain the average crack spacing is 14 mm in LS1, 22 mm in LS2, 26 mm in LS3 and 19 mm at 0.8% strain in LS4.

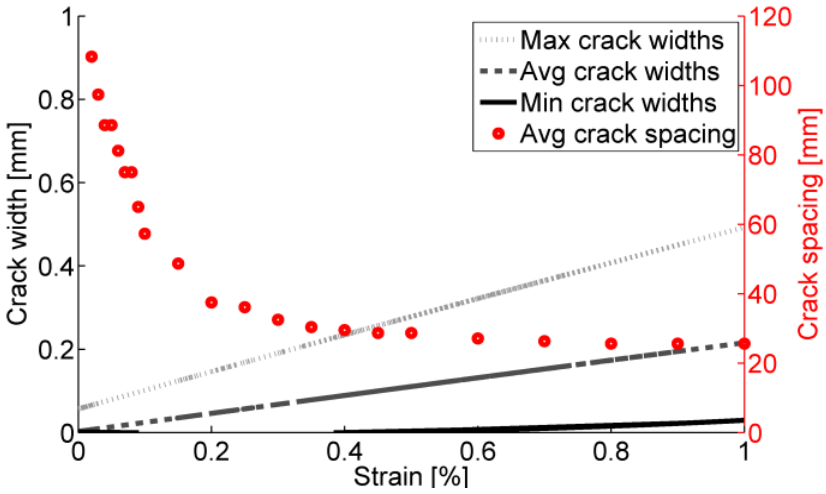

a) LS3

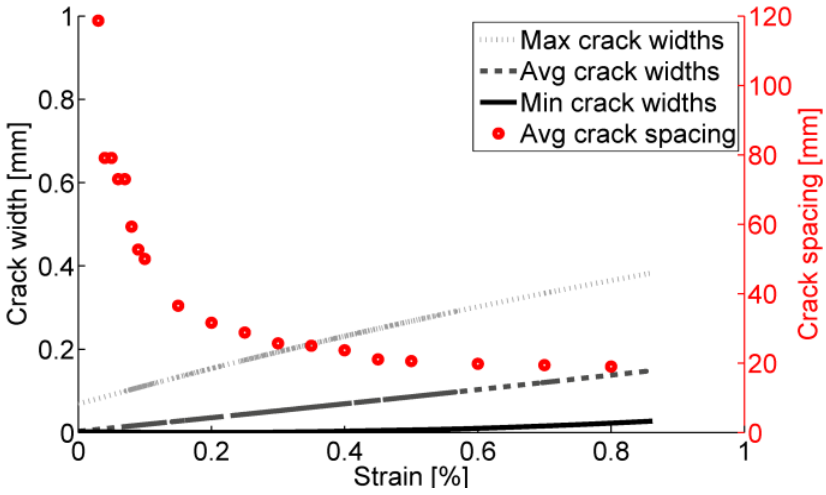

b) LS4

Figure 5-22 Average crack spacing in comparison to maximum, average and minimum crack widths compared with development of crack spacing as a function of tensile strain for a): LS3 and b): LS4.

5.5 Discussion

For the link slab design concept suggested herein the aim of the experimental program is to obtain a high number of cracks evenly distributed and well confined within the

active part of the link slab. Furthermore, a minimum load resistance of link slab it is desired in order minimized the forces exerted into the transition zones. Moreover, to sustain the structural performance of the link slab, a minimum degradation of the rebar-matrix interface is preferred in order to maintain small crack widths.

5.5.1 Composite response

The difference between the composite response and bare reinforcement in tension is generally referred to as tension stiffening as was illustrated in Figure 5-4, i.e. the concretes contribution to the composite response. In this context the increase or decrease in the load carrying capacity of ECC (i.e. the tension stiffening) is an indicator of the residual composite interaction and the integrity of ECC at each strain level, i.e. the degree of debonding and degradation of the rebar – matrix interface is directly proportional to tension stiffening behavior. It is therefore relevant to compare the composite response of the link slabs to that of the bare reinforcement in order to evaluate and predict the long term behavior.

In Figure 5-13 and Figure 5-14 the upper limit of the load-strain envelope of all load sequences demonstrate the overall stiffness of each link slab element during tensile loading. Furthermore, from Figure 5-13 and Figure 5-14 the overall stiffness response of all link slabs during the static load sequences are summarized and compared against the load-strain response of the bare GFRP reinforcement in Figure 5-23.

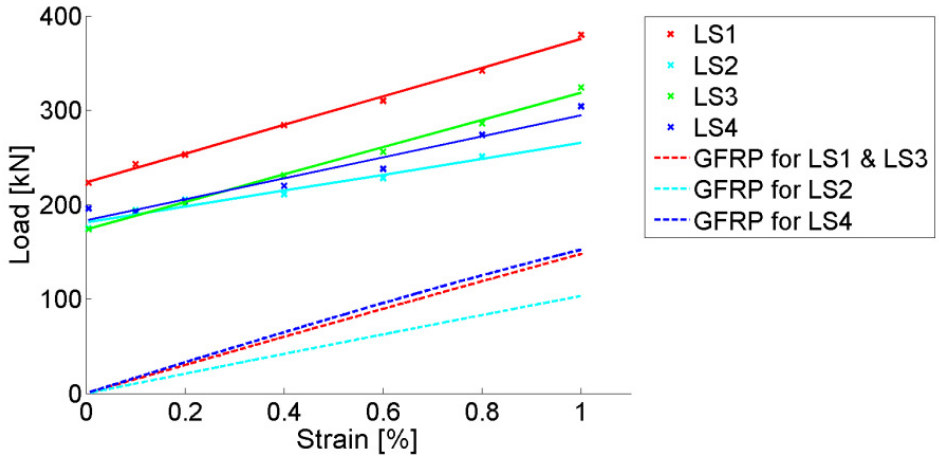

Figure 5-23 Comparison between the composite link slabs stiffens (obtained from load-strain envelope) for all link slab specimens as well as load strain response for the bare GFRP reinforcements.

The residual load carrying contribution of ECC, i.e. the tension stiffening- and strengthening effect (Chapter 4), shown in Figure 5-23 as the difference between link slab response and bare GFRP response, suggests that the interface between the rebar and the surrounding ECC matrix is intact and effectively transferring stresses between matrix and rebar. However, due to the strain compatibility between ECC and the rein-

forcement these stresses are relatively small in comparison to R/C (Fischer and Li 2004; Lárusson and Fischer 2012). This is possible due to the formation of multiple cracks in the matrix as a result of fiber bridging. Consequently the fiber bridging and multiple cracking enable an evenly distributed stress in the reinforcement as opposed to the localized stress concentration generally observed in conventional R/C under tensile loading. This explanation is supported by results found in the investigations in Chapters 3 and 4. These investigations observed that the GFRP reinforced ECC specimens exhibited a good composite interaction due to multiple cracking which resulted in minimum degradation of the rebar-matrix interface.

The response of LS1 in cyclic loading (presented in Figure 5-15) indicates a fully conserved composite behavior of the link slab, i.e. negligible decrease in composite interaction and no localization of cracking in the link slab. Furthermore, no increases in crack widths were observed during cyclic loading of LS1.

During cyclic loading of LS2 (presented in Figure 5-16), a decreased load response was observed, however only a slight increase (3-5%) in crack widths was measured on LS2 throughout the entire cyclic testing.

Cyclic loading of LS3 and LS4 were discontinued shortly after they were initialized when crack localization was observed. Failure of LS3 occurred at the joint between R/C deck structure and link slab due to insufficient anchorage length (150mm) of the link slab reinforcement embedment into the R/C deck (see Figure 5-9 and Figure 5-11b). Failure of LS4 occurred due to fatigue failure of the GFRP (GFRP2) after a crack at the center of the link slab had localized.

5.5.2 Crack development

Crack widths and crack spacing affects the performance of the link slabs in many ways, they indicate the degree of interfacial degradation and composite stiffness through the tension stiffening effect, as well as determining potential ingress pathways for surface water. Utilizing DIC on the link slab surfaced therefore allows us to correlate crack development with structural performance.

Figure 5-18, Figure 5-19 and Figure 5-20 give a clear overview of crack formation and the crack width development in all link slab specimens during tensile loading up to 1.0% strain.

The maximum crack widths in all the link slab specimens where found to be below the AASHTO limit of 0.33 mm at tensile strain levels below 0.55%. However, LS1 exhibited lower maximum crack widths than LS2, LS3 and LS4 with the maximum crack width of 0.33 mm (equal to the AASHTO limit) at the 1.0% target tensile strain (see Figure 5-19a).

The maximum crack widths of LS2 and LS3 at 1.0% tensile strain were found to be 0.55 mm and 0.49 mm respectively (see Figure 5-19b and Figure 5-20a). At a tensile

strain of 0.85% LS4 exhibited maximum crack widths of 0.38 mm, however by extrapolating the results up to 1.0% strain the maximum crack width of 0.43 mm is obtained for LS4 at 1.0% strain.

The crack development (Figure 5-19 and Figure 5-20), as well as the composite tensile response of the link slabs (Figure 5-13 and Figure 5-14) demonstrate similar behavior as the tensile response of GFRP reinforced ECC (GFRP/ECC) prisms presented in previous studies (Lárusson et al., 2009; Lárusson and Fischer, 2011). In those experimental programs the contribution of the ECC is apparent in the tension stiffening process and in particular in the cracked stage, i.e. the combination of the tensile strengthening of ECC and the tension stiffening effect leads to the enhanced composite behavior.

However, maximum crack widths on the link slabs were found to be 0.3-0.6 mm at 1.0% strain, which is notably larger than the 0.15-0.2 mm maximum crack widths observed on the GFRP/ECC prisms at 1.0% tensile strain. This could be attributed to the difference in reinforcement diameter and ratio, cover thickness, size-effect and geometry of the tested specimens.

The governing factors affecting crack width development in reinforced concrete include cover thickness and rebar diameter, where the rebar circumference is one of the key components. However, due to fiber bridging and limited crack widths in ECC, research has shown that the effect of cover thickness in significantly reduced in reinforced ECC members. Consequently, if the reinforcement ratio is kept constant, the reinforcement layout for the link slab can be optimized in terms of crack width limitations by employing more rebars with smaller diameters rather than fewer rebars with larger diameter.

5.5.3 Link slab performance

The reinforcement layout in LS1, with 10 GFRP rebars with 6mm diameter reinforcing the active part of the link slab (Figure 5-8), resulted in the best overall performance, i.e. based on sustained composite load-deformation response (the least interface degradation) and the crack width and crack spacing measurements. Fewer rebars in the active cross section, such as in the reinforcement layout of LS2 (with 7 GFRP rebars) (Figure 5-8), resulted in deterioration of the composite interaction during cyclic loading and produced excessive crack widths when compared to LS1. Despite crack width limitations in ECC, which have been described as a material property (Lepech and Li 2010), the results of LS1 and LS2 indicate that the reinforcement layout significantly affects the crack development of the composite elements.

Although LS3 had the same reinforcement layout as LS1 at the active section of the link slab, both the composite response and the crack width measurements were significantly different. This is most likely due to the difference in material properties of ECC as a result of the casting procedures, i.e. LS3 was cast in place whereas LS1 was

prefabricated before installation. The difference is most evident in the dissimilarity of the first crack composite stresses of LS1 (3.1 MPa) and LS3 (2.3 MPa) as well as the subsequent tensile contribution of ECC (tension stiffening effect) (see Figure 5-13 and Figure 5-14). It is noted the failure mode of LS3, where the rebars ends were embedded into the R/C deck could have been avoided with proper anchorage length.

As a result of the reinforcement type utilized in the reinforcement layout of LS4 (10 GFRP2 rebars) a gradual deterioration of the composite response was observed with increased tensile straining.

Based on the decreased stiffness response of the bare GFRP2 reinforcement (see Figure 5-6), the deterioration of the composite response and the failure mode of LS4 where the GFRP2 rebars ruptured, the use of GFRP2 reinforcement type is not recommended in the link slab design.

5.5.4 Link slab design concept

When rehabilitating deteriorated expansion joints between simply supported bridge spans, the design approaches are usually aimed at maintaining the simply supported design functionality of the structure. One favorable approach, as mentioned before, has been to utilize a link slab, which is appropriate for both rehabilitation and new structures. However, currently implemented link slabs, usually designed fully or partially according to design recommendations presented by Caner and Zia (1998), introduce negative moments into the girder ends due to the inherent stiffness of the link slab. This negative moment can adversely affect the performance of the structure as well as introduce undesirable resulting forces. Furthermore, although the link slab concept is a relatively simple approach, it still requires a detailed redesign of the R/C deck structure and even girder ends.

To address some of these issues, one of the primary objectives in the presented research was to design a relatively thin durable prefabricated link slab element with a low stiffness to allow axial deformations in the link slab due to temperature and shrinkage as well as girder rotations at the supports (see Figure 5-24).

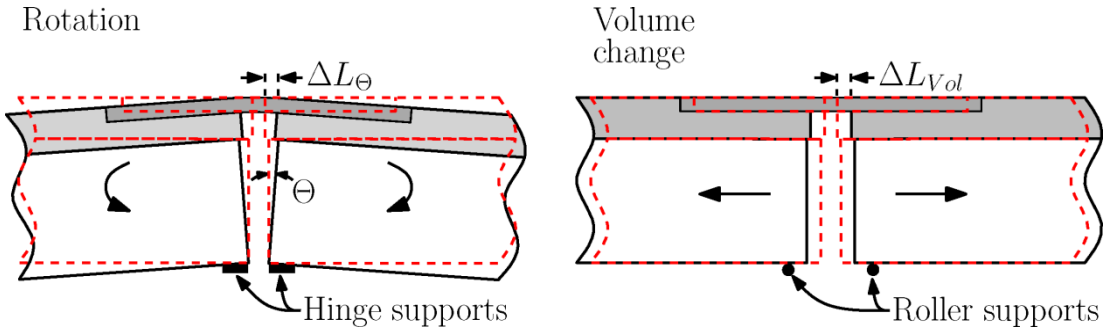

Figure 5-24 Schematic of the expected deformations in the link slab.

The analysis and measurements herein assume the link slab to be primarily subjected tensile deformations due to the slender design of the link slab with respect to the overall structural height of the bridge structure (including girders and R/C deck). While this assumption may not be entirely correct, it is assumed to be sufficient to establish a model for the design of the link slab suggested in this study.

5.5.5 Link slab design example

A simple design example is presented herein to emphasize the expected deformations in the link slab and to illustrate the ability of the suggested link slab design to facilitate them.

The maximum rotation angle (Figure 5-24) of the end girders of a simply supported bridge span can be derived independently of the span length L by assuming the maximum allowable deflection of the span. Utilizing the maximum allowable deflection according to AASTHO of L/800, the maximum rotation can be derived as:

$$\Theta_{max} = \frac{u_{max}}{u_{defl.}}\ \Theta_{defl.} = \frac{\left(\frac{L_{sp}}{800}\right)}{\left(\frac{5}{384}\ qL_{sp}^4\right)}\left(\frac{1}{24}qL_{sp}^3\right) = \frac{1}{250} \qquad (5.1)$$
$$= 0.004\ rad$$

Where Θ is the rotation angle at the supports, u is the mid-span deflection, L_{sp} is the span length and EI is the flexural stiffness of the bridge section. It should be noted that Caner and Zia (1998) derived and used significantly lower end rotation values in their design examples, i.e. 0.0015-0.0016 rad. Based on the rotation angle derived herein, the corresponding strain $\Delta\varepsilon_\Theta$ deformation in the link slab can be obtained as a function of the structural height of the bridge section h:

$$\Delta\varepsilon_\Theta = \frac{2 \cdot (\Theta_{max} \cdot h)}{L_{ls}} = \frac{0.008 \cdot h}{L_{ls}} \qquad (5.2)$$

Where L_{ls} is the active length of the link slab. As an example: with a structural height of 550 mm and an active link slab length of 1000 mm (as in the experimental program), $\Delta\varepsilon_\Theta$ is found to be 0.44%. Here, hinged supports are assumed, however, it should be noted that significantly smaller rotation induced strains are expected if roller supports are assumed instead of hinge supports.

Furthermore, the axial deformations in the link slab $\Delta\varepsilon_T$ caused by thermal expansion ΔL_{Vol} of the bridge sections can be derived. Assuming that the active link slab length L_{ls} is 5% of each span length L_{sp} and assuming equal span lengths, $\Delta\varepsilon_T$ can be formulated as follows:

$$\Delta\varepsilon_T = \frac{\alpha_T \cdot \Delta T \cdot L_{sp}}{L_{ls}} = \frac{1.2 \cdot 10^{-5} \cdot 50° \cdot L_{sp}}{2 \cdot \left(0.05 \cdot L_{sp}\right)} = 0.6\% \qquad (5.3)$$

Where α_T is the expansion coefficient for reinforced concrete and ΔT (assumed 50° (Li and Lepech, 2005)) is the annual temperature variance. Due to the proposed pre-fabrication procedure, deformations due to shrinkage are not considered. The sum of the rotation induced strain and the volume change induced strain yields 1.04% total strain which is approximately equal to the target tensile strain of 1.0% in the experimental program presented herein.

Although the two strain values expected in the link slab ($\Delta\varepsilon_\Theta$ and $\Delta\varepsilon_T$) are derived based on two types of support configurations (to maximize the displacements in each one), combining the two gives a conservative estimate.

5.5.6 Effectiveness of the active part of the link slab

One of the design criteria for the link slab concept was to concentrate the axial deformations induced by the adjacent spans to the active part of the link slab. This was achieved by adding secondary reinforcement sections in the transfer zone at both ends of the link slab specimens (see Figure 5-8), and by providing a de-bonding layer between the link slab and the R/C deck structure. The additional reinforcement placed in the passive transfer zone between link slab and adjacent span ensure the force transfer at this interface while the deformations are limited to the active part of the link slab.

To evaluate how effective the link slab design is in confining the longitudinal deformations to the middle section, the deformations over the 1 m long active middle section are compared to the total elongations of the whole 2 m link slab element in Figure 5-25 for LS1. Results show a less than 1.0 mm deformation difference (at a 10 mm overall deformation) between the 1 m mid section and the 2 m total link slab length, indicating that nearly all deformations occur within the active part of the link slab.

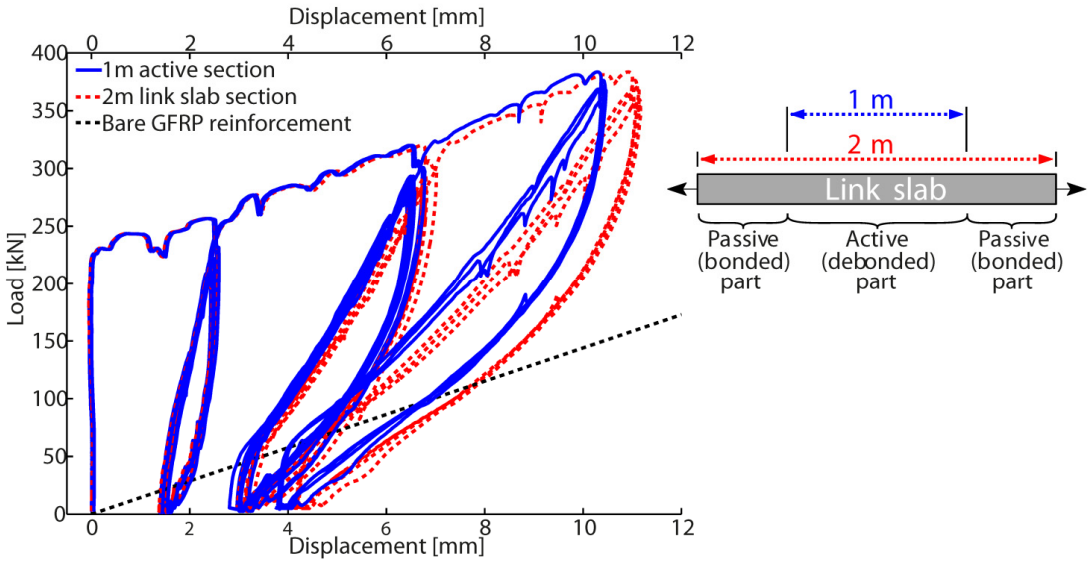

Figure 5-25 Applied load versus tensile strain of the active part of LS1 and total longitudinal displacement measured in the link slab.

5.6 Conclusions

The investigation presented herein demonstrated the application of a thin prefabricated Glass Fiber Reinforced Polymer (GFRP) reinforced Engineered Cementitious Composite (ECC) link slab subjected to monotonic and cyclic tensile deformations. This concept is suggested as a replacement for mechanical expansion joints to alleviate some of the inherent disadvantages of mechanical systems which are expensive and difficult to maintain.

By combining the ductile behavior of ECC, with multiple cracking and limited crack widths, and the low stiffness of GFRP the composite interaction of the two materials results in compatible deformations, i.e. strain compatibility. This compatibility attribute of the composite increases structural integrity by decreasing the interfacial degradation between the reinforcement and surrounding matrix. With the GFRP reinforced ECC composite in a slender prefabricated link slab design, the objectives of the suggested design approach was to distribute the expected deformations evenly in the link slab while maintaining low crack widths and structural integrity of the composite.

The innovative features of the link slab presented herein include a relatively thin precast element with low stiffness composed of ductile ECC and corrosion resistant GFRP. The suggested link slab features a de-bonded active section and the passive load transfer zones intended to concentrate or “absorb” induced deformations in the active part of the link slab.

The crack formation and development observed on the link slab was shown to exhibit a uniform deformation with crack widths below 0.22 mm at 0.5% strain and equal to

0.33 mm at 1.0% tensile strain during both monotonic and cyclic loading. As a consequence, the degradation of interfacial bond between the rebar and the matrix is significantly decreased as a result of the strain compatibility obtained in the composite.

The strain hardening attribute of ECC with limited crack widths and improved interfacial bonding between rebar and surrounding matrix resulted in increased durability of the link slab in terms of ECCs ability to maintain structural integrity of the matrix. This attribute of ECC, together with the low stiffness response of GFRP, is essential in order to obtain and maintain strain compatibility at relatively high strain levels.

Due to the noncorrosive nature of GFRP reinforcement combined with the limited crack widths of ECC results in improved corrosion resistance of the suggested link slab in field applications. Furthermore, the use of GFRP reinforcement instead of conventional steel reinforcement provides the link slab design with minimum reaction forces due to the lower stiffness of the GFRP reinforcement compared to that of steel reinforcement.

The load transfer zones (where additional reinforcement was provided) were found to effectively concentrate the imposed deformations of the adjacent bridge span sections into the active section of the link slab. The deformations were subsequently distributed evenly throughout active middle part while the passive parts did not deform.

The thin, prefabricated GFRP reinforced ECC link slab concept has shown promising results in terms of load response and crack development. The benefits of utilizing prefabrication production can ensure high production quality and alleviates shrinkage induced problems as well as offer a relatively fast and simple installation.

Bibliography

Aktan, H., Koyuncu,Y., Rutyna, J., Ahlborn, T.M. & Kasper, J.M., 2002. Causes and cures for prestressed concrete I-beam deterioration. Research report RC-1412. Michigan Department of Transportation. Lansing. Michigan.

Alampalli, S. & Yannotti, A. P., 1998. In-service performance of integral bridges and jointless decks Transportation Research Record, pp. 1-7.

Burke, M. J., 2009, Integral and Semi-Integral Bridges, John Wiley & Sons

Caner, A. & Zia, P. 1998, Behavior and Design of Link Slab for Jointless Bridge Decks. Precast Concrete Institute Journal, 43, pp. 68-80.

Fischer, G. & Li, V. C., 2002, Influence of matrix ductility on tension-stiffening behavior of steel reinforced engineered cementitious composites (ECC), ACI Structural Journal, American Concrete Institute, 99, 104-111

Ho,E, Lukashenko,J. 2011. Link Slab Deck Joints. In: TAC Conference & Exhibition -Trancportaion successes: Lets build on them.; Transportation Assosiation of Canada. Edmonton. Canada.

Kim, Y. Y. & Li, V. C., 2004, Fatigue Response of Bridge Deck Link Slabs Designed with Ductile Engineered Cementitious Composite (ECC), Proceedings of International Conference on Concrete under Severe Conditions, Seoul, Korea, pp. 832-841.

Kim, Y. Y., Fischer, G. & Li, V. C., 2004, Performance of bridge deck link slabs designed with ductile engineered cementitious composite ACI Structural Journal, American Concrete Institute101, 792-801

Lárusson, L. H. & Fischer, G., 2012, Bond slip and crack development in FRC and regular concrete specimens longitudinally reinforced with FRP or steel under tension loading, Bond In Concrete, Brescia, Italy

Lárusson, L. H., Fischer, G. & Jönsson, J., 2009, Mechanical interaction of Engineered Cementitious Composite (ECC) reinforced with Fiber Reinforced Polymer (FRP) rebar in tensile loading. part of: Advances in cement based materials, pp. 83-90: 313

Lárusson, L. H., Fischer, G. & Jönsson, J., 2011, Mechanical interaction between concrete and structural reinforcement in the tension stiffening process, HPFRCC 6-High Performance Fiber Reinforced Cement Composites, Ann Arbor, USA

Lawler, J. S., Zampini, D. & Shah, S. P., 2002. Permeability of cracked hybrid fiber-reinforced mortar under load. ACI Materials J., 99 (4), pp. 379-385.

Lepech, M. D. & Li, V.C., 2005. Design and Field Demonstration of ECC Link Slabs for Jointless Bridge Decks, Presentation at the 3rd International Conference on Construction Materials (CONMAT): Performance, Innovations and Structural Implications, Vancouver, British Columbia

Lepech, M. D. & Li, V. C. Design and Field Demonstration of ECC Link Slabs for Jointless Bridge Decks", to appear in Proceedings of CONMAT-5, 2005, 22-24

Lepech, M. D. & Li, V. C., 2006, Long Term Durability Performance of Engineered Cementitious Composites, RESTORATION OF BUILDINGS AND MONUMENTS, 12, 119-132

Lepech, M. D. & Li, V. C., 2009, Application of ECC for bridge deck link slabs, Materials and Structures, 42, 1185-1195

Li, V. C., 1993. From micromechanics to structural engineering -the design of cementitious composites for civil engineering applications, Structural Engineering/Earthquake Engineering, 10, pp. 1-34.

Li, V.C., & Lepech, M. D., 2004. Crack Resistant Concrete Material for Transportation Construction, Transportation Research Board 83rd Annual Meeting Compendium of Papers, Paper No. 04-4680. Washington, D.C.

Li, V.C., 1998. Engineered Cementitious Composites – Tailored Composites Through Micromechanical Modeling, in Fiber Reinforced Concrete: Present and the Future. Eds. N. Banthia et al, CSCE, Montreal, pp. 64-97.

Li, V.C., and M. Lepech, 2005. Demonstration of Durable Link Slabs for Jointless Bridge Decks Based on Strain-Hardening Cementitious Composites – Michigan Department of Transportation research report RC- 1471Field, Michigan DOT, Lansing

Li, V.C., T. Horikoshi, A. Ogawa, S. Torigoe & T. Saito, Micromechanics-based Durability Study of Polyvinyl Alcohol-Engineered Cementitious Composite (PVA-ECC) , ACI Materials J., 101 (3), pp. 242-248, (2004)

Mehta, P. K. & Monteiro, P. J. M., 2006, Concrete / microstructure, properties and materials McGraw-Hill, p. 659.

Naaman, A. & Reinhardt, H., 2006. Proposed classification of HPFRC composites based on their tensile response, Materials and Structures, Volume 39, Number 5, pp. 547-555.

Qian, S., Lepech, M. D., Kim, Y. Y. & Li, V. C., 2009. Introduction of transition zone design for bridge deck link slabs using ductile concrete, ACI Structural Journal, American Concrete Institute, 106, pp. 96-105.

RILEM-TC-208-HFC, SC3, 2011. Strain Hardening Cement Composites (SHCC): Structural Design and Performance: State-of-the-Art Report of the RILEM Technical Committee (TC) 208-HFC, SC3, Ed. Li, V. C.

Tsukamoto, M., 1990. Tightness of fibre concrete," Darmstadt Concrete: Annual Journal on Concrete and Concrete Structures, 5 () 215–225.

Wang, K., Jansen D. C. & Shah, S. P., 1997. Permeability study of cracked concrete, Cement and Concrete Research, Vol. 27, No. 3, pp. 381-393.

Webb, Z. L., 2005. Manual: Snow and Ice Control Operations Manual. Texas Department of Transportation (TxDOT). Obtained 25.09.12, http://onlinemanuals.txdot.gov/txdotmanuals/sic/manual_notice.htm

Wolde-Tinsae, A. M., & Klinger J. E., 1987. Integral Bridge Design and Construction. Report FHWA/MD-87/04. Maryland Department of Transportation, Jan. 1987.

Yamaguchi, T., Fujishiro, M., Suda, K. & Nagata, Y., 2008. Jointless prestressed concrete viaduct using Engineered Cementitious composite (ECC), Proceedings of the International fib Symposium, Tailor made concrete structures: New solutions for our society, Amsterdam, Holland

AASHTO, "Standard Specifications for Highway Bridges," 17th Edition, American Association of State Highway and Transportation Officials, Washington D.C., 2002, 1052 pp.

Chapter 6

Other applications

To illustrate the versatility of SHCC in structural applications, an experimental program concerning prefabricated floor panels, composed of a relatively thin ECC slabs connected to steel substructures is presented. The aim of this research program was to design and analyze structural performance of light weight prefabricated floor panels. The study focuses on the design, manufacturing, structural improvements and behavior of the floor systems at serviceability- and ultimate limit states loading.

6.1 Introduction

The unique tension stiffening ability of ECC allows structural elements to be designed with minimum reinforcement, and potentially even omitting reinforcement entirely. As a result, structural elements can be designed with much thinner cross sections than what is typically achieved with reinforced conventional concrete. Based on this concept, the presented study examines the use of ECC in a relatively thin, unreinforced slab connected to a steel substructure. Extending on previous research (Fischer, 2007) were thin-walled steel joists were integrally cast into a thin ECC slab in so-called integrally cast panels (ICP), the focus of the study herein was to further examine structural details of the ICP concept along with developing and testing a modular structure consisting of an ECC slab and post-mounted steel truss substructure.

The fine grain composition and lack of coarse aggregates in ECC causes shrinkage deformations to be more extensive in comparison to conventional concrete. Drying shrinkage of ECC has been found in related studies to reach 0.10-0.15% strain at 40-70% Relative Humidity (RH), which is approximately 80% higher than drying shrinkage deformations of conventional concrete (Wang and Li, 2005).

In an attempt to resolve some of the problems associated with the expected shrinkage deformation the idea behind the modular panel (MP) is to separate the ECC slab from the substructure. The MP concept features a novel design approach were individual anchor points are integrally cast with the ECC slab, thus allowing the slab to shrink and deform independent of the substructure. By adapting this approach prior to as-

sembly of the composite floor panel, shrinkage induced stresses and cracking and undesirable deflections are avoided in the deck panel.

The modular construction concept furthermore offers flexibility in the assembly process, the ability to adapt to various load and boundary requirements, and efficient utilization of material properties that result in a light weight prefabricated structural element. In the presented experimental program, full-scale experiments were carried out to verify the structural behavior of ICP's and the MP's with various substructure configurations as well as a comparison to analytical and numerical results. Examples of the both the ICP and the MP concepts are shown in Figure 6-1.

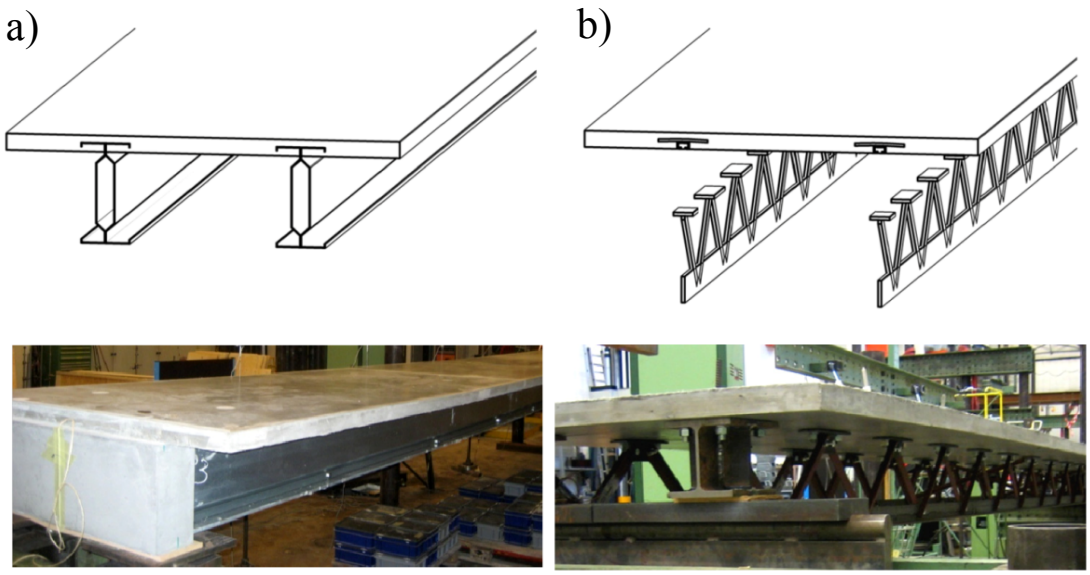

Figure 6-1 Examples of a) Integrally cast panel (ICP) and b) Modular panel (MP).

6.1.1 Prefabricated or semi-prefabricated floor systems

Prefabricated or semi-prefabricated structural concrete elements such as floor- or roof panel are widely used in the construction industry today. These systems, in contrast to fully cast-in-place floors slabs, typically offer a faster construction time, lower self weight and cost. The most frequently used prefabricated concrete floor panels in the building industry today are hollow core decks (HCD) and double-T panels which are suitable for most building types (FIP, 2008; Martin and Perry, 2004; Ching, 1995). A diverse selection of fully precast structural floor systems can be found in the literature, such as Timber-Concrete composites (Kuhlmann and Schanzlig, 2008) and Hambro® composite concrete-steel floors systems (Hambro, 2009). Other systems include semi precast elements such as pan decking, reinforced concrete filigrees, Bubbledeck® or cobiax® floor deck systems (Schnellenbach-Held and Pfeffer, 2002; Abramski et al., 2010) all utilize a thin prefabricated element as formwork prior to casting of a concrete overlay at the construction site. More details and comparison on

these structural floor systems can be found in the appended paper, Lárusson et al. (2013).

6.2 Concept and design

The main objective of the proposed ICP system, initially introduced by Fischer (2007), and the MP approach presented herein, was to implement ECC as a relatively thin structural deck layer in lightweight, easy to install alternative to traditional and heavier prefabricated floor systems. The main design criteria for both the ICP and MP concepts were to accommodate a necessary load capacity, deflection limits and dynamic response according to codes of practice. In continuation of the initial investigation on ICPs, structural details of the systems support footings and cross bracing of the joists were addressed specifically. The modular assembly of the ECC slab and the steel sub-structure in the MP approach was furthermore investigated with a variation of different substructure geometries and designs.

The aim of the modular concept applied in this study is to separate the casting of the ECC deck slab and the attachment of the substructure by embedding anchors into the ECC slab, thus avoiding unfavorable deformations and cracking due to shrinkage typically encountered in the integrally cast floor panels (Fischer, 2007). By embedding individual attachment devices that later can be connected to a steel truss substructure, the modular system offers increased flexibility in assembly and transportation of the deck system. Moreover, the concept allows for high versatility in the substructure design and the ability to adapt to different required loading capacities and deflection limits as well as architectural requirements.

Numerical models were used to aid in the design and dimensioning of the steel trusses in the MP's. The models were furthermore utilized to obtain predictions of the structural behavior at serviceability limit state (SLS) as well as predict load capacities at ultimate limit states (ULS).

6.3 Analytical calculations of structural properties

To obtain analytical expressions for the structural response of the proposed ICP and MP deck sections, a few assumptions need to be made: a linear elastic strain distribution through the depth of the sections is presumed, and plane sections remain plane after deformations (see Figure 6-2). Furthermore, assuming that the deck panels are subjected to a uniformly distributed load, the bending stresses in the cross section can be determined by employing the equivalent stiffness of cross sections. From the geometry and the material properties the equivalent stiffness ($E \cdot I_{Eq}$) can be determined, were E is the elastic modulus and I_{Eq} is the equivalent moment of inertia of the cross section.

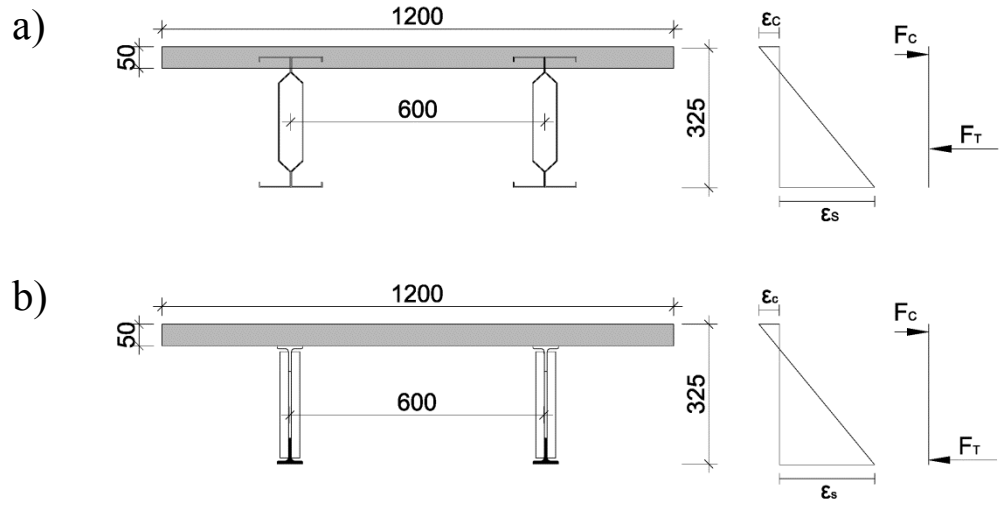

Figure 6-2 Section view and assumed stress and force distribution of: a) the integrally cast panel (ICP), b) the modular deck panel (MP). Dimensions are given in mm.

Using the equivalent stiffness of the cross section and assuming a simply supported beam with a uniformly distributed load, q, the maximum deflection, v_{Max}, of panels can be now be estimated as follows:

$$v_{Max} = \frac{-q}{24EI_{Eq}}\left(\frac{L^3}{2} - \frac{9L^4}{16}\right) \tag{6.1}$$

Where q is the uniformly distributed line load and L is the span length of the deck element.

Based on two failure modes, i.e. the compression capacity of ECC is reached and yielding of the steel substructure, the resisting bending moment capacity of each deck section can be estimated.

From the equation of motion, the natural frequency (f) of the floor panels with a constant stiffness ($E{\cdot}I_{Eq}$) and mass (m) is determined as:

$$f = \frac{n^2\pi}{2L^2}\sqrt{\frac{EI_{Eq}}{m}} \qquad n = 1,2,3,\ldots \tag{6.2}$$

To evaluate the damping ratio (ζ) of the structure, low damping is assumed, i.e. $\sqrt{1-\zeta^2} \approx 1$ and the damping ratio can be written as:

$$\zeta \approx \frac{ln\left(\frac{u(t)}{u(t+T)}\right)}{2\pi} \tag{6.3}$$

where $u(t)$ is the peak amplitude at time t and T is the time of one period (Chopra, 2007).

6.4 Experimental program

In the experimental program the structural response of two integrally cast panels, i.e. ICP1 and ICP2, and four variations of modular panels, i.e. MP1 – MP4, were experimentally evaluated at SLS and at ULS.

6.4.1 Casting

Four ECC slabs were cast in total, two ICPs, and two slabs were cast with embedded anchor points (MP's). Two slabs were cast each time using the mix proportion for ECC given in Table 2-1. For each of the two casts, 1.5 m^3 of ECC were produced and mixed in a 3.0 m^3 force mixer at a local concrete plant in an attempt to utilized large scale industrial facility without any modifications. The ECC mix was furthermore transported from the local concrete plant in a conventional concrete truck with a rotating drum.

6.4.2 Specimen configuration

The design of the ICP consists of four thin walled cold – formed steel joists, which constituted the panels substructure, were positioned in two pairs, 600 mm apart, along the bottom of a ECC slab. The steel joists are 300 mm high, 70 mm wide, thickness of 2.66 mm, and yield strength of 350 MPa. The joists are embedded 25 mm into the 50 mm thick ECC deck slab resulting in an overall structural height of 325 mm (see Figure 6-2a). To ensure sufficient shear strength in the connection between the steel joists and the ECC slab, cut-outs in the steel profiles were made in the top part along the length of the profiles that connects to the slab.

The cast-in anchors used in the MP design were positioned in two rows side along the length of the bottom side of the ECC slab (see Figure 6-3). Due to the small thickness of the ECC slab (t=50 mm), no suitable commercially produced cast-in place attachments were available and had to be custom fabricated to fit within the shallow depth of the ECC slab (see Figure 6-4).

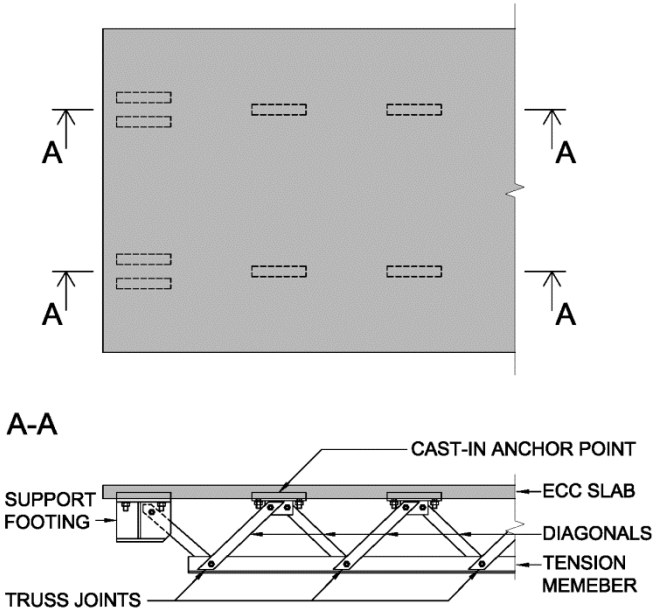

Figure 6-3 a) Plan over-view of the modular deck, b) longitudinal cross section of truss structure connected to ECC deck panel

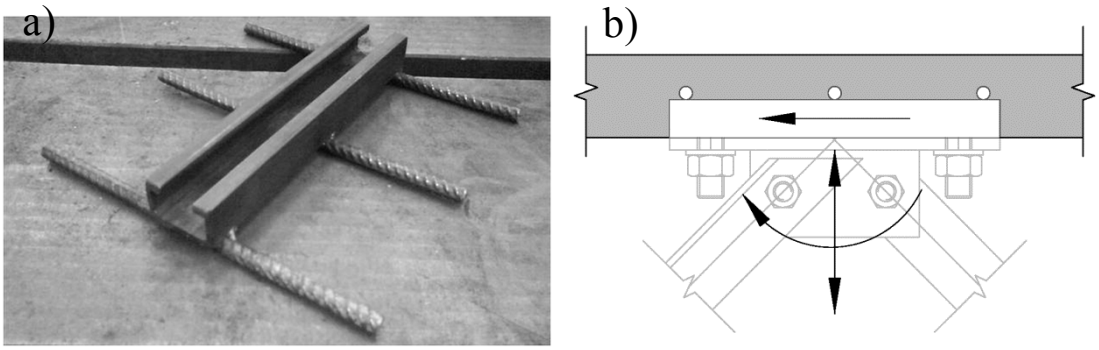

Figure 6-4 a) Cast-in anchor. b) Resultant forces expected in cast-in anchor, forces shown in vertical and longitudinal direction.

Four variations of the steel truss configurations for the MP concept were tested (MP1-MP4). In MP1, MP2 and MP3 the same ECC slab was used and re-used, while a second ECC slab (identical to the first slab) was used in MP4. The truss structures in MP1, MP2 and MP3 all had a S235 steel grade and were all bolted together.

The substructure design of MP4 was based on the experience from testing of specimens MP1, MP2 and MP3 at the SLS and USL. The truss structure of MP4 was all welded together using steel grade S350. Consequently the MP4 was designed and built to have a moment resistance of 260 kNm, equivalent to that of a hollow core deck with the same span and similar structural height. Detailed description of each truss design is found in the appended paper: Lárusson et al. (2013).

6.4.3 Test configuration and sequence

The overall dimensions of all deck panels were 1.2 m in width, an ECC slab thickness of 50 mm and an overall built height of 325 mm. the substructures were aligned in two rows, 0.6 m apart, along the length of the panels. The total length of the panels was 8.2 m, spanning 8.0 m from supported to support.

At SLS loading a uniformly distributed line load was applied to the panels over the 8.0 m span, up to an equivalent area load of 4.08 kN/m^2. The distributed loading was applied in four steps, at increments of 1.02 kN/m^2 per step. The loads were applied in a line-load configuration directly above the substructures as the objective of these tests was to examine the behavior of the deck element in its longitudinal direction. At each load increment (0-4.08 kN/m^2), deflections and dynamic response, i.e. the natural frequency and the damping ratio, of the panels were measured (see Figure 6-5a).

At ULS loading the panels were subjected to a four point bending configuration when assessing the structural response of the deck panels. The load configuration consisted of two point load couples (or transverse line loads) positioned on the deck at 2.0 m (1/4 L) and 6.0 m (3/4 L) relative to the 8 m span to induce a bending moment (see Figure 6-5b).

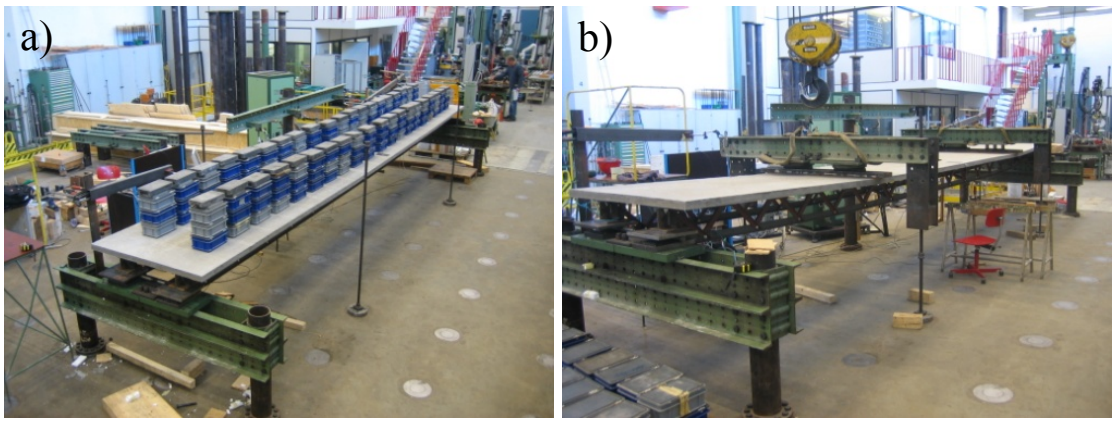

Figure 6-5 Overview of test setups: a) at serviceability limit state (SLS), and b) at ultimate limit state (ULS) loading

6.4.4 Material properties

The evolution of strength and elastic modulus of the ECC was followed closely throughout the experimental program. The compressive strength, f_{ck}, of the ECC on the day of testing was 60 MPa and the elastic modulus, E_{cm}, was found to be 18 GPa. In addition, the drying shrinkage of the ECC was measured to be approximately 0.12% after 30 days at relative humidity (RH) approximately 70% (Figure 6-6). This is in good agreement with shrinkage measurements presented by Wang and Li (2005),

which showed drying shrinkage deformations of ECC to be 0.12% at approximately 60% RH.

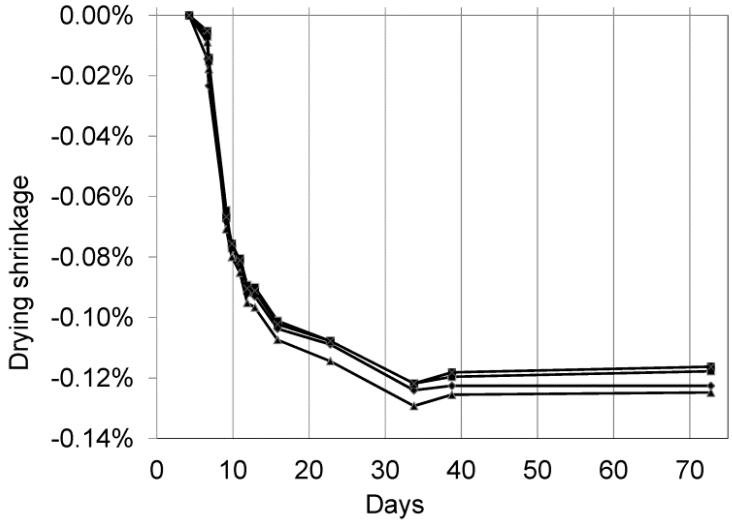

Figure 6-6 Drying shrinkage measurements of ECC.

6.5 Experimental observations

6.5.1 Testing at serviceability limit state (SLS)

Each panel specimen was subjected to a number of loading schemes to evaluate their structural behavior at the serviceability state, i.e. deflection, internal force distribution and dynamic response.

In Figure 6-7 the load versus mid span deflection response of all specimens during SLS loading is shown, for comparison, a load deflection response of a hollow core deck with similar structural height is also shown. It should be noted the due to virtually identical test results for ICP1 and ICP2 during SLS testing, results are shown for both specimens collectively as ICP.

Selected truss members of the MP substructures were fitted with strain gauges in order to monitor the development of strain during SLS loading. Based on the measured strain, the consequent stresses in elements of the steel substructure were obtained during testing. The stress and equivalent force distribution in truss structures MP1, MP2 and MP3 during SLS loading was in good agreement with the expected distribution found analytically and numerically.

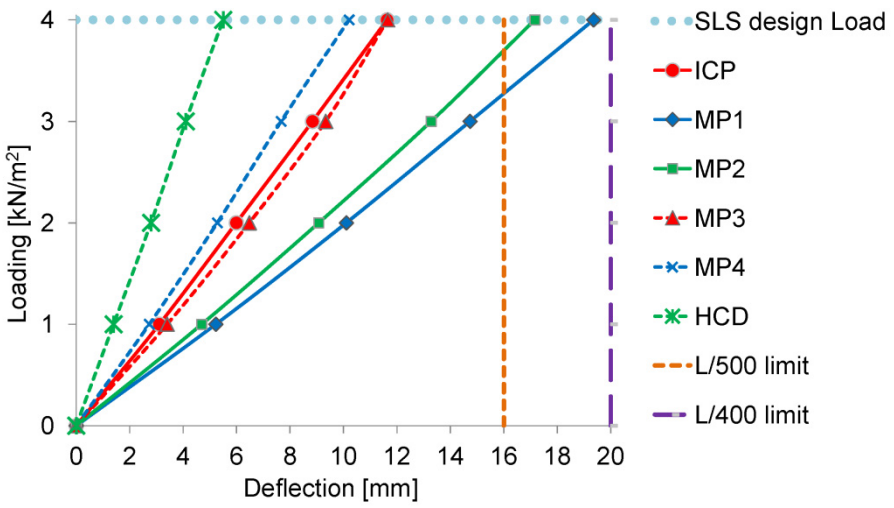

Figure 6-7 Comparison of mid-span deflection of specimen MP1, MP2, MP3, MP4, ICP and HCD as a function of the applied load.

The dynamic response of the structures, i.e. the natural frequencies and damping ratios, were assessed by utilizing an accelerometers positioned at the mid span of the deck panel. The natural frequencies and damping ratios of the deck panels were measured during SLS loading by inducing a vibration in the decks and measuring its decay at each load increment (Figure 6-8).

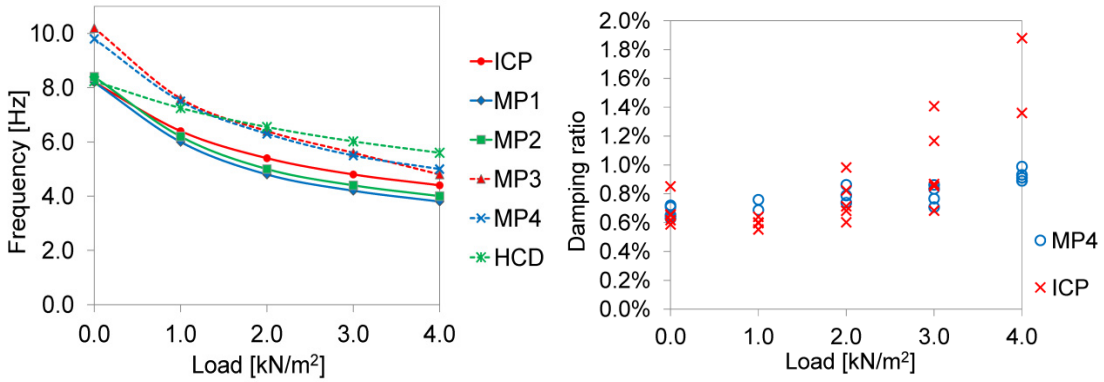

a) *b)*

Figure 6-8 a) The measured natural frequency as a function of applied service load, and b) Measured damping ratios for specimens MP4 and ICP as a function of applied service load.

From Figure 6-8a the increase in the natural frequency between the different specimens is directly related to the increase in stiffness of the composite panels and inversely related to its mass and applied load as equation 6.2 indicates.

During the SLS testing, slip in the bolted connections of MP1, MP2 and MP3, was observed as acoustic events. As a result, the damping ratios measurements for the bolted elements were disregarded due to the unknown effect of slip.

The damping ratio results for ICP and MP4 are shown in Figure 6-8b. The damping ratio appears to be dependent on the change in mass which increases as more loading is applied. The increase in damping at increasing loads indicates more damping mechanisms are activated in the specimens.

6.5.2 Testing at ultimate limit state (ULS)

The load resistance and deflections of the deck panels were monitored during ULS loading. In addition, the tension member and selected diagonals of the MP's substructure, which had been fitted with strain gauges, monitored the strains and equivalent stresses. The total load applied versus mid-span deflection for all specimens are shown in Figure 6-9. All specimens were loaded up to failure or until excessive deflection occurred.

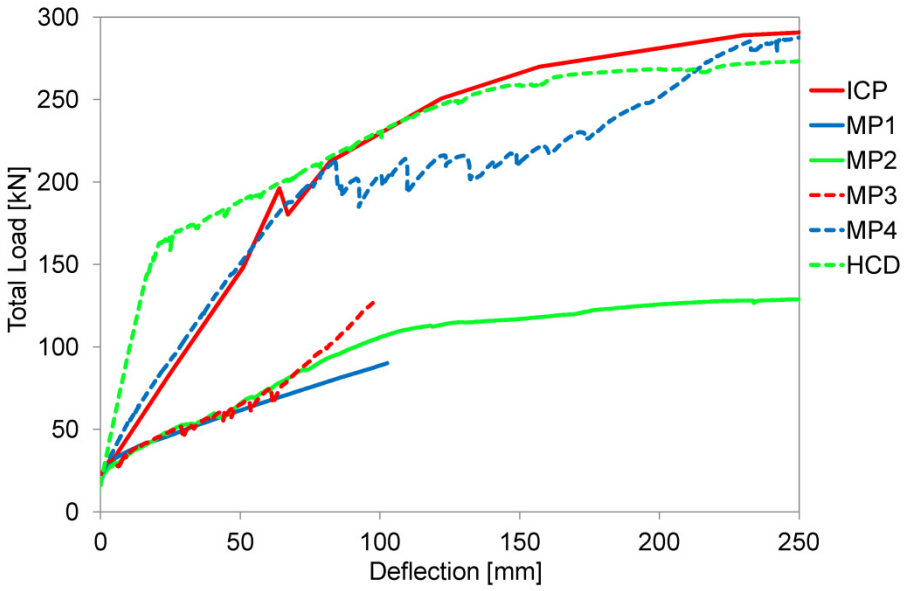

Figure 6-9 Total load applied versus mid-span deflections for specimens MP1, MP2, MP3, MP4, ICP and a hollow core deck panel (HCD).

Both the ICP specimens (ICP1 and ICP2) exhibited almost identical load-deflection response during ULS loading and are consequently collectively referred to as ICP in Figure 6-9. Specimen ICP1 ultimately failed when one of the thin walled steel joists fractured after reaching a total load of 276 kN. The fracture of the steel profile initiated in a preexisting hole, close to the bottom part of the substructure. Testing of specimen ICP2 was terminated after a compression failure occurred in the ECC slab at a mid span deflection in excess of 500 mm. The failure was observed as a compression – sliding crack across the deck element at mid-span.

Specimens MP1, MP2 and MP3 all exhibited a similar load-deflection response (see Figure 6-9), however, it should be noted that once the slip in MP3 stopped at approximately 70 kN, the stiffness increased significantly.

Testing of MP1 was discontinued when buckling of critical compression diagonals occurred close to the end supports of the deck element (Figure 6-10a), while testing of MP2 was terminated when mid-span deflections exceeded 500 mm (Figure 6-11a). Element MP3 failed abruptly due to shearing in the bolts connecting the diagonals of the steel truss. Testing of MP4 was terminated when ECC slab ruptured and the substructure yielded directly below where loading was applied (Figure 6-10b). MP4 ultimately reached 291 kN and a mid-span deflection of 282 mm before loading was discontinued.

Figure 6-10 a) Buckling of compression diagonals in specimen MP1, and b) A combination of compression and flexural failure during ULS testing of specimen MP4.

6.6 Discussion

The experimental program presented in this chapter has shown that the composite panel concepts (ICP and MP) can potentially be substituted for the much heavier commonly used prefabricated deck panels while still meeting deflection limits, load capacity and dynamic response according to codes of practice. Among the numerous advantages of the ICP and MP concepts over currently used prefabricated panels, the most pronounced improvement is the superimposed load to weight ratio.

6.6.1 Serviceability Limit State

The measured mid-span deflections of elements ICP, MP3 and MP4 during SLS loading were found to be below L/500 (16 mm) while all panels were shown to be below L/400 (20 mm) limit. Furthermore, both the analytical and numerical predictions for the SLS loading were shown to be in reasonably good agreement with the measured values. The structural behavior of selected specimens during SLS loading is compared in Table 6-1.

As a result of the low weight of the composite panels, any superimposed loading will significantly affect the behavior of the panels. Therefore, any additional weight will decrease the natural frequency of lighter deck systems proportionally more than for heavier, conventional deck systems. However, alternating the position and the cross sectional area of the tension member, a desired reduced deflection and natural frequency can be achieved to meet a wide range of design requirements on the composite ECC floor panels. Moreover, by optimizing the substructure, the self weight of the panels can be further reduced without compromising performance.

Table 6-1 Comparison of: mid-span deflections, natural frequencies and mid-span stresses from analytical results (Ana.), numerical results (Num.) and actual measurements (Meas.) of selected elements during SLS testing. Stresses are shown for a 4.0 kN/m2 loading.

	Specimen MP2			Specimen MP4			Specimen ICP		
	Ana.	Num.	Meas.	Ana.	Num.	Meas.	Ana.	Num.	Meas.
Deflection [mm]									
At 4.0 kN/m^2	17.9	15.2	17.2	12.8	9.6	10.2	10.8	-	12.8
Span / defl.	447	526	465	625	833	784	741	-	625
Frequency [Hz]									
At self weight	7.10	8.22	8.40	7.97	9.99	9.85	9.5	-	8.1
At 4.0 kN/m^2	3.37	-	4.00	3.93	-	5.00	4.7	-	4.5
Stresses [MPa] At 4.0 kN/m2 loading									
σ_{ECC}	4.7	3.8	-	5.6	3.2	-	1.6	-	-
σ_S	150.8	114.0	132.8	105.8	48.7	-	121.0	-	-

The measured decay of the free vibrations of the deck panels or damping ratios of ICP (0.6-1.0%) and MP4 (0.6-1.8%) correspond to those expected in composite sport and dance floors where the damping ratios have a minimum value of 0.8% and a maximum value of 2.5% (CEB bulletin, 1991).

One of the main design requirements for structural elements such as floor panels is a ductile failure mode at the ultimate limit state. In order for the proposed panels to comply with this requirement, the tension member in the steel substructure must yield before the compression capacity of the slab is reached. At the maximum SLS load, 4.0 kN/m^2, the force in the tension member of specimens MP1 and MP2 reached 55% of the yielding capacity of the steel while only utilizing 5% of the compression strength of the ECC slab. Likewise, specimens MP3 and MP4 reached 20% of the yielding capacity of the tension member while utilizing about 10% of the compression capacity of ECC.

6.6.2 Ultimate loading

The initial load – deflection response of the ICP's was found to be softer than that of the hollow core deck (HCD) (see Figure 6-9), however, with increased deflections the ICP's reached the same load capacity as the HCD, equivalent area load of 30 kN/m^2.

Although failure in the ICP caused a mix of severe cracking to occur, the panels were still intact after testing was terminated and still able to carry some residual load.

Beside the premature failures of MP1 (due to buckling of a compression diagonal) and MP3 (due to shearing of bolted connection) the modular panels performed as expected. MP2 and MP4 both displayed a ductile failure mode with multiple flexural cracks forming on the bottom of the ECC slab at mid-span and directly below the load couples (see Figure 6-11).

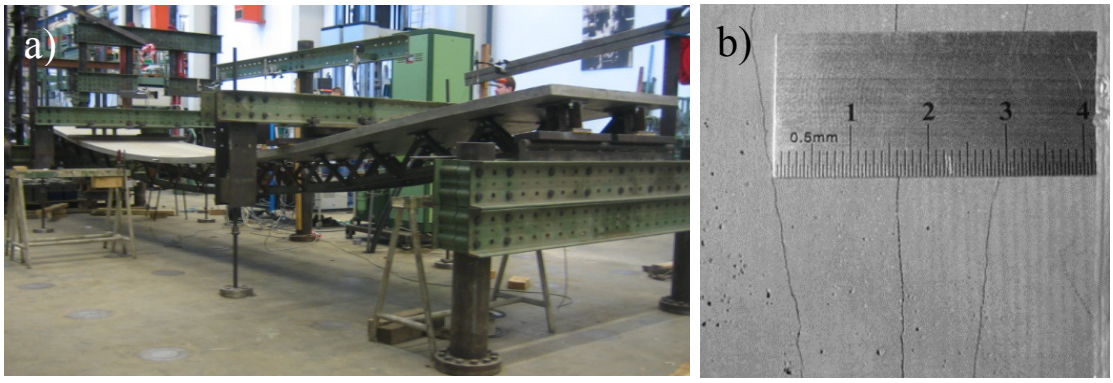

Figure 6-11 a) Deformed shape of specimen MP2 during ULS loading, and b) example of multiple flexural cracks on bottom of ECC slab at mid-span.

The load – deflection response of the modular elements are governed by the equivalent stiffness of the panels cross section. However, any slip, either in the bolted connections of the truss or in the interlocking connection between truss and slab will influence the structural response significantly as can be seen in MP3 and MP4 in Figure 6-9. The load – deflection response of MP4 exhibits a similar response as the ICP's despite the observed slip and ultimately reached the same load capacity as the HCD.

Both the slip in the bolted truss structure of MP3 and the slip in the interlocking connection between truss and embedded anchors of MP4 (seen as small load drops in Figure 6-9) were clearly audible as acoustic events during testing.

6.7 Conclusions

An investigation of the structural behavior of novel prefabricated, light-weight composite deck elements, composed of a slender ECC slab and a steel substructure was presented in this study. Two types of deck elements, the integrally cast panels (ICP) and the modular panels (MP), were studied and compared in a experimental program.

The load-deflection behavior of both panels types were shown to be consistent with predicted results and the failure modes were found to be ductile. Furthermore, it was demonstrated that by altering the steel truss substructure, desired changes in the structural response can be achieved.

An evaluation of the proposed panels at serviceability reviled that the deflections and natural frequencies to be within acceptable limits. The dynamic response of the tested specimens were shown to meet typical structural performance requirements, however, additional research is needed to further improve the dynamic behavior towards higher natural frequencies and improved damping.

The flexibility and versatility of the ICP and MP concepts lies in the specific combination of ECC deck and steel substructure, thereby controlling the strength and stiffness properties of the panel. This allows the proposed panel concept to adapt to a multitude of different performance requirements.

The experimental program furthermore, demonstrated a practical utilization of unmodified large scale industrial facilities to mix and transport ECC. The benefits of using a SHCC such as ECC in the proposed concepts are most evident in the tensile loading capacity and ductility of ECC which can eliminate transverse steel reinforcement and enables a ductile failure mode of the panel. However some transverse steel reinforcement could be provided for redundancy and safety.

Due to the light weight design of the ICP and MP concepts, both approaches offer a 70% weight reduction in comparison to hollow core decks while meeting structural performance requirements.

A detailed study of the long-term behavior of the composite panels influenced by creep in the ECC slab, cyclic loading under service conditions and shear capacity is currently under way. In this context, due to the lack of conventional reinforcements and thin ECC slab design, punching shear needs to be examined particularly to further develop the concept and pursue commercialization.

Bibliography

Abramski, M., Schnell, J., Albert, A. & Pfeffer, K., 2010. Experimental and numerical investigation of the bearing behaviour of hollow core slabs. BETON- UND STAHLBETONBAU. Volume 105, Issue 6. pp. 349-361.

CEB, 1991. Vibration problems in structures: Practical guidelines. CEB bulletin, Comité Euro-international du Béton. Contribution à la 28.session plénière du CEB. Vienna.

Ching, F. D. K., 1995. A Visual Dictionary of Architecture. Publisher: John Wiley and Sons. NY, USA. pp. 203-206.

Chopra, A. K., 2007. Dynamics Of Structures, Theory And Applications To Earthquake Engineering. 3rd edition. Prentice Hall. pp. 48-50.

FIP, 1988. Precast Prestressed Hollow Core Floors: FIP Recommendations. 2 CEN European Committee for Standardisation. Thomas Telford. London. UK. 1988. pp. 1-31.

Fischer, G., 2007. Fiber reinforced concrete for precast applications: an Overview on Recent Developments and Applications. Internaltional concrete conference & exhibition. ICCX. Cape Town. South Africa. pp.56-60.

Hambro, 2009. Hambro Technical Manual (Canada): Composite Floor Systems. Technical publications. <http://www.hambro-floors.ws> (Obtained Sep. 2, 2011).

Kuhlmann, U. & Schanzlig, J., 2008. A Timber-Concrete Composite Slab System for Use in Tall Buildings. Structural Engineering Internartional. SEI Volume 18. Issue 2. pp. 174-178.

Lárusson, L. H., Fischer, G. & Jönsson, J., 2013. Prefabricated floor panels composed of fiber reinforced concrete and a steel substructure. Engineering Structures, 46, pp. 104 – 115.

Martin L. D. & Perry C. J., 2004. PCI Design Handbook: Precast and Prestressed Concrete, 6th edition. Publisher: Precast/Prestressed Concrete Institute. CA. USA

Schnellenbach-Held, M. & Pfeffer, K., 2002. Punching behavior of biaxial hollow slabs, Cement & Concrete Composites. Volume 24. Issue 6. pp. 551-556.

Wang, S. & Li, V.C., 2005. Polyvinyl Alcohol Fiber Reinforced Engineered Cementitious Composites: Material Design and Performances, Proceedings of Int'l workshop on HPFRCC in structural applications. Honolulu. Hawaii. pp.104-111.

Chapter 7

Conclusions

In this chapter, the main findings and conclusions from the experimental investigations and analysis carried out throughout this project are summarized. Based on these findings, an outlook for future work is presented and discussed.

7.1 Summary

The objective of the presented work was to establish sufficient background knowledge of the composite tensile behavior and interaction of reinforcement and surrounding cementitious matrix, in particular the composite behavior of Engineered Cementitious Composite (ECC) reinforced with Glass Fiber Reinforced Polymer (GFRP) rebars, for the purpose of implementing the composite in a flexible link slab design.

The research work presented was divided into four main aspects, i.e. material characterization of the constituents utilized in the study, analysis of the interfacial behavior between reinforcement and surrounding matrix, the composite load – deformation response and cracking process of reinforced prisms, and design, detailing and testing a GFRP reinforced ECC link slab concept. In addition, an experimental program concerning implementation of ECC in prefabricated floor panel elements was presented.

Throughout the research activities presented herein, two cement based materials, i.e. conventional concrete and ductile ECC, and two reinforcement types, i.e. standard deformed steel rebars and linear elastic GFRP rebars, where experimentally evaluated in four different combinations. Various material characteristics of conventional concrete and ECC were examined experimentally with special emphasis on the crack formation and development in ECC, both at a single crack level and during multiple crack formation. In contrast to conventional brittle concrete, ECC was found to exhibit a highly ductile tensile behavior with pseudo strain hardening stress – strain response. By employing an image based deformation measuring technique on ECC specimens in direct tension, detailed measurements reviled crack widths limited to 0.2 mm and average crack spacing of 4.0 mm at 4% tensile strain.

A comprehensive investigation was carried out on the interface between the constituents (the reinforcement and surrounding matrix) in order to characterize the transverse

crack development and interfacial debonding during direct tensile loading. For this purpose, a novel test configuration was utilized with a partially exposed reinforcement in combination with a high definition Digital Image Correlation (DIC) technique which allowed the initiation, propagation and development of cracking to be monitored and quantified in detail at micro-scale.

A relationship between transverse crack development and interfacial debonding propagation was identified and quantified. The transverse cracking and the resulting debonding mechanism at the rebar – matrix interface were analyzed extensively and the degree of damage at the interface was quantified in terms of slip and opening (separation) displacements. The transverse cracking process of reinforced ECC members consistently showed multiple cracking with considerably smaller crack widths than those in reinforced concrete members. Consequently, the overall degradation of the rebar – matrix interface is distinctly less in reinforced ECC members than reinforced concrete members, approximately 40-50% less, as a result of the load shearing between reinforcement and ECC.

A closed form solution for the load – transverse crack width was presented and compared to the interface test results. The analytical solution, which incorporates a cohesive law for concrete in tension and a cohesive shear law for the interface between reinforcement and surrounding matrix, was shown to predict the response of reinforced concrete members reasonably well when the linear hardening interface law was chosen with an initial bond – stress component. The analytical solution presented herein is however limited to a reinforced member with a single transverse crack and is therefore not applicable for the analysis of members which exhibits multiple cracking such as the ECC reinforced members.

Extensive work was carried out to investigate the load – deformation response and surface crack development of reinforced prisms during monotonic tension and cyclic loading. In addition to the tension stiffening effect observed in reinforced concrete and reinforced ECC tensile member, a tension strengthening effect was observed and identified in reinforced ECC specimens. Based on these findings, a conceptual model for the tensile contribution of ECC was presented where the tension stiffening and tension strengthening were conceptually defined and schematically represented as overlapping events. The additional strengthening effect results in significant improvement of the composite response in terms of continued load shearing between the matrix and reinforcement. The load shearing ability of ECC consequently led to strain compatibility which maintained structural integrity of the composite throughout monotonic tension and cyclic testing. The strain compatibility observed in the reinforced ECC tension prisms and the limited interfacial debonding shown in the interfacial tests, are both a direct result of the load shearing- and restricted crack width ability of ECC.

The cracking process of the reinforced ECC prisms consistently showed multiple cracking with considerably smaller crack widths and crack spacing than those in reinforced concrete prisms, i.e. approximately 60-80% lower maximum crack widths and approximately 80% lower crack spacing at 1% tensile strain.

As expected, the maximum crack widths in the GFRP reinforced concrete were shown to be larger than in steel reinforced concrete (approximately 0.87 mm vs. 0.65 mm respectively) due to the lower elastic modulus of GFRP. However, the maximum crack widths in GFRP reinforced ECC prisms were found to be lower than steel reinforced ECC prisms (approximately 0.15 mm vs. 0.21-0.29 mm respectively).

Based on the experimental results from both the interfacial tests and the reinforced prisms tests, prefabricated flexible link slabs, composed of relatively thin prefabricated GFRP reinforced ECC elements, were constructed and subjected to monotonic- and cyclic deformations up to the target tensile strain of 1%. The innovative features of the link slab included a highly flexible prefabricated element composed of ductile ECC and low stiffness GFRP, a de-bonded active section, and passive load transfer zones intended to concentrate the induced deformations in the active part of the link slab.

The use of GFRP reinforcement instead of conventional steel reinforcement provides the link slab design with minimum axial resistance due to the lower stiffness of the GFRP reinforcement compared to that of steel reinforcement, thus effectively reducing the anchorage needed to secure the prefabricated element to the adjacent bridge spans. Furthermore, the non-corrosive nature of GFRP reinforcement combined with the limited crack widths of ECC is likely to provide the link slab, as well as the substructure, with improved corrosion resistance and extended service-life.

The load – deformation response of the link slab elements showed similar behavior as the GFRP reinforced ECC prisms where the continuous load carrying contribution of ECC, i.e. tension stiffening and tension strengthening effects, were observed throughout both the monotonic tension and cyclic loading. The crack formation and development observed on the active part of the link slab was shown to exhibit a uniform deformation with crack widths below 0.22 mm at 0.5% tensile strain and equal to 0.33 mm at the target 1.0% tensile strain during both the static and cyclic loading.

The overall structural performance of the link slab, i.e. in terms of the tensile load – deformation response and the cracking process, exhibited promising results where the limited crack widths, reduced interfacial debonding, and tension strengthening effect all contribute to maintaining structural integrity of the element throughout testing. Furthermore, the design details of the passive transition zones were found to effectively concentrate the imposed deformations of the adjacent bridge span sections into the active section of the link slab.

In addition to the comprehensive investigation of the composite interaction of reinforcement and surrounding matrix during tensile loading, a large scale experimental

program which examined prefabricated, light-weight composite floor panels composed of a relatively thin ECC slab and a steel substructure. The composite deck panels highlight the versatility of ECC to be utilized in various structural applications.

Two types of deck elements, the integrally cast panels (ICP) and the modular panels (MP), were studied and compared in an experimental program. One of the main advantages of such floor panels is the low self weight, being 70% lighter than a hollow core decks, while still maintaining the required structural performance. In addition, the panel system can be adapted to a multitude of different performance requirements by controlling the strength and stiffness properties of the panel by choosing a specific combination of ECC deck and steel substructure.

During the experimental program, which focused on serviceability- and limit state loading, the load–deflection behavior of both types of panels was shown to be consistent with predicted results and the failure modes were found to be ductile.

The tensile load capacity and ductility of ECC allowed transverse steel reinforcement to be omitted while enabling a ductile failure mode of the panel. However some transverse steel reinforcement could be provided for redundancy and safety. In addition, the experimental program demonstrated a practical utilization of un-modified large scale industrial facilities to mix and transport ECC.

7.2 Outlook and discussion

The presented research project has contributed to the understanding of the interaction of reinforcement and surrounding cement-based matrix during tensile loading at different relevant scale levels, i.e. the interface interactions at a meso-scale, the composite prisms at a macro-scale, and the link slabs and floor panels at a macro-structural scale. During the project a number of questions which call for further clarification were identified. In addition, issues which have not been treated in the presented work are discussed briefly in this section.

7.2.1 Interface investigation

The test results from the interface configuration with a partially exposed rebar gave a good indication of the crack process at the rebar – matrix interface during tensile loading. However, it is acknowledged that the lack of full confinement will influence the results as the radial pressure provided by the matrix surrounding the rebar is reduced. To partially compensate for this effect while monitoring the exposed interface during loading, a transverse confinement force might be provided in future work to reduce the affect of the removed matrix. The challenge here is to provide a transverse confinement, e.g. by clamping the specimen on the sides, without hindering lateral movement, by utilizing sliding or rolling bearings plates.

Other suggested additions to the interface investigation include:

- Interface analysis during cyclic loading displacements, the most challenging obstacle here is to monitor and control the deformations in real time.
- Utilizing the obtained transverse crack width profiles and debonding (separation) measurements to determine the potential ingress and corrosion of steel reinforced concrete structures in terms of durability.
- Further develop the bond-slip (shear lag) model to include the effect of multiple cracking particularly for the analysis of SHCC reinforced members.
- A parametric study examining different matrix strengths and variations of reinforcement sizes and ratios.

7.2.2 Composite prism investigation

The aim of the reinforced prism test configuration design was to isolate the composite behavior of the reinforced prisms in a representative section of the specimens during direct tension. Different configurations and geometries were explored before the configuration presented in this thesis was obtained. To further develop and examine the potential of the setup the following is suggested for future work:

- Scale effect between specimen sizes as well as different geometries and reinforcement ratios.
- Long term behavior of the composite, including fatigue (not just cyclic loading) and aging.
- A parametric study which examines the influence of different matrix strengths, variations of reinforcement sizes and ratios with regards to crack widths and spacing.

7.2.3 Link slab investigation

During the development of the presented link slab concept a number of different test approaches and details were discussed, some of whom were implemented, others suggestions include:

- Decreasing the overall length of the prefabricated element by providing hooked ends on the protruding GFRP rebars on each end of the prefabricated link slab, this would furthermore provide a more secure anchoring connection between the link slab and the bridge spans.
- Implementing even smaller reinforcement sizes or even utilizing reinforcement grids could be beneficial in terms of reducing crack widths and spacing even more.
- Investigation focusing on reverse cyclic loading of the link slab design, i.e. establishing the behavior and limitations of the design in compression events.

7.2.4 Panel investigation

Further development of the prefabricated panels is currently underway at the Technical University of Denmark were the following aspects are being evaluated:

- A detailed study of the long-term behavior of the composite panels influenced by creep of the ECC slab.
- Cyclic loading of the panels under service conditions.
- Bending and shear capacity of the unreinforced part of the ECC slab, i.e. spanning or protruding in the transverse direction of the panel length.

List of Figures

List of Tables

Appendix

Appended Paper

Paper I

"Prefabricated floor panels composed of fiber reinforced concrete and a steel substructure"

Lárus H. Lárusson, Gregor Fischer & Jeppe Jönsson

Published in: Engineering Structures, 2013

Engineering Structures 46 (2013) 104–115

Contents lists available at SciVerse ScienceDirect

Engineering Structures

journal homepage: www.elsevier.com/locate/engstruct

Prefabricated floor panels composed of fiber reinforced concrete and a steel substructure

Lárus H. Lárusson *, Gregor Fischer, Jeppe Jönsson

Technical University of Denmark, Department of Civil Engineering, Brovej, Building 118, 2800 Kgs. Lyngby, Denmark

ARTICLE INFO

Article history:
Received 16 January 2012
Revised 7 June 2012
Accepted 27 June 2012

Keywords:
Composite
ECC
Lightweight deck panel
Modular deck system

ABSTRACT

This paper reports on a study on prefabricated composite and modular floor deck panels composed of relatively thin fiber reinforced concrete slabs connected to steel substructures. The study focuses on the design, manufacturing, structural improvements and behavior of the floor systems during loading at the serviceability and ultimate limit states. The composite construction concept offers flexibility in the assembly process, the ability to adapt to various load and boundary requirements, and efficient utilization of material properties that result in a light weight prefabricated structural element.

The activities described in this paper are an extension of previous work where composite floor panels composed of light gauge steel joists were integrally cast with a thin-walled Engineered Cementitious Composite (ECC) slab. The main focus of the present study was to revise and improve the design detailing of these integrally cast deck panels and to modify them by providing individually cast anchor points in the precast ECC slab, which are subsequently used to attach a steel truss substructure.

Full-scale experiments were carried out to verify the structural behavior of the integrally cast panels and the modular panels with various substructure configurations along with comparison to analytical and numerical results.

1. Introduction

1.1. Background

The motivation behind the project presented in this paper was to research and develop an alternative to current prefabricated floor systems with the goal of increasing production efficiency while reducing weight by using new and innovative building materials.

An increasing number of innovative structural floor systems both prefabricated and cast-in place have been previously implemented in the construction industry. The most commonly used prefabricated structural floor systems are hollow core decks (Fig. 1a) and double-T decks (Fig. 1b). Other semi prefabricated systems include filigrees (Fig. 1c), steel pan decks (Fig. 1d) and more recently biaxial hollow core decks (Fig. 2a), all of which are requiring casting of a concrete overlay at the construction site (in situ).

Design requirements and targets for prefabricated building products frequently include light weight, durability, implementation versatility, reduced construction time and cost. All of these requirements interact and affect each other and need to be addressed during the design process.

In this context, by utilizing the properties of new and innovative materials such as Fiber Reinforced Concretes (FRCs) in structural elements such as prefabricated floor panels allows for a more efficient construction process.

High Performance Fiber Reinforced Cementitious Composites (HPFRCCs) [1] such as Engineered Cementitious Composites (ECCs) have the ability to exhibit tensile strain hardening due to a specifically designed interaction between the cementitious matrix, the fibers and their interfacial bond. The strain hardening behavior of ECC is realized through an engineered interaction between a particular tensile stress–crack opening relationship and the formation of multiple cracking [2]. As a result of the ductile tensile load–deformation behavior of ECC, structural members can be designed with reduced sectional dimensions compared to those of normal steel reinforced concrete. This is possible due to the tensile strain hardening property of ECC, which has the same effect as steel reinforcement has in regular concrete and can reduce the amount of required reinforcement in a structural member, particularly in thin-walled structural elements.

In extension of previous work on Integrally Cast Panels (ICPs) (Fig. 3a), which examined thin-walled steel joists integrally cast into a thin ECC slab [3], the focus of this study was to further examine structural details of the ICP along with developing and testing a modular structure consisting of an ECC slab and a subsequently mounted steel truss substructure. The unique feature of the proposed modular segmented design are individual anchor points

* Corresponding author. Tel.: +45 3025 2774; fax: +45 4588 3282.
E-mail addresses: larus@byg.dtu.dk (L.H. Lárusson), gf@byg.dtu.dk (G. Fischer), Jej@byg.dtu.dk (J. Jönsson).

0141-0296/$ - see front matter © 2012 Elsevier Ltd. All rights reserved.
http://dx.doi.org/10.1016/j.engstruct.2012.06.035

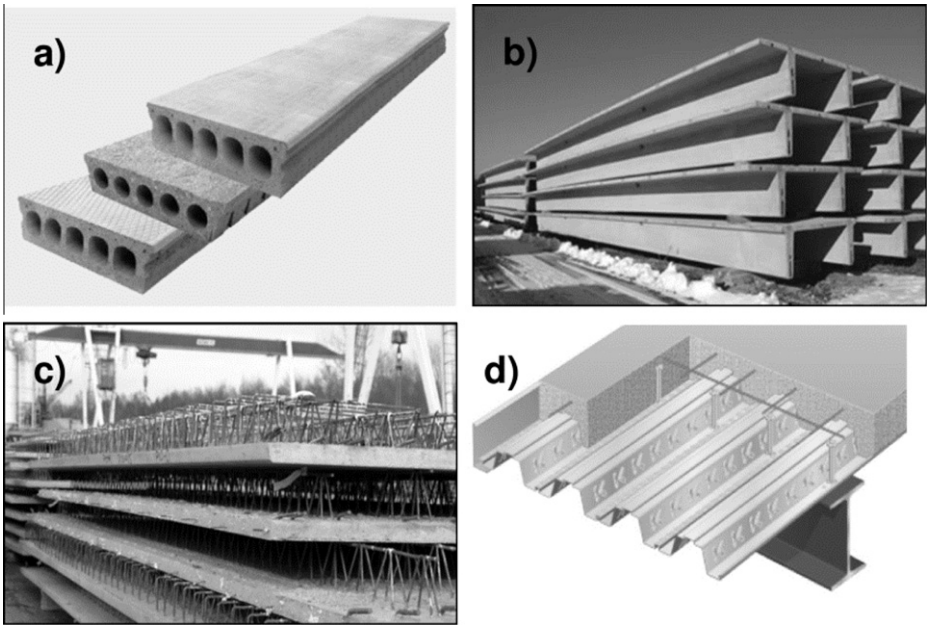

Fig. 1. Commercially available floor systems: (a) hollow core decks [19], (b) double T-deck elements [20], (c) filigree slabs with embedded lattice stirrup ridges [21], and (d) concrete on a pan deck supported by a steel joist [22].

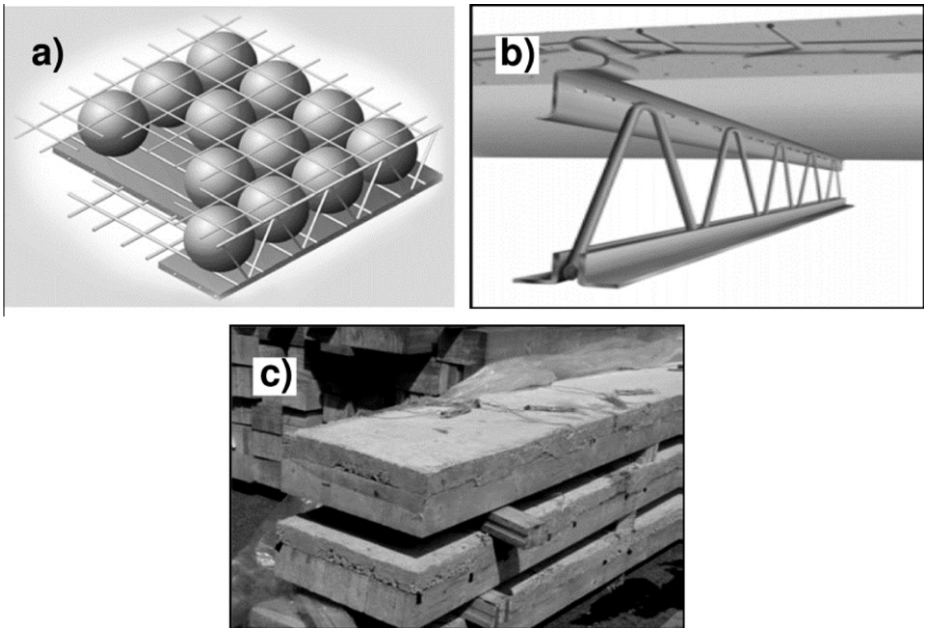

Fig. 2. Commercially available floor systems: (a) Bubble deck in Principe [7], (b) Hambro deck system in principle [11]. (c) Timber–concrete composite slab system [12].

integrally cast with the ECC slab, which are subsequently used to attach a steel truss substructure (Fig. 3b). By casting individual anchor points into the deck, the slab is allowed to shrink and deform independent of the substructure prior to assembly of the composite floor panel without causing shrinkage induced stresses and cracking and undesirable deflections of the deck panel during curing.

1.2. Overview of traditional prefabricated and semi-prefabricated floor deck systems

Prestressed hollow core decks (HCDs) [4,5] are widely used prefabricated elements suitable for most building types (Fig. 1a). The HCD have tubular voids running along the entire length of the element to reduce weight and consequently optimizing the tension and compression zones of the cross-section by removing ineffective concrete. The cross-section is utilized in compression by prestressing the element with high strength steel tendons to induce a clamping load that increases the active area and in effect the moment of inertia of the cross-section. As a result of reducing the weight and increasing the stiffness (moment of inertia), the deflections of the prefabricated element are decreased and allow a reduced structural height of the deck panels. The structural height of HCD elements typically ranges between 150 and 450 mm with a width of 1.2 m and a span ranging from 4 to 16 m depending on the expected loading and configuration.

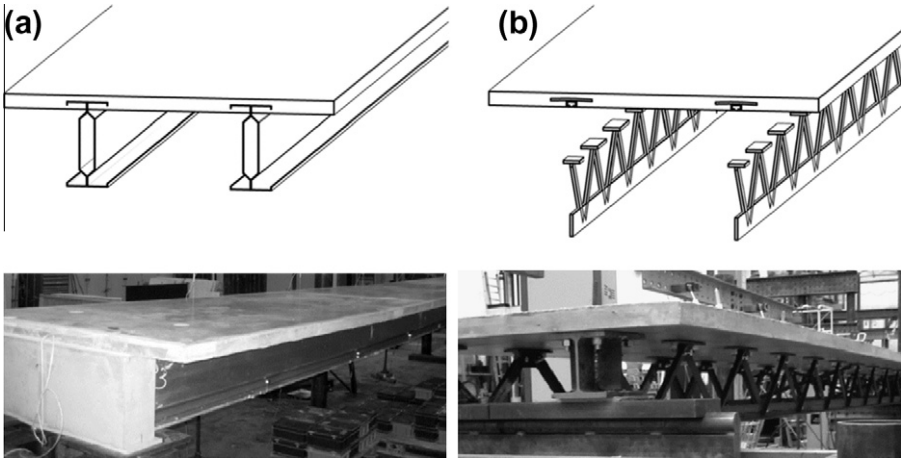

Fig. 3. (a) The integrally cast panel and (b) the modular concept.

Prestressed T- and double T-deck or slab elements (TD), also known as T- and double T-beams [5,6], are also widely used prefabricated elements (Fig. 1b). These elements are usually suitable for all building types but are more commonly used where loads are higher and spans are longer than normal (10–25 m spans). The structural heights of these elements are typically larger than other deck types as the structural concept of the TD is to utilize the distance between the compression zone and the tendons which are typically either prestressed or post-tensioned.

The casting procedure for factory produced elements such as HCD and TD allows for a relatively fast and accurate construction process where high product quality can be ensured. In this context, various techniques have been developed and are being implemented in the building sectors that combine the advantages of in situ casting and factory-made elements to optimize the design and further improve the implementation process.

Filigree plates (Fig. 1c) are one type of semi-prefabricated deck elements [7]. They combine regular Reinforced Concrete (R/C) slabs with prefabricated elements by utilizing the filigree as formwork during construction and as a structural component at the service load stage. A filigree slab is essentially the lower reinforcement grid of a regular R/C slab cast into a thin layer of concrete. In addition, lattice stirrup ridges on the filigree ensure a composite connection of the upper reinforcement and cast in place concrete with the lower prefabricated element. A number of different variations of the filigree concept have been developed with the purpose of eliminating the need for regular formwork and reducing installation and build time.

Biaxial hollow core deck systems, known as Bubbledeck® (Fig. 2a) or Cobiax®, are recently developed methods of constructing floor decks [8,9]. In principle, the concept is similar to that of traditional HCD. By utilizing the compression strength of concrete and tensile strength of the reinforcement and tendons, ineffective concrete can be removed and replaced with hollow plastic spheres (bubbles). Unlike traditional HCD, Bubbledeck is a biaxially spanning slab system, which carries load along both axes of its plane, similar to two way reinforced concrete slabs. It consists of a prefabricated filigree element with plastic spheres firmly locked in a reinforcement lattice while the lower parts of the spheres are cast in concrete to complete the Bubbledeck.

Reinforced concrete on a corrugated steel deck, also known as pan deck (Fig. 1d), performs in the same way as filigrees by integrating the steel pan as part of the reinforcement and formwork during construction [10]. It allows for thinner- and lighter decks compared to regular reinforced concrete slabs. Steel pan decking is widely used in high rise buildings with steel frames and is generally considered a short span system with max spans in the range of 4–6 m. Once these filigree or corrugated panel elements have been put into place, the upper reinforcement lattice and anchoring is finalized before the concrete slab is cast in place, allowing for a continuous floor.

Hambro composite concrete-steel floor system is yet another innovative concept (Fig. 2b) [11]. Structural components include a relatively thin reinforced concrete slab and a steel truss integrally cast into the slab. This system is currently being produced and marketed as an alternative to heavier floor systems.

Timber–concrete composite slab systems (Fig. 2c) are also used in practice [12]. They utilize the tension properties of timber combined with the compression strength of concrete to create relatively light and slim floor decks. The main benefits of such systems are the reduced dead load, allowing for longer spans and a rapid construction time.

Table 1 compares relevant characteristics of various structural floor systems to give a general schematic overview of the different

Table 1
Comparison of different deck types, approximated range of spans and dead loads. For comparison reasons most of the structural heights compared are in the same range.

Deck types	Height (mm)	Width (m)	Spans (m)	Self weight (kN/m^2)
Composite ECC[a], MP, ICP	325	1.2	6–12	1.3
Hambro D500TM	350	1.25	6–9	2.6
Hollow core 1	265	1.2	4–10	3.6
Hollow core 2	320	1.2	4–12	4.0
Steel pan, Ribdeck AL	200	0.6–0.8	4–6	4.3
Bubbledeck	285	1–3	8–12	4.6
T-section	500	1.4	10–25	5.5
R/C and reg. filigree	300	6–8/1–3	6–8	7.5

[a] The composite ECC deck panels that are the focus of this study.

systems including the composite ECC deck panels presented in this paper.

1.3. Material properties

Engineered Cementitious Composites (ECCs) is a fiber reinforced cementitious composite material, which exhibits strain hardening and multiple cracking up to relatively large inelastic deformations (see Table 2). The micromechanical design of ECC results in the ability to increase its tensile loading capacity after first crack formation, which is realized through particular interaction between fibers, cementitious matrix, and their interfacial bond. This results in multiple cracking during tensile loading with an intrinsically controlled crack width on the order of 200–300 μm at reaching the tensile strength [1,13] The strain hardening and multiple cracking properties of ECC distinguishes it from regular brittle concrete and conventional tension softening Fiber Reinforced Concrete (FRC) as illustrated in Fig. 4. The elastic and post crack inelastic behavior of ECC can be described as being analogous to that of metals with a similar elastic/plastic load deformation behavior.

ECC is composed of ingredients commonly used in concrete including cement, fly ash, sand, water, admixtures and fibers at a volume fraction of 2%. The lack of coarse aggregate in ECC results from the requirements imposed by the micromechanical design concept, which limits the allowable fracture toughness of the cementitious matrix and therefore limiting the maximum size of the aggregates. The Polyvinyl Alcohol (PVA) fibers used in this study are 8 mm long with a diameter of 40 μm and were developed for optimal performance in ECC and to meet the specific micromechanical requirements.

Due to the composition of ECC, shrinkage is more extensive compared to conventional concrete. Drying shrinkage of ECC has been found in related studies to reach 0.10–0.15% strain at 40–70% Relative Humidity (RH), which is approximately 80% higher than drying shrinkage deformations of normal concrete [14].

Due to the ductile nature of ECC, the composite interaction of ECC and steel reinforcement (R/ECC) is significantly different from the interaction of regular concrete and steel reinforcement (R/C) with a distinctly different post cracking stress distribution in the R/ECC as a result of the formation of multiple cracking instead of localized cracking [15]. This evenly distributed load transfer between the rebar-matrix interfaces makes the composite interaction of ECC and steel substantially more compatible than that in R/C [16].

2. Concept and design

The objective of the panel systems presented in this paper was to develop a lightweight, easy to install alternative to traditional and heavier prefabricated floor systems by implementing High Performance Fiber Reinforced Cementitious Composites (HPFRCCs) such as ECC.

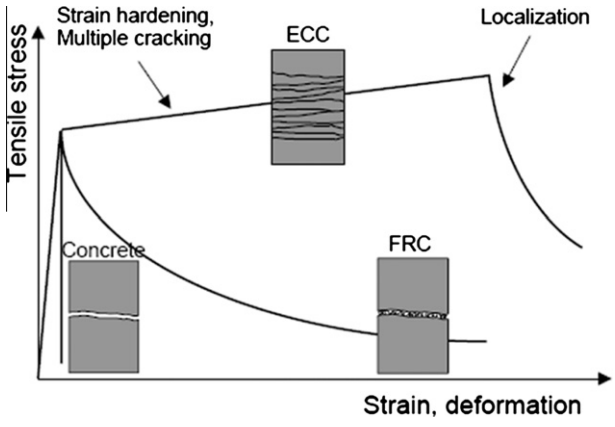

Fig. 4. Schematic tensile stress–strain behavior of cementitious matrices [1].

In previous studies [3], thin-walled steel profiles integrally cast with a thin ECC deck slab were fabricated and their structural behavior was investigated. These Integrally Cast Panels (ICPs) have been developed to meet some of the necessary criteria for floor decks according to codes of practice, such as loading capacity, deflection limits and dynamic response.

In continuation of this initial investigation on integrally cast panels, structural details of the segments support footings and cross bracing of the joists were addressed and a modular assembly of the ECC slab and the steel sub-structure was investigated. In these previous ICP studies, the casting forms and the thin-wall steel profiles were laid out in a shallow parabolic shape to compensate for shrinkage induced deformations of the deck element. The deformations previously observed in the integrally cast panels resulted from shrinkage of the ECC, due to which undesirable deflections and cracking had formed in the ICP decks.

The aim of the modular concept applied in this study is to separate the casting of the ECC deck slab and the attachment of the substructure by embedding anchors into the ECC slab, thus avoiding unfavorable deformations and cracking due to shrinkage typically encountered in the integrally cast floor panels [3]. By embedding individual attachment devices that later can be connected to a steel truss substructure, the modular system offers increased flexibility in assembly and transportation of the deck system. Moreover, the concept allows for high versatility in the substructure design and the ability to adapt to different required loading capacities and deflection limits as well as architectural requirements. Furthermore, the modular panel assembly allows for a precamber in the ECC slab of the modular floor panel to compensate for deformations due to self weight and creep during the initial use phase of the panel.

The flexibility of such a system lies in the design of the panel sub-structure where height, weight and architectural needs can be met without compromising structural integrity. The possibility of having wiring, ventilation and piping located within the structural height of the deck element allows the overall height of the floor construction to be reduced.

In the design of the modular panels, numerical models were implemented to aid in the dimensioning of the steel trusses. Two types of elements constitute the structural elements of the numerical models of the modular floor panel. The steel truss components were modeled as frame elements, while the ECC deck slab on top of the two trusses was modeled with shell elements (Fig. 5). The models were used to obtain static forces and natural frequencies for at the serviceability limit state and to predict the capacity at the ultimate limit state as well as to estimate the applied forces at failure observed during testing.

3. Analytical calculations of structural properties

To estimate the bending stress distribution in the panels, the following assumptions were made: a linear elastic strain distribution through the depth of the sections and plane sections remain plane after deformations (Fig. 6). Furthermore, assuming the deck panels are subjected to a uniformly distributed load, the bending stresses in the cross-section can be determined by employing the equivalent stiffness of the integrally cast- and the modular cross-sections. This equivalent stiffness ($E \cdot I_{Eq}$) is determined from the geometry and the material properties where E is the elastic modulus and I_{Eq} is the equivalent moment of inertia of the cross-section.

Assuming a linear elastic behavior of the materials, the resisting bending moment of the deck sections is estimated based on two

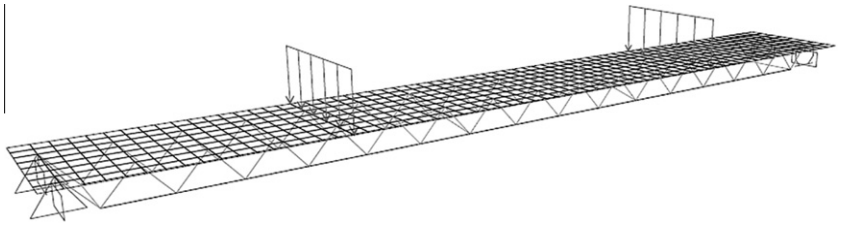

Fig. 5. Numerical model of modular panel, example of ultimate limit loading applied as line load over quarter points.

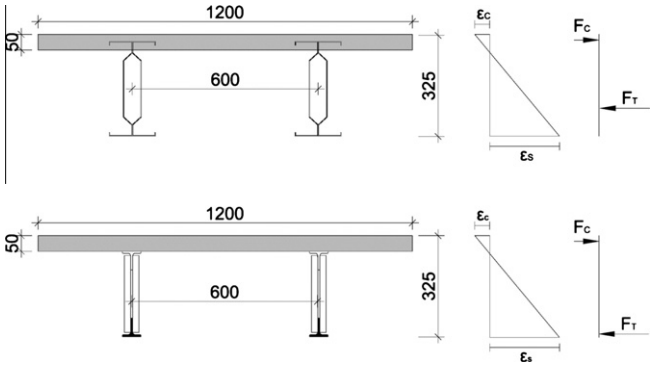

Fig. 6. Section view and assumed stress and force distribution of: (a) the Integrally Cast Panel (ICP), b) the modular deck panel (MP). Dimensions are given in mm.

failure criteria: the compression capacity of ECC is reached and yielding of the steel substructure. The contribution of the diagonals in the modular panel substructures is not taken into account in the analytical assessment of the bending stresses.

The deflections (v) of the panels are determined using equations for a simply supported beam with uniformly distributed load (q). For maximum deflection:

$$v = -q/(24 \cdot E \cdot I_{Eq}) \cdot (L^3/2 - 9L^4/16)$$

where q is the uniformly distributed line load and L is the span length of the deck element.

From the equation of motion, the natural frequency (f) of the system with a constant stiffness ($E \cdot I_{Eq}$) and mass (m) is determined as:

$$f = (n^2 \cdot \pi)/(2 \cdot L^2) \cdot ((E \cdot I_{Eq})/m)^{1/2} \quad n = 1, 2, 3, \ldots$$

To evaluate the damping ratio (ζ) of the structure, low damping is assumed, i.e. $(1 = \zeta^2)^{1/2} \approx 1$, and the damping ratio can be written as:

$$\zeta \approx \ln(u(t)/u)(t + T))/(2 \cdot \pi)$$

where $u(t)$ is the peak amplitude at time t and T is the time of one period [17].

4. Experimental program

In this study, the structural response of two integrally cast ECC-Steel joist deck panels (ICP1–ICP2) and four ECC modular deck panels (MP1–MP4) were experimentally evaluated. The overall dimensions of the deck panels are 1.2 m in width, an ECC slab thickness of 50 mm and an overall built height of 325 mm. The lengths of the panels are 8.2 m for the ICP and modular panels.

4.1. Test configuration and sequence

The deck elements were simply supported at both ends with a clear span of 8.0 m. At each end, the specimens were supported at two points in the transverse direction at a spacing of 0.6 m coinciding with the spacing of the trusses (Fig. 6).

Testing was carried out at two levels, at the serviceability limit state (SLS) and at the ultimate limit state (ULS). Loading at SLS was applied to the panels by a uniformly distributed line load over the 8.0 m span resulting in an equivalent area load of 4.08 kN/m^2. The distributed loading was applied in four steps at increments of 1.02 kN/m^2 at each step. The loads were applied in a line-load configuration directly above the trusses as the objective of these tests was to examine the behavior of the deck element in its longitudinal direction. During SLS loading, the dynamic response of the panels was measured by inducing a vibration in the deck elements and measuring its decay. From the obtained data the natural frequency and damping ratio were determined for each load increment (0–4.08 kN/m^2).

To evaluate the behavior of the floor panels at ULS, a four point bending configuration was used consisting of two point load couples (or transverse line loads) positioned on the deck at 2.0 m ($^1/_4$ L) and 6.0 m ($^3/_4$ L) relative to the 8 m span (Fig. 5) to induce a bending moment. Loading at ULS was increased gradually until failure occurred.

4.2. Specimen configuration

In constructing the ICP decks, four thin walled steel joists (cold-formed sigma profiles) (Fig. 6a), which constitute the substructure of each panel, were positioned in the bottom of the ECC deck slab (Fig. 3a). The steel joists are 300 mm high, 70 mm wide and have a thickness of 2.66 mm and a yield strength of 350 MPa. The thin walled profiles are embedded 25 mm into the 50 mm thick ECC deck slab resulting in an overall structural height of 325 mm. To ensure sufficient shear strength in the connection between the steel joists and the ECC slab, cut-outs in the steel profiles were made in the top part along the length of the profiles that connects to the slab (Fig. 7). Furthermore the ICP were cast with a slight

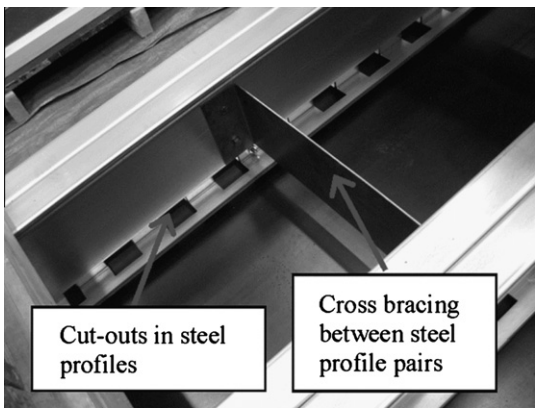

Fig. 7. Cut-outs in the steel profiles and cross bracing between steel profile pairs before ECC was cast.

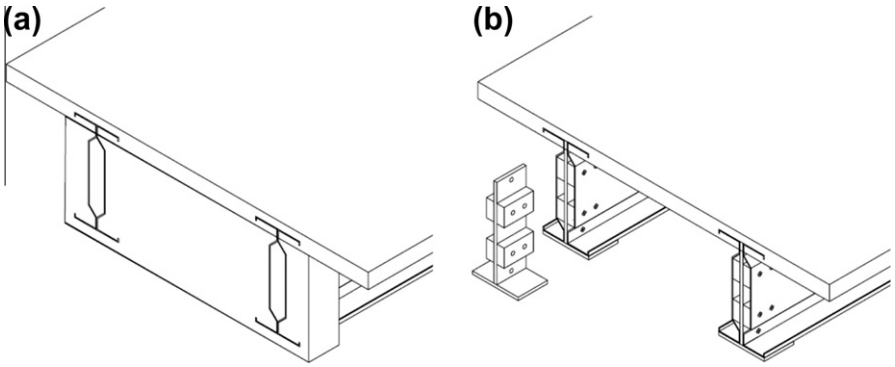

Fig. 8. A visual comparison of (a) Integrally Cast Panel 1 (ICP1) and (b) Integrally Cast Panel 2 (ICP2).

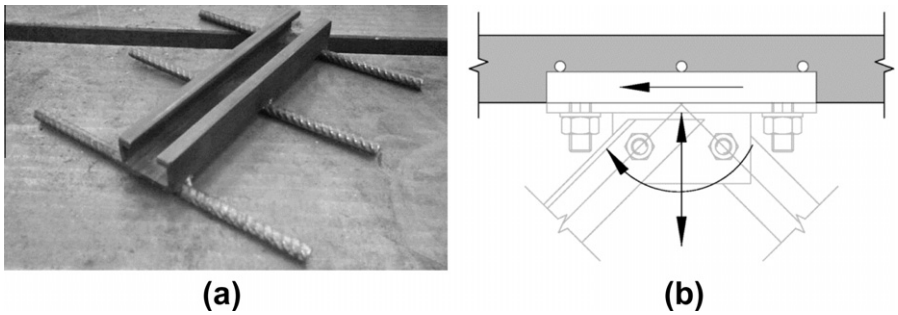

Fig. 9. (a) Cast-in anchor. (b) Resultant forces expected in cast-in anchor, forces shown in vertical and longitudinal direction.

curvature to account for shrinkage in the ECC and to create a negative deflection over the length of the panel. Structural improvements to the ICP design from the previous study [3] included cross bracing between the two pairs of steel joists (Fig. 7) and strengthening of the support footings. Difference in the structural detailing of the support footings separate the two ICP panels: ICP1 has the integrally cast steel joists confined in a block of ECC while the design of ICP2 features a steel strengthening element located between the steel profiles at the support (Fig. 8).

The modular floor slabs were manufactured with cast-in anchors (Fig. 9) positioned at the bottom of the ECC slabs, which are subsequently used to connect a steel truss assembly to the underside of the floor slab resulting in a complete composite deck element.

Due to the small thickness of the ECC slab (t = 50 mm), no suitable commercially produced cast-in place attachments were available and had to be custom fabricated to fit within the shallow depth of the ECC slab. To make the cast-in anchors, a system of interlocking steel channels and matching bolts was used to secure the channel segment firmly in the ECC slab with transverse anchor bars welded to the bottom of the channel (Fig. 9). To further increase the connection of the support footings to the ECC slab at the end of the floor segment, two channels were used for each anchor (Fig. 10). The geometry of the cast-in anchors was based on expected forces at the critical anchor points according to a numerical model of the composite panel.

The dimensions of the modular deck panel substructure (steel girders) were determined to have a height of 275 mm, resulting in a total structural height of 325 mm of the composite panel.

Four different steel truss configurations for the Modular Panels (MPs) were tested; specimens MP1, MP2, MP3 and MP4. In MP1, MP2 and MP3, the same ECC slab was used and re-used, while a second ECC slab (identical to the first slab) was used in MP4. Furthermore, the steel grade of the trusses in MP1, MP2 and MP3 was S235 while the steel grade in MP4 was S350.

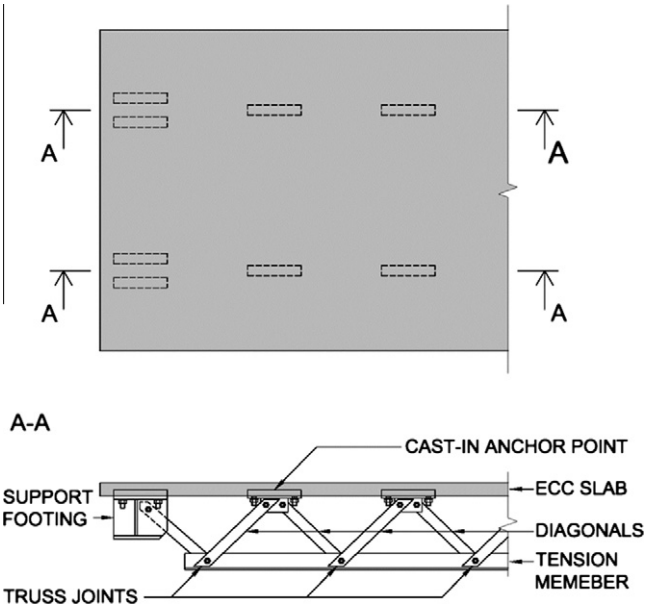

Fig. 10. (a) Plan over-view of the modular deck, (b) longitudinal cross-section of truss structure connected to ECC deck panel.

The first steel truss configuration in specimen MP1, was composed of 60 × 60 × 7 mm steel T-profiles as the tension member and 40 × 20 × 4 mm L-profiles as the diagonals. After testing of specimen MP1, the steel truss substructure was modified by replacing the diagonals of both trusses (9 on each end) with stronger 50 × 50 × 6 mm L-profile diagonals (specimen MP2). After testing of specimen MP2, the tension member of the trusses were replaced with a larger 80 × 80 × 9 mm T-profile resulting in specimen MP3. The steel trusses for specimens MP1, MP2 and

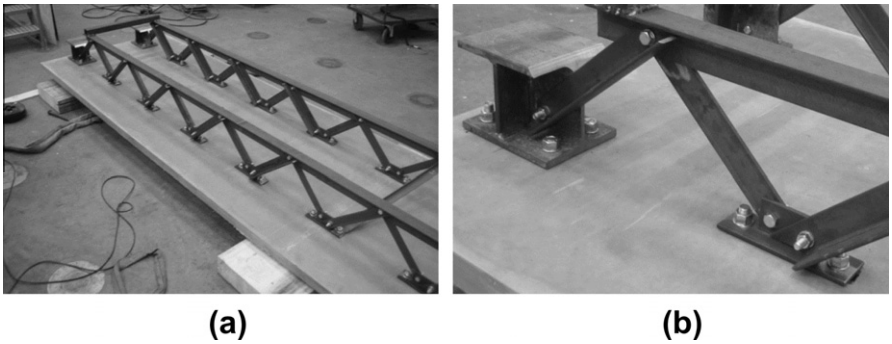

Fig. 11. (a) Steel truss assembly. (b) Bolted connection to ECC slab.

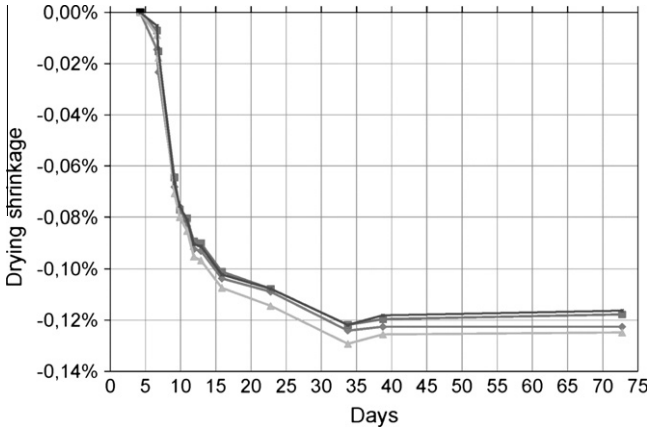

Fig. 12. Drying shrinkage of ECC over a period of 72 days.

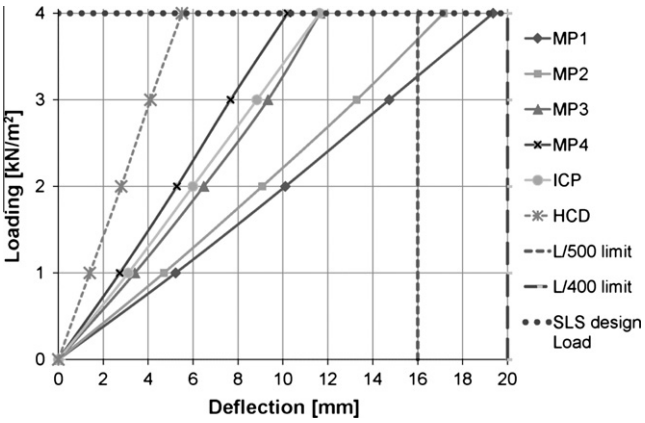

Fig. 13. Comparison of mid-span deflection of specimen MP1, MP2, MP3, MP4, ICP and HCD as a function of the applied load.

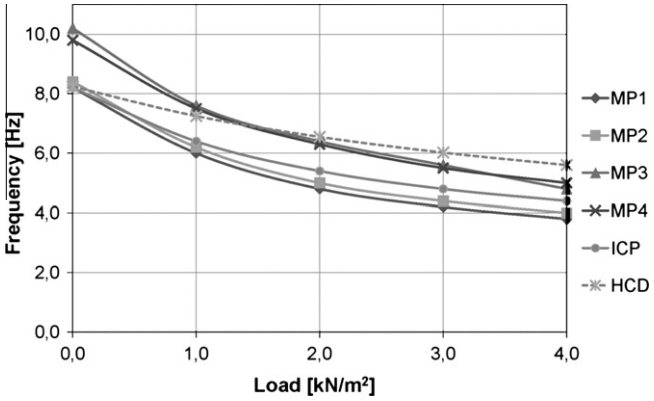

Fig. 14. The measured natural frequency as a function of applied service load.

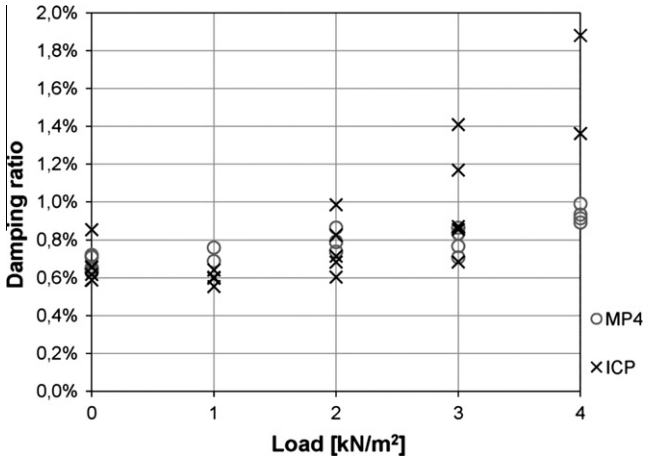

Fig. 15. Measured damping ratios for specimens MP4 and ICP as a function of additional live load.

MP3 were bolted together using M12 steel bolts, thus allowing for changing and replacing individual truss elements (Fig. 11). The truss-joint connections which connect the truss to the cast-ins in the slab were fabricated using the $60 \times 60 \times 7$ mm T-profiles (Fig. 9 b and Fig. 11).

Based on the experience from testing of specimens MP1, MP2 and MP3 at the service- and at ultimate state, the substructure connections of specimen MP4 were welded together using a 80×20 mm plate profile as the tension member, 40×8 mm plate profiles as tension diagonals, and $40 \times 40 \times 4$ mm RHS profiles as compression diagonals. The 40×8 mm plate-profile was also used to fabricate the truss-joint connections. As a conclusion to testing and revising of preceding designs (specimens MP1, MP2 and MP3), specimen MP4 was designed and built to have a moment resistance of 260 kNm, equivalent to that of a hollow core deck with the same span and similar structural height.

To ensure that the shear forces in the truss structures at the end-supports did not transfer directly into the thin ECC slab, the supports-footings were designed as rigid blocks made from 200 mm long HE160B steel profiles (two for each truss). These

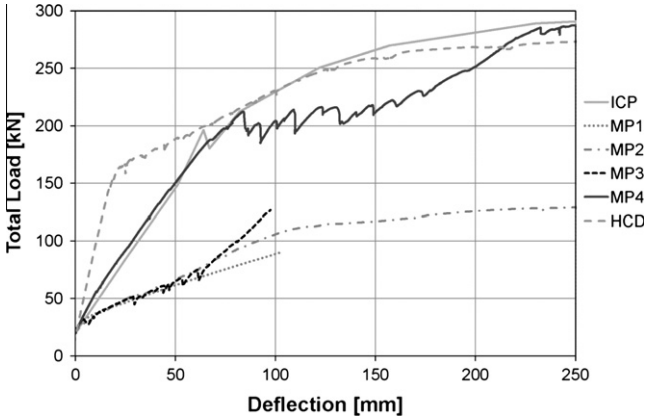

Fig. 16. Deflection at mid-span as a function of the total load of specimens MP1, MP2, MP4, ICP and the hollow core deck panel (HCD). Loading starts at 20 kN due to test configuration.

support footings were secured to the embedded cast-in anchors located at the ends of the deck element (Figs. 10 and 11b).

4.3. Material properties

Material tests were carried out to evaluate the mechanical properties of the ECC, including compressive strength, modulus of elasticity and drying shrinkage deformations. To insure analog development of the material properties of the test specimens to those of the actual panel specimen, all material specimens were cured in the same way as the panel specimens, i.e. at the same temperature and humidity. The compressive strength f_{ck} of the ECC on the day of testing was found to be 60 MPa with an elastic modulus of E_{cm} = 18 GPa. In addition, the drying shrinkage of the ECC was measured over a 68 day period using 270 mm long, test specimens with a cross-section of 25 × 25 mm^2. The results show that the drying shrinkage strain is approximately 0.12% after 30 days (Fig. 12) which is in good agreement with previously reported data [14], which showed drying shrinkage deformations of ECC to be 0.12% at 50–60% RH.

4.4. Experimental observations

4.4.1. Testing at serviceability limit state (SLS)

The specimens were subjected to a number of loading schemes to evaluate their structural behavior at the serviceability state, i.e. deflection, internal force distribution and dynamic response. For SLS loading, the deflection measurements were determined during the un-loading phase, i.e. the specimen was loaded with the full 4.0 kN/m^2 before being unloaded at increments of 1.0 kN/m^2 while measurements were taken. By doing so, any slip that occurs at this load level does not influence the measurements during unloading.

Due to virtually identical test results for ICP1 and ICP2 during SLS testing, results are shown for both specimens collectively as ICP.

A load deflection diagram for all specimens during SLS loading is shown in Fig. 13 and for comparison, a load deflection response of a hollow core deck with similar structural height is also shown.

The ICP specimens deflected 2.9 mm at mid-span for each 1.0 kN/m^2 applied, MP1 deflected 4.9 mm, MP2 deflected 4.3 mm, MP3 deflected 2.9 mm and MP4 deflected 2.5 mm at each load increment. All specimens except MP3 showed a linear load–deflection response during SLS loading while all specimens deflected less than the L/400 limit of 20 mm (Fig. 13).

Strain gauges placed on selected truss members of the modular substructure monitored the strain and consequently the stresses in elements of the steel substructure could be assessed during testing. The obtained stress and equivalent force distribution in truss structures MP1, MP2 and MP3 during SLS loading was in good agreement with the expected distribution found analytically and numerically.

Accelerometers positioned at the mid span of the deck panel were used to assess the dynamic response of the structure. The natural frequencies and damping ratios of the deck panels were measured by inducing a vibration in the decks and measuring its decay (Figs. 14 and 15). The natural frequency of specimens MP3 and MP4 was approximately 10 Hz at 0 kN/m^2 and 5 Hz at 4 kN/m^2 applied loading, which is 30% higher than that for specimens MP1 and MP2 at 0 kN/m^2 and 25% higher at 4 kN/m^2 (Fig. 14). The difference is a result of the changes made to the tension member and consequently increased effective stiffness of specimens

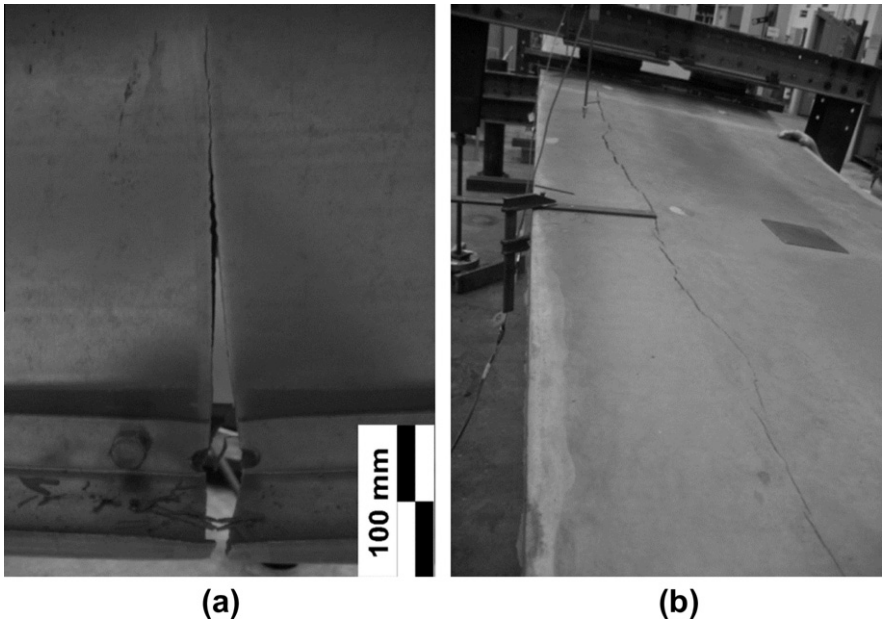

Fig. 17. Failure of specimen ICP1, (a) crack in the steel substructure and (b) a subsequent failure of the ECC deck.

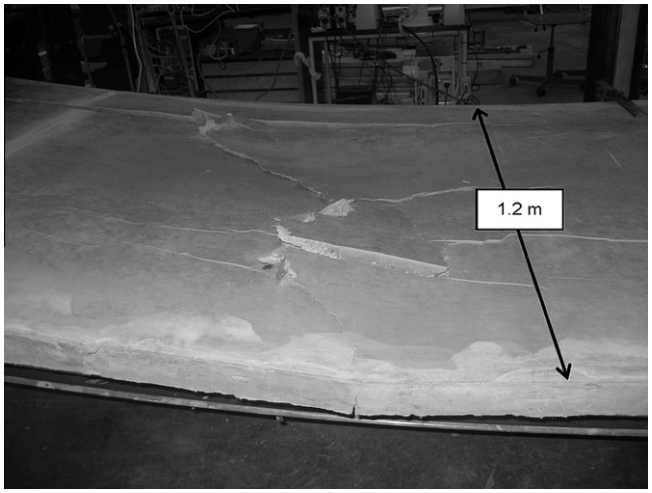

Fig. 18. Compression failure at mid-span of ICP2.

Fig. 19. Buckling of compression diagonals in specimen MP1.

MP3 and MP4. The increase in the natural frequency between the different specimens is directly related to the increase in stiffness of the composite panels and inversely related to its mass and applied load.

Due to the unknown effect of slip in the bolted connections of MP1, MP2 and MP3 on the damping measurements, the results from these tests were disregarded. Results from testing of ICP and MP4 are shown in Fig. 15. The damping ratio for the ICP specimens was found to be in the range of 0.6–1.8% and 0.6–1.0% for MP4 depending on the load arrangement. The damping ratio appears to be dependent on the change in mass and increasing as more loading is applied, indicating at increasing loads more damping mechanisms are activated in the specimens.

4.4.2. Testing at ultimate limit state (ULS)

During the ULS testing procedure, the deflections and load values were monitored along with strains of the tension member and selected diagonals of the steel trusses. The total load applied versus mid-span deflection for all specimens is shown in Fig. 16.

Specimen ICP1 reached a total load of 276 kN before one pair of the thin walled steel profiles fractured and the testing was terminated. The crack initiated and propagated from a small pre-existing hole close to the tension flange at mid-span resulting in a failure of the deck panel (Fig. 17).

Testing of specimen ICP2 was terminated after a compression failure occurred in the ECC slab, observed as a compression – sliding crack across the deck element at mid-span (Fig. 18). Prior to ultimate failure, a crack had formed over the length of the ECC deck slab at the interface of one of the embedded steel profiles, starting at mid-span and propagating to both ends. The total load ultimately reached 292 kN with a mid-span deflection in excess of 500 mm before failure occurred.

At a total load of 90 kN, testing of specimen MP1 was terminated when buckling of the compression diagonals occurred close to the end supports of the deck element due to shear (Fig. 19). Buckling of the diagonals was accompanied by twisting of the tension member of the truss structure due to eccentric positioning of the diagonal members relative to the longitudinal centerline of each truss; this detail was revised in subsequent specimens MP2, MP3 and MP4.

Testing of specimen MP2 was terminated when mid-span deflections exceeded 500 mm in a parabolic shape (Fig. 20). The tension member yielded between the quarter-points (points of loading) and ultimately reached 140 kN total applied load before testing was discontinued (Figs. 16 and 20). After testing, the ECC slab showed limited cracking, mainly propagating from the cast-in anchors directly below the point of loading, while multiple flexural cracking was observed at mid span (Fig. 21).

After testing of specimen MP2, the yielded tension members were replaced with profile members with a larger cross-section before the panel was reinstalled and tested as specimen MP3.

Testing of specimen MP3 resulted in an abrupt failure of the deck element due to shearing in the bolts connecting the diagonals of the steel truss. The total load reached 126 kN before shear failure occurred while slip in the bolted connections was apparent in the load–deflection graph (Fig. 16) as small drops in the load during ULS loading of specimen MP3. Slipping is observed up to about 70 mm deflection, above which no slip is observed and the load-deformation response becomes linear up until failure.

Specimen MP4 reached a total load of 291 kN before the test was terminated when the specimen ruptured and the substructure yielded directly below the points of loading (quarter points) (Fig. 22). At ultimate load, the specimen reached a mid-span deflection of 282 mm before structural failure occurred, resulting

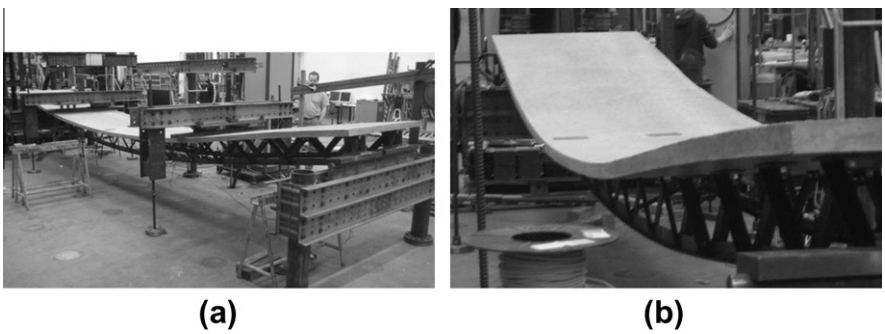

Fig. 20. Deformed shape of specimen MP2 during (a) and after (b) ULS loading.

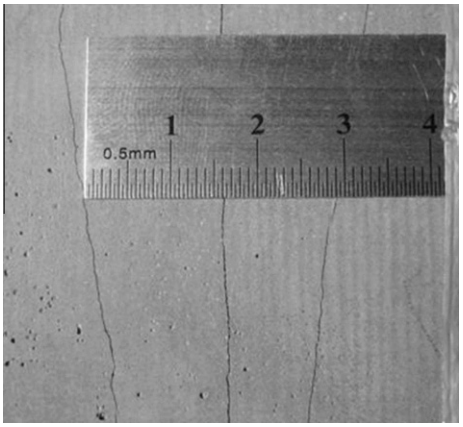

Fig. 21. Example of resulting cracks after ULS loading, figure shows multiple flexural cracks on bottom of ECC deck at mid-span.

Fig. 22. A combination of compression and flexural failure during ULS testing of specimen MP4.

in a reduced load carrying capacity. It was observed that the interlocking connections between the truss substructure and the anchor points next to the support footings had slipped, causing a crack to form directly above the support footings as well as bending of the connecting tension diagonal (Fig. 23).

Fig. 23. Excessive deformations at support due to slip in interlocking connection between truss and anchor point.

5. Discussion

The design criteria for the composite ECC deck panels included the loading capacity, a ductile failure mode by yielding of the steel substructure during ULS loading, a deflection limit, and a limited natural frequency (eigenfrequency) during SLS loading.

To evaluate these criteria, an experimental program was employed for the Integrally Cast Panel (ICP) and the Modular Panel (MP).

The concept of the Integrally Cast Panels (ICPs) and the Modular Panels (MPs) has numerous advantages over currently used prefabricated elements, most importantly the superimposed load to weight ratio (Table 1).

The ICP offers a simple construction concept, where lightweight steel profiles are joined directly with ECC slab to form a deck element, while the modular construction concept with the embedded anchors resolved some of the technical issues encountered in the ICPs specifically the shrinkage induced deformation of the panels. The Modular Panels (MPs) offer the possibility to assemble the panels after drying shrinkage deformations in the ECC slab occur, which results in a significant reduction of the required precamber of the panels prior to installation and testing.

The purpose of the experimental program described in this paper is to analyze the structural behavior of the panel concept and to revise and improve the design through a trial and error methodology. The revised design obtained from these tests will serve as a foundation for a more detailed study in order to potentially commercialize the thin ECC floor panel concept (see Table 2).

5.1. Serviceability limit state

The measured deflections of the deck panels during SLS loading were all found to be below the required limit of L/400 (20 mm), furthermore all but deck panels MP1 and MP2 were below L/500 (16 mm) (Fig. 13). Furthermore the linear load–deflection responses in Fig. 13 indicate a full composite interaction of the deck slab with the substructure. While the analytical results for the modular panels (MP1–MP4) were consistently higher than the predicted results obtained from the numerical models, all of them are in good agreement with the experimental results (Table 3).

The natural frequencies of the panels (without additional loading) were measured to be in the range of 7.1 Hz (for MP1)–8.2 Hz (for ICP) and 3.8 Hz (for MP1)–5.0 Hz (for MP4) for the decks loaded with 4.0 kN/m^2 (see Fig. 14 for detailed results).

The decrease in deflection and increase in dynamic response between specimens MP1–MP4 and the ICP specimens relates directly to the increase in equivalent stiffness of the specimens. Due to the low weight of the composite panels, any superimposed loading is significant considering the low self weight of the specimens. Therefore, any additional weight will decrease the natural frequency of lighter deck systems proportionally more than for heavier, conventional deck systems. By alternating the position and the cross-sectional area of the tension member, a desired reduced deflection and natural frequency can be achieved to meet a wide range of design requirements on the static and dynamic performance of the composite ECC floor panels. Moreover, by optimizing the cross-section of each part in the steel substructure, the self weight

Table 2
Properties of ECC.

Flexural strength	16 MPa
Tensile strength	4–6 MPa
Tensile strain capacity	3–4%
Compressive strength	60 MPa
Modulus of elasticity	18 GPa
Density	2000 kg/m^3

Table 3
Comparison of: mid-span deflections, natural frequencies and mid-span stresses from analytical results (Ana.), numerical results (Num.) and actual measurements (Meas.) during SLS testing. Stresses are shown for a 4.0 kN/m^2 loading.

	Specimen MP1			Specimen MP2			Specimen MP3			Specimen MP4			Specimen ICP		
	Ana.	Num.	Meas	Ana.	Num.	Meas	Ana	Num.	Meas	Ana.	Num.	Meas	Ana.	Num.	Meas
Deflection (mm)															
At 4.0 kN/m^2	17.9	15.7	19.4	17.9	15.2	17.2	14.2	9.9	11.7	12.8	9.6	10.2	10.8	–	12.8
Span/defl.	447	510	412	447	526	465	563	808	684	625	833	784	741	–	625
Frequency (Hz)															
At self weight	7.23	8.12	8.20	7.10	8.22	8.40	7.74	9.85	10.20	7.97	9.99	9.85	9.5	–	8.1
At 4.0 kN/m^2	3.39	–	3.80	3.37	–	4.00	3.76	–	4.80	3.93	–	5.00	4.7	–	4.5
Stresses (MPa) at 4.0 kN/m^2 loading															
σ_{ECC}	4.7	3.8	–	4.7	3.8	–	5.2	3.2	–	5.6	3.2	–	1.6	–	–
σ_S	149.5	114.2	143.7	150.8	114.0	132.8	108.4	64.1	70.9	105.8	48.7	–	121.0	–	–

of the panels can be further reduced without compromising performance.

The measured decay of the free vibrations of the deck panels or damping ratios were found to be 0.6–1.0% for MP4 and 0.6–1.8% for ICP depending on the applied load (Fig. 15). As an example, according to CEB bulletin on vibrations in structures [18], the damping ratios found in the testing program correspond to those expected in composite sport and dance floors where the damping ratios have a minimum value of 0.8% and a maximum value of 2.5%.

Strain development in selected members of the truss structures of modular deck panels MP1, MP2 and MP3 were monitored during testing to verify the analytical and numerical predictions. In Table 3, a comparison of the equivalent stresses in the tension member (σ_S) and in the deck slab at mid-span (σ_{ECC}) is shown for all deck panels. The predicted diagonal forces obtained from the numerical models of MP1, MP2 and MP3 at SLS loading were all similar, whereas the values for MP4 were about 10–15% lower. The measured values in the diagonal members were consistently higher than the numerical predictions and rather scattered. The inconsistency of the measured force-distribution is most likely due to several factors including: inaccuracy in the fabrication of the individual truss elements, bolted connections, placement of strain gauges and precamber procedure, i.e. how the whole structure was assembled to create a negative deflection of the panels. As a result, the critical compression diagonals in the truss structure of MP1 (which ultimately failed due to bucking) were measured to have reached 85% of their theoretical buckling load at SLS loading of 4.0 kN/m^2.

At a 4.0 kN/m^2 loading of the composite panel, the load in the tension member of specimens MP1 and MP2 reached 55% of the yielding capacity of the steel while only utilizing 5% of the compression strength of the ECC slab. Equivalently, specimens MP3 and MP4 reached 20% of the yielding capacity of the tension member while utilizing about 10% of ECC compression capacity. To ensure a ductile failure mode at the ultimate limit state, the yielding capacity of the tension member of the truss structure must be lower than the compression capacity of the ECC slab as has been shown for MP2, MP4, ICP1 and ICP2 (Fig. 16).

5.2. Ultimate loading

Besides the structural detailing of the support footings, specimens ICP1 and ICP2 are identical and test results were are very similar, accordingly. The thin-walled steel profiles for both ICP1 and ICP2 started to yield at a total load of about 200 kN (equivalent to an area load of 21 kN/m^2) and continued to yield up to relatively large deflections of the specimens.

Specimen ICP1 failed unexpectedly when one pair of the thin-walled steel joists failed in tension (Fig. 17a). The failure caused a crack to form in the ECC deck slab immediately above the un-cracked profiles (Fig. 17b). This abrupt failure of the steel profiles resulted in a shift in the force distribution of the deck specimen causing the crack to form between the transversely protruding edge of the steel profile and the rest of the deck slab (Fig. 17b).

ICP2 reached a total load of 292 kN, equivalent to an area load of 30 kN/m^2, before its load carrying capacity was reached. Due to the large deflections in the deck panel, the tension and compression components of the cross-section associated with the moment of the deck panel also have vertical components. This vertical force resulted in a crack forming at the interface of the steel joist and the ECC slab, which consequently became the weak part of the cross-section due to the embedded steel joists (see Fig. 6a).

Beside the premature buckling and twisting of the steel substructure of specimen MP1, it was observed after testing had been terminated that cracks had begun to propagate from the corners of the embedded cast-ins directly below the quarter-points.

Testing of specimen MP2 resulted in a ductile failure mode, where the tension members began to yield at a total load of 110 kN (equivalent to an area load of 11 kN/m^2) and ultimately reaching 140 kN (equivalent to 15 kN/m^2) before testing was terminated. The tension member yielded over a 4.0 m mid-span section between the quarter points where the moment and consequently the tensile force in the cross-section of the truss was highest. The 4.0 m yield zone is furthermore restrained due to the additional stiffness of the replaced diagonals on each side of the yield zone.

At reaching the ultimate loading capacity, the cracking in the vicinity of the cast-in anchors had increased slightly and some flexural cracks had formed on the bottom side of the ECC slab at mid-span of the deck panel (Fig. 21).

As a result of the slip observed during testing of specimen MP3, a bolt in the bolted truss substructure sheared, causing the failure of the specimen. From about 60 kN (70 mm deflection) up to failure, the load–deflection response of MP3 is linear (Fig. 16), indicating that no slip occurred during that load interval. Furthermore, this linear response implies that the composite stiffness of MP3 is slightly less than that of MP4.

Testing of specimen MP4 was stopped once the element had exhibited a combination of a flexural and compression failure directly at the point of loading (quarter points) (Fig. 22). Prior to this failure, the interlocking connection between the steel truss and single-channel cast-in anchors had reached its ultimate load capacity and slipped, resulting in cracking of the ECC slab directly above the supports and bending of the end diagonal (Fig. 23). This slip in MP4 can be seen in Fig. 16 as relatively small drops in the load from 80 mm to about 230 mm deflection of the deck panel.

Both the slip in the bolted truss structure of MP3 and the slip in the interlocking connection between truss and embedded anchors of MP4 (as seen in Fig. 16) were clearly audible as acoustic events during testing.

6. Conclusions

An investigation of the structural behavior of prefabricated, light-weight composite deck elements, composed of high performance fiber reinforced cementitious composite and a steel substructure was presented in this paper. Two types of deck elements, the Integrally Cast Panels (ICPs) and the Modular Panels (MPs), were studied and compared.

The integrally cast panel design utilizes the simplicity of thin walled steel joists integrally joined with an ECC slab to form a deck panel. The modular panel concept expands on the benefits of the ICP by embedding anchors into the ECC deck slab, which are subsequently used to attach a steel truss substructure.

During the experimental program, the load–deflection behavior of both types of panels was shown to be consistent with predicted results and the failure modes were found to be ductile. Furthermore, it was demonstrated that by altering the steel truss substructure desired changes in the structural response can be achieved.

The deflections and natural frequencies of both types of panels were found to be within acceptable limits. The dynamic properties of the tested specimens were shown to meet typical structural performance requirements, however, additional research is needed to further improve the dynamic behavior towards higher natural frequencies and improved damping.

Both the ICP and MP concept offer the flexibility of adapting to a multitude of different performance requirements by selection of a specific combination of ECC deck and steel substructure, thereby controlling the strength and stiffness properties of the panel. Furthermore, the integrally cast and the modular concept with the embedded anchors allow the ECC slab and the attached substructure to behave as one composite element during loading.

The benefits of using a strain hardening concrete such as ECC are most evident in the tensile loading capacity and ductility of ECC which can eliminate transverse steel reinforcement and enables a ductile failure mode of the panel. However some transverse steel reinforcement could be provided for redundancy and safety. Furthermore, the significantly reduced amount of cementitious material and the high amount of recycled materials such as fly-ash (about 45% by weight) in ECC leads to reduced natural resource demands.

The design concept of both the ICP and the MP system offer a 70% weight reduction in comparison to hollow core decks while meeting structural performance requirements. Due to the layout of individual anchor points in the modular panels, shrinkage deformations of ECC do not cause initial deflections in the modular floor panel concept.

To meet fire resistance requirements for the presented design concepts, a few methods have been proposed for a similar structural floor concept [11]. For example, by placing gypsum boards under the steel substructure and thus isolating both the steel structure and the ECC slab from fire, or by spray-applying a fire-resistance material directly onto the substructure and ECC slab. Both approaches have been tested and rated for 1–3 h fire-resistance, depending on the thickness of gypsum boards or applied spray-on layer. Such fire resistance measures would also improve the acoustic resonance of the design.

A detailed study of the long-term behavior of the composite panels influenced by creep of the ECC slab, cyclic loading under service conditions and shear capacity is currently under way. In this context, due to the lack of conventional reinforcements and thin ECC slab design, punching shear needs to be examined particularly to further develop the concept and pursue commercialization.

References

[1] Naaman AE, Reinhardt HW. Proposed classification of HPFRC composites based on their tensile response. Mater Struct 2006;39(5):547–55.
[2] Lárusson LH, Fischer G, Jönsson J. Mechanical interaction of ECC reinforced with FRP rebar in tensile loading. In: Proceedings of advanced concrete materials. Stellenbosch, South Africa; 2009. p. 83–90.
[3] Fischer G. Fiber reinforced concrete for precast applications: an overview on recent developments and applications. In: International concrete conference & exhibition. ICCX. Cape Town, South Africa; 2007. p. 56–60.
[4] FIP Recommendations. Precast prestressed hollow core floors. 2 CEN European Committee for Standardisation. London (UK): Thomas Telford; 1988. p. 1–31.
[5] Martin LD, Perry CJ. PCI design handbook: precast and prestressed concrete. 6th ed. CA (USA): Precast/Prestressed Concrete Institute; 2004.
[6] Ching FDK. A visual dictionary of architecture. NY (USA): John Wiley and Sons; 1995. p. 203–6.
[7] Knudson B. Alternative concrete. Construction-Today Magazine; March 2009. p. 106–7.
[8] Schnellenbach-Held M, Pfeffer K. Punching behavior of biaxial hollow slabs. Cem Concr Compos 2002;24(6):551–6.
[9] Abramski M, Schnell J, Albert A, Pfeffer K. Experimental and numerical investigation of the bearing behaviour of hollow core slabs. Beton Stahlbetonbau 2010;105(6):349–61.
[10] Porter ML, Ekberg CE. Design recommendations for steel deck floor slabs. J Struct Div 1976;102(11):2121–36.
[11] Hambro. Hambro Technical Manual (Canada): Composite floor systems. Technical Publications; 2009. <http://www.hambro-floors.ws> [02.09.11].
[12] Kuhlmann U, Schanzlig J. A timber–concrete composite slab system for use in tall buildings. Struct Eng Int 2008;18(2):174–8.
[13] Lárusson L, Fischer G, Jönsson J. Mechanical interaction between concrete and structural reinforcement in the tension stiffening process. In: Proceedings of HPFRCC-6, Michigan, USA; 2011.
[14] Wang S, Li VC. Polyvinyl alcohol fiber reinforced engineered cementitious composites: material design and performances. In: Proceedings of international workshop on HPFRCC in structural applications. Honolulu, Hawaii; 2005. p. 104–11.
[15] Li VC, Fischer G. Reinforced ECC – an evolution from materials to structures. In: Proceedings of the first FIB congress, Osaka, Japan; October 2002. p. 105–22.
[16] Fischer G, Li VC. Influence of matrix ductility on the tension-stiffening behavior of steel reinforced Engineered Cementitious Composites (ECC). ACI Struct J 2002;99(1):104–11.
[17] Chopra AK. Dynamics of structures, theory and applications to earthquake engineering. 3rd ed. Prentice Hall; 2007. p. 48–50.
[18] Comité Euro-international du Béton. Vibration problems in structures: practical guidelines. Contribution à la 28.session plénière du CEB. Vienna; 1991.
[19] Flarus NV. "Concrete". "Stamped hollow core Damman Croes.jpg"; 2005. <http://www.flarus.com/Concrete.html> [08.04.11].
[20] United States Department of Transportation – Federal Highway Administration. "Focus – Desember 2003". "ibeams.jpg"; 2003. <https://www.fhwa.dot.gov/publications/focus/03dec/03.cfm> [08.04.11].
[21] Borecki M. "Filigran floor". "plyta6.jpg"; 2011. <http://www.marekborecki.pl/plyty_en.php> [08.04.11].
[22] RLSD. Richard Lees Steel Decking. "Ribdeck AL". From technical manual; 2008. <http://www.rlsd.co.uk/pages/ribdeck-al.php> [20.08.08].